

ABSTRACT

Title of Dissertation: THEORETICAL AND EXPERIMENTAL
STUDY OF AUTOIGNITION OF WOOD

Nathasak Boonmee,
Doctor of Philosophy, 2004

Dissertation Directed By: Professor James G. Quintiere
Department of Fire Protection Engineering

A theoretical and experimental study of the autoignition of wood is performed. In the experiment, a wood sample (redwood) of 4 by 4 cm surface area with 4 cm thickness is exposed vertically to a heater panel in a cone calorimeter. The surface temperature is continuously measured by an infrared thermocouple and mass loss is monitored by a load cell. Incident heat flux is varied until glowing ignition could not occur. Times to glowing ignition and flaming autoignition are measured. It is found experimentally that the critical heat flux for flaming autoignition is 20 kW/m^2 and for glowing ignition is 10 kW/m^2 .

A theoretical model for autoignition of wood is developed. The model considers the processes occurring in both solid and gas phases. In the solid phase, a one-dimensional heat conduction model is employed. Char surface oxidation, which can lead to glowing ignition, is taken into account at the solid-gas interface surface. By “glowing ignition”, it means the onset of surface combustion. Criteria for glowing ignition are developed based on a surface energy balance. A numerical result shows

that according to the present glowing ignition criteria, an inflection point of the surface temperature history can indicate glowing ignition. In the gas phase, a transient two-dimensional laminar boundary layer approximation for gas phase transport equations is constructed. The gas phase model is coupled with the solid phase model via the solid-gas interface surface. Flaming autoignition occurs when the maximum gas reaction rate exceeds a critical value. A numerical result from the coupled gas phase and solid phase models shows that autoignition of the combustible gases behaves in two fashions as autoignition type I at high heat flux and autoignition type II at low heat flux. In the type I autoignition, the flaming occurs just an instant after glowing ignition is initiated, while in the type II autoignition, the solid undergoes glowing ignition long before the flaming is achieved.

Comparisons between the theoretical and experimental results are presented to demonstrate capabilities and limitations of the proposed model.

THEORETICAL AND EXPERIMENTAL STUDY OF AUTOIGNITION OF WOOD

By

Nathasak Boonmee

Dissertation submitted to the Faculty of the Graduate School of the
University of Maryland, College Park, in partial fulfillment
of the requirements for the degree of
Doctor of Philosophy
2004

Advisory Committee:
Professor James G. Quintiere, Chair
Professor Arnaud Trouvé
Professor Andre Marshall
Professor Gregory Jackson
Professor Kenneth Yu

Acknowledgements

First of all, I would like to express my deepest gratitude to Dr. James Quintiere, my advisor, who teaches me how to look to a fire in a way that I have never thought before and it's really fun! I am also grateful to his supervising, supporting, and encouraging me to do the best work. Without him, my degree would never have been completed. I am thankful to Dr. Arnaud Trouvé for his invaluable suggestions and comments in my numerical programming. I would like to thank Dr. Andre Marshall and Dr. Gregory Jackson for their valuable comments and for serving me as a committee. I am grateful to Dr. Kenneth Yu for serving me on the committee as the Dean's representative. A special thank also goes to Dr. James Milke, a professor in Fire Protection Engineering who I first met in Thailand, for accepting me to the graduate program when I first came here.

I am grateful to Ariya Jirapatwong (Aey), who always understands, supports, and inspires me to reach my goal. I would like to thank Yunyong Utiskul (Pock) for helping me set-up the experiment, Kaoru Wakatsuki for a fun trip in Japan, Yi Wang and Tingguang Ma for a fun discussion in CFD stuff, Kate for proof reading my English and my Thai friends for a life outside the office. A sincere thank also goes to my friends in the ENFP graduate office, Potomac Lab, FETS lab, and the entire staff of the Department of Fire Protection Engineering for being such good friends and making me feel as though this is my second home.

I would like to thank the John L. Bryan Chair Fund (Department of Fire Protection Engineering), National Science Foundation (NSF), and the Department of Mechanical Engineering, Kasetsart University, Thailand for their financial support.

Finally I am extremely indebted to my family in Thailand, Mom, Dad, Na Rat, P'Tom, P'Tik, and P'Wan. Without them, I would never have had a chance to come to study in the USA and make my dreams come true!!!

Table of Contents

List of Tables	vii
List of Figures	viii
List of Abbreviations	xv
Chapter 1: Introduction	1
1.1 Introduction	1
1.2 Literature Review	3
1.2.1 Experimental Studies	3
1.2.2 Theoretical Studies	7
1.3 Problem Descriptions	22
1.4 Objective and Plan	24
Chapter 2: Experiment	26
2.1 Introduction	26
2.2 Experimental Descriptions	27
2.2.1 A Wood Sample	27
2.2.2 Experimental Setup and Procedures	28
2.3 Experimental Observations	31
2.4 Surface Temperature Measurement	33
2.4.1 An Infrared Thermocouple and Its Calibration	33
2.4.2 A Measurement of Wood Surface Temperature	38
2.5 Mass Loss Measurements	45
2.6 Glowing Ignition and Flaming Autoignition Experimental Data	47
2.7 Conclusions	51
Chapter 3: A Kinetic Modeling of Wood Pyrolysis	52
3.1 Introduction	52
3.2 Thermogravimetric Experiments	54
3.3 Methods to Determine the Wood Kinetic Parameters	57
3.3.1 Differential Method	58
3.3.2 Integral Method	60
3.4 Application to Wood Pyrolysis	63
3.5 Derivation of Activation Energy and Pre-exponential Factor	65
3.6 Kinetic Modeling of Wood Pyrolysis	71
3.7 Comparisons of Wood Kinetic Parameters	79
3.8 Heat of Wood Pyrolysis	83
3.9 Conclusions	84
Chapter 4: The Solid Phase	88
4.1 Introduction	88

4.2 Theoretical Model	89
4.2.1 Assumptions	89
4.2.2 Description of a Decomposing Wood System	91
4.2.3 Species Conservation	93
4.2.4 Mass Conservation	95
4.2.5 Energy Conservation	95
4.2.6 Boundary Conditions	101
4.2.7 Non-dimensional Governing Equations	103
4.3 Char Surface Oxidation Model	105
4.3.1 Theoretical Model	107
4.3.2 Diffusion-Controlled Char Surface Oxidation	107
4.3.3 Kinetic-Controlled Char Surface Oxidation	114
4.3.4 Overall Char Surface Oxidation	116
4.4 Glowing Ignition Criteria	120
4.5 Solid Phase Results and Discussions	127
4.5.1 Numerical Grid Refinement	127
4.5.2 Gasification Rate in N ₂ Atmosphere	129
4.5.3 Wood Combustion	134
4.5.4 In-depth Solid Profiles	134
4.5.5 Glowing Ignition: Experimental and Theoretical Results	137
4.5.6 Effects of the Surrounding Oxygen Concentration	142
4.6 Conclusions	145
Chapter 5: The Gas Phase	147
5.1 Introduction	147
5.2 Theoretical Model	148
5.2.1 Assumptions	148
5.2.2 Governing Equations and Boundary Conditions	150
5.2.3 Non-dimensional Governing Equations and Boundary Conditions	155
5.2.4 Coupled Procedure for Solid and Gas Phase Calculations	160
5.3 Numerical Validation	162
5.3.1 A Natural Convection Flow over a Vertical Isothermal Hot Wall	162
5.3.2 Grid Refinement Study	165
5.4 Flaming Autoignition Criteria	167
5.5 Gas Phase Results and Discussions	176
5.5.1 Flaming Autoignition Behavior	176
5.5.2 Flaming Autoignition: Theoretical and Experimental Results	184
5.5.3 Flammability Diagram	191
5.6 Conclusions	193
Chapter 6: Conclusions and Future Work	195
6.1 Conclusions	195
6.2 Future Work	197

Appendices	200
Appendix A: Solid Phase Numerical Methods	200
A-1: Solid Phase Model	200
A-2: Moving Boundary Algorithm	205
Appendix B: Gas Phase Numerical Method	208
Appendix C: Summary of Experimental Data	213
References	227

List of Tables

Table 1.1: Summary of literature theoretical models	16
Table 3.1: Summary of E_a and a_p at different degrees of α_i for (a) isothermal and (b) non-isothermal based on Eq. (3.7) and (3.8)	66
Table 3.2: Summary of E_a and a_p at different degrees of α_i for non-isothermal based on Eq. (3.15) and (3.16) ($X_c = 0.2$)	67
Table 3.3: Summary of wood kinetic parameters and heat of pyrolysis	86
Table 4.1: Summary of the numerical input parameters	131
Table 5.1: A summary of mesh size in grid refinement study	165
Table 5.2: Summary of the flaming ignition criteria	170
Table 5.3: Summary of the gas kinetic parameters	174
Table B1: Definition of variables in Eq. (B2)	208
Table C1: Summary of Experimental Data; Heating Along the Grain	213
Table C2: Summary of Experimental Data; Heating Across the Grain	214

List of Figures

Figure 1.1: A schematic diagram of the processes involving in autoignition of wood	22
Figure 2.1: Sample grain orientation (picture adopted from Ref. [23])	28
Figure 2.2: Schematic diagram of the experimental setup	29
Figure 2.3: Calibration curve for the cone heater temperature	30
Figure 2.4: A sequence of wood glowing ignition leading to gas flaming autoignition ($\dot{q}_i'' = 30 \text{ kW/m}^2$, heating across the grain), the cone heater panel is located on the left of each picture.	32
Figure 2.5: Schematic diagram for the IR thermocouple aspect ratio and its view area: the reading temperature represents an average surface temperature over the shading area (Not draw in scale)	34
Figure 2.6: (a) Output signals from IR thermocouple and (b) Output signal from conventional thermocouple for various heat fluxes	36
Figure 2.7: (a) calibration correlations and (b) the rate of change of the IR thermocouple signal (The plot shows only 1 test per heat flux to avoid overcrowded)	36
Figure 2.8: Comparisons of the surface temperatures measured by IR and conventional thermocouples	38
Figure 2.9: Measurement of wood surface temperature by an IR thermocouple: a raw signal time history ($\dot{q}_i'' = 25 \text{ kW/m}^2$, heating across the grain; $t_{glowing} = 229 \text{ s}$; $t_{flaming} = 1600 \text{ s}$)	39
Figure 2.10: Surrounding (ambient) temperatures around the IR thermocouple ($\dot{q}_i'' = 25 \text{ kW/m}^2$, heating across the grain)	42
Figure 2.11: Systematic diagram illustrates the total radiant energy detected by the IR thermocouple	42

Figure 2.12: A plot of surface temperature time history ($\dot{q}_i'' = 25 \text{ kW/m}^2$, heating across the grain; $t_{\text{glowing}} = 229 \text{ s}$, $T_{\text{glowing}} = 391 \text{ }^\circ\text{C}$; $t_{\text{flaming}} = 1600 \text{ s}$, $T_{\text{flaming}} = 667 \text{ }^\circ\text{C}$)	44
Figure 2.13: A plot of typical mass loss time histories for various heat fluxes	45
Figure 2.14: A plot of typical mass loss rate per unit area (mass flux) for various heat fluxes	46
Figure 2.15: Experimental glowing and flaming autoignition times	47
Figure 2.16: Experimental glowing and flaming autoignition surface temperature	50
Figure 2.17: Experimental glowing and flaming autoignition mass flux	50
Figure 3.1: (a) Isothermal (various constant temperatures) and (b) non-isothermal (various constant heating rates) mass loss history	56
Figure 3.2: Isothermal and non-isothermal plots of $\ln[(d\alpha/dt)_i]$ against $1/T(\alpha_i)$ for various α_i	69
Figure 3.3: Non-isothermal plot of $\ln \beta$ against $1/T(\alpha_i)$ for various α_i	70
Figure 3.4: Plot of Arrhenius rate constant ($k(T)$) of wood pyrolysis for non-isothermal TGA, $\beta = 1 \text{ }^\circ\text{C/min}$	70
Figure 3.5: Plot of 1- experimental $k(T)$; 2 - calculated $k(T)$; 3-remaining fractional density ($1 - \alpha$); and 4-experimental $d\alpha/dt$ for non-isothermal TGA, $\beta = 1 \text{ }^\circ\text{C/min}$	73
Figure 3.6: Plot of non-isothermal wood decomposition rate ($d\alpha/dt$) for various β	73
Figure 3.7: Plot of 1- overall wood decomposition rate (Eq. (3.23)); 2- $X_1 d\alpha_1/dt$, cellulose decomposition rate; 3- $X_2 d\alpha_2/dt$, hemicellulose decomposition rate; 4- $X_3 d\alpha_3/dt$, lignin decomposition rate; 5-single global wood decomposition rate; 6- experimental data, for non-isothermal TGA, $\beta = 10 \text{ }^\circ\text{C/min}$	78
Figure 3.8: Plot of experimental and calculated remaining mass conversion ($1 - \alpha$) for non-isothermal TGA, $\beta = 10 \text{ }^\circ\text{C/min}$	78

Figure 4.1: Systematic diagram for one-film model diffusion-controlled char surface oxidation	109
Figure 4.2: Systematic diagram for char surface oxidation electrical circuit series	118
Figure 4.3: Diffusion and kinetic resistances as a function of surface temperature ($\dot{q}'' = 40 \text{ kW/m}^2$, $Y_{O,\infty} = 0.233$)	119
Figure 4.4: Surface energy balance and its corresponding T_s history ($\dot{q}_i'' = 15 \text{ kW/m}^2$, $Y_{O,\infty} = 0.4$)	123
Figure 4.5: $dG(T_s)/dT_s$ vs. T_s and its surface energy balance ($\dot{q}_i'' = 50 \text{ kW/m}^2$, $Y_{O,\infty} = 0.40$)	124
Figure 4.6: A plot of $\dot{q}_{OX,glowing}'' / \dot{q}_i''$ vs. \dot{q}_i'' for various $Y_{O,\infty}$ ($\gamma \rightarrow 0$, in the char surface oxidation model)	126
Figure 4.7: Surface temperature and pyrolysis mass flux history for various grid sizes	128
Figure 4.8: Percent difference for (a) surface temperature and (b) pyrolysis mass flux	128
Figure 4.9: Gasification rate in N_2 atmosphere for (a) $\dot{q}_i'' = 20 \text{ kW/m}^2$, (b) $\dot{q}_i'' = 40 \text{ kW/m}^2$, and (c) $\dot{q}_i'' = 60 \text{ kW/m}^2$; experimental gasification rates were taken from Ritchie et al. [33]	130
Figure 4.10: (a) surface temperature, and (b) pyrolysis mass flux histories ($\dot{q}_i'' = 25 \text{ kW/m}^2$, $Y_{O,\infty} = 0.233$)	132
Figure 4.11: (a) char surface oxidation mass flux, and (b) surface oxygen mass fraction histories; ($\dot{q}_i'' = 25 \text{ kW/m}^2$, $Y_{O,\infty} = 0.233$)	134
Figure 4.12: (a) in-depth non-dimensional wood density profiles, (b) in-depth temperature profiles, and (c) in-depth solid reaction rate profiles; profiles starting at 44.80 seconds with 44.80 second time-step increments ($\dot{q}_i'' = 25 \text{ kW/m}^2$, $Y_{O,\infty} = 0.233$)	136
Figure 4.13: Glowing ignition time as a function of incident heat flux	138

Figure 4.14: Glowing ignition surface temperature as a function of incident heat flux	139
Figure 4.15: Glowing ignition mass flux as a function of incident heat flux	141
Figure 4.16: Theoretical glowing ignition surface temperature and mass flux as a function of incident heat flux for various oxygen mass fraction	143
Figure 4.17: Theoretical glowing ignition time and $Y_{O,glowing} / Y_{O,\infty}$ as a function of incident heat flux for various ambient oxygen mass fraction	144
Figure 5.1: Systematic diagram for gas phase boundary layer model	148
Figure 5.2: Problem configuration of a natural convection over a vertical wall	162
Figure 5.3: Comparisons of steady state v -velocity and temperature for a natural convection flow over a vertical isothermal wall of 400 K; the exact solution is taken from Ref.[63]	164
Figure 5.4: Plots of maximum gas temperature history for various mesh sizes	166
Figure 5.5: Plots of maximum gas reaction rate history for various mesh sizes	167
Figure 5.6: Plot of the maximum gas reaction rate ($\dot{\omega}_{g,max}'''$) history for various sets of the gas kinetic parameters listed Table 5.3 ($\dot{q}_i'' = 60 \text{ kW/m}^2$)	175
Figure 5.7: (a) Gas maximum temperature, and wood and insulator surface temperature time histories and (b) pyrolysis mass flux time history (Autoignition type I, $\dot{q}_i'' = 50 \text{ kW/m}^2$, $t_{flaming} = 32 \text{ s}$, $t_{glowing} = 30 \text{ s}$)	178
Figure 5.8: Contour plots of (a) fuel and (b) oxygen mass fraction at the instant of flaming autoignition (Autoignition type I, $\dot{q}_i'' = 50 \text{ kW/m}^2$, $t_{flaming} = 32 \text{ s}$)	179
Figure 5.9: Contour plots of (a) gas temperature and (b) gas reaction rate at the instant of flaming autoignition (Autoignition type I, $\dot{q}_i'' = 50 \text{ kW/m}^2$, $t_{flaming} = 32 \text{ s}$)	179
Figure 5.10: Velocity vector field and streamlines at the instant of flaming autoignition (Autoignition type I, $\dot{q}_i'' = 50 \text{ kW/m}^2$, $t_{flaming} = 32 \text{ s}$)	180

Figure 5.11: (a) Gas maximum temperature, and wood and insulator surface temperature time histories and (b) pyrolysis mass flux time history (Autoignition type II, $\dot{q}_i'' = 30 \text{ kW/m}^2$, $t_{flaming} = 126 \text{ s}$, $t_{glowing} = 86 \text{ s}$)	181
Figure 5.12: Contour plots of (a) fuel and (b) oxygen mass fraction at the instant of flaming autoignition (Autoignition type II, $\dot{q}_i'' = 30 \text{ kW/m}^2$, $t_{flaming} = 126 \text{ s}$)	182
Figure 5.13: Contour plots of (a) gas temperature and (b) gas reaction rate at the instant of flaming autoignition (Autoignition type II, $\dot{q}_i'' = 30 \text{ kW/m}^2$, $t_{flaming} = 126 \text{ s}$)	182
Figure 5.14: Velocity vector field and streamlines at the instant of flaming autoignition (Autoignition type II, $\dot{q}_i'' = 30 \text{ kW/m}^2$, $t_{flaming} = 126 \text{ s}$)	183
Figure 5.15 Flaming autoignition and glowing ignition time as a function of incident heat flux	185
Figure 5.16 Flaming piloted ignition and glowing ignition times as a function of incident heat flux	186
Figure 5.17 Flaming autoignition and glowing ignition temperature as a function of incident heat flux	189
Figure 5.18: Flaming autoignition and glowing ignition mass flux as a function of incident heat flux	190
Figure 5.19: Flammability diagram of wood	192
Figure A1: Schematics of the finite grid	200
Figure A2: Systematic diagram for moving boundary algorithm	205
Figure C1: (a) surface temperature and (b) mass flux time histories (Test ID: 30-4-AL)	215
Figure C2: (a) surface temperature and (b) mass flux time histories (Test ID: 30-5-AL)	215
Figure C3: (a) surface temperature and (b) mass flux time histories (Test ID: 25-10-AL)	216

Figure C4: (a) surface temperature and (b) mass flux time histories (Test ID: 25-11-AL)	216
Figure C5: (a) surface temperature and (b) mass flux time histories (Test ID: 20-14-AL)	217
Figure C6: (a) surface temperature and (b) mass flux time histories (Test ID: 20-15-AL)	217
Figure C7: (a) surface temperature and (b) mass flux time histories (Test ID: 20-16-AL)	218
Figure C8: (a) surface temperature and (b) mass flux time histories (Test ID: 18-18-AL)	218
Figure C9: (a) surface temperature and (b) mass flux time histories (Test ID: 18-20-AL)	219
Figure C10: (a) surface temperature and (b) mass flux time histories (Test ID: 10-22-AL): Note a spike peak on the mass flux plot was a noise from the load cell signal	219
Figure C11: (a) surface temperature and (b) mass flux time histories (Test ID: 10-31-AL)	220
Figure C12: (a) surface temperature and (b) mass flux time histories (Test ID: 9-25-AL)	220
Figure C13: (a) surface temperature and (b) mass flux time histories (Test ID: 30-7-AC)	221
Figure C14: (a) surface temperature and (b) mass flux time histories (Test ID: 30-9-AC)	221
Figure C15: (a) surface temperature and (b) mass flux time histories (Test ID: 25-12-AC)	222
Figure C16: (a) surface temperature and (b) mass flux time histories (Test ID: 25-13-AC)	222
Figure C17: (a) surface temperature and (b) mass flux time histories (Test ID: 20-17-AC)	223
Figure C18: (a) surface temperature and (b) mass flux time histories (Test ID: 20-23-AC)	223

Figure C19: (a) surface temperature and (b) mass flux time histories (Test ID: 18-19-AC)	224
Figure C20: (a) surface temperature and (b) mass flux time histories (Test ID: 18-25-AC)	224
Figure C21: (a) surface temperature and (b) mass flux time histories (Test ID: 10-26-AC)	225
Figure C22: (a) surface temperature and (b) mass flux time histories (Test ID: 10-29-AC)	225
Figure C23: (a) surface temperature and (b) mass flux time histories (Test ID: 9-34-AC)	226

List of Abbreviations

a_p	pre-exponential factor (wood decomposition)
A_g	pre-exponential factor (gas kinetic reaction)
A_C	pre-exponential factor (char surface oxidation)
B	mass transfer number
c_p	specific heat at constant pressure
C	a constant
m	the slope of a linear line
D	mass diffusivity coefficient
E_a	activation energy
g	gravity
IR	infrared signal
h	enthalpy, heat transfer coefficient
ΔH	heat of combustion
k	thermal conductivity, Arrhenius rate constant
L	sample thickness, characteristic length
\dot{m}''	mass flux
P	pressure
np_x	number of points
\dot{q}''	heat flux
Q_p	heat of pyrolysis

R	the universal gas constant
t	time
T	temperature
u	cross-velocity component
v	streamwise velocity component
x, y	coordinate axis
Y	mass fraction
LFL	lower flammable limit
CFL	Courant-Friedrichs-Lewy number
Fo	Fourier number
Le	Lewis number
Pr	Prandtl number
Gr	Grashof number

Greek Symbols

α	thermal diffusivity, mass conversion fraction
β	thermal expansion coefficient, heating rate
δ	thermal diffusion length, boundary layer thickness
σ	Stefan-Boltzmann Constant
ε	surface emissivity
ϕ	independent variables
ν	dynamics viscosity, stoichiometric reaction ratio
μ	kinematics viscosity,

ρ	density, surface reflectivity
$\dot{\omega}$	reaction rate
θ	non-dimensional temperature
η	similarity variable
$\hat{\Sigma}$	dimensionless Stefan-Boltzmann constant
\hat{H}	dimensionless heat transfer coefficient

Superscripts

$()''$	per unit area
$()'''$	per unit volume
\wedge	non-dimensional variables
—	average value
0	enthalpy of formation at reference condition

Subscripts

∞	ambient
a	active wood
0	initial condition
act	actual
sur	surrounding condition for an infrared thermocouple calibration
break	break temperature, break point
exp	experimental values
e	emitted

<i>r</i>	reflected
<i>i</i>	incident, i^{th} degree of mass conversion fraction
<i>ref</i>	reference condition
<i>ig</i>	ignition
<i>flaming</i>	flaming autoignition
<i>glowing</i>	glowing ignition
<i>py</i>	pyrolysis
<i>mix</i>	mixing
<i>chem</i>	chemical
<i>j</i>	the j^{th} component of wood
<i>in</i>	insulator
<i>g</i>	gas
<i>W</i>	wood
<i>C</i>	char, carbon
<i>OX</i>	oxidation
<i>Cal</i>	calibration value
<i>f</i>	final, enthalpy of formation
<i>S</i>	surface, solid, sensible enthalpy
<i>In</i>	inert gas
<i>F</i>	fuel
<i>O</i>	oxygen
<i>IR</i>	infrared

Chapter 1

Introduction

1.1 Introduction

Ignition is the initial stage of combustion in fires. Understanding the ignition process is crucial in fire safety research because this basic knowledge provides ample scientific and engineering judgment that can be applied to reduce the chance of ignition and ultimately to minimize fire hazards. Since wood is a common material utilized for building construction, furniture, and various decorative purposes, understanding the ignition process of wood is very important.

The ignition phenomenon of wood is complex. It involves chemical reactions, and heat and mass transfer processes. First, wood must be heated by an external heat source (i.e. from a radiant heater or a building fire) until it reaches some critical temperature (pyrolysis temperature); then the wood starts to decompose producing pyrolysis gases. The pyrolysis gases are then released and mix with fresh air from the surroundings creating a boundary layer of the combustible mixture. When the combustible mixture reaches a suitable concentration (i.e. within flammable limit) and the mixture temperature is sufficient to accelerate the chemical reactions that can cause a gas thermal runaway, ignition occurs.

Generally, when wood is heated, two types of ignition are possible: (1) piloted (forced) ignition, where the ignition initiates with help of an external energy source, and (2) autoignition (spontaneous ignition), where the ignition initiates without any help of an external energy source. In previous investigations, Boonmee and Quintiere [1, 2] observed that the autoignition of wood could be further categorized into two regimes depending on an intensity of the incident heat flux: (1) flaming autoignition and (2) glowing ignition. Flaming autoignition occurs when the incident heat flux to the wood surface is high. The gas temperature is high enough to trigger the gas phase thermal runaway. The flame first appears in the gas phase above the wood surface and then propagates back to the surface. Glowing ignition is more likely noticed when the incident heat flux to the wood surface is relatively low. As the wood surface is heated, it becomes char; then oxygen from the surroundings diffuses to the char layer and reacts resulting in a char surface combustion or a glowing surface. The exothermic surface combustion adds energy to the combustible mixture adjacent to the char surface. When the combustible mixture temperature is sufficiently high, the glowing surface causes a transition to the flaming autoignition.

In this work, a theoretical and experimental study for ignition of wood is presented. The investigation mainly focuses on the autoignition regime; however, the theoretical model developed here can be used in predicting piloted ignition as well. Effects of char surface combustion, which is an important mechanism leading to glowing ignition and flaming autoignition, are discussed.

1.2. Literature Review

A number of studies on ignition and subsequent events (i.e. burning and flame spread) of solid fuels have been carried out, for example the reviews of piloted ignition of wood [3, 4], autoignition of wood [5], and ignition and flame spread over solid fuels [6, 7]. It is not possible to reference every investigation conducted; however, a review of relevant work is given here in two groups: (1) experimental studies, and (2) theoretical studies.

1.2.1 Experimental Studies

In order to develop comprehensive theoretical models, accurate experimental data must be provided as benchmark values. Many aspects of ignition and burning of solid fuels were studied by varying the experimental setup and conditions for instance the moisture content in the sample, the heating configuration (heating horizontally or vertically), the wood grain orientation (heating along or across the wood grain) and the atmosphere oxygen concentration. A brief summary of these experimental observations is presented.

Simms, one of the pioneer researchers, examined piloted ignition [8] and autoignition [9] of cellulosic materials. He suggested that the factors such as an intensity of external heat flux, an external draught and an exhaustion of volatiles appeared to determine whether the ignition would occur or not. He also reported that at the onset of flaming ignition, the flame first appeared in the gas phase then it propagated back to the solid surface. Simms and Law [10] studied the effects of moisture content on both piloted and auto- ignition of wood. They commented that moisture content in wood affected the ignition delay of

wood by changing the heat transfer and thus the temperature rise in three ways: (1) it increased the values of wood thermal properties, (2) heat was transferred directly by molecular diffusion of water, and (3) evaporation cooled the hotter regions and condensation heated the cooler regions. As a result, the ignition delay time increased with the moisture content. These moisture effects were experimentally confirmed by Lee and Diehl [11]. In addition, they also commented that an interaction between the water and wood decomposition was not significant. For instance, the wood surface regression rate at steady state burning obtained from wet and dry samples was the same. This was because the burning rate of wood was primarily controlled by the oxygen supply to the char surface.

Vyas et al. [12] examined effects of wood grain orientation on piloted ignition. They found that because of a difference in the wood thermal conductivity, the piloted ignition time when heating wood along the grain was shorter than when heating across the grain. Effects of attenuation of radiation on surface temperature of PMMA and wood were examined by Kashiwagi [13-15] in both piloted ignition and autoignition. It was observed that attenuation caused by the decomposition products in the gas phase was significant enough to affect the surface temperature as high attenuation tended to absorb the radiative heat flux resulting in decreasing the net heat flux to the surface. The ignition temperature for PMMA seemed to be independent of the radiant heat flux; nevertheless, the ignition temperature of wood increased with decreasing incident heat flux. Kashiwagi and Ohlemiller [16] experimentally investigated oxygen effects on non-flaming gasification process of polymer material (PMMA, and PE). The experiment showed that

the gasification rate of PMMA and PE strongly increased as the oxygen concentration increased; however, the surface temperature weakly depended on the oxygen concentration. An increase in oxygen concentration slightly reduced the surface temperature of PMMA but it increased the surface temperature of PE.

Yoshizawa and Kubota [17] experimentally investigated autoignition of cellulosic materials. The time and space variations of temperature and fuel concentration in the gas phase were examined by means of a high-speed camera and an interferometer. They found that the flame first appeared in the gas region where the fuel concentration was extremely rich. However, they commented that this ignition condition was not universal; it was experiment dependent. Atreya et al. [18] experimentally examined heating orientation effects on piloted ignition of wood (heating horizontally and vertically). In their findings, the piloted ignition results appeared to be orientation independent. They also observed that before flaming ignition was sustained, flashes indicating an unsustained flame occurred.

Suuberg et al. [19] extensively investigated burning behavior of charring materials in fire environments. This work gives an excellent choice of data, which serves as an input to develop a theoretical model for ignition and burning of wood. Martin [20] comprehensively studied ignition of cellulosic materials. He commented that the ignition behavior of cellulose could be categorized into three regions as convection-controlled when an incident heat flux was low, diffusion-controlled when an incident heat flux was intermediate, and ablation-controlled when an incident heat flux was very high.

Anthenien and Fernandez-Pello [21] studied the smoldering (glowing) process of polyurethane foam. They found that to obtain a sustained smoldering process, an igniter power flux and a time the igniter was powered must be greater than some critical values. Recently investigation of smoldering combustion of wood was given by Bilbao et al. [22]. They suggested that the smoldering ignition temperature of wood increased with incident heat flux and approached a constant value when the incident heat flux was higher than 40 kW/m^2 .

Spearpoint and Quintiere [23-25] studied piloted ignition and burning for a variety of wood species. The effects of heating along and across the wood grain orientation were examined. Boonmee and Quintiere [1, 2] extended the work [23-25] to the autoignition regime. They found that at high incident heat fluxes, the wood sample flaming ignited shortly after exposed to the heater. In contrast, at low heat fluxes, the wood sample first ignited by glowing. This was followed by a substantial char surface combustion before in some cases the char surface combustion caused a visible flame in the gas phase. However, the limit of the wood glowing ignition (i.e. a critical heat flux for glowing ignition) was not examined.

1.2.2 Theoretical Studies

Theoretical studies of ignition and burning of solid fuels have started several decades ago with an aim to improve an understanding of the controlling mechanisms of ignition and burning processes. Generally, the theoretical models fall into two categories. In first group, the theoretical models consider the physical and chemical processes involving in the solid phase only. This simplification greatly reduces complexities of the problem because the gas phase problem can be omitted; hence an analytical solution is possible. However, the models in this group need some critical criteria (i.e. critical mass flux or critical surface temperature) to determine the ignition, which sometimes base on empirical rules. In second categories, the models consider the processes occurring in both solid and gas phases; thus the governing equations in both phases must be solved simultaneously. The coupled conditions between the solid and gas phases can be made through the solid-gas interface conditions. Because of difficulties in solving the gas phase conservation equations, a closed form solution generally cannot be obtained; thus a numerical solution is required.

The first type of the theoretical models considers the solid phase only. Generally a uniform incident heat flux to the solid surface is assumed allowing that the solid phase governing equations are formulated as a one-dimensional transient heat conduction problem. A single-step Arrhenius rate is assumed to describe the solid degradation process.

Kung [26] proposed a mathematical model for a pyrolysis of a wood slab. He developed the model based on the processes involving in the solid phase only. A one-dimensional transient heat conduction was solved numerically. He assumed that the wood decomposed to volatiles following a single-step Arrhenius rate. As soon as the volatiles were formed, they instantly left the solid matrix. Variations of the wood and char thermal properties were included. Kung [27] reformulated his mode for a cylindrical geometry. In this work the study was focused on the effects of heat of pyrolysis of wood to the burning rate. Sibulkin [28] developed a model for thermal degradation of charring materials. His work was focused on the heat of gasification of the pyrolysis process. He commented that the heat of gasification of charring materials is not a material property which can be determined from thermodynamic properties alone, but it has to be estimated from experiment. Parker [29] broke a wood slab into thin slices parallel to the wood heated surface. The pyrolysis mass flux was the summation of the mass flux from each slice. Char shrinkage parallel and normal to the surface was also accounted in the model. His calculated heat release rate correlated well with the measurement values.

Tinney [30] theoretically examined combustion processes of wooden dowels. A simple transient heat conduction model was utilized. He postulated that in order to obtained good agreement between the model and experiment, two sets of the wood kinetic parameters had to be introduced. Weatherford and Sheppard [31] theoretical studied ignition mechanisms of cellulosic materials. They suggested that in order to adequately describe the critical condition at ignition, a critical value of the time required for the thermal wave propagating from the heated surface to the center of the wood sample must be satisfied.

This critical time was found to be approximately constant for both inert and non-inert solid for constant thermal properties. Roberts [32] theoretical studies a burning process of wood. His one dimensional heat conduction model was employed to examine the effects due to variations of the wood thermal properties on the burning process.

To avoid solving the gas phase governing equations, Ritchie et al. [33] used a global analytical model to determine the net heat flux to the wood surface. For the solid phase model, a one-dimensional char-forming material with variations of density and thermal properties as a function of time, local solid temperature, and position was used. The ignition was determined when the mass flux reached a critical value.

Since the wood pyrolysis process is complex, the virgin wood can decompose to char, tar, and volatiles in a number of ways depending on heating rate and configuration; thus a multi-step wood decomposition reaction may be a preferred approach to model wood pyrolysis. Panton and Rittmann [34] proposed multi-step reaction mechanism in their wood degradation model. They assumed that the virgin wood would decompose to a second solid species plus volatiles, which flowed out to the surface. The second solid species then further decomposed to yield inert solid and another volatile. The total wood pyrolysis rate was obtained by summation of all the volatiles involving in all the reactions. The porous effect due to gas leaving the solid matrix was also included in their model. Di Blasi [35] considered a wood kinetic pyrolysis model including both primary and secondary reactions. The primary reaction was expressed as the virgin wood decomposing to char, fuel gases, and tar. Then the secondary reaction of tar further

generated fuel gases. Her study was mainly focused on influences of the thermal properties on the devolatilization rate of biomass.

An analytical approach to pyrolysis of charring materials was introduced by Wichman and Atreya [36]. In this approach, the pyrolysis process was divided into four distinct stages as (1) inert heating, (2) transition regime, (3) thin char, and (4) thick char. Their numerical calculation suggested that the surface temperature controlled the volatile production rate in the initial stage (kinetic-controlled regime), while the temperature gradient controlled the volatile production rate in the thick char stage (diffusion-controlled regime).

Rhodes and Quintiere [37] introduced an integral model for prediction piloted ignition and burning of non-charring material (PMMA) in a cone calorimeter. The model was modified to include charring effects by Spearpoint and Quintiere [23-25]. Boonmee and Quintiere [2] further demonstrated that the model could also be used in predicting autoignition of wood. In this integral model, a polynomial temperature profile was assumed inside the solid phase. The theoretical ignition time based on a critical ignition temperature was in good agreement with experimental values when reasonable thermal properties of the solid were employed. Delichatsios et al. [38] applied an integral method to determine the ignition time for wood. Their solutions were in good comparison to the experimental values and the semi-infinite heat transfer problem.

Porous and permeable structure effects on the flow of volatiles were included in the wood degradation model introduced by Kansa et al. [39]. Besides instantaneously removing the volatiles from the solid matrix as typical models assumed, they suggested that the volatile flowed through the solid matrix. This assumption was achieved by including the Darcy law in the momentum equation for the volatile flow inside the solid matrix. They also found that the mass flux reached its peak value at the instant when the wood surface completely became char. The Darcy law was also included in a numerical study of Di Blasi [40] where a two-dimensional model for heat and mass transfer inside the solid was considered.

As a uniform incident heat flux to the solid surface is satisfied, the solid phase model can reduce to a one-dimensional problem. However, in some situations, the incident heat flux is not uniform; thus, a multi-dimensional model in the solid phase was introduced such as a two-dimensional transient model [41], and a three-dimensional transient model [42]. However, the multi-dimensional models are rather expensive in computational cost and the applications of these models are limited.

The second category of the theoretical models considers the processes in both solid and gas phases. The governing equations in both phases are solved simultaneously and the connections between the two phases are made through the solid-gas interface surface. A major difficulty in this type of models is due to complexities in nature of the gas phase governing equations namely the Navier-Stokes equations. To overcome these difficulties, clever simplifications must be introduced.

Gandhi and Kanury [43, 44] simplified the gas phase governing equations by assuming that the gas boundary layer above the solid surface was well-stirred in the direction parallel to the solid surface. This reduced the gas phase problem to a one-dimensional problem in the direction normal to the solid surface. The solid phase was modeled as a one-dimensional transient heat conduction with a finite first order pyrolysis rate. The ignition occurred when the temperature gradient at the solid-gas interface reversed its sign. Kashiwagi [45] constructed a one-dimensional model considering the processes in both solid and gas phases in predicting autoignition of solid fuels. In the solid phase, in-depth radiation absorption of the fuel was included while in the gas phase, a finite rate gas kinetics was considered. Ignition was accomplished when the total reaction rate in the gas boundary layer exceeded an arbitrary but reasonable value. Di Blasi et al. [46] postulated that in predicting radiant ignition of solid fuels, the gas phase radiation absorption played an important role and must be included in the gas phase energy equation. They found that in some particular heat fluxes, without the gas phase radiation absorption, ignition did not occur at all. Atreya and Wichman [4, 47] developed a semi-analytical model for piloted ignition. They assumed that a stagnant boundary layer existed in the gas phase and the incident heat flux to the solid surface was uniform. With these assumptions, their problem could then reduce to a one-dimensional transient model in both phases. Their simplified solution suggested that at piloted ignition the solid surface temperature and pyrolysis mass flux remained constant.

For the coupled problem considering both solid and gas phases, the gas phase boundary conditions at the solid-gas interface must be provided via solving the solid phase

governing equations. However, if an appropriate fuel pyrolysis rate from the solid is given as a function of time, the coupled problem can be reduced to the gas phase problem only. This idea was utilized by Tzeng et al. [48].

Kung [49] extended his solid phase model [26] to couple with a gas phase model in an investigation of burning of vertical wood slabs. A boundary layer approximation was made to simplify the gas transport equations of mass, momentum, species, and energy. He assumed that the similarity variables hold in the gas phase; then coupled the gas phase model with the one-dimensional solid phase via the solid-gas interface surface. Kim et al. [50] theoretically examined laminar free-convective burning rate of a vertical fuel surface. A similarity type solution was introduced in order to simplify the gas phase transport equations. Their approximate solution correlated well with experimental data for a wide range of fuels with low molecular weight; however, for fuels with high molecular weight, Lewis number effects appeared to be important. Ahmad [51] proposed a model for burning of a vertical wall fire by assuming the similarity and non-similarity solutions coexisted in the gas phase. In his approach, if the non-similarity terms were neglected, the problem would collapse to a classical solution of natural convection over a vertical flat plate.

Zhou [52], and Zhou et al. [53] solved piloted ignition of PMMA in a horizontal heating configuration. By assuming the gas phase momentum equation satisfied the Blasius solution, the gas phase velocity field could be calculated. Once the velocity field was obtained, the gas phase species and energy equations and the solid phase governing

equations were solved simultaneously. Piloted ignition was considered to occur when the gas maximum temperature exceeded a predefined value (e.g. a piloted igniter temperature).

Progress in computer technology has made it possible to consider the Navier-Stokes equations in more complete descriptions (e.g. two or three dimensions with convective and pressure variation effects). The “low Mach number” assumption, which describes the low speed motion of a gas driven by a chemical reaction and buoyancy forces [54] is usually employed. The assumption is widely utilized in dealing with ignition of a plume in various gravity levels and flame spread.

Tsai et al. [55] numerically examined autoignition and piloted ignition of PMMA in a cone calorimeter. The transient axisymmetric Navier-Stokes equations were solved to obtain the gas phase solution. In the solid phase, only a simple one-dimensional heat conduction model was solved to provide the solid-gas coupled conditions. A global gas kinetic reaction was included and ignition was achieved when the increasing rate of the maximum gas temperature was equal to zero. The numerical prediction of ignition time was in good agreement with experimental data for high heat flux. However, for low heat flux ($< 25 \text{ kW/m}^2$), the numerical calculation was not performed since at low heat flux it was claimed that the global gas kinetic reaction was inadequate to capture the gas chemical reactions.

Nakabe et al. [56] and subsequent studies by Nakamura et al. [57, 58] developed an axisymmetric transient gas phase model to study autoignition and transition to flame spread over a thin cellulose in microgravity environment. The effects of ambient oxygen concentration were examined. They found that ignition behavior in various gravity levels and oxygen concentrations falls into two groups [57]. In the first group when the ambient oxygen concentration is high the ignition occurs at the tip of the buoyancy plume while in the second group when the ambient oxygen concentration is low the ignition takes place inside the plume.

In studying flame spread, Dibiasi [6, 7] solved the transient two-dimensional Navier-Stokes equations for the gas phase momentum equation. Then the species and energy equations had been updated once the velocity field was obtained. The gas phase model was coupled via the boundary equations through the solid phase. An in-depth radiation absorption by the solid fuel was included in the model. They found that the ignition process occurred in the gas phase in a premixed fashion, rapidly followed by the transition to a diffusion flame. As the radiative heat flux increased, the solid surface temperature and pyrolysis mass flux increased. The ignition occurred closer to the surface and the ignition time decreased.

Shih and Tien [59] and Nakamura et al. [60] studied a low speed flame spread in a microgravity tunnel. Two- and three- dimensional Navier-Stokes models were solved numerically. The main findings of their work were to examine effects of the tunnel dimension to the numerical solution. The effects of two- and three- dimensional frame

spread models were also investigated by Mell and Kashiwagi [61]. They found that once a steady flame spread was established, the two- or three- dimensional models gave little differences in the numerical results.

It is needless to say that numerous theoretical models have been developed to examine ignition and its subsequent events. Each model has its own merit. We shall summarize the main features of those models in Table 1.1.

Table 1.1: Summary of literature theoretical models

References	Solid phase model	Gas phase model	Solid-gas interface conditions
Kung [26, 27]	-1D transient heat conduction model for charring material - Single-step first order Arrhenius pyrolysis rate	NA	- Account for radiative and convective heat losses
Sibulkin [28]	-1D transient heat conduction model for charring material - Single-step first order Arrhenius pyrolysis rate	NA	- Account for radiative and convective heat losses
Parker [29]	-1D transient heat conduction model for charring material - Single-step first order Arrhenius pyrolysis rate - Including char shrinkage effects	NA	- Account for radiative and convective heat losses
Tinney [30]	-1D transient heat conduction model for charring material - Single-step first order Arrhenius pyrolysis rate	NA	- Account for radiative and convective heat losses

Weatherford and Sheppard [31]	-1D transient heat conduction model for charring material - Single-step first order Arrhenius pyrolysis rate	NA	- Account for radiative and convective heat losses
Roberts [32]	-1D transient heat conduction model for charring material - Single-step zero order Arrhenius pyrolysis rate	NA	- Account for radiative and convective heat losses
Ritchie et al. [33]	-1D transient heat conduction model for charring material - Single-step first order Arrhenius pyrolysis rate - Global analytical model to determine the radiative feedback from the flame	NA	- Account for radiative and convective heat losses - Including heat feedback from the flame
Panton and Rittmann [34]	-1D transient heat conduction model for charring material - Multi-step first order Arrhenius pyrolysis rate	NA	- Account for radiative and convective heat losses
Di Blasi [35]	- 1D transient heat conduction model for charring material - Multi-step first order Arrhenius pyrolysis rate - Include Darcy law for flow of volatiles in the solid matrix	NA	- Account for radiative and convective heat losses
Wichman and Atreya [36]	- 1D Similarity solution for charring material - Single-step first order Arrhenius pyrolysis rate	NA	- Account for radiative and convective heat losses
Rhodes and Quintiere [37]	- 1D Integral solution for non-charring material	NA	- Account for radiative and convective heat losses - Including heat feedback from the flame
Spearpoint and Quintiere [23-25]	- 1D integral solution for charring material	NA	- Account for radiative and convective heat losses

Delichatsios et al. [38]	- 1D integral solution for charring material	NA	- Account for radiative and convective heat losses
Kansa et al. [39]	- 1D transient heat conduction model for charring material - Single-step first order Arrhenius pyrolysis rate - Include Darcy law for flow of volatiles in the solid matrix	NA	- Account for radiative and convective heat losses
Di Blasi [40]	- 2D transient heat conduction model for charring material - Multi-step first order Arrhenius pyrolysis rate - Include Darcy law for flow of volatiles in the solid matrix	NA	- Account for radiative and convective heat losses
Fredlund [41]	-2D transient heat conduction model for charring material - Single-step first order Arrhenius pyrolysis rate	NA	- Account for radiative and convective heat losses - Including kinetic char surface oxidation
Yuen et al. [42]	-3D transient heat conduction model for charring material - Single-step first order Arrhenius pyrolysis rate -Include Darcy law for flow of volatiles in the solid matrix	NA	- Account for radiative and convective heat losses
Gandhi and Kanury [43, 44]	-1D transient heat conduction model - Single-step first order Arrhenius pyrolysis rate	- 1D transient model - Global second order gas kinetic reaction - Similarity solution	- Account for radiative and convective heat losses - Account for blowing velocity due to pyrolysis mass flux

Kashiwagi [45]	-1D transient heat conduction model - Single-step first order Arrhenius pyrolysis rate - Include in-depth solid radiation absorption	- 1D transient model - Global second order gas kinetic reaction - Similarity solution	- Account for radiative and convective heat losses - Account for blowing velocity due to pyrolysis mass flux
Di Blasi et al. [46]	-1D transient heat conduction model - Single-step first order Arrhenius pyrolysis rate - Include in-depth solid radiation absorption	- 1D transient model - Global second order gas kinetic reaction - Include gas radiation absorption	- Account for radiative and convective heat losses - Account for blowing velocity due to pyrolysis mass flux
Atreya and Wichman [4, 47]	-1D transient heat conduction model - Single-step first order Arrhenius pyrolysis rate	- 1D transient model - Global second order gas kinetic reaction - Similarity solution	- Account for radiative and convective heat losses - Account for blowing velocity due to pyrolysis mass flux
Tzeng et al. [48]	NA	- 1D transient model - Global second order gas kinetic reaction - Similarity solution	- Prescribe mass flux as a function of time
Kung [49]	-1D transient heat conduction model - Single-step first order Arrhenius pyrolysis rate	- 2D quasi-steady boundary layer approximation - Similarity solution	- Account for radiative and convective heat losses - Account for blowing velocity due to pyrolysis mass flux
Kim et al. [50]	NA	- 2D quasi-steady boundary layer approximation - Similarity solution	- Fuel vaporizing at the surface

Ahmad [51]	NA	- 2D quasi-steady boundary layer approximation - Similarity and non-similarity variables coexist in the gas phase	- Fuel vaporizing at the surface
Zhou [52] and Zhou et al. [53]	- 1D transient heat conduction model for non-charring materials - Include in-depth solid radiation absorption	- 2D boundary layer approximation - Velocity field obtained from the Blasius solution - Global second order gas kinetic reaction	- Account for radiative and convective heat losses - Neglect blowing velocity in the momentum boundary but include in the species boundaries
Tsai et al. [55]	- 1D heat conduction model for solid surface temperature	- 2D transient axisymmetric Navier-Stokes equations - Global second order gas kinetic reaction	- Account for heat conduction from gas to solid surface - Fuel vaporizing at the surface - Account for blowing velocity due to pyrolysis mass flux
Di Blasi [6, 7]	- 2D transient heat conduction for charring materials - Single-step first order Arrhenius pyrolysis rate - Include in-depth solid radiation absorption	- 2D transient Navier-Stokes equations - Global second order gas kinetic reaction	- Account for heat conduction from gas to solid surface - Account for blowing velocity due to pyrolysis mass flux
Nakabe et al. [56]	- Zero dimension transient heat conduction model - Multi-step first order Arrhenius pyrolysis rate	- 2D transient axisymmetric Navier-Stokes equations - Global second order gas kinetic reaction	- Account for radiative and convective heat losses - Fuel vaporizing at the surface - Account for blowing velocity due to pyrolysis mass flux

Nakamura et al. [57, 58]	<ul style="list-style-type: none"> - Zero dimension transient heat conduction model - Multi-step first order Arrhenius pyrolysis rate 	<ul style="list-style-type: none"> - 2D transient axisymmetric Navier-Stokes equations - Global second order gas kinetic reaction 	<ul style="list-style-type: none"> - Account for radiative and convective heat losses - Fuel vaporizing at the surface - Account for blowing velocity due to pyrolysis mass flux
Shin and Tien [59]	<ul style="list-style-type: none"> - Zero dimension transient heat conduction model - Single-step zero order Arrhenius pyrolysis rate 	<ul style="list-style-type: none"> - 2D and 3D quasi-steady Navier-Stokes equations - Global second order gas kinetic reaction 	<ul style="list-style-type: none"> - Account for radiative and convective heat losses - Fuel vaporizing at the surface - Account for blowing velocity due to pyrolysis mass flux
Nakamura et al. [60]	<ul style="list-style-type: none"> - Zero dimension transient heat conduction model - Multi-step first order Arrhenius pyrolysis rate 	<ul style="list-style-type: none"> - 2D and 3D transient Navier-Stokes equations - Global second order gas kinetic reaction 	<ul style="list-style-type: none"> - Account for radiative and convective heat losses - Fuel vaporizing at the surface - Account for blowing velocity due to pyrolysis mass flux
Mell and Kashiwagi [61]	<ul style="list-style-type: none"> - Zero dimension transient heat conduction model - Multi-step first order Arrhenius pyrolysis rate 	<ul style="list-style-type: none"> - 2D and 3D transient Navier-Stokes equations - Global second order gas kinetic reaction 	<ul style="list-style-type: none"> - Account for radiative and convective heat losses - Fuel vaporizing at the surface - Account for blowing velocity due to pyrolysis mass flux

1.3 Problem Descriptions

As reviewed in the previous section, a numerous ignition models for solid fuels (precisely wood) have been proposed. However, few attentions have been paid to the effects of char surface oxidation, which seems to be important when the incident heat flux to the wood surface is low. For this reason, the present study is performed. The problem considering in this work is described in Fig. 1.1.

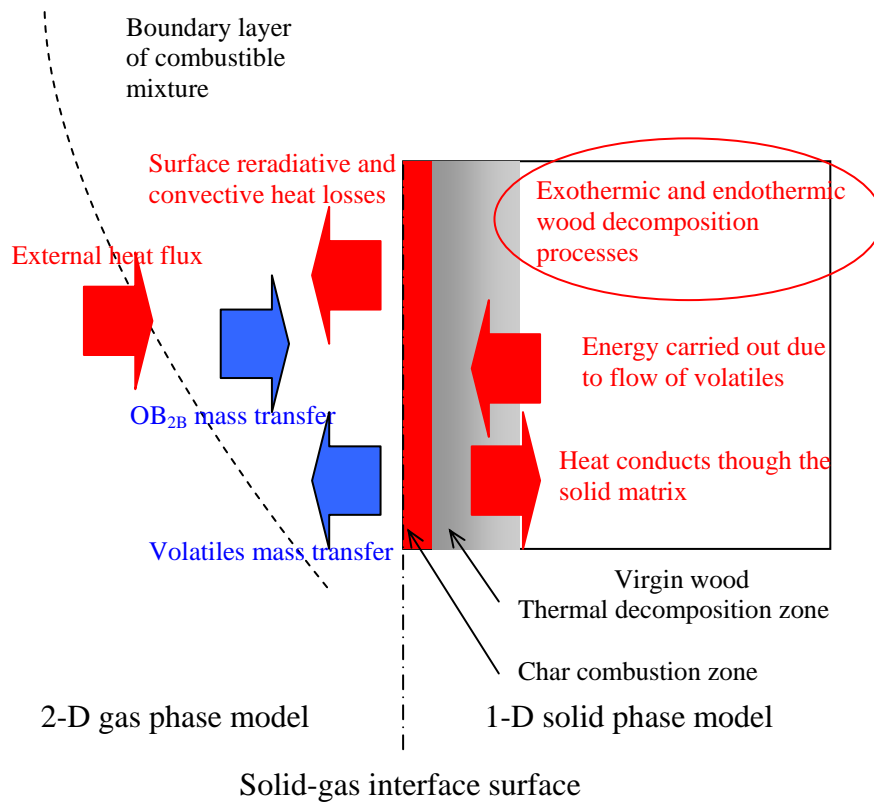


Figure 1.1: A schematic diagram of the processes involved in autoignition of wood

As the wood is subjected to an external heat flux, its temperature increases. When the temperature reaches the pyrolysis temperature, the wood starts to decompose producing pyrolysis gases and residual char. The pyrolysis gases flow out and mix with fresh air from the surroundings creating a boundary layer of combustible mixture. As the combustible mixture reaches a critical condition (both concentration and temperature), ignition occurs. Depending on an intensity of the incident heat flux, the char layer on the wood surface could react heterogeneously (char surface combustion) with the oxygen diffusing from the surroundings. The char surface combustion would add more energy to the combustible mixtures near the surface. Eventually, flaming autoignition of the combustible mixtures occurs.

In this study, a theoretical model for autoignition of wood will consider the processes occurring in both solid and gas phases. The solid phase model will be formulated as a one-dimensional transient heat conduction problem. The effects of solid density change due to wood pyrolysis, heat of wood pyrolysis, heat transfer due to volatiles flow through the solid matrix, and variations of thermal properties with the solid temperature are included. In the gas phase model, two-dimensional laminar boundary layer approximation equations for mass, momentum, species, and energy will be considered. The solid and gas phase models will be coupled via the solid-gas interface surface. The char surface combustion is taken into account at the solid-gas interface surface.

1.4 Objective and Plan

The objective of this dissertation is to experimentally and theoretically study radiant autoignition of wood. Details and discussions of experimental and theoretical approaches are planned to present as the followings.

In Chapter 2, an experimental study for autoignition of wood is conducted. A redwood sample is exposed to incident heat fluxes ranging from 9 kW/m^2 to 30 kW/m^2 . Times to glowing and flaming autoignition are measured. The sample surface temperature is continuously monitored by an infrared thermocouple. The sample mass loss is recorded via a load cell. Important ignition parameters such as ignition time, ignition mass flux, and ignition surface temperature are reported. The purpose of the experiment is to provide reliable experimental data to be used as a guideline in developing the theoretical solid and gas phase models.

In Chapter 3, a kinetic modeling of wood pyrolysis is developed. A thermogravimetric analysis (TGA), where a few milligrams of redwood sample is inserted into a furnace, is utilized. A series of isothermal and non-isothermal TGA are carried out; then the wood kinetic parameters (pre-exponential factor and activation energy) are extracted from the sample mass loss. The derived wood kinetic parameters will be used as inputs from the wood kinetic decomposition model. The wood kinetic decomposition is considered as three independent single-step first-order reaction taking place in parallel corresponding to the main three components of wood (cellulose, hemicellulose, and lignin). The main

object of this chapter is to develop a wood kinetic decomposition model to couple with the solid phase model of wood pyrolysis for predicting the overall processes of autoignition of wood.

A solid phase model for wood pyrolysis is constructed in Chapter 4. The model includes the effect of char surface oxidation, which is an important mechanism leading to surface glowing ignition and gas flaming autoignition. Criteria for surface glowing ignition are developed based on a surface energy balance. Comparisons between theoretical predictions and experimental results are given.

In Chapter 5, a gas phase model for flaming autoignition of wood is proposed. The gas phase model is formulated as two-dimensional, transient, laminar boundary layer approximation with gas density variation. The gas phase model will be coupled with the solid phase model via the solid-gas interface surface. A flaming autoignition criterion is developed. Flaming autoignition is considered to accomplish when the maximum gas reaction rate exceeds a critical value. Two autoignition behaviors namely (1) flaming autoignition and (2) glowing ignition leading to flaming autoignition are distinguished. Comparisons between theoretical and experimental results at flaming autoignition are presented.

Finally, conclusions from the theoretical and experimental investigation will be drawn in Chapter 6. Limitations of the present solid and gas phase theoretical models are discussed. Recommendations for future developments are given.

Chapter 2

Experiment

2.1 Introduction

In previous investigations [1, 2], experimental studies of autoignition of wood exposed to a radiant heater were conducted with incident heat fluxes ranging from 30 kW/m² to 70 kW/m². It was found that at high incident heat flux (> 40 kW/m²), the wood sample underwent flaming autoignition shortly after exposed to the heat flux. The flame first appeared in the gas phase away from the heated surface and then propagated back to the surface. On the other hand at low incident heat flux (< 40 kW/m²), the wood sample experienced significant char surface combustion, which was a consequence of a surface glowing ignition before in some cases, the char surface combustion eventually transitioned to flaming autoignition. In the case that the flaming autoignition occurred, the flame was initiated relatively close to the char surface. The char surface oxidation plays an important role on the surface “glowing” ignition as well as the transition to flaming autoignition. However, the previous studies did not examine the limit of glowing ignition, which could extend to a very low heat flux. For this reason, the experimental study of glowing ignition for wood under low incident heat fluxes was performed.

The main object of the present experiment is to investigate the wood ignition behavior under a low incident heat flux condition. The experiments were conducted between

incident heat fluxes below 30 kW/m^2 down to the heat flux that the surface glowing ignition does not occur (critical heat flux for glowing ignition). The limit of surface glowing ignition is examined. A surface temperature of the sample was measured continuously by an infrared thermocouple and mass loss was recorded by a load cell. Ignition parameters, such as ignition time, ignition mass flux and ignition surface temperature for both glowing and flaming auto- ignition were measured and documented.

2.2 Experimental Description

2.2.1 A Wood Sample

Ignition characteristics of a redwood sample were examined. A redwood sample was cut to 4 by 4 cm of exposed surface area with 4 cm thickness. The wood grain orientation was aligned either parallel (heating along the grain) or perpendicular (heating across the grain) to an incident heat flux. Fig. 2.1 illustrates how the sample was aligned to an incident heat flux as desired in this study.

The wood grain structure affects ignition mechanism as follows. Considering two heating scenarios where a wood sample is heated (1) along the grain, and (2) across the grain. In the first scenario, when the wood sample is heated along the grain, the pyrolysis volatiles can easily travel out from the wood sample because the flow is parallel to the wood grain orientation. In contrast, when the wood sample is heated across the grain, the cell walls of the wood fiber-tubes must first decompose before the pyrolysis products can escape to the surface. Because flaming ignition can occur when the fuel concentration is in a proper

limit, we might expect that flaming ignition would occur earlier for heating along the grain than heating across the grain.

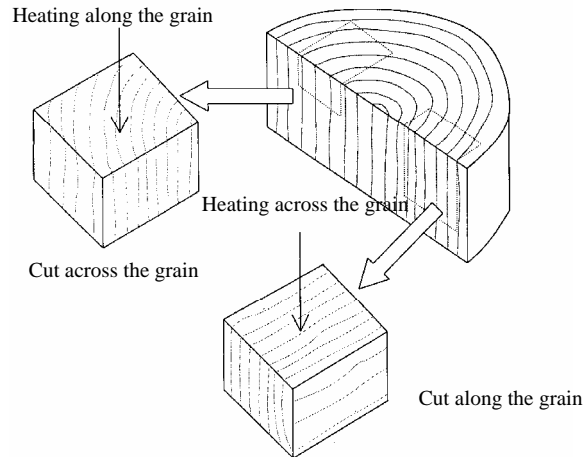


Figure 2.1: Sample grain orientation (picture adopted from Ref. [23])

2.2.2 Experimental Setup and Procedures

The redwood samples were dried in an oven at 100 °C for 24 hours and then kept in a desiccator at 13% relative humidity and 20 °C to control moisture content. Prior to each test, the sample was insulated on the back and sides with fiber insulation (Kaowool® type M board) in order to promote a one-dimensional heat and mass transfer. The redwood sample was exposed vertically to a radiant heater in a cone calorimeter. A normal video camera was used to record the ignition and combustion processes on the wood surface. A schematic diagram for the experimental setup is illustrated in Fig. 2.2.

The samples were exposed to incident heat fluxes ranging from 9 kW/m² to 30 kW/m². The incident heat flux from the cone heater was controlled by varying the cone heater

temperature to a desired value then the heat flux intensity was calculated from a calibration curve shown in Fig. 2.3.

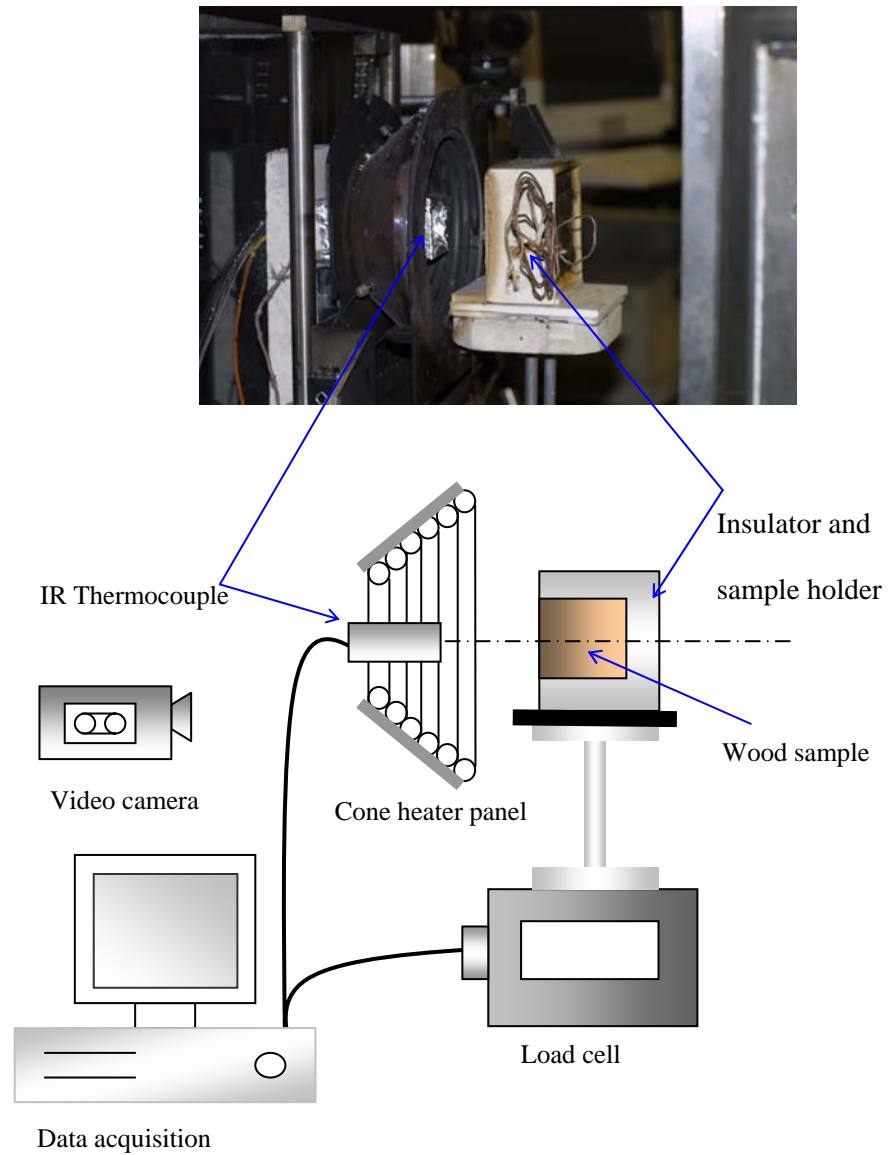


Figure 2.2: Schematic diagram of the experimental setup

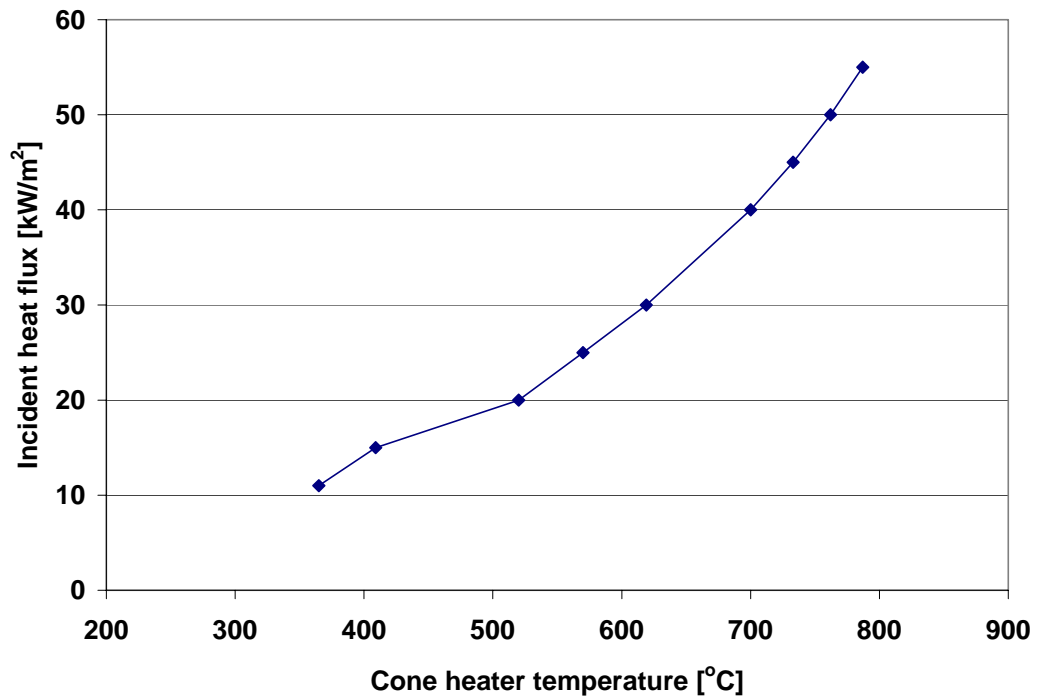


Figure 2.3: Calibration curve for the cone heater temperature

Prior each run, the heat flux was fine-tuned with a heat flux meter (Gordon type) to ensure that the heat flux intensity was at a desired value. However, because of an AC power supply to the cone calorimeter and a slow time response of the heater controller, the cone heater temperature (as well as heat flux) slightly fluctuated like a sinusoidal wave. A typical amplitude of the fluctuation was approximately $\pm 2 \text{ kW/m}^2$. Thus, it should be noted that the incident heat flux reported in the experimental data was an average value between the upper and lower heat flux readings.

Before the experiment started, an aluminum foil shutter was placed in front of the sample surface. To begin the experiment, the shutter was taken away manually providing a

uniform heat flux on the sample surface; then the data acquisition system began to record the data.

Each test was conducted until a flaming autoignition of the combustible gases adjacent to the sample surface occurred. Then the sample was removed from the cone and the flame was extinguished immediately. In the case that flaming autoignition did not accomplish, the test was kept running up to about 2 hours or until the entire sample was consumed by a char combustion. The times from exposure of the sample until glowing ignition or flaming autoignition occurred are defined as glowing ignition or flaming autoignition time respectively. At the end of each test, the glowing ignition and flaming autoignition times were documented.

2.3 Experimental Observations

A video recorded from the experiment was digitized to a digital format with a resolution of approximately 30 frames per second. By carefully examining frame-by-frame a process of the wood surface glowing ignition leading to the gas flaming autoignition can be revealed.

As the wood surface was exposed to an incident heat flux, it pyrolyzed. The wood surface became black as it turned to char. Later, localized glowing areas could be observed as red spots started at the edges of the surface (Fig 2.4a). Subsequently the localized glowing spots propagated over the entire surface (glowing ignition). At this stage, the entire

surface became red because of the char surface combustion (Fig. 2.4b). Typically at this point, the surface temperature measured from an IR thermocouple dramatically increased. The char surface combustion consumed the char layers on the wood surface; hence the wood surface regressed. Eventually the char surface combustion caused a transition to the gas flaming autoignition (Fig. 2.4c).

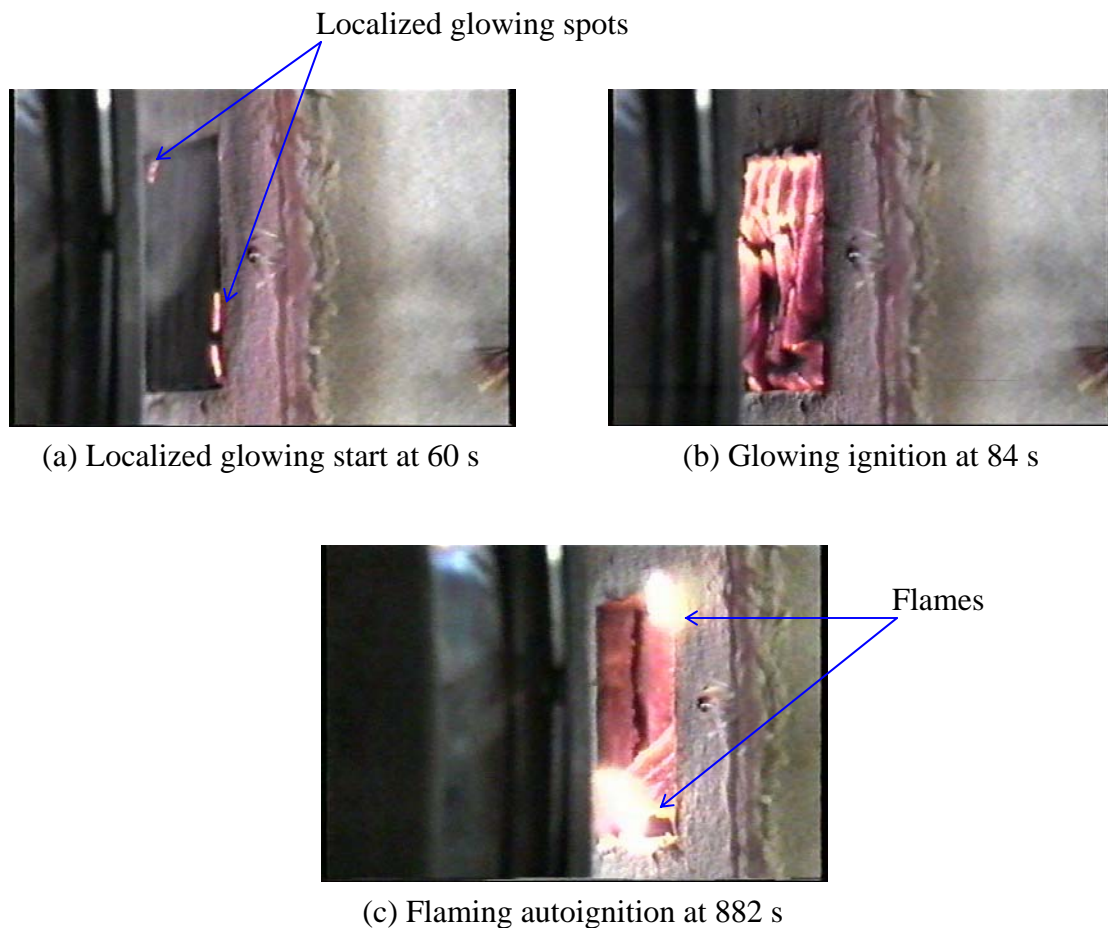


Figure 2.4: A sequence of wood glowing ignition leading to gas flaming autoignition ($\dot{q}_i'' = 30 \text{ kW/m}^2$, heating across the grain), the cone heater panel is located on the left of each picture.

2.4 Surface Temperature Measurements

2.4.1 An Infrared Thermocouple and Its Calibration

To obtain a good measurement of surface temperature with a conventional thermocouple, the thermocouple must be in good contact with the measured surface. However, it is very difficult to maintain the thermocouple in good contact to a wood surface because when the wood surface undergoes surface oxidation, it usually cracks. The cracks cause the thermocouple to drift away from the measured surface. It is impossible to predict where the cracks will occur [62]. Thus, measuring the wood surface temperature with a conventional thermocouple is not recommended. However, this problem can be overcome by using a non-contact infrared thermocouple where the measured surface temperature is estimated from the surface radiant energy. For this reason, an infrared (IR) thermocouple was utilized in present experiment.

An infrared (IR) thermocouple model Omega® OS37-K-10 was employed to measure the sample surface temperature. The IR thermocouple measures an average surface temperature over the area that it views (see Fig. 2.5). The IR thermocouple has an aspect ratio of 1:10, which is defined as a diameter of the measured surface area to a distance from the measured surface. In the experimental setup, the IR thermocouple was located approximately 10 cm away from the sample surface providing that the measured surface was a circle of 1 cm diameter. Therefore, the temperature reading from the IR thermocouple essentially represented an average surface temperature of this circle.

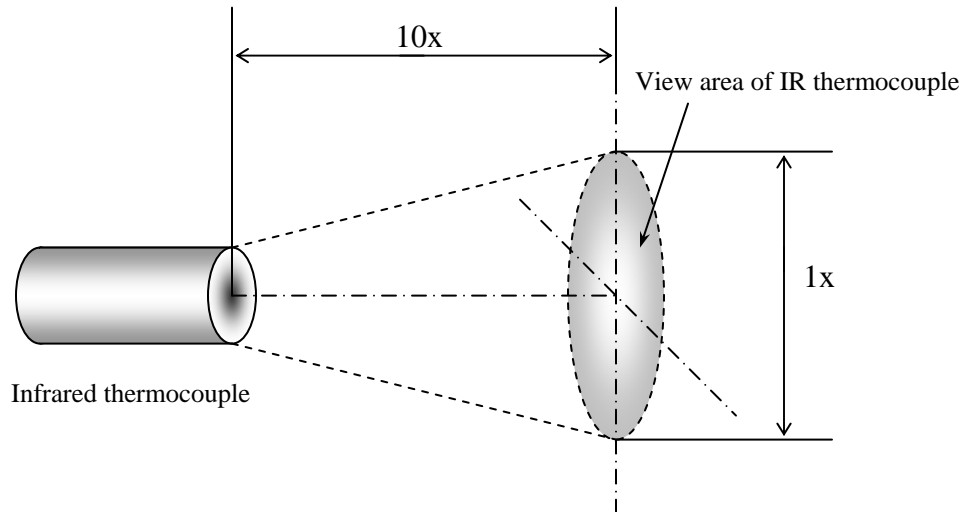


Figure 2.5: Schematic diagram for the IR thermocouple aspect ratio and its view area: the reading temperature represents an average surface temperature over the shading area.

(Not draw in scale)

The output signal of the IR thermocouple is compatible to a conventional type K thermocouple. The IR thermocouple sensing range is from $-45\text{ }^{\circ}\text{C}$ to $1370\text{ }^{\circ}\text{C}$ with a proper calibration function. The IR thermocouple was connected to a data acquisition board from National Instruments PCI-MIO-16-E-4 DAQ Card, which was installed to a 1.0 GHz Pentium III 128 MB memory Dell-PC. The IR thermocouple has a response time of 80 ms which is vary fast compared to a data sampling rate of the data acquisition (about 1 second); thus, the “shutter effect” observed in the previous study [1] can be avoided. LabVIEW® version 5.1 was used to acquire, display and save data from the data

acquisition system. The output signal from the IR thermocouple was recorded every 1 second.

The IR thermocouple was insulated with Kaowool® board type M and wrapped with aluminum foil. It was installed at approximately the center of the cone heater panel and pointed to the wood surface (see Fig. 2.2). To maintain a surrounding temperature around the IR thermocouple within its operating temperature ($< 250\text{ }^{\circ}\text{C}$) an air purge flow was utilized to cool the IR thermocouple. The air flow was provided to a built-in air purge socket by the pneumatic air pump of the cone calorimeter. Since the IR thermocouple was installed near the cone heater panel; the surrounding temperature around the IR thermocouple was relatively high. The surrounding temperature changed as the heat flux was changed. These changes of the surrounding temperature affected the reading signal of the IR thermocouple. To minimize this effect, the following calibrations were employed.

Prior each test, the IR thermocouple was used to measure a known surface temperature of an insulator board located at the same position of the wood sample as desired in the experiment. The readout IR thermocouple signal was set to mV (Fig. 2.6a). A known surface temperature was obtained from a conventional type K thermocouple measuring the surface temperature at the center of the view area of the IR thermocouple (Fig. 2.6b). To ensure that the thermocouple was in good contact with the measured surface, the thermocouple bead was flattened to obtain a thin film before installed approximately less than 1 mm underneath the surface.

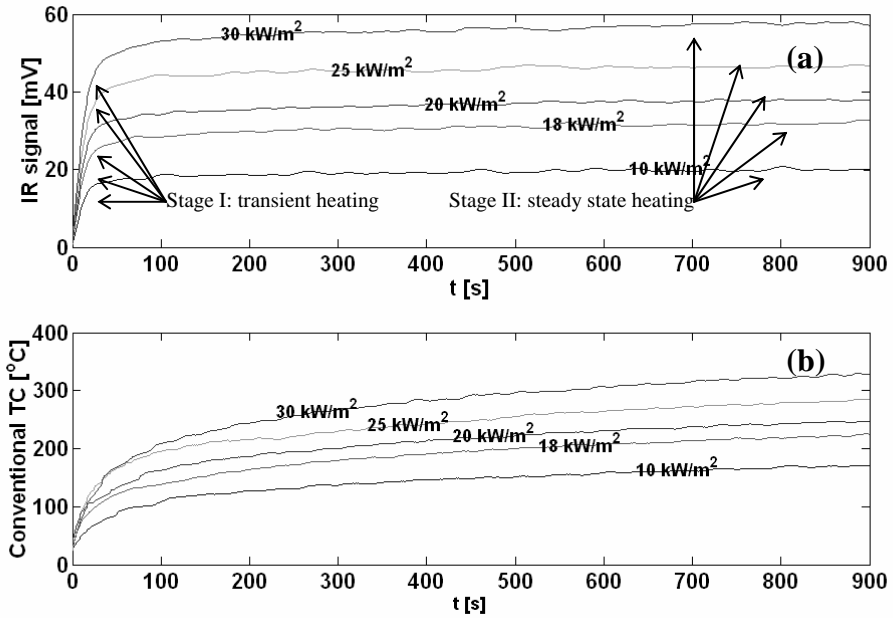


Figure 2.6: (a) Output signals from IR thermocouple and (b) Output signal from conventional thermocouple for various heat fluxes.

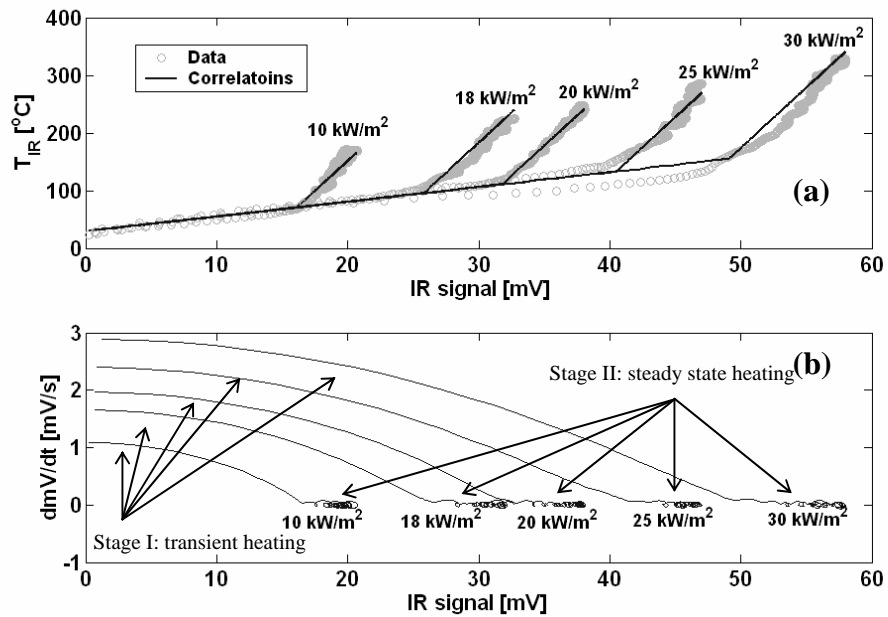


Figure 2.7: (a) calibration correlations and (b) the rate of change of the IR thermocouple signal (The plot shows only 1 test per heat flux to avoid overcrowded)

The reading temperature from IR thermocouple in °C must be the same as that from the conventional thermocouple. Moreover, the IR thermocouple output signal in °C is also a function of the output in mV. Taking these facts, calibration correlations for various heat fluxes can be calculated. Fig. 2.7 shows that the signals from the IR thermocouple in mV and °C are correlated well with two linear lines with different slopes expressed in the form:

$$T_{IR}[^{\circ}C] = m \cdot IR[mV] + C, \quad (2.1)$$

where $T_{IR}[^{\circ}C]$ is the IR thermocouple reading temperature in °C (taking from a reading value of the conventional thermocouple), $IR[mV]$ is the IR thermocouple reading signal in mV, m is the slope of the calibration correlation, and C is a constant.

The rising IR signal in mV with time shows two distinct behaviors (see Fig. 2.6a). At the beginning of the calibration process, the IR signal rapidly increases with time until it reaches approximately a constant value (stage I: transient heating); then the IR signal stays fairly flat through the end of calibration process (stage II: steady state heating). A transition point of the IR signal from stage I to stage II (see Fig. 2.7b) is considered when the rate of change of the IR signal in mV with time (dmV/dt) is less than a prescribed value (typically 0.1 mV/s). At stage I, the slope $m = m_I = 2.56$ °C/mV ($C = 30$ °C) provides the best fit to the data, and at stage II, the slope m is $m = m_{II} = 20.89$ °C/mV.

Good agreement between the surface temperatures measured by IR and conventional thermocouples is demonstrated in Fig. 2.8. The fluctuation of the temperature measured by IR thermocouple is because the IR thermocouple has a very fast response time; therefore it is sensitive to the fluctuation of the cone heater. The temperature fluctuation is approximately ± 20 °C.

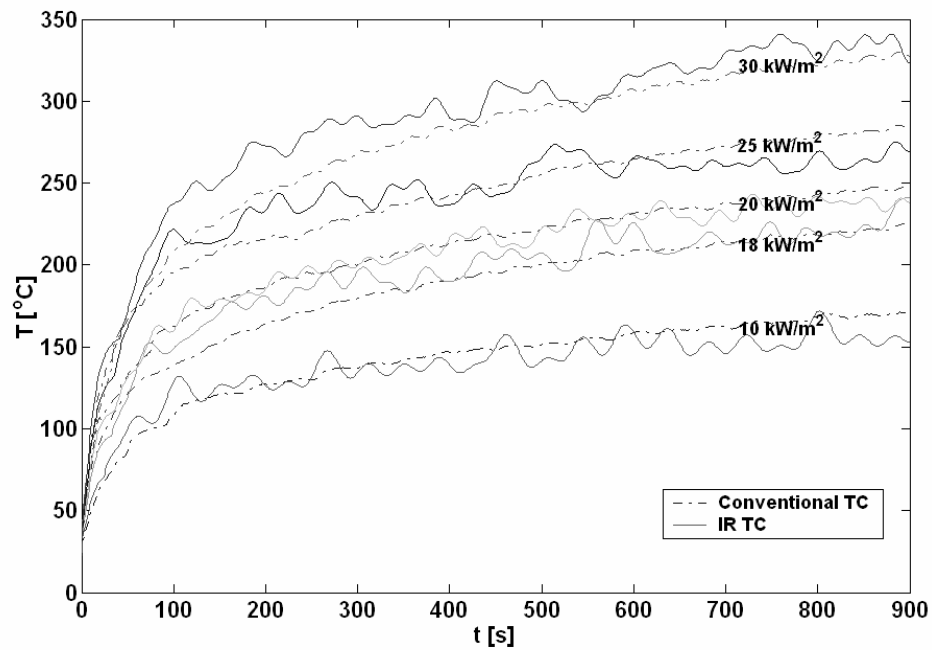


Figure 2.8: Comparisons of the surface temperatures measured by IR and conventional thermocouples

2.4.2 A Measurement of Wood Surface Temperature

As mentioned earlier, when the wood surface is exposed to a low incident heat flux, the wood surface undergoes glowing ignition following by a significant char surface combustion. Eventually the char surface combustion could cause a transition to flaming autoignition in the gas phase. These physical processes can be elucidated from analyzing

a signal of the IR thermocouple. A time history of the IR thermocouple signal in mV is shown in Fig. 2.9. We may divide the IR signal into 4 stages: I transient inert heating, II steady inert heating, III transient glowing ignition and IV steady char combustion.

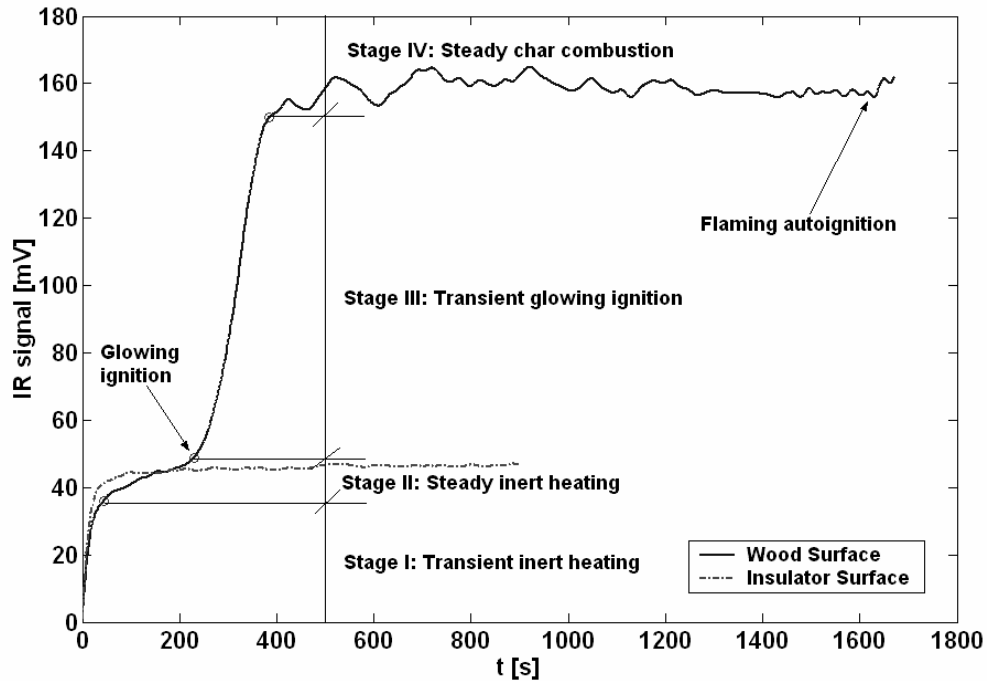


Figure 2.9: Measurement of wood surface temperature by an IR thermocouple: a raw signal time history

$$(\dot{q}_i'' = 25 \text{ kW/m}^2, \text{ heating across the grain; } t_{\text{glowing}} = 229 \text{ s; } t_{\text{flaming}} = 1600 \text{ s})$$

At the first stage, the IR signal (which directly relates to the wood surface temperature) monotonically increases with time. The monotonic increasing implies that the wood surface temperature follows the solution of a semi-infinite solid heat conduction subjected to a constant heat flux. As reradiation loss dominates the surface energy balance, the IR signal approaches approximately a constant value, which we call steady

inert heating stage (stage II). When the char surface oxidation becomes significant, excessive energy from the exothermic oxidation dramatically increases the surface temperature. The rapid increase in the surface temperature results in an inflection point, a “jump” in the IR signal, which we define as the point of “glowing ignition” (stage III). The IR signal deviates from the inert heating process at approximately 229 seconds. After the transient glowing ignition stage, the char surface combustion takes place. A constant IR signal implies that char layers on the surface are steadily burning (stage IV). Eventually the char surface combustion causes a transition to a gas phase flaming autoignition, which can be noticed as a second “jump” of the IR signal time history. Here the flaming autoignition occurs at about 1600 seconds. It should be noted that the flaming autoignition does not always cause a jump on the IR signal. This is because when flaming autoignition occurs, the flame tends to wander over the char surface. As a result the IR thermocouple might not view the flame. Generally, the experimental flaming autoignition was detected from re-running the video records.

Transition points from for one stage to another are defined as when the rate of change of the IR signal (dmV / dt) is equal to a prescribed value (typically 0.1 mV/s). The IR signal in mV is then converted to the corresponding surface temperature in °C from Eq. (2.1).

The effect of surface emissivity of the insulator is embedded in Eq. (2.1) since it was used in the calibration. To correct for the emissivity difference between the wood surface and insulator, we assume that at the same surface temperature, the radiant energy from the wood surface is equal to that from the insulator surface; thus

$$\varepsilon_w \sigma T_w^4 = \varepsilon_{in} \sigma T_{in}^4,$$

or

$$T_w = \left(\frac{\varepsilon_{in}}{\varepsilon_w} \right)^{1/4} T_{in}, \quad (2.2)$$

where T_w is the corrected wood surface temperature, T_{in} is the wood surface temperature calculated from Eq. (2.1), ε_w and ε_{in} are the emissivity of wood (0.7 from Ref. [19]) and insulator (0.95, asbestos) respectively, and σ is the Stefan-Boltzmann constant.

It should be noted that changes in surface colors do not affect the measured temperature. This is because the IR thermocouple detects a radiant energy in the wavelengths from 2 to 10 μm (10^{-6} m), which is approximately 10 times longer than the wavelengths that indicates colors, 0.4 to 0.7 μm [63].

As the wood surface underwent char surface combustion, the surrounding temperature around the IR thermocouple increased from the temperature at calibration, (see Fig. 2.10). An increasing of the surrounding temperature could affect the IR reading temperature because the IR thermocouple calculates the measured surface temperature for the total radiant energy that it receives. Considering Fig. 2.11, the total radiant energy receiving by the IR thermocouple is

$$q_{IR} = q_r + q_e, \quad (2.3)$$

where q_{IR} is the total radiant energy received by the IR thermocouple, q_r is the radiant energy reflected from the surface, and q_e is the radiant energy emitted from the surface.

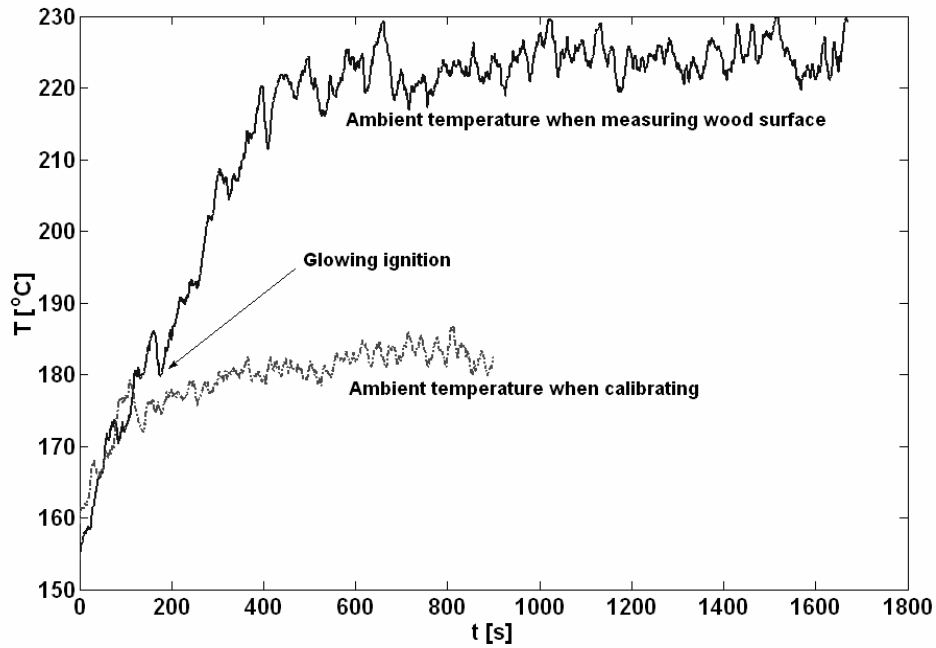


Figure 2.10: Surrounding (ambient) temperatures around the IR thermocouple

($\dot{q}_i'' = 25 \text{ kW/m}^2$, heating across the grain)

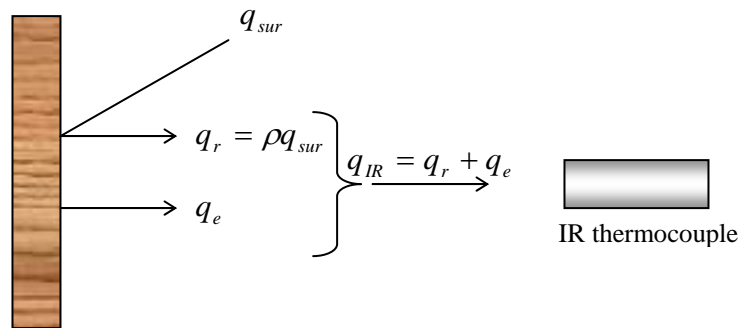


Figure 2.11: Systematic diagram illustrates the total radiant energy detected by the IR thermocouple

The radiant energy emitted from the surface is $q_e = \varepsilon\sigma T_{S,act}^4$, where ε is the surface emissivity, and $T_{S,act}$ is the actual surface temperature. The radiant energy reflected from the surface is equal to the energy radiated from the surrounding times the surface reflectivity or $q_r = \rho q_{sur}$, where ρ is the surface reflectivity, and q_{sur} is the ambient radiation, which can be estimated as $q_{sur} = \sigma T_{sur}^4$, where T_{sur} is the surrounding temperature. For a non-transparent surface the sum of surface reflectivity and surface emissivity is always unity thus, $\rho = 1 - \varepsilon$. Accordingly, we can rewrite Eq. (2.3) as

$$q_{IR} = (1 - \varepsilon)\sigma T_{sur}^4 + \varepsilon\sigma T_{S,act}^4. \quad (2.4)$$

The radiant energy received by the IR thermocouple is directly related to the reading (apparent) surface temperature as

$$q_{IR} = \varepsilon\sigma T_{S,ap}^4, \quad (2.5)$$

where $T_{S,ap}$ is the reading (apparent) surface temperature. Equating Eqs. (2.4) and (2.5), we can solve for the actual surface temperature as

$$T_{S,act}^4 = T_{S,ap}^4 - \left(\frac{1 - \varepsilon}{\varepsilon} \right) T_{sur}^4 \quad (2.6)$$

In the calibration correlation (Eq. (2.1)), the effect of surrounding radiation already included. Therefore, the change of the surrounding temperature from the calibration to experimental conditions can be taken into account as

$$T_{S,act}^4 = T_{S,ap}^4 - \left(\frac{1-\varepsilon}{\varepsilon} \right) (T_{sur}^4 - T_{sur,Cal}^4) , \quad (2.7)$$

where $T_{sur,Cal}$ is the surrounding temperature at the calibration and T_{sur} is the surrounding temperature at the test . The surface temperature after corrected for the emissivity and surrounding temperature difference from the calibration condition is plotted in Fig. 2.12. Here, the wood surface glowing ignites at 299 second and 391 °C and flaming ignites at 1600 second and 667 °C.

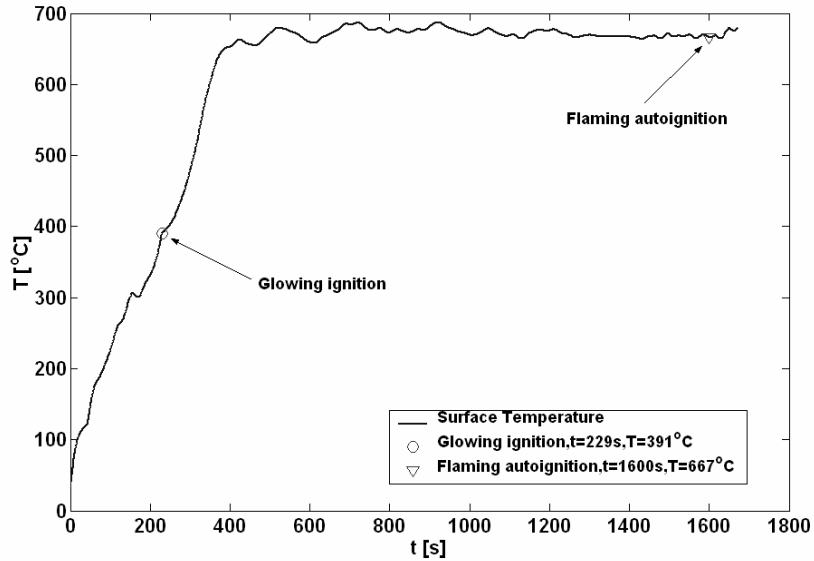


Figure 2.12: A plot of surface temperature time history ($\dot{q}_i'' = 25 \text{ kW/m}^2$, heating across

the grain; $t_{glowing} = 229 \text{ s}$, $T_{glowing} = 391 \text{ °C}$; $t_{flaming} = 1600 \text{ s}$, $T_{flaming} = 667 \text{ °C}$)

2.5 Mass Loss Measurements

A sample mass loss was continuously measured by a load cell, Automatic Timing and Controls model 6005D-050E01. The load cell measurement span is 0 – 250 g with 2.0 kg maximum capacity. The load cell was connected to a data acquisition, and the mass loss was continuously monitored every 1 second. The raw mass loss data was smoothed by a 3-point moving average to minimize noise signals from the measurement. Typical smoothed mass losses of the samples for various heat fluxes are plotted in Fig. 2.13.

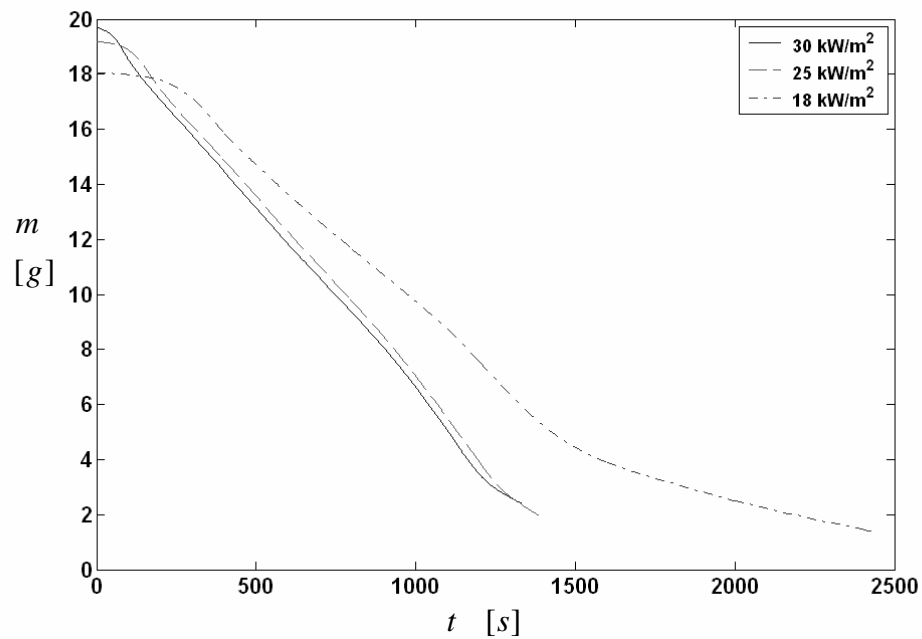


Figure 2.13: A plot of typical mass loss time histories for various heat fluxes

A mass loss rate per unit area of the sample (mass flux) was calculated by a second-order central finite difference. At the first and last data points, first-order forward and backward

finite differences were used respectively. Typical mass loss rate per unit area time histories for various heat fluxes are illustrated in Fig. 2.14.

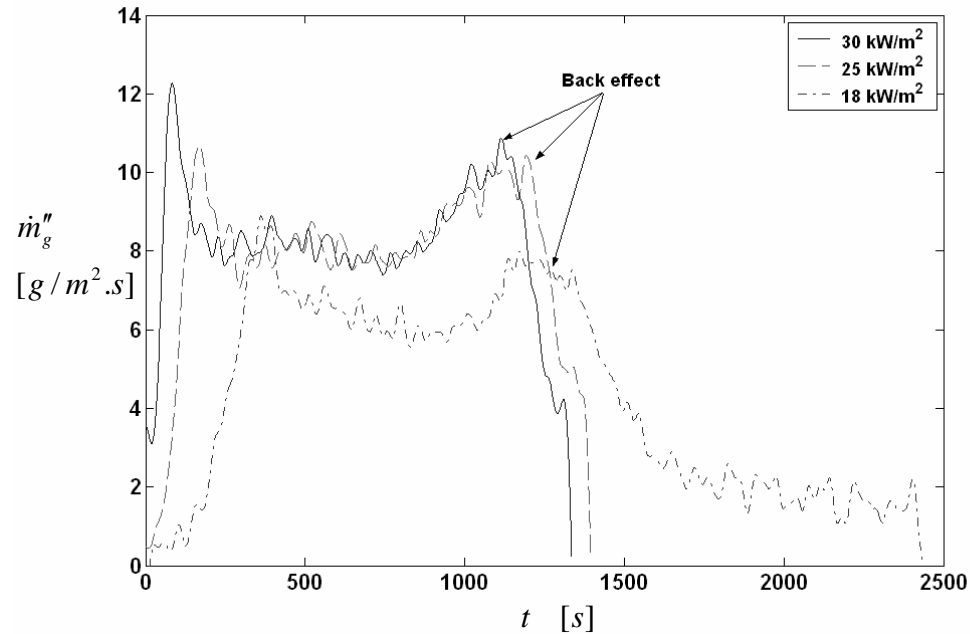


Figure 2.14: A plot of typical mass loss rate per unit area (mass flux) for various heat fluxes

As one might expect, mass loss rate decreases with decreasing incident heat flux. The peak of the mass loss rate shifts forward in time as the incident heat flux decreases. For a given heat flux, the mass loss rate increases with time at the beginning of the heating process. This is because at this time, char does not significantly form on the wood surface; thus, the mass loss rate behaves like the burning of non-charring materials. When the char layer become thicker, it blocks the flow of the volatiles, the mass loss rate decreases, and then approaches a steady burning. Once the thermal wave reaches the

back of the sample, the mass loss rate increases due to the back insulated (back effect) [23]. Finally, the mass loss rate decreases because of depletion of the sample.

2.6 Glowing Ignition and Flaming Autoignition Experimental Data

Complete experimental results for mass loss rate and surface temperature measurements are reported in Appendix C. Here, only the experimental data at glowing ignition and flaming autoignition are presented.

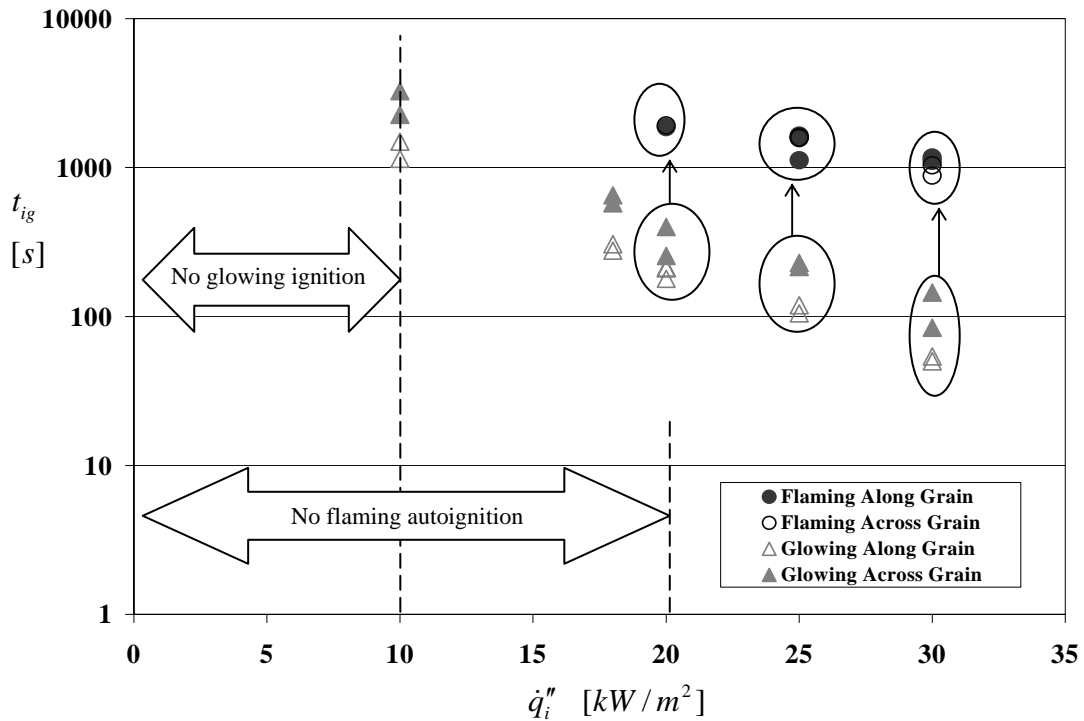


Figure 2.15: Experimental glowing and flaming autoignition times

Fig. 2.15 plots glowing ignition and flaming autoignition times as a function of incident heat flux. The circles around the data points and the arrows indicate a time sequence of

the sample starting from glowing ignition followed by flaming autoignition. As the incident heat flux decreases, glowing and flaming ignition are more difficult to achieve; hence they occur at longer ignition times. Below some critical heat flux, ignition cannot be obtained. We define this heat flux as the critical heat flux for ignition. It was found experimentally that at incident heat fluxes lower than 20 kW/m^2 , flaming autoignition did not occur. Therefore the incident heat flux of 20 kW/m^2 is considered as the critical heat flux for flaming autoignition. Babrauskas [5] summarized experimental critical heat fluxes for flaming autoignition of wood from various sources. He reported that an autoignition critical heat flux of 20 kW/m^2 might best capture those reported data. Indeed, the critical heat flux found in this experiment is surprisingly identical to the Babrauskas value. As the incident heat flux was further decreased, glowing ignition did not occur for incident heat fluxes lower than 10 kW/m^2 ; thus, the critical heat flux for glowing ignition is 10 kW/m^2 . It should be noted that the glowing ignition critical heat flux in this study is comparable to the critical heat flux for the piloted ignition of redwood reported by Spearpoint [23] (13 kW/m^2 for heating across the grain and 9 kW/m^2 for heating along the grain). This may imply that if a piloted source is presented, flaming ignition might occur at a heat flux as low as the critical heat flux for glowing ignition.

When heating along the grain, the wood surface tended to crack easily leaving large porous volumes. In contrast, when heating across the grain, the wood surface pyrolyzed without significant cracks followed by the entire layer of the wood surface fell off as the cell walls of the wood fiber-tubes decomposed. The porous volumes on the surface when heating along the grain provides greater surface areas for char on the wood surface to

oxidize with oxygen; thus, glowing ignition can occur faster when heating along the grain than across the grain.

Experimental glowing ignition and flaming autoignition surface temperatures as a function of incident heat flux are reported in Fig. 2.16. A $\pm 10\%$ error bar ($\pm 20\text{ }^\circ\text{C}$) indicates an uncertainty due to the IR thermocouple temperature measurement. The ignition surface temperatures (both glowing and flaming) slightly increase with decreasing incident heat flux when an incident heat flux is greater than the critical heat flux for flaming autoignition (20 kW/m^2). This is because the ignition times (glowing and flaming) decrease with increasing incident heat flux; thus less time for the wood surface to raise its temperature. Accordingly, the ignition surface temperatures decrease as the incident heat flux increases. On the other hand when the incident heat flux is lower than the critical heat flux for flaming autoignition, the external heat flux becomes a dominant factor for glowing ignition. Therefore the higher the incident heat flux, the faster the rising rate of the surface temperature and thus the higher the ignition surface temperature. The glowing ignition surface temperature decreases with decreasing incident heat flux

The ignition surface temperature when heating across the grain is greater than when heating along the grain. This may come from a difference in the wood thermal conductivity. As the wood thermal conductivity is higher when heating along the grain than across the grain [12], less heat would accumulate at the surface before the ignition occurs; thus the ignition surface temperature is lower when heating along the grain than when heating across the grain.

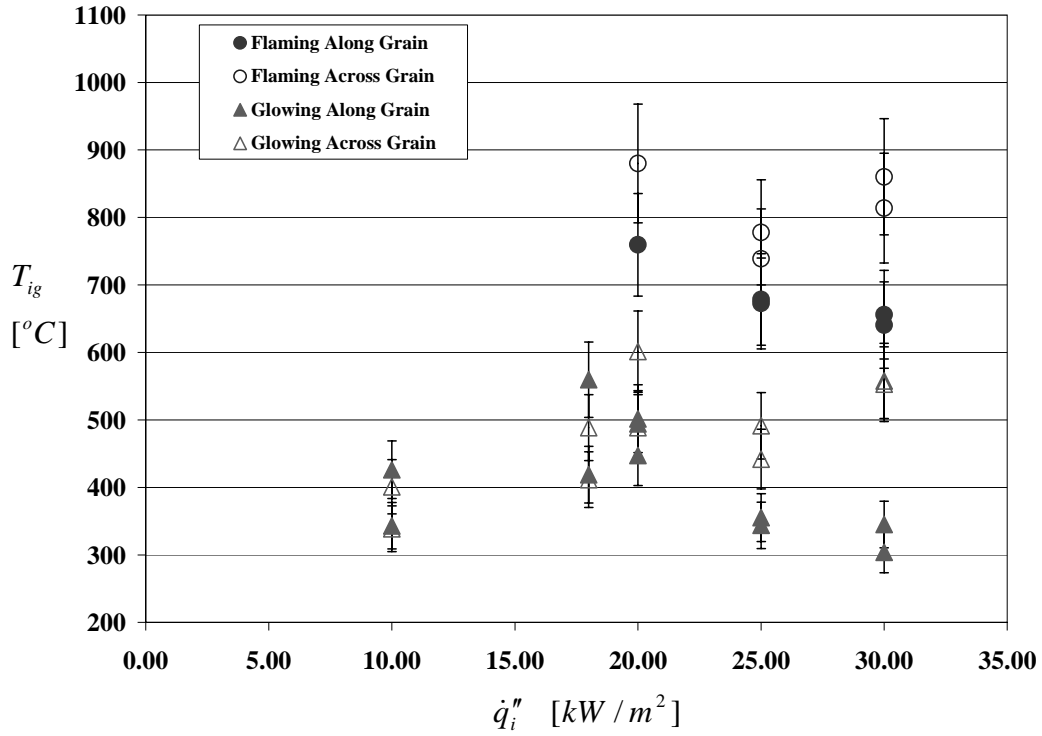


Figure 2.16: Experimental glowing and flaming autoignition surface temperature

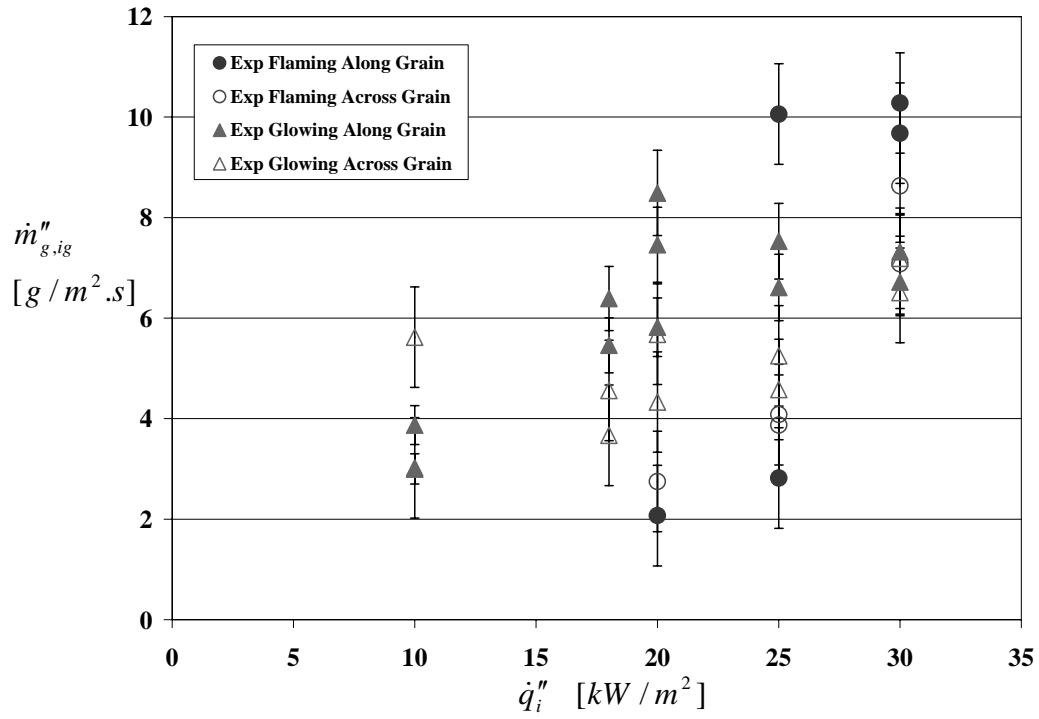


Figure 2.17: Experimental glowing and flaming autoignition mass flux

Fig. 2.17 shows ignition mass flux at glowing ignition and flaming autoignition for various heat fluxes. The error bar ($\pm 1 \text{ g/m}^2 \cdot \text{s}$) indicates the maximum and minimum limits of a moving average of the raw mass loss rate data. As the incident heat flux increases, the mass loss rate increases and thus the ignition mass flux (glowing and flaming) increases with incident heat flux. Regarding heating grain orientation, heating along the grain gives higher ignition mass flux than that across the grain. The reason is that when heating along the grain, the flows of the volatiles are not retarded by the wood grain fiber-tubes as they are when heating across the grain. As a result, a higher mass loss rate is obtained at ignition.

2.7 Conclusions

Experimental study of glowing ignition and flaming autoignition of wood was conducted. The heat fluxes employed were ranging from 9 kW/m^2 to 30 kW/m^2 . A wood surface temperature was continuously monitored by an infrared (IR) thermocouple. A mass loss was also recorded by a load cell. Glowing ignition and flaming autoignition times were measured. It was found that the critical heat flux for flaming autoignition is 20 kW/m^2 and for glowing ignition is 10 kW/m^2 . The process of glowing ignition leading to flaming autoignition was elucidated from analyzing video records and IR thermocouple signals. The experimental data given here will be used to compare with theoretical models developed in the following chapters.

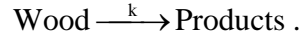
Chapter 3

A Kinetic Modeling of Wood Pyrolysis

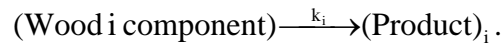
3.1 Introduction

In order to develop a theoretical model to describe the overall processes for ignition and combustion of wood, the kinetics of wood pyrolysis needs to be understood and modeled. When attempting to model many difficulties arise not only by the complexities of physical and chemical processes, but also by the lacking of reliable kinetic data inputs [7, 64]. Several studies have been performed in modeling the pyrolysis kinetics of wood and its main components (see the reviews of Refs [7, 64, 65]). Roughly, the wood pyrolysis kinetics can be described as two stages relating to primary reactions of virgin wood decomposition and secondary reactions of the primary products. Significant effects of the primary and secondary reactions depend a temperature range of interest and wood components [7]. In general, the wood kinetic models are segmented into three main groups: a single-step global reaction, single-step multiple parallel reactions and multi-step reactions.

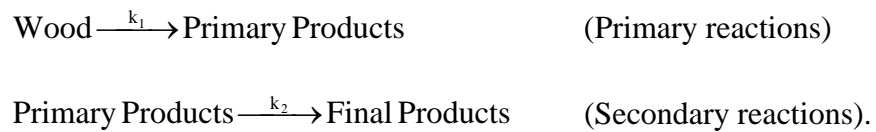
A simplest scheme to model the wood pyrolysis kinetics is to consider a single-step global reaction when the wood decomposes directly into products. Such a scheme is expressed as:



The single-step global model is widely used [19, 28, 30-32, 66-69] due to its simplicity. However, the wood degradation process is complex; thus it may not be appropriated to describe such a complex process with only one global model. An alternative choice to model is achieved by considering multiple independent single-step reactions taking place in parallel corresponding to each component of wood. Then the overall reaction is a linear combination of those components. The models that fall in this category can be written as [70-73]:



A final group used to model the wood pyrolysis kinetics is considered the kinetic processes in both primary and secondary reactions [7, 34, 35, 74]. The degradation processes are described first by the virgin wood decomposing to primary products, which they undergo secondary reactions. A general scheme of kinetic models in this group is



In present study, single-step three parallel independent reactions accounting for the main components of wood (hemicellulose, cellulose, and lignin) are considered. The thermogravimetry analysis (TGA) is employed to derive the kinetic parameters from the

proposed model. The main object of this chapter is to construct a kinetic model for wood pyrolysis to couple with heat and mass transport models for predicting the overall processes of autoignition and combustion of wood.

3.2 Thermogravimetric Experiments

In order to determine the kinetic parameters (the activation energy, E_a , and pre-exponential factor, a_p), a series of experiments were carried out using a PERKIN ELMER TAC7/DX apparatus for isothermal TGA, and a METTLER TOLEDO TGA/SDTA851 apparatus for non-isothermal TGA. The wood sample was redwood. Prior the tests, the samples were oven dry at 100 °C for 24 hours to control the moisture content. The wood samples were cut into small pieces with an initial mass ranging from 5 to 9 mg (the mean initial mass \approx 7.46 mg).

In the isothermal tests, a series of experiments were performed at constant temperatures of 300, 350, 400, 450, and 600 °C in a nitrogen environment with a purge flow of 20 ml/min. For the non-isothermal tests, a series of constant heating rates (β) of 1, 3, 10, 30, and 100 °C/min, raising a furnace temperature from a room temperature to a final pyrolysis temperature of 700 °C, were performed in a nitrogen environment with a purge flow of 30 ml/min. Typical experimental mass loss histories for both isothermal and non-isothermal are plotted in Fig. 3.1.

For the isothermal data (Fig. 3.1 (a)), the sample mass gradually decreases when the pyrolysis temperature is relatively low (300 °C). Increasing the pyrolysis temperature, the sample mass decreases more rapidly. The sample mass suddenly decreases to a final char when the pyrolysis temperature is greater than 450°C. The overall decomposition rate is controlled either by heat diffusion (conduction) into the solid or chemical reaction (Arrhenius reaction rate) depending on the heat transfer rate. For a high pyrolysis (furnace) temperature, high heat transfer rate, the chemical reaction occurs very fast; thus the decomposition rate is controlled by the heat diffusion. On the other hand, when the pyrolysis temperature is low, the heat transfer rate is minimal and the chemical reaction is slow; therefore, the overall decomposition rate depends on the chemical reaction. The gradual decrease of the sample mass loss at low pyrolysis temperature (around 300 °C) may be considered as the chemical limit while the suddenly decrease of the sample mass loss at high pyrolysis temperature (> 450 °C) can be classified as the heat diffusion limit. A low pyrolysis temperature favors cross-linking and atomization of the active cellulose to form char while a high furnace heating temperature accelerates reactions of the active cellulose to gas [7, 74]. Thus, the isothermal char yield at a low pyrolysis temperature is higher than when at a high pyrolysis temperature.

For the non-isothermal data (Fig. 3.1 (b)), at high heating rate (> 10 °C/min), the sample mass decreases almost instantaneously as the heating process starts. This indicates the decomposition process is in the heat diffusion limit region. At low heating rate (< 10 °C/min), the sample mass gradually decreases as the decomposition process is controlled by kinetics. For a given heating rate (e.g. 3 °C/min), the sample mass decreases uniformly

with one slope until its remaining mass reaches approximately 30% of the original mass; then the mass loss curve transitions to a lower slope. A presence of two slopes may imply that more than one kinetic reaction takes place, at least in this temperature range of interest.

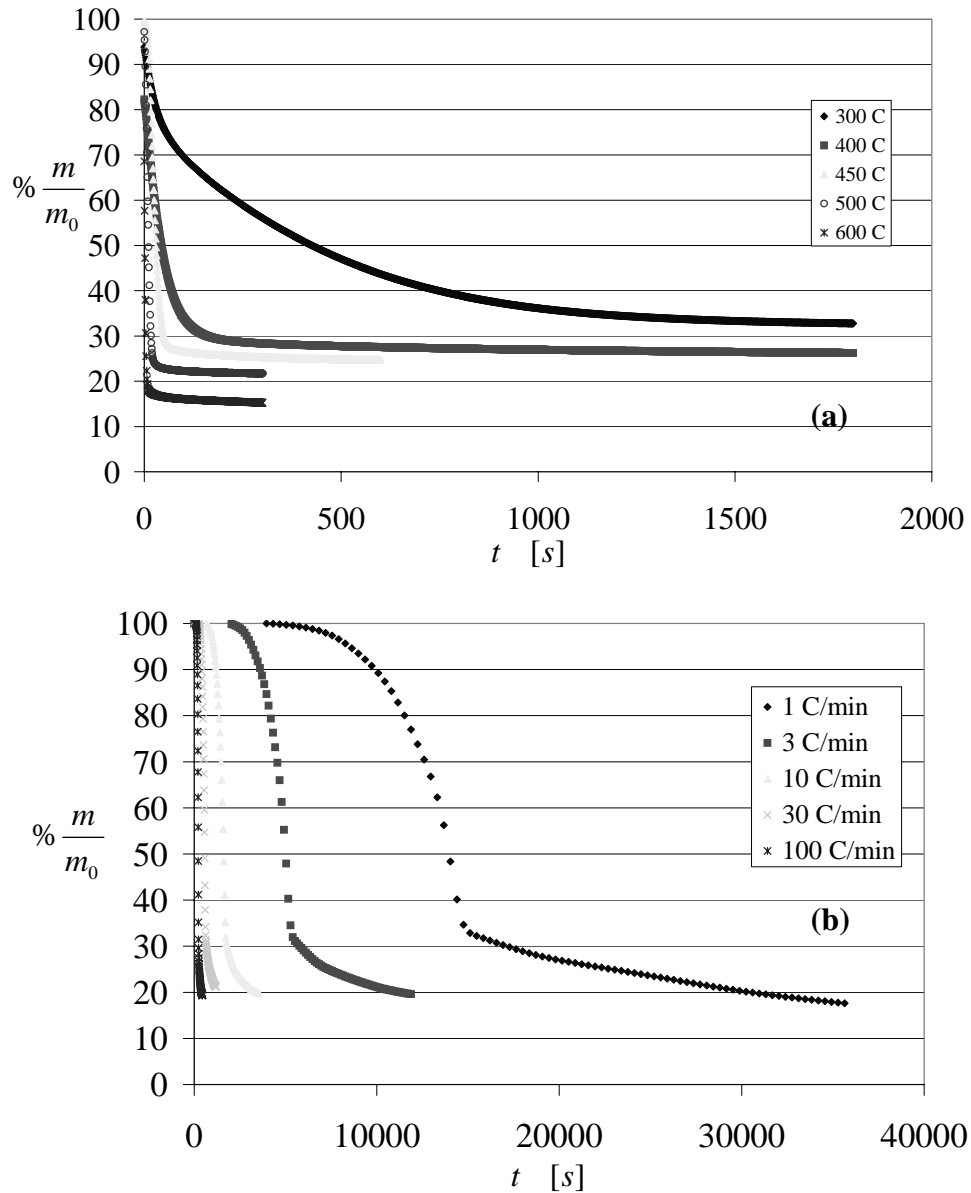


Figure 3.1: (a) Isothermal (various constant temperatures) and (b) non-isothermal (various constant heating rates) mass loss history

3.3 Methods to Determine the Wood Kinetic Parameters

In this section, methods to determine the kinetic parameters are discussed. The total wood density (ρ) changes as it undergoes the pyrolysis process. A continuum representation for decomposition considers the active wood with the char in a fixed volume. It is convenient to write an instantaneous fraction of the total wood density in terms of a mass conversion fraction (α) such that

$$\alpha = \frac{\rho - \rho_w}{\rho_f - \rho_w}; \quad (3.1)$$

Thus, the remaining fractional wood density can be given by

$$1 - \alpha = \frac{\rho - \rho_f}{\rho_w - \rho_f}. \quad (3.2)$$

The value of α goes from zero to unity as the total wood density ρ goes from ρ_w , the virgin wood density to ρ_f , the final density (i.e. char density). The rate of change of the conversion factor can be expressed in a general differential equation form as

$$\frac{d\alpha}{dt} = +f(\alpha)k(T), \quad (3.3)$$

where $f(\alpha)$ is a reaction order function depending on the local conversion factor, and $k(T)$ is the rate constant which can be expressed as the Arrhenius rate equation:

$$k(T) = a_p \exp(-E_a / RT), \quad (3.4)$$

where a_p is the pre-exponential factor, E_a is the activation energy, and R is the universal gas constant.

The positive sign in Eq. (3.3) has the physical meaning as a *production* rate of α . However, this production rate will be a *destruction* rate of the wood density (e.g. the rate of change of ρ with respect to time is negative). A primary problem of determining the rate of change of the conversion fraction (Eq. (3.3)) is how to obtain the $f(\alpha)$, and a_p and E_a in Eq. (3.4). Generally, There are two methods: (1) differential, and (2) integral methods, to determine E_a and a_p . We shall first consider the differential method following Flynn [75].

3.3.1 Differential Method

Combining Eq. (3.3) and (3.4) together provides

$$\frac{d\alpha}{dt} = f(\alpha)a_p \exp(-E_a / RT). \quad (3.5)$$

Taking the natural logarithms on both sides of Eq. (3.5) gives

$$\ln\left(\frac{d\alpha}{dt}\right) = \ln(f(\alpha)a_p) - \frac{E_a}{R}\left(\frac{1}{T}\right).$$

Flynn [75] suggested that the reaction rate at degree i of the conversion factor $((d\alpha/dt)_i)$ is a function of $f(\alpha_i)$ and $T(\alpha_i)$ or

$$\ln\left[\left(\frac{d\alpha}{dt}\right)_i\right] = \ln(f(\alpha_i)a_p) - \frac{E_a}{R}\left(\frac{1}{T(\alpha_i)}\right). \quad (3.6)$$

From Eq. (3.6), one might plot $\ln[(d\alpha/dt)_i]$ against the reciprocal of temperature, $1/T(\alpha_i)$. If the plot is linear, then the slope is $-E_a/R$ and the ordinate interception is $\ln(f(\alpha_i)a_p)$. Thus, the activation energy at α_i ($E_a(\alpha_i)$) can be estimated as

$$E_a = -R.m_1. \quad (3.7)$$

Upon which we know the form of $f(\alpha)$, the pre-exponential factor, a_p , can be calculated such that

$$a_p = \frac{e^{b_1}}{f(\alpha)}, \quad (3.8)$$

where m_1 and b_1 are the slope and the ordinate interception of the plot of $\ln[(d\alpha/dt)]$ against $1/T(\alpha)$ respectively.

Eq. (3.7) and (3.8) are widely used in determining the kinetic parameters for isothermal TGA; nonetheless, it can also be employed for non-isothermal TGA with a constant heating rate [75].

3.3.2 Integral Method

Alternately, if the rate constant $k(T)$ is not a function of α , and $f(\alpha)$ is independent of T , separation of variables in Eq. (3.3) gives

$$F(\alpha) = \int_{\alpha_0}^{\alpha} \frac{d\alpha'}{f(\alpha')} = \int_0^t k(T) dt'. \quad (3.9)$$

If the heating rate $\beta = dT / dt$ is constant, we can change the integration limit of Eq. (3.9) as

$$\int_0^t k(T) dt' = \frac{1}{\beta} \int_0^t k(T') dt' \frac{dT'}{dt'} = \frac{1}{\beta} \int_{T_0}^T k(T') dT' = \frac{a_p}{\beta} \int_{T_0}^T \exp(-E_a / RT')' dT';$$

hence,

$$F(\alpha) = \frac{a_p}{\beta} \int_{T_0}^T \exp(-E_a / RT')' dT'. \quad (3.10)$$

In this context, the sample temperature is assumed to be uniform yet varying linearly from T_0 to T in the time interval of 0 to t . Unfortunately, $F(\alpha)$ cannot be integrated explicitly; therefore, a numerical integral or approximate solutions are required. Invoking integration-by-parts of Eq. (3.10), Lyon [76] obtained the approximate solution of $F(\alpha)$ as

$$F(\alpha) \approx \frac{a_p E_a}{\beta R} \frac{e^x}{x(x-2)} = \frac{a_p RT(\alpha)^2}{\beta(E_a + 2RT(\alpha))}, \quad (3.11)$$

where $x = x(\alpha) = -E_a / RT(\alpha)$.

Take the natural logarithms on both sides of Eq. (3.11) provides

$$\ln[F(\alpha)] = \ln a_p - \ln \beta - \ln \frac{1}{T(\alpha)} - \ln(2-x) + x. \quad (3.12)$$

Since $f(\alpha)$ is independent of T , $F(\alpha)$ is not a function of T , and if a_p is also not a function of T , differentiating Eq. (3.12) with respect to the reciprocal of temperature, $1/T(\alpha)$, gives

$$\frac{d \ln \beta}{d(1/T(\alpha))} = -T(\alpha) \left[2 - x - \frac{2}{2-x} \right]. \quad (3.13)$$

The term $2/(2-x)$ in the bracket can be neglected since in a typical temperature range of interest, this term is small [76]; thus Eq. (3.13) becomes

$$\frac{d \ln \beta}{d(1/T(\alpha))} = - \left[\frac{E_a}{R} - 2T(\alpha) \right]. \quad (3.14)$$

If we plot $\ln \beta$ as an ordinate axis and $1/T(\alpha)$ as an abscissa axis, the slope of the graph is Eq. (3.14) (e.g. $d(\ln \beta)/d(1/T(\alpha)) = m_2$) providing that the activation energy at a particular conversion factor α_i is

$$E_a(\alpha_i) = -R \left[\frac{d \ln \beta}{d(1/T(\alpha_i))} + 2T(\alpha) \right] = -R[m_2 + 2T(\alpha_i)], \quad (3.15)$$

where m_2 is a slope of the plot of $\ln \beta$ against $1/T(\alpha)$.

Rearrange Eq. (3.12), we can obtain the pre-exponential factor, a_p , as

$$a_p = F(\alpha_i) \beta \left(\frac{E_a + 2RT(\alpha_i)}{RT(\alpha_i)^2} \right) \exp(E_a / RT(\alpha_i)). \quad (3.16)$$

From Eq. (3.16), a_p depends on both the heating rate β , and the conversion factor α_i (e.g. $a_p = a_p(\beta, \alpha_i)$).

Apparently, determining E_a from Eq. (3.7) or (3.15) does not require a knowledge of a form of $f(\alpha)$ or $F(\alpha)$, yet determining a_p from Eq. (3.8) or (3.16) does. Therefore, it is worthwhile to develop an expression for $f(\alpha)$ and $F(\alpha)$ to obtain a consistent pre-exponential factor for wood pyrolysis in general.

3.4 Application to Wood Pyrolysis

The wood pyrolysis process shall be described as follows. As a virgin wood is heated, it pyrolyzes to volatile gas and residual char. Let ρ_a be the time-dependence of active wood. Initially its density is equal to the virgin wood ρ_w . As the decomposition process takes place, the active wood gradually pyrolyzes leaving only final char density, ρ_f . Thus at any given time, t , the total density ρ could be written as

$$\rho(t) = (1 - X_c) \rho_a(t) + \rho_f, \quad (3.17)$$

where $X_c = \rho_f / \rho_w$ is the char fraction.

Assuming the total wood density decomposes following a first-order Arrhenius reaction rate, we can write the decomposition rate as

$$\frac{d\rho}{dt} = -\rho_a k(T) = -\rho_a a_p \exp(-E_a / RT). \quad (3.18)$$

The negative sign indicates that the total wood density decreases with time.

From definition of α (Eq. (3.1)), we can write ρ_a in term of α as

$$\rho_a = (1 - \alpha)\rho_w \quad (3.19)$$

Differentiating Eq. (3.17) and Eq. (3.19) with respect to time gives

$$\frac{d\rho_a}{dt} = \frac{1}{(1 - X_c)} \frac{d\rho}{dt}, \text{ and } \frac{d\rho_a}{dt} = -\rho_w \frac{d\alpha}{dt}.$$

Thus

$$\frac{d\rho}{dt} = -[(1 - X_c)\rho_w] \frac{d\alpha}{dt}. \quad (3.20)$$

Substituting the definition of $d\alpha/dt$ from Eq. (3.3) and $d\rho/dt$ from Eq. (3.18) into Eq.

(3.20) provides

$$\begin{aligned} \frac{d\rho}{dt} &= -\rho_a k(T) = -[(1 - \alpha)\rho_w] k(T) \\ &= -[(1 - X_c)\rho_w] \frac{d\alpha}{dt} = -[(1 - X_c)\rho_w] f(\alpha) k(T); \end{aligned}$$

Thus we obtain the form of $f(\alpha)$ as

$$f(\alpha) = \frac{(1-\alpha)}{(1-X_c)}. \quad (3.21)$$

The expression of $f(\alpha)$ in Eq. (3.21) is a general form of a first order reaction function [75]. Eq. (3.21) can then be integrated explicitly to obtain $F(\alpha)$ as

$$\begin{aligned} F(\alpha) &= \int_{\alpha_0}^{\alpha} \frac{d\alpha'}{f(\alpha')} = (1-X_c) \int_{\alpha_0}^{\alpha} \frac{d\alpha'}{(1-\alpha')} \\ &= (1-X_c) \ln\left(\frac{1-\alpha}{1-\alpha_0}\right). \end{aligned}$$

Since $\alpha_0 = 0$, $F(\alpha)$ becomes

$$F(\alpha) = (1-X_c) \ln(1-\alpha). \quad (3.22)$$

The expressions of $f(\alpha)$ in Eq. (3.21) and $F(\alpha)$ in Eq. (3.22) are based on the assumption that the wood pyrolysis is a first-order Arrhenius reaction.

3.5 Derivation of Activation Energy and Pre-exponential Factor

First we shall determine E_a and a_p based on Eq. (3.7) and (3.8). Plots of $\ln[(d\alpha/dt)_i]$ against the reciprocal of temperature, $1/T(\alpha_i)$ for various degrees of α_i are shown in

Fig. 3.2 (a) for isothermal and Fig. 3.2 (b) for non-isothermal. The degree i of α represents the percent of char converting from the virgin wood. A linear relation is obtained hence the slopes of the straight lines represent $-E_a/R$ and the ordinate interceptions are $\ln(f(\alpha)a_p)$. The E_a , and corresponding a_p at different degrees of α_i calculated from Eq. (3.7) and (3.8), are presented in Table 3.1.

Table 3.1: Summary of E_a and a_p at different degrees of α_i for (a) isothermal and (b) non-isothermal based on Eq. (3.7) and (3.8)

(a) Isothermal ($X_C = 0.2$)

α_i	$f(\alpha_i)$	$a_p (s^{-1})$	E_a (kJ/mol)
0.25	0.9375	2.185×10^4	79
0.50	0.6250	3.837×10^4	84
0.75	0.3125	1.071×10^5	89
0.95	0.0625	5.167×10^4	87

(b) Non-isothermal ($X_C = 0.2$)

α_i	$f(\alpha_i)$	$a_p (s^{-1})$	E_a (kJ/mol)
0.40	0.7500	3.575×10^{13}	194
0.80	0.2500	1.989×10^{13}	195
0.99	0.1250	2.244×10^{10}	209

Alternatively, for non-isothermal data, we can estimate E_a and a_p based on Eq. (3.15) and (3.16). A plot of $\ln \beta$ against $1/T(\alpha)$ for various α_i is shown in Fig. 3.3. From the slopes of the linear lines, the E_a can be calculated from Eq. (3.15) and then a_p from Eq. (3.16). A summary of E_a and a_p is presented in Table 3.2.

Table 3.2: Summary of E_a and a_p at different degrees of α_i for non-isothermal based on Eq. (3.15) and (3.16) ($X_c = 0.2$)

α_i	$F(\alpha_i)$	$a_p (s^{-1})$	E_a (kJ/mol)
0.02	1.616×10^{-2}	1.568×10^4	141
0.20	1.785×10^{-1}	1.281×10^7	172
0.40	4.087×10^{-1}	1.442×10^8	184
0.80	1.288	5.167×10^8	182
0.99	3.684	5.167×10^{10}	220

Comparing between E_a obtained from isothermal and non-isothermal, the isothermal E_a is somehow lower than the non-isothermal E_a by approximately two times. The difference may be due to differences in the heating method since TGA techniques are sensitive to experimental conditions [64, 73, 77]. Both the heating rate and furnace temperature are important. The other explanation is that in the isothermal TGA, all the active wood components undergo decomposition processes simultaneously rather than sequentially decomposing as they do in the non-isothermal TGA. As a result, the mass rate for the isothermal TGA is higher and the E_a is lower than if the decomposition processes were examined separately as in the non-isothermal TGA. However, the E_a from isothermal is comparable to the value of 79.8 kJ/mol suggested by Kanury [66] while the E_a from non-isothermal is consistent with most of the other literature's values in Table 3.3.

It should be noted that in isothermal TGA, the sample remains at the fixed furnace (pyrolysis) temperature for most of the decomposition while in non-isothermal TGA the furnace temperature increases over a range of values like each point in the wood would

experience due to heating at the surface (by a constant fire or radiant temperature). For this reason, the non-isothermal TGA is more like a real fire environment than the isothermal TGA.

Considering the non-isothermal E_a only, little difference is obtained between the E_a calculated from differential (Eq. (3.7)) and integral (Eq. (3.15)) methods suggesting that both approaches are consistent. The E_a increases as more fractions of virgin wood convert to char (i.e. α_i increases). The E_a shows two distinct types of behavior (see Fig. 3.4) : (1) the primary stage of wood pyrolysis process ($T < 350$ °C), when a low E_a of 141 kJ/mol is obtained, and (2) the secondary stage of the pyrolysis process ($T > 350$ °C), when a high E_a of 220 kJ/mol is observed.

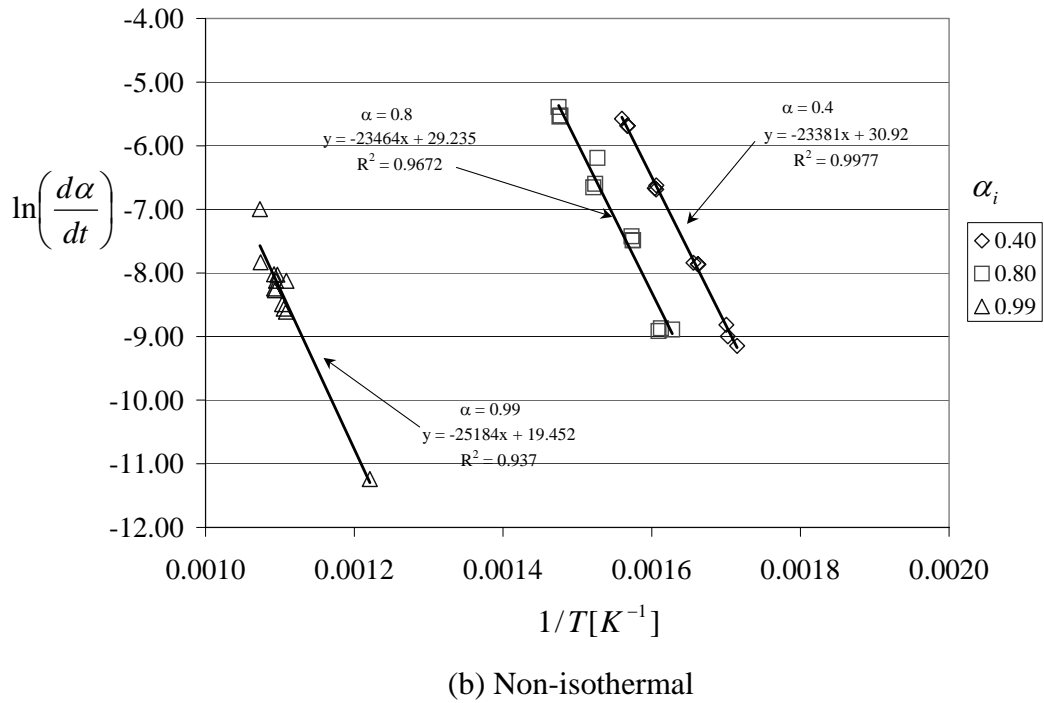
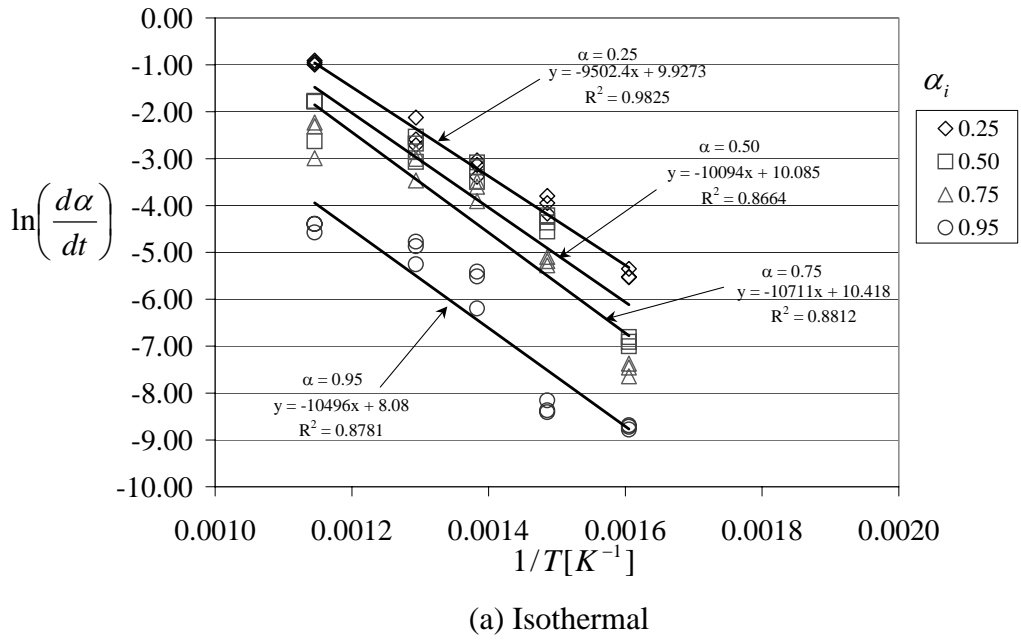


Figure 3.2: Isothermal and non-isothermal plots of $\ln[(d\alpha/dt)_i]$ against $1/T(\alpha_i)$ for various α_i

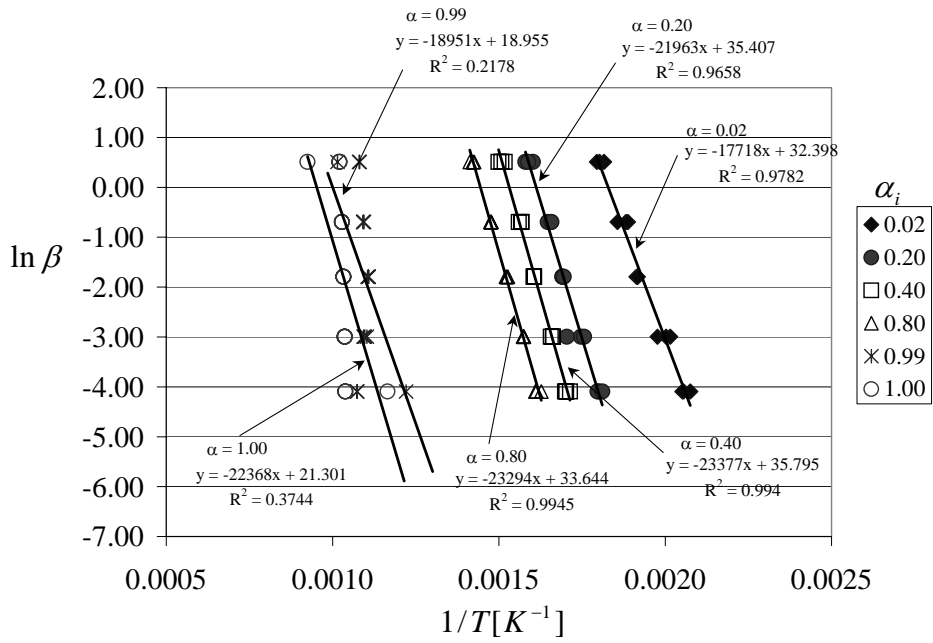


Figure 3.3: Non-isothermal plot of $\ln \beta$ against $1/T(\alpha_i)$ for various α_i

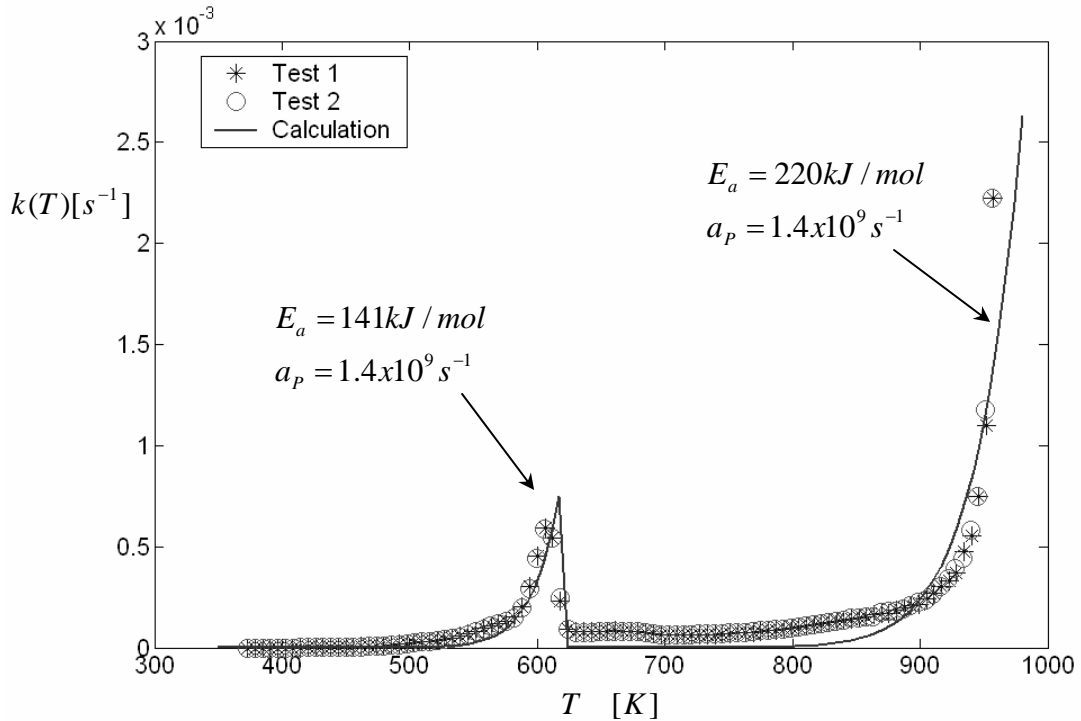


Figure 3.4: Plot of Arrhenius rate constant ($k(T)$) of wood pyrolysis for non-isothermal

TGA, $\beta = 1 \text{ }^\circ\text{C/min}$

3.6 Kinetic Modeling of Wood Pyrolysis

A low E_a results in a lower temperature corresponding to the peak of the rate constant than for a high E_a . Extracting from the experimental data, a plot of Arrhenius rate constant for $\beta = 1$ °C/min comparing with the calculated Arrhenius rate constant is shown in Fig. 3.4. The calculated Arrhenius rate constant is estimated from Eq. (3.4) with two different values of E_a . The low E_a of 141 kJ/mol is used for $T < T_{\text{break}}$ and the high E_a of 220 kJ/mol is employed for $T > T_{\text{break}}$. The T_{break} of 350 °C is introduced to obtain a best fit to the experimental rate constant; however, the T_{break} also reflects the temperature at which the primary reactions transition to the secondary reactions [30, 78] (i.e. the temperature at which a slope of mass loss curve transitions from one to another slope; see mass loss curve Fig. 3.1). The low E_a has the peak at approximately 350 °C (e.g. T_{break}) after this temperature, the rate constant drops down to almost zero and peaks again at about 700 °C, which corresponds to the peak of the high E_a rate constant. However, most of the reaction rate occurs in the primary reaction regime as one can see in Fig. 3.5, which plots experimental and calculated Arrhenius rate constant $k(T)$ (Eq. (3.4)), the experimental remaining fractional density $1 - \alpha$, and the experimental mass loss rate ($d\alpha/dt$) on the same coordinate for non-isothermal TGA with $\beta = 1$ °C/min.

The $d\alpha/dt$ is a product of $f(\alpha)$ (i.e. $(1 - \alpha)$) and $k(T)$. As earlier indicated, the $k(T)$ has two peaks where the first and second peaks correspond to the peaks of the primary and secondary rate constant respectively. However, after the first peak of $k(T)$ ($T >$

350°C), the remaining mass diminishes drastically (i.e. $(1-\alpha) \rightarrow 0$) resulting in a significant decrease of $d\alpha/dt$. At the second peak of $k(T)$, the remaining mass is almost consumed ($1-\alpha \approx 0$); thus $d\alpha/dt$ is approximately zero. This observation implies that most of the wood degradation rate is mainly due to the primary reactions occurring in a vicinity of the temperature of 350 °C, thus the secondary reactions at the temperature of 700 °C can be neglected.

Considering the wood degradation rate as a function of heating rates, Fig. 3.6 shows a peak value of $d\alpha/dt$ that remarkably increases as the heating rate β increases suggesting that the decomposition rate strongly depends on the heating rate. However, the corresponding temperatures to the peaks slightly increase as the heating rates increases. The corresponding peak temperatures vary in a narrow range from approximately 350 °C to 450°C. The narrow range of the corresponding peak temperatures confirms the assumption that only the primary reactions dominate the overall wood decomposition rate at least in this temperature range of interest.

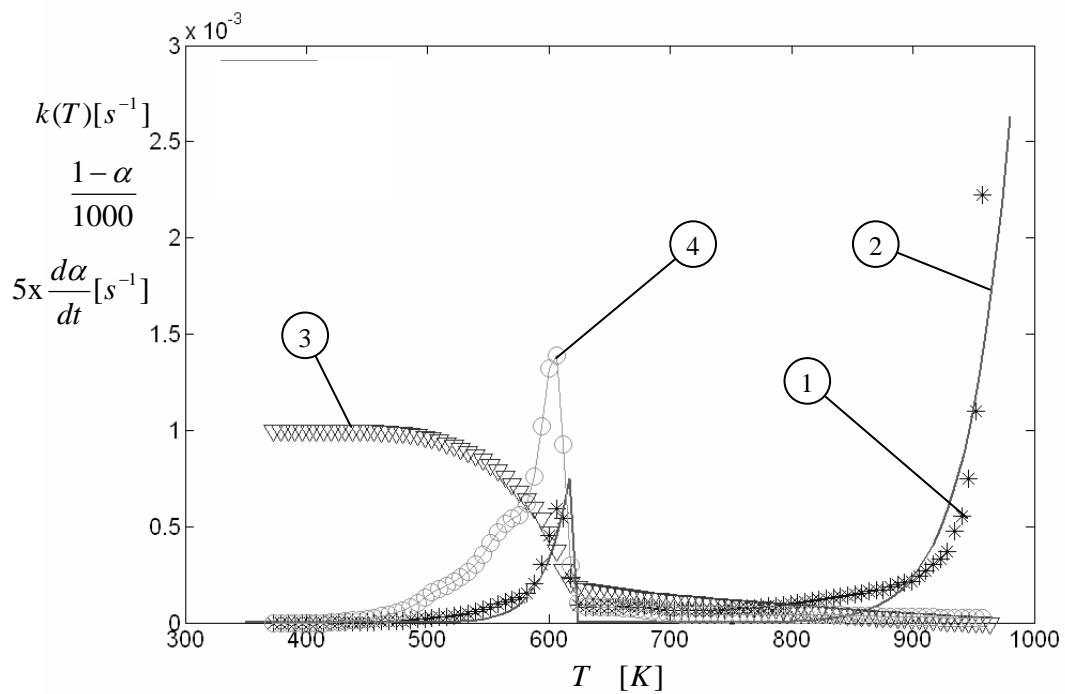


Figure 3.5: Plot of 1- experimental $k(T)$; 2 - calculated $k(T)$; 3-remaining fractional density $(1 - \alpha)$; and 4-experimental $d\alpha/dt$ for non-isothermal TGA, $\beta = 1$ °C/min

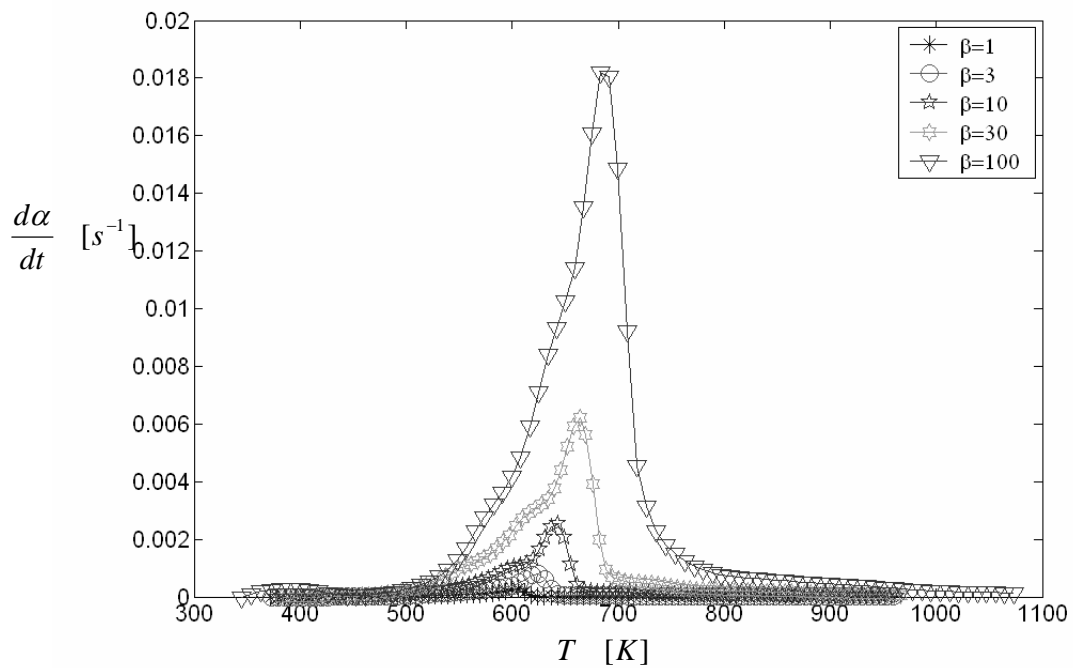
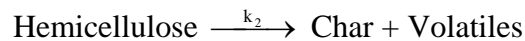
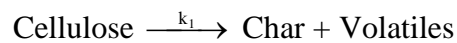


Figure 3.6: Plot of non-isothermal wood decomposition rate $(d\alpha/dt)$ for various β

As we carefully observe the decomposition rate curve (Fig. 3.6), there appears to be (at least) three separate peaks merged together to make the overall decomposition rate peaks. Thus it is possible to model each peak separately depending on different kinetic reactions. The overall wood decomposition rate is the weighted sum of those independent decomposition rates, based on mass fraction of each component, contributing to the overall mass of the virgin wood.

Generally, wood is mainly composed of cellulose (50%), hemicellulose (25%), and lignin (25%) [64]. The hemicellulose is found to decompose first in a temperature range between 200 °C and 260 °C. The second component decomposing is cellulose, which occurs in a temperature range of 240 °C to 350 °C. Finally, the decomposition of lignin takes place around 280 °C to 500 °C. If we assume the main three wood components in the mixture behave in the same way as they do separately [70, 71], we may model the decomposition rate of each component independently in three parallel reactions as:



The overall wood decomposition rate ($d\alpha/dt$) is the weighted sum of the three parallel reactions:

$$\frac{d\alpha}{dt} = \sum_{j=1}^3 X_j \frac{d\alpha_j}{dt}, \quad (3.23)$$

and

$$\frac{d\alpha_j}{dt} = f(\alpha_j)k_j(T), \quad (3.24)$$

where X_j is the mass fraction of the j^{th} component of wood (consider wood to be a mixture); $\sum_{j=1}^3 X_j = 1$, α_j is the mass conversion of wood component j ; $\sum_{j=1}^3 X_j \alpha_j = \alpha$ (the total mass conversion), and $j = 1$, cellulose; $j = 2$, hemicellulose; $j = 3$, lignin. The reaction order functions $f(\alpha_j)$ are expressed according to Eq. (3.21) and the rate constant $k_j(T)$ follows Eq. (3.4); thus.

$$f(\alpha_j) = \frac{(1 - \alpha_j)}{(1 - X_{C,j})} \quad (3.25)$$

and

$$k_j(T) = a_{p,j} \exp(-E_{a,j} / RT). \quad (3.26)$$

The $X_{C,j}$ is the char fraction of the j^{th} component; however, for simplicity we assume all components have the same char fraction. As we observed from the residual mass in Fig.

3.1 for both isothermal and non-isothermal TGA, the final char mass fraction is approximately 20% thus $X_{c,j} = 0.20$.

To fit the theoretical decomposition rate (Eq. (3.23)) to the experimental value, first we assume the main three fractions are $X_1 = 0.75$, $X_2 = 0.15$, and $X_3 = 0.10$. As indicated earlier, the E_a of 141 kJ/mol is a dominant value for the overall mass loss rate, consequently this activation energy is assigned for the cellulose component ($E_{a,1} = 141$ kJ/mol, and $a_{p,1} = 1.41 \times 10^9$ s⁻¹). The other two E_a are estimated based on the least squared method [70] in order to minimize the summation function:

$$S = \sum_{n=1}^N \left[\left(\frac{d\alpha}{dt} \right)_{\text{exp}} - \left(\frac{d\alpha}{dt} \right)_{\text{cal}} \right]^2. \quad (3.27)$$

The subscript “exp” refers to the experimental value and “cal” refers to the calculation value (Eq. (3.23)). The summation is performed over the data points N .

We may define the average deviation [70] as

$$Div(\%) = 100 \times \frac{\sqrt{S/N}}{\max(d\alpha/dt)_{\text{exp}}}. \quad (3.28)$$

Within 5% of the average deviation, the $E_{a,2} = 125$ kJ/mol and $E_{a,3} = 165$ kJ/mol with the $a_{p,2} = a_{p,3} = a_{p,1}$ are obtained. A plot of the experimental and calculation decomposition rate is shown in Fig. 3.7. The calculation degradation rate captures the experimental value reasonably well as we express the very complex process of wood decomposition with three parallel single-step reactions. For comparison, a single global reaction model (i.e. $X_1 = 1$, $X_2 = X_3 = 0$) with the $E_a = 141$ kJ/mol and $a_p = 1.41 \times 10^9$ s⁻¹ is also plotted on Fig 3.7. It is obvious that the single global reaction model over predicts the overall decomposition rate; nevertheless, the temperature at the peak of the decomposition rate matches fairly well with the experimental data.

As we integrate the decomposition rate, the remaining mass conversion fraction ($1 - \alpha$) can be obtained. Fig. 3.8 plots the remaining mass conversion fraction for the three parallel reaction model, and single global reaction model comparing to the experimental data as a function of temperature. Good agreement between the experimental data and the three parallel reaction model is obtained. It can be implied from the plot that about 90% of the active part of wood components is composed of cellulose and hemicellulose. The other 10% remaining of the active part is responsible by the lignin component, which decomposes at a slightly higher pyrolysis temperature. Although the single global reaction model is able to reproduce the experimental remaining mass conversion fraction at the middle stage of the decomposition process, it cannot capture the experimental value at the early and final stages.

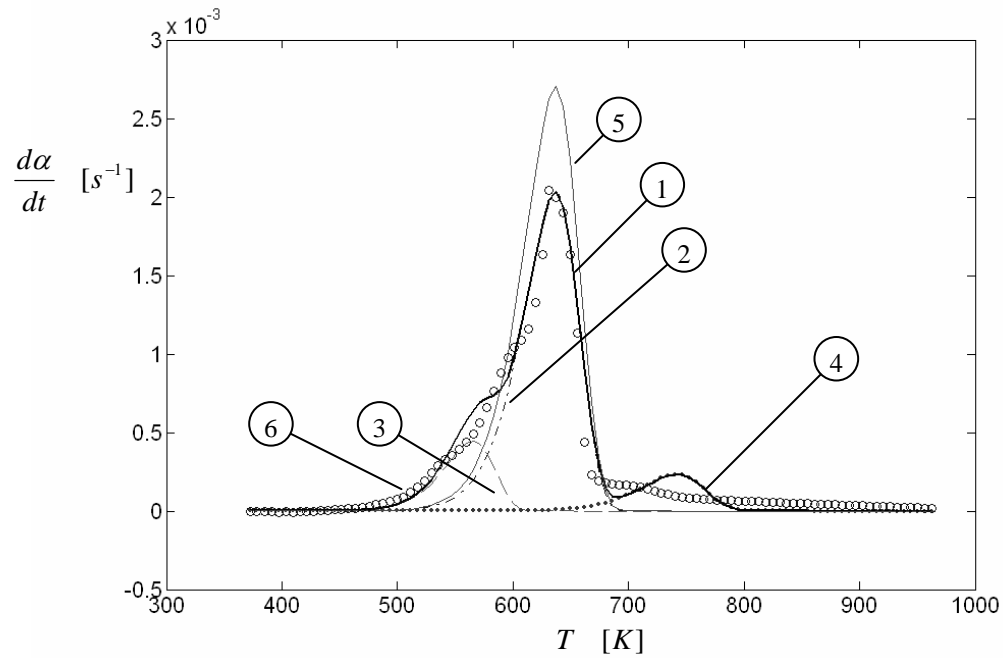


Figure 3.7: Plot of 1- overall wood decomposition rate (Eq. (3.23)); 2- $X_1 d\alpha_1 / dt$, cellulose decomposition rate; 3- $X_2 d\alpha_2 / dt$, hemicellulose decomposition rate; 4- $X_3 d\alpha_3 / dt$, lignin decomposition rate; 5-single global wood decomposition rate; 6- experimental data, for non-isothermal TGA, $\beta = 10^\circ\text{C}/\text{min}$.

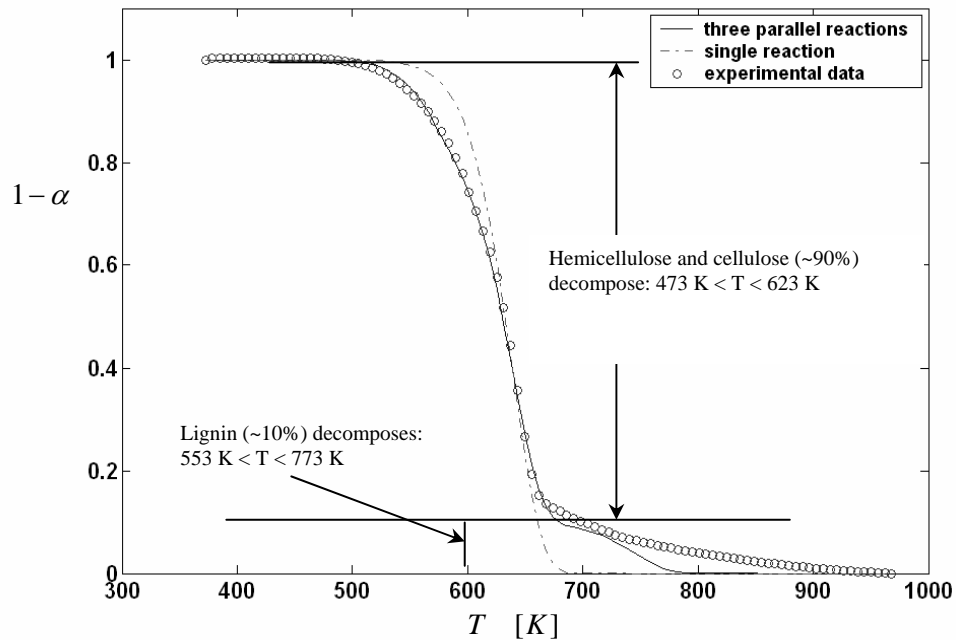


Figure 3.8: Plot of experimental and calculated remaining mass conversion ($1 - \alpha$) for non-isothermal TGA, $\beta = 10^\circ\text{C}/\text{min}$

3.7 Comparisons of Wood Kinetic Parameters

In a simulation of wood pyrolysis and ignition, the wood kinetic parameters play an important role. These parameters sometimes depend on experimental conditions, preparations of samples, types of samples (e.g. wood species), as well as treatments of the experimental data. Consequently, the kinetic parameters may vary from one particular experiment to another. A variety of kinetic values are obtained as we search through the literature; there is merit to summarize them for comparison purposes. The literature's values for E_a , and a_p summarized here are categorized mainly into two groups: (1) the values deduced from experimental studies chiefly from TGA techniques, and (2) the estimated values that researchers employed to obtain best fit for their overall wood degradation and combustion models.

In the first group in which E_a and a_p are deduced from experiments, Milosavljevic et al. [68] and Suurberg et al. [19, 69] conducted non-isothermal TGA, which the samples were heating with a constant rate until reached final pyrolysis temperatures. They suggested that E_a and a_p of wood depended on char yield, heating rate, and a final pyrolysis temperature of interest. Different values were obtained as slow or rapid heating rates were used. For low final pyrolysis temperatures (<327 °C) with slow heating rate ($\beta \approx 6$ °C/min), they obtained a relatively high E_a of 221 kJ/mol and a corresponding a_p of $1.13 \times 10^{17} \text{ s}^{-1}$. For high final pyrolysis temperature (>327 °C) with rapid heating rate ($\beta \approx 60$ °C/min), the E_a would yield a value of 139 kJ/mol with a_p of $9.13 \times 10^{11} \text{ s}^{-1}$.

Roberts [64] pointed out that with highly purified cellulose, the pyrolysis would proceed with a high E_a of 235 kJ/mol when the pyrolysis was unaffected by autocatalysis. When autocatalytic effects took place, however, the pyrolysis would yield a low E_a of 126 kJ/mol. Differences in sample size and heating rates were also studied. A large sample with rapid heating rates would give a low E_a while a small sample with slow heating rates yields a higher E_a . Kanury [66] employed a radiograph technique where a density changing of a specimen was monitored continuously by a series of X-ray images. The sample was heated with a constant heating rate until it reached a final pyrolysis temperature. With a best linear fit to his data, he obtained E_a of 79.8 kJ/mol with a_p of $2.5 \times 10^4 \text{ s}^{-1}$. Lewellen et al. [67] deduced E_a and a_p from the experimental data by assuming the pyrolysis followed a single-step first order process. They suggested values of 140 kJ/mol for E_a and $6.79 \times 10^9 \text{ s}^{-1}$ for a_p . Broido et al. [74] studied a decomposition process for a relatively large cellulose sample ($> 100 \text{ mg}$), and obtained an E_a of 74 kJ/mol. They proposed that the cellulose pyrolysis could proceed with two different paths where the ratio of the rate constant of these two paths remaining approximately constant. However, the Broido's pyrolysis mechanism was refuted by recent researchers [65, 70] due to the experimental conditions were strongly in the heat transfer limit. Frenlund [41] obtained a relatively low value of E_a (26.3 kJ/mol). His kinetic values differed greatly from those of other researches. The discrepancy may be due to the technique employed in his experiment where the Frenlund samples were relatively larger than others and hence the Frenlund E_a would fall into the range of heat and mass transfer limit.

Regarding an initial sample mass/size and heating rate, we may point out that at high heating rate (or large sample mass/size), the pyrolysis rate of cellulose would be controlled by heat and mass transfer diffusion resulting in a low E_a . On the other hand, at a low heating rate (or small sample mass/size), the pyrolysis rate is in a chemical limit resulting in a high E_a .

Recently, single-step multiple independent parallel reactions accounting for the main components of cellulosic materials have been proposed by many researchers [70-73]. Orfao et al. [70, 71] assumed three independent parallel reactions to express decomposition processes for a variety of wood species. They obtained E_{a1} of 201 ± 7 kJ/mol with a_{p1} of $(1.14 \pm 0.4) \times 10^{15} \text{ s}^{-1}$ for pseudo-component 1, E_{a2} of 88.4 kJ/mol with a_{p2} of $5.27 \times 10^5 \text{ s}^{-1}$ for pseudo-component 2, and E_{a3} of 18.1 kJ/mol with a_{p3} of $1.57 \times 10^{-2} \text{ s}^{-1}$ for pseudo-component 3 where pseudo-component 1, 2, and 3 are related to the primary decompositions of cellulose, hemicellulose, and lignin respectively. Gronli et al. [73] studied degradation processes of various species of hard and soft woods. They found that with three parallel first-order reactions for the main three components and two extractive reactions of wood, the simulation model could describe the degradation processes of hard and soft woods with good accuracy. They suggested a set for E_a of 100, 236, and 46 kJ/mol for the main components (hemicellulose, cellulose, and lignin respectively), and 105 and 127 for the two extractive components. Wu et al. [72] assumed two parallel first-order reactions to simulate a kinetic degradation of red oak. With E_{a1} of

220 kJ/mol and E_{a2} of 240 kJ/mol, good agreement between the simulation and the experiment was obtained.

The above E_a and a_p were derived based on a first-order reaction model; however, it is possible to model the kinetic pyrolysis with other reaction order. For example, Kashiwagi and Nambu [79] employed a non-isothermal TGA technique (heating rate ranging from 0.5 to 1 °C/min) to determine the kinetic constants of a thin cellulosic paper. They found that the simulated pyrolysis rates agreed well with the experiments when the reaction order was assumed to be 1.8. They obtained E_a of 220 kJ/mol with a_p of $2 \times 10^{17} \text{ s}^{-1}$ for the degradation processes in a nitrogen atmosphere, and E_a of 160 kJ/mol with a_p of $2 \times 10^{12} \text{ s}^{-1}$ for the degradation processes in air.

In the second group of E_a and a_p results in which the investigators assumed values to obtain the best fit for their modeling predictions of thick decomposing wood samples, Kung [26] used the values for E_a of 139 kJ/mol with a_p of $5.3 \times 10^8 \text{ s}^{-1}$. Tinney [30], when computing weight loss of heated wooden dowels, found that it was necessary to introduce a break point into the computations to obtain good agreement with the experimental weight loss values. He suggested that for the first stage of computation, ($\rho / \rho_w < 0.33 \sim 0.5$), the E_a would be 124 kJ/mol with a_p of $6 \times 10^7 \sim 7.5 \times 10^8 \text{ s}^{-1}$. For the final stage of the decomposition ($\rho / \rho_w > 0.33 \sim 0.5$), the E_a would be 150~180 kJ/mol with a_p of $4 \times 10^8 \sim 2 \times 10^9 \text{ s}^{-1}$. If we convert the Tinney's break point based on the density ratio (ρ / ρ_w) to our present study of mass conversion fraction (α), the Tinney's break

point in terms of α would be 0.6 ~ 0.8 and thus the T_{break} would be 300~400°C. This observation shows that the T_{break} of 350°C in the present study is consistent with Tinney's T_{break} . Other estimated literature's values of E_a and a_p are summarized in Table 3.3.

3.8 Heat of Wood Pyrolysis

Though the present TGA study could not provide information for the heat of pyrolysis of wood (Q_p), it is worthwhile to summarize the values from others literature. The heat of pyrolysis is the energy released from, or required to break the molecular bonds of the wood. Among the literature's values, there is great confusion in terms of Q_p as endothermic or exothermic, as well as its magnitude.

Suuberg et al. [19] reported that as the wood pyrolysis proceeded, a number of exothermic and endothermic processes are involved; however, the overall pyrolysis process is endothermic. He suggested that the endothermic heat of pyrolysis was in the range of 70 to 400 kJ/kg depending on the char yield. In contrast, Roberts [32] argued that the bulk pyrolysis process of wood should be exothermic due to the wood lignin content. He suggested that as the wood decompose to yield cellulosic material and lignin. The lignin would further decompose to give volatiles and residual solid, and thus this process is exothermic which controls the overall heat of pyrolysis of wood. He calculated the exothermic heat of pyrolysis of wood as 192 kJ/kg. Recently study on the heat of wood pyrolysis was carried out by Rath et al. [78], where they employed TGA and DSC (differential scanning calorimeter) techniques with a heating rate of 10 °C/min to two

species of woods (beech and spruce). They found that as the wood underwent the primary reaction (200 to 390 °C), the heat of pyrolysis was endothermic; however, as the secondary reaction took place (from 390 to 500 °C), the heat of pyrolysis shifted to be exothermic. The primary reaction reflected the degradation process of virgin wood to primary char, while the secondary reaction was the further reaction of the primary char. The overall heat of pyrolysis was the sum of the heat of pyrolysis from the primary and secondary reactions. Depending on wood species, they calculated the overall heat of pyrolysis of beech as 122 kJ/kg (endothermic) and spruce as 289 kJ/kg (endothermic).

In dealing with the uncertainty whether wood pyrolysis is exothermic or endothermic process, Atreya [4] suggested that the energy due to the pyrolysis term was small compared to other terms in the transport energy equation of the wood pyrolysis process and shall be neglected for simplicity. This assumption was also assumed by various investigators [29, 41]. A summary of literature on the heat of pyrolysis of wood is presented in Table 3.3.

3.9 Conclusions

Isothermal and non-isothermal TGA studies of wood pyrolysis (redwood) were performed. A kinetic model was constructed. Conclusions can be drawn as the followings. The activation energy obtained from isothermal TGA is less than that from non-isothermal TGA by about a factor of 2. However, the non-isothermal activation energy is recommended in modeling wood pyrolysis since in a fire environment the wood

is more likely to be heated with constant heating rate rather than constant temperature. Most of the wood decomposes in the temperature vicinity of 350°C confirming that the primary reactions dominate the overall wood decomposition process in the temperature range of 300 to 700 °C. The primary reactions can be further modeled by three independent parallel first-order reactions corresponding to the main three components of wood (cellulose, hemicellulose, and lignin). The activation energy of 125 kJ/mol for hemicellulose, 141 kJ/mol for cellulose, and 165 kJ/mol for lignin are found to be the best fit to the experimental decomposition rate and remaining mass conversion fraction.

Table 3.3: Summary of wood kinetic parameters and heat of pyrolysis

References	a_p [s ⁻¹]	E_a [kJ/mol]	Q_p^c [kJ/kg]	Sample
Milosavljevic et al. [68] and Suuberg et al. [19, 69] ^a	9.13x10 ¹¹ (>327°C, and rapid β), 1.13x10 ¹⁷ (<327°C, and slow β)	139 (>327°C, and rapid β), 221 (<327°C, and slow β)	+70 ~ +400	Cellulose powder (Whatman CF-11 powder)
Kanury [66] ^a	2.5x10 ⁴	79.80	-	α -Cellulose
Roberts [64] ^a	7x10 ⁷	126 (rapid β , with autocatalytic effects), 235 (slow β , without autocatalytic effects)	-	Cellulosic material
Fredlund [41] ^a	0.54	26.3	0	Spruce
Lewellen et al. [67] ^a	6.79x10 ⁹	140	-	Cellulosic material
Orfao et al. [70, 71] ^a	$a_{p1} =$ (1.14 ± 0.4)x10 ¹⁵ $a_{p2} = 5.27x10^5$ $a_{p3} = 1.57x10^{-2} s^{-1}$	$E_{a1} = 201 \pm 7$ (cellulose) $E_{a2} = 88.4$ (hemicellulose) $E_{a3} = 18.1$ (lignin)	-	Pine, Eucalyptus, Pine bark
Gronli et al. [73] ^a	2.63x10 ¹⁷ (cellulose) 2.29x10 ⁶ (hemicellulose) 3.98 (lignin) 8.13x10 ⁸ (extractive 1) 1.78x10 ¹⁰ (extractive 2)	236 (cellulose) 100 (hemicellulose) 46 (lignin) 105 (extractive 1) 127 (extractive 2)	-	Redwood
Wu et al. [72] ^a	$a_{p1} = 1x10^{15}$ $a_{p2} = 1x10^{15}$	$E_{a1} = 220$ $E_{a2} = 240$	-	Red Oak

Broido and Nelson [74] ^a	-	74	-	Cellulosic material (> 100 mg)
Kashiwagi et al. [79] ^a	2x10 ¹⁷ (in N ₂) 2x10 ¹² (in Air)	220 (in N ₂) 160 (in Air)	-	Paper
Rath et al. [78] ^a	-	-	+122 +289	Beech Spruce
Weatherford and Sheppard [31] ^b	5.3x10 ⁸	139	+360	-
Gandhi and Kanury [44] ^b	7x10 ⁷	126	+360	-
Ritchie et al. [33] ^b	2.5x10 ⁸	126	+126	-
Roberts [32] ^b	7x10 ⁷	126	-192	-
Parker [29] ^b	5.94x10 ⁷	121	0	-
Tinney [30] ^b	6x10 ⁷ ~7.5x10 ⁸ ($\rho/\rho_w < 0.33 \sim 0.5$), 4x10 ⁸ ~2x10 ⁹ ($\rho/\rho_w > 0.33 \sim 0.5$)	124 ($\rho/\rho_w < 0.33 \sim 0.5$) 150~180 ($\rho/\rho_w > 0.33 \sim 0.5$)	-	-
Atreya [4] ^b	1x10 ⁸	125	0	-
Sibulkin [28] ^b	1x10 ¹⁰	150	+500	-
Present Study	1.41x10 ⁹	125 (hemicellulose) 141 (cellulose) 165 (lignin)		Redwood

^a obtained from experimental study

^b obtained from the best fit to their numerical models

^c positive sign indicates endothermic, negative sign indicates exothermic.

Chapter 4

The Solid Phase

4.1 Introduction

As wood is subjected to a heat flux, it undergoes decomposition. The wood decomposes generating fuel gases flowing to the surrounding while leaving a residual char matrix over the virgin wood. As the fuel gases flow, they mix with air creating a combustible mixture. At a critical condition of the combustible mixture (e.g. suitable fuel/air concentration and sufficient gas temperature), flaming ignition can occur without any help of a piloted source (e.g. autoignition).

When the heat flux to the wood surface is high, the ignition occurs relatively fast before char significantly forms on the surface. The flame first appears in the gas phase away from the heated surface [2, 9]. However, when the heat flux is low, the char formation on the surface is considerable before flaming ignition occurs [2]. The char layer behaves like a thermal insulator by blocking heat transfer to the virgin wood; hence, a high surface temperature of the char layer is observed. Because of the high surface temperature, the char layer can react heterogeneously with the oxygen from the surroundings resulting in “surface oxidation” and eventually “glowing ignition” at the surface [2]. By “glowing ignition”, we mean the onset of surface combustion. Glowing ignition is the stage in which the surface undergoes rapid oxidation [80]. Typically, the corresponding surface

temperature can drastically increase over few seconds. This rapid increase is due to an imbalance of energy on the surface, with the release of chemical energy to thermal energy becoming dominant. Consequently, the surface oxidation transitions to “surface combustion” or “glowing surface”. The glowing surface is exothermic. It adds energy to the combustible gas mixture adjacent to the char surface. When the combustible mixture temperature is sufficiently high, the glowing surface could cause transition to flaming ignition.

In this chapter, a theoretical model for solid phase wood combustion is developed. The physical and chemical processes accounting for heat and mass transfer in the solid matrix are investigated. The char surface oxidation, which can lead to “glowing ignition”, is included at the solid-gas interface. Criteria for glowing ignition based on a critical point for the surface energy balance are proposed and validated with the experimental data.

4.2 Theoretical Model

4.2.1 Assumptions

To account for heat and mass transfer during the wood decomposition, a mathematical model is developed after Kung [26]. Modifications have been made to account for char surface oxidation and temperature dependency of wood thermal properties. The following assumptions are imposed in order to simplify the problem:

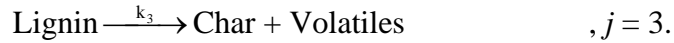
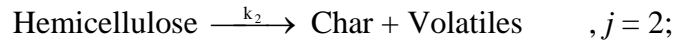
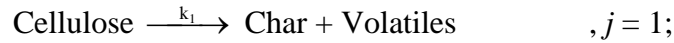
1. Since the incident heat flux to the solid surface is uniform, the problem could then be formulated as a one-dimensional transient heat conduction problem.

2. At any instant, the continuum volume of wood consists of three species: active wood, char, and volatiles.
3. The wood decomposition processes can be expressed by three independent single-step parallel reactions as described in chapter 3.
4. As soon as the volatiles are formed, they instantaneously flow to the surface.
5. The pressure inside the solid matrix is constant (No Darcy law for the flow of volatiles).
6. The volatile density is small comparing to active wood and char, and shall be neglected in the mass conservation of the continuum volume.
7. The volatiles and the solid matrix are in thermal equilibrium (e.g. $T_{gas} = T_{solid}$).
8. The effect of water vaporization of the wood sample is small and can be neglected since the experiments were conducted on a dry base.
9. Local thermal properties and solid density vary with temperature and they can be determined from a weighted average of the active wood and char.
10. Convective and radiative heat losses are taken into account at the solid surface.
11. No heat or mass losses occur at the back of the solid (e.g. the solid back boundary is perfectly insulated for both heat and mass transfer).
12. The char oxidation takes place only at the solid surface, (no in-depth char oxidation) and it is taken into account at the front boundary of the energy equation.
13. The char surface oxidation depends on the surface oxygen concentration and surface temperature. A one-dimensional stagnant layer model is assumed to compute the oxygen diffusion from the surroundings to the oxidizing surface.

14. Surface regression due to char surface oxidation is taken into account via a moving boundary.

4.2.2 Description of a Decomposing Wood System

Consider the wood system as a continuum volume. At any time, the wood system is consisted of virgin wood, char, and volatiles. As discussed in Chapter 3, the decomposition of the virgin wood can be described by the main three components of wood as cellulose ($j=1$), hemicellulose ($j=2$), and lignin ($j=3$). The decomposition of the j^{th} component can be described as:



Assuming each component of wood decomposes following a single-step first order Arrhenius reaction rate, we can write the decomposition rate of the j^{th} component as

$$\frac{\partial \rho_j}{\partial t} = -\rho_{a,j} a_{p,j} \exp(-E_{a,j} / RT) \quad ; \text{ for } j = 1, 2, 3, \quad (4.1)$$

where ρ_j is the total density of the j^{th} component, $\rho_{a,j}$ is the active density of j^{th} component. $E_{a,j}$ and $a_{p,j}$ are the activation energy and pre-exponential factor of the j^{th} component respectively.

It is convenient to represent the total density of the j^{th} component, ρ_j , in term of the active density, $\rho_{a,j}$. Initially the active density is equal to the virgin wood density, $\rho_{w,j}$. As the decomposition process takes place, the active density gradually pyrolyzes to zero, leaving only the final char density, $\rho_{f,j}$. Thus, at any instant, the total density of the j^{th} component, ρ_j , is expressed as

$$\rho_j = (1 - X_{c,j})\rho_{a,j} + \rho_{f,j}, \quad (4.2)$$

where $X_{c,j} = \rho_{f,j} / \rho_{w,j}$ is the char mass fraction and $\rho_{f,j}$ is the final char density of the j^{th} component. Combining Eq. (4.1) and (4.2) the j^{th} component decomposition becomes

$$\frac{\partial \rho_j}{\partial t} = -a_{p,j} \left(\frac{\rho_j - \rho_{f,j}}{1 - X_{c,j}} \right) \exp(-E_{a,j} / RT). \quad (4.3)$$

The overall decomposition rate is the sum of each component; thus,

$$\frac{\partial \rho}{\partial t} = \sum_{j=1}^3 X_j \frac{\partial \rho_j}{\partial t}, \quad (4.4)$$

where X_j is the mass fraction of the j^{th} component in the continuum volume of wood.

4.2.3 Species Conservation

The continuum volume of wood is composed of three species: active wood, char, and volatile;

$$\rho = \rho_a + \rho_c + \rho_g \nearrow \approx 0, \quad (4.5)$$

where $\rho = \sum_{j=1}^3 X_j \rho_j$ is the total wood density, $\rho_a = \sum_{j=1}^3 X_j \rho_{a,j}$ is the total active density

species, $\rho_c = \sum_{j=1}^3 X_j \rho_{c,j}$ is the total char density species, and ρ_g is the volatile species

which is small, and we assume can be neglected.

The rate of change of the total density in the continuum is

$$\frac{\partial \rho}{\partial t} = \frac{\partial \rho_a}{\partial t} + \frac{\partial \rho_c}{\partial t} + \frac{\partial \rho_g}{\partial t}. \quad (4.6^*)$$

The effect of ignoring the gas density might be considered here. From the equation of state, the gas density within the solid matrix may be estimated as $\rho_g = P / RT_g$, where P is the pressure inside the solid matrix taken as a constant. Thus $\partial \rho_g / \partial t = (P/R)(-1/T_g^2)(\partial T_g / \partial t) = -(\rho_g / T_g)(\partial T_g / \partial t)$, which is generally small (because $\rho_g \approx 0$). The rate of change of the total density becomes

$$\frac{\partial \rho}{\partial t} = \frac{\partial \rho_a}{\partial t} + \frac{\partial \rho_c}{\partial t}. \quad (4.6)$$

Differentiating Eq. (4.2) with respect to time and substituting into Eq. (4.4) we can also write the rate of change of the total density as

$$\frac{\partial \rho}{\partial t} = (1 - X_c) \frac{\partial \rho_a}{\partial t}, \quad (4.7)$$

where $X_c = X_{c,j}$ is the char mass fraction which is constant for all wood components (cellulose, hemicellulose, lignin).

Rearranging Eq. (4.6), and (4.7) we obtain the rate of change of the total active and char density as

$$\frac{\partial \rho_a}{\partial t} = \sum_{j=1}^3 X_j \frac{\partial \rho_{a,j}}{\partial t} = \left(\frac{1}{(1 - X_c)} \right) \frac{\partial \rho}{\partial t}, \quad (4.8a)$$

and

$$\frac{\partial \rho_c}{\partial t} = \sum_{j=1}^3 X_j \frac{\partial \rho_{c,j}}{\partial t} = \left(\frac{-X_c}{(1 - X_c)} \right) \frac{\partial \rho}{\partial t}, \quad (4.8b)$$

The summation is made over the main three components of the active wood (cellulose, hemicellulose, and lignin).

4.2.4 Mass Conservation

A one-dimensional mass conservation is

$$\frac{\partial \rho}{\partial t} + \frac{\partial(\rho_a v_a)}{\partial x} + \frac{\partial(\rho_c v_c)}{\partial x} + \frac{\partial(\rho_g v_g)}{\partial x} = 0. \quad (4.9^*)$$

Since $v_a = v_c = 0$, the active wood and char do not flow, and $\rho_g v_g = -\dot{m}''$, the pyrolysis mass flux of the volatiles (the negative sign indicates the pyrolysis mass flux flows out in the negative x-direction). The mass conservation becomes

$$\frac{\partial \rho}{\partial t} = \frac{\partial \dot{m}''}{\partial x}. \quad (4.9)$$

4.2.5 Energy Conservation

A one-dimension energy conservation of the solid matrix is

$$\frac{\partial(\rho_a h_a + \rho_c h_c + \rho_g h_g)}{\partial t} + \frac{\partial}{\partial x}(\rho_a v_a h_a + \rho_c v_c h_c + \rho_g v_g h_g) = -\frac{\partial(\dot{q}'')}{\partial x}, \quad (4.10a)$$

where $\rho_a h_a = \sum_{j=1}^3 X_j \rho_{a,j} h_{a,j}$ is the total enthalpy of the active wood (sum over cellulose,

hemicellulose and lignin), $\rho_c h_c = \sum_{j=1}^3 X_j \rho_{c,j} h_{c,j}$ is the total enthalpy of char, and $\rho_g h_g$

is the total enthalpy of the volatiles. The subscript “a” is for active wood, “C” is for char,

and “g” is for volatiles. \dot{q}'' is the heat conduction within the solid matrix, which can be written as $-k(\partial T / \partial x)$.

Recalling that there is no flow for the active wood and char species; thus $v_a = v_c = 0$, and $\rho_g v_g = -\dot{m}_g''$, we can rewrite the energy equation as

$$\frac{\partial(\rho_a h_a + \rho_c h_c + \rho_g h_g)}{\partial t} - \frac{\partial}{\partial x}(\dot{m}_g'' h_g) = \frac{\partial}{\partial x} \left(k \frac{\partial T}{\partial x} \right). \quad (4.10b)$$

The total enthalpy is composed of the sensible enthalpy ($h_{s,i}$) and the enthalpy of formation ($h_{f,i}^0$). Replacing the total enthalpy with its definition, the energy equation becomes

$$\begin{aligned} & \frac{\partial(\rho_a h_{s,a} + \rho_c h_{s,c} + \rho_g h_{s,g})}{\partial t} + \frac{\partial(\rho_a h_{f,a}^0 + \rho_c h_{f,c}^0 + \rho_g h_{f,g}^0)}{\partial t} - \left(\frac{\partial}{\partial x}(\dot{m}_g'' h_{s,g}) + \frac{\partial}{\partial x}(\dot{m}_g'' h_{f,g}^0) \right) = \frac{\partial}{\partial x} \left(k \frac{\partial T}{\partial x} \right). \end{aligned} \quad (4.10c)$$

The rate of change of the gas total enthalpy can be neglected for the following reasons:

The gas sensible enthalpy term ($dh_{s,g} = c_{p,g} dT_g$):

$$\frac{\partial(\rho_g h_{s,g})}{\partial t} = c_{p,g} \frac{\partial(\rho_g T_g)}{\partial t} = c_{p,g} \frac{\partial(RP)}{\partial t} = c_{p,g} R \frac{\partial P}{\partial t} \approx 0,$$

where R is the universal gas constant, P is the pressure within the solid matrix. In this consideration, the pressure is constant. In general, the pressure could be allowed to change as determined by the porosity of the system. This would require an incorporation of Darcy's law which we believe would only add more complexity and uncertainty without any significant advantage.

The gas enthalpy of formation term ($h_{f,g}^0$ is a constant):

$$\frac{\partial(\rho_g h_{f,g}^0)}{\partial t} = \rho_g \frac{\partial(h_{f,g}^0)}{\partial t} + h_{f,g}^0 \frac{\partial(\rho_g)}{\partial t} \approx 0.$$

Neglecting the rate of change of the gas enthalpies, the energy equation reduces to

$$\frac{\partial(\rho_a h_{s,a} + \rho_c h_{s,c})}{\partial t} + \frac{\partial(\rho_a h_{f,a}^0 + \rho_c h_{f,c}^0)}{\partial t} - \frac{\partial}{\partial x}(\dot{m}_g'' h_{s,g}) - \frac{\partial}{\partial x}(\dot{m}_g'' h_{f,g}^0) = \frac{\partial}{\partial x} \left(k \frac{\partial T}{\partial x} \right) \quad (4.10e)$$

From Eq. (4.8a) and (4.8b), the second term on the LHS of Eq. (4.10e) can be rearranged as

$$\begin{aligned} \frac{\partial(\rho_a h_{f,a}^0 + \rho_c h_{f,c}^0)}{\partial t} &= h_{f,a}^0 \frac{\partial \rho_a}{\partial t} + h_{f,c}^0 \frac{\partial \rho_c}{\partial t} \\ &= \left(\frac{h_{f,a}^0}{1 - X_c} - \frac{X_c h_{f,c}^0}{1 - X_c} \right) \frac{\partial \rho}{\partial t}. \end{aligned} \quad (a)$$

The fourth term on the LHS of Eq. (4.10e) can be rewritten as

$$\frac{\partial}{\partial x}(\dot{m}_g'' h_{f,g}^0) = h_{f,g}^0 \frac{\partial \dot{m}_g''}{\partial x} = h_{f,g}^0 \frac{\partial \rho}{\partial t}. \quad (\text{b})$$

Substituting Eqs. (a) and (b) back into the second and the fourth terms of Eq. (4.10e) and rearranging, we obtain

$$\frac{\partial(\rho_a h_{s,a} + \rho_c h_{s,c})}{\partial t} - \frac{\partial}{\partial x}(\dot{m}_g'' h_{s,g}) + \left[\frac{h_{f,a}^0}{1 - X_c} - \frac{X_c h_{f,c}^0}{1 - X_c} - h_{f,g}^0 \right] \frac{\partial \rho}{\partial t} = \frac{\partial}{\partial x} \left(k \frac{\partial T}{\partial x} \right). \quad (\text{4.10f})$$

The energy term in the square bracket on the LHS of Eq. (4.10f) is defined as the heat of pyrolysis (Q_p):

$$Q_p = - \left[\frac{h_{f,a}^0}{1 - X_c} - \frac{X_c h_{f,c}^0}{1 - X_c} - h_{f,g}^0 \right]. \quad (\text{4.10g})$$

The heat of pyrolysis represents the energy released (exothermic) or required (endothermic) due to the active wood decomposes to char and volatiles. In this consideration, Q_p is positive for endothermic decomposition and negative for exothermic decomposition.

We can rearrange Eq. (4.10g) to gain a physical meaning of the energy equation as the rate of change of the sensible enthalpy of active wood and char is balanced by (1) the heat conducted through the solid matrix, (2) the energy convected due to the flow of volatiles, and (3) the energy required/generated due to endothermic/exothermic kinetic decomposition. Consequently, the energy equation can be expressed as

$$\frac{\partial(\rho_a h_{s,a} + \rho_c h_{s,c})}{\partial t} = \frac{\partial}{\partial x} \left(k \frac{\partial T}{\partial x} \right) + \frac{\partial}{\partial x} (\dot{m}_g'' h_{s,g}) + Q_p \left(\frac{\partial \rho}{\partial t} \right), \quad (4.10h)$$

The sensible enthalpy $h_{s,i}$ is defined as

$$h_{s,i} = \int_{T_\infty}^T c_{p,i}(T) dT, \quad (4.11)$$

where $c_{p,i}(T)$ is the specific heat capacity of the i^{th} species (active wood, char, and volatiles).

Expanding the LHS of Eq. (4.10h), we obtain

$$\frac{\partial(\rho_a h_{s,a} + \rho_c h_{s,c})}{\partial t} = \rho_a \frac{\partial h_{s,a}}{\partial t} + \rho_c \frac{\partial h_{s,c}}{\partial t} + h_{s,a} \frac{\partial \rho_a}{\partial t} + h_{s,c} \frac{\partial \rho_c}{\partial t}.$$

From the sensible enthalpy definition ($dh_s = c_p dT$) and Eq. (4.8) the previous equation can be rewritten as

$$\frac{\partial(\rho_a h_{S,a} + \rho_c h_{S,c})}{\partial t} = (\rho_a c_{P,a} + \rho_c c_{P,c}) \frac{\partial T}{\partial t} + \left(\frac{h_{S,a}}{(1-X_c)} - \frac{X_c h_{S,c}}{(1-X_c)} \right) \frac{\partial \rho}{\partial t}. \quad (4.12)$$

Substituting Eq. (4.12) into Eq. (4.10h) and rearranging, the energy balance becomes

$$\rho c_{PS} \frac{\partial T}{\partial t} = \frac{\partial}{\partial x} \left(k \frac{\partial T}{\partial x} \right) + \dot{m}_g'' \frac{\partial h_{S,g}}{\partial x} + h_{S,g} \frac{\partial \dot{m}_g''}{\partial x} + \left[Q_p - \frac{h_{S,a}}{(1-X_c)} + \frac{X_c h_{S,c}}{(1-X_c)} \right] \frac{\partial \rho}{\partial t},$$

$$\rho c_{PS} \frac{\partial T}{\partial t} = \frac{\partial}{\partial x} \left(k \frac{\partial T}{\partial x} \right) + \dot{m}_g'' \frac{\partial h_{S,g}}{\partial x} + \left[Q_p - \frac{h_{S,a}}{(1-X_c)} + \frac{X_c h_{S,c}}{(1-X_c)} + h_{S,g} \right] \frac{\partial \rho}{\partial t}, \quad (4.13)$$

where ρc_{PS} is the average heat capacity per unit volume of active wood and char such that $\rho c_{PS} = \rho_a c_{P,a} + \rho_c c_{P,c}$.

The energy terms in the bracket of Eq. (4.13) have their own physical meanings as Q_p is the heat of pyrolysis per unit mass, $(h_{S,a}/(1-X_c))$ is the energy released due to active wood decompose per unit mass (active wood sensible enthalpy), $(X_c h_{S,c}/(1-X_c))$ is the energy required to produce char per unit mass (char sensible enthalpy), and $h_{S,g}$ is the energy required to generate volatiles per unit mass (volatile sensible enthalpy).

The specific heat capacity and thermal conductivity of partially pyrolyzed wood are calculated from a linear interpolation between the properties of active wood and solid char as

$$\rho c_{PS} = \frac{(\rho - \rho_f)}{(\rho_w - \rho_f)} c_{P,a} + \frac{(\rho_w - \rho)}{(\rho_w - \rho_f)} c_{P,C}, \quad (4.14a)$$

$$k = \frac{(\rho - \rho_f)}{(\rho_w - \rho_f)} k_a + \frac{(\rho_w - \rho)}{(\rho_w - \rho_f)} k_C. \quad (4.14b)$$

Assuming the thermal properties of cellulose, hemicellulose, and lignin are the same as the active wood, the temperature dependence thermal properties of active wood, char, and volatiles are taken from Ritchie et al. [33] as:

Specific heat capacity:

$$\text{Active wood: } c_{P,a} = 10 + 3.7T \quad (\text{J/kg.K}), \quad (4.15a)$$

$$\text{Solid char: } c_{P,C} = 1430 + 0.355T - 0.732T^{-2} \quad (\text{J/kg.K}), \quad (4.15b)$$

$$\text{Volatiles: } c_{P,g} = 66.8T^{1/2} - 136 \quad (\text{J/kg.K}). \quad (4.15c)$$

Thermal conductivity:

$$\text{Active wood: } k_a = 3.054 \times 10^{-4} T + 0.0362 \quad (\text{W/m.K}), \quad (4.16a)$$

$$\text{Solid char: } k_C = 9.46 \times 10^{-5} T + 0.0488 \quad (\text{W/m.K}). \quad (4.16b)$$

4.2.6 Boundary Conditions

The boundary conditions for mass and energy equations can be described as follows:

Mass: No mass transfers at the back boundary (i.e. $x = L$), and the total pyrolysis mass flux is equal to the mass flux at the surface (i.e. $x = 0$), the mathematical expression for mass boundary conditions are

$$\text{at } x = L, \quad \dot{m}_g''(L) = 0, \quad (4.17a)$$

$$\text{at } x = 0, \quad \dot{m}_g''(0) = \dot{m}_{g,s}'' . \quad (4.17b)$$

The mass flux for any given position can be determined by integrating Eq. (4.9) from the back boundary to that location, i.e.

$$\dot{m}_g''(x) = \int_L^x \left(\frac{\partial \rho}{\partial t} \right) dx, \quad (4.18)$$

Energy: At the back surface, the wood is insulated; thus an adiabatic boundary is employed, i.e.

$$\text{at } x = L, \quad \frac{\partial T}{\partial x} = 0. \quad (4.19a)$$

The char surface oxidation is important [2] as it marks the transition from surface oxidation to surface combustion (glowing ignition). It is necessary to include these effects in the front surface boundary of the energy equation. Accordingly the front energy boundary condition with char surface oxidation is

$$\text{at } x = 0, \quad \dot{q}_i'' + \dot{m}_c'' \Delta H_C = -k_s \frac{\partial T}{\partial x} + h(T_s - T_\infty) + \varepsilon \sigma (T_s^4 - T_{ref}^4), \quad (4.19b)$$

where \dot{q}_i'' is the incident heat flux, h is the average convective heat transfer coefficient, and ε is the surface emissivity. \dot{m}_c'' is mass of char surface oxidation per unit area, and ΔH_C is heat of combustion of char. T_{ref} is the reference temperature (surrounding temperature). The char surface oxidation model will be discussed at length in section 4.3. Other variable and subscript meanings can be found in the list of abbreviations.

4.2.7 Non-dimensional Governing Equations

Introducing non-dimensional variables as

$$\begin{aligned} \hat{x} &= \frac{x}{L}, \quad \hat{k}_i = \frac{k_i}{k_w}, \quad \hat{T} = \frac{T}{T_\infty}, \quad T_{e,j} = \frac{E_{a,j}}{RT_\infty}, \quad \hat{t} = \frac{t}{L^2 / \alpha_w}, \quad \hat{\rho}_j = \frac{\rho_j}{\rho_w}, \quad \hat{m}_g'' = \frac{\dot{m}_g'' c_{P,W} L}{k_w}, \\ \hat{m}_c'' &= \frac{\dot{m}_c'' c_{P,W} L}{k_w}, \quad \hat{h}_{S,i} = \frac{h_{S,i}}{c_{P,W} T_\infty}, \quad \hat{a}_{P,j} = \frac{a_{P,j} c_{P,W} L^2}{k_w (1 - X_{C,j})}, \quad \hat{Q}_P = \frac{Q_P}{c_{P,W} T_\infty}, \quad \hat{H} = \frac{hL}{k_w}, \\ \hat{\Sigma} &= \frac{\sigma T_\infty^3 L}{k_w}, \quad \hat{q}_i'' = \frac{\dot{q}_i'' L}{k_w T_\infty}, \quad \Delta \hat{H}_C = \frac{\Delta H_C}{c_{P,W} T_\infty}, \end{aligned}$$

where $\alpha_w = k_w / \rho_w c_{P,W}$, thermal diffusivity of virgin wood. The subscript of “W” refers to the properties of virgin wood. The subscript “j” refers to the j^{th} component of wood (cellulose, hemicellulose, and lignin). The subscript of “i” can be either “a” (active

wood), “C” (char), or “f” (final density). L is the wood sample thickness. Substitute the dimensionless variables into the governing and boundary equations leads to a set of non-dimensional equations as follows

Kinetic Decomposition:

$$\frac{\partial \hat{\rho}_j}{\partial \hat{t}} = -\hat{a}_{P,j}(\hat{\rho}_j - X_{C,j}) \exp(-T_{e,j}/\hat{T}), \quad (4.20a)$$

and

$$\frac{\partial \hat{\rho}}{\partial \hat{t}} = \sum_{j=1}^3 X_j \frac{\partial \hat{\rho}_j}{\partial \hat{t}}, \quad (4.20b)$$

Mass Conservation:

$$\frac{\partial \hat{m}_g''}{\partial \hat{x}} = \frac{\partial \hat{\rho}}{\partial \hat{t}}, \quad (4.21)$$

Energy Conservation:

$$\hat{\rho} \hat{c}_{PS} \frac{\partial \hat{T}}{\partial \hat{t}} = \frac{\partial}{\partial \hat{x}} \left(\hat{k} \frac{\partial \hat{T}}{\partial \hat{x}} \right) + \hat{m}_g'' \frac{\partial \hat{h}_{S,g}}{\partial \hat{x}} + \left[\hat{Q}_P - \frac{1}{1 - \hat{\rho}_f} \hat{h}_{S,a} + \frac{\hat{\rho}_f}{1 - \hat{\rho}_f} \hat{h}_{S,c} + \hat{h}_{S,g} \right] \frac{\partial \hat{\rho}}{\partial \hat{t}}, \quad (4.22)$$

Mass boundary conditions:

$$\text{at } \hat{x} = 1, \quad \hat{m}_g''(1) = 0, \quad (4.23a)$$

$$\text{at } \hat{x} = 0, \quad \hat{m}_g''(0) = \hat{m}_{g,s}'', \quad (4.23b)$$

Energy boundary conditions:

$$\text{at } \hat{x} = 1, \quad \frac{\partial \hat{T}}{\partial \hat{x}} = 0, \quad (4.24a)$$

$$\text{at } \hat{x} = 0, \quad \hat{q}_i'' + \hat{m}_c'' \Delta \hat{H}_c = -\hat{k}_s \frac{\partial \hat{T}}{\partial \hat{x}} + \hat{H}(\hat{T}_s - 1) + \varepsilon \hat{\Sigma}(\hat{T}_s^4 - 1). \quad (4.24b)$$

4.3 Char Surface Oxidation Model

Char surface oxidation plays a significant role for glowing ignition (a transition from surface oxidation to surface combustion) when an incident heat flux to the solid surface is low. The char surface combustion is exothermic. It is an additional source term in the energy balance at the surface (see Eq. (4.24b)). Eventually, the char surface combustion could cause transition from glowing ignition to flaming ignition.

Although the surface glowing ignition is important, very little systematic studies have been conducted [80]. An early study of surface glowing ignition was done by Baer et al. [81] for composite propellants. In their work, a simple heat conduction model was considered. The surface oxidation effect was included through the boundary condition.

The surface oxidation was considered to depend on the surface temperature only (zero-order Arrhenius rate reaction). Ignition was assumed to occur when the energy from surface oxidation was greater than from the external heat source. Although, propellants are substances different from cellulosic materials (e.g. wood), the same treatment for the surface oxidation could be used [5]. Fredlund [41] considered a slightly different equation for the surface oxidation in predicting wood combustion. The model was used to predict the wood temperature and pyrolysis rate. However, the study was not extended into the glowing ignition regime. Moussa et al. [82] studied smoldering combustion of cellulosic materials. In this work, the effect of the ambient oxygen concentration to the surface oxidation was taken into account. The char oxidation term was considered as a heat source driving the smoldering process. Based on the ratio of the time for surface oxidation (chemical time) to the time for oxygen diffusion (diffusion time), they could categorize two limits for a smoldering as leading to either extinction or self-sustained smoldering. Saastamoinen et al. [83] experimentally and theoretically examined coal combustion. They presented a model for coal particle combustion and concluded that to obtain the maximum combustion rate, a coal particle must be in an optimum size. Bilbao et al. [22] examined the ignition and smoldering of *Pinus Pinaster* wood samples. They suggested experimentally that under low heat flux conditions ($< 40\text{kW/m}^2$), the smoldering temperature was approximately the same as the critical temperature for piloted ignition, which increases proportionally with the heat flux. For high heat flux conditions ($> 40\text{kW/m}^2$), the smoldering temperature approached a constant value of $525\text{ }^\circ\text{C}$ independent of the heat flux.

Some aspects of surface oxidation were studied; however, little attention has been paid to glowing ignition or the onset of surface combustion. A criterion for glowing ignition is not well established, and has been based on empirical rules. For these reasons, the present char surface oxidation model is constructed to investigate the physical and chemical processes governing the glowing ignition mechanism.

4.3.1 Theoretical Model

In order for solid char at the surface to react with the oxygen from the surroundings, five important steps are listed sequentially [84]:

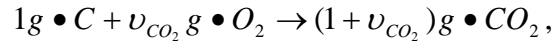
- i) Oxygen has to diffuse to the solid surface,
- ii) Diffused oxygen has to be absorbed by the surface,
- iii) Absorbed oxygen has to react with the solid to form absorbed products,
- iv) Absorbed products have to be desorbed from the surface,
- v) Desorbed products have to diffuse away from the surface.

Steps i) and v) are diffusion-controlled, while step iii) is kinetic-controlled. Since these steps occur in series, the slowest step of them determines the surface oxidation rate. Typically, steps ii) and iv) are relatively fast compared to the other steps; thus the surface oxidation rate would depend on either diffusion-controlled or kinetic-controlled.

4.3.2 Diffusion-Controlled Char Surface Oxidation

Analysis for char surface oxidation in the diffusion-controlled regime shall be adopted the one-film model for the charcoal combustion as suggested by Turns [85]. Modifications have been made in order to account for the blowing effects due char oxidation mass flux ($\dot{m}_{C,diff}''$) and unburnt pyrolysis mass flux ($\dot{m}_{g,S}''$). The one-film model as shown in Fig. 4.1 is based on the following assumptions:

1. The one-dimensional stagnant layer (δ) for the oxygen diffusion from the surroundings to the char surface exists,
2. The combustion process occurs only at the surface, no combustion in the gas phase,
3. The combustion process is quasi-steady,
4. The char at the surface is assumed to be carbon which reacts with oxygen at the surface following the chemical reaction:



where ν_{CO_2} is stoichiometric oxygen to carbon mass ratio,

5. The thermal properties in the gas phase are constant and the unity Lewis number assumption is applied.

At the oxidation surface (i.e. $x = 0$) the mass balance is given as

$$\dot{m}_{C,diff}'' + \dot{m}_{g,S}'' = \dot{m}_{CO_2}'' - \dot{m}_O'' = \dot{m}_{net}'', \quad (4.25)$$

where \dot{m}_{net}'' is the net mass flux convected outward from the oxidation surface.

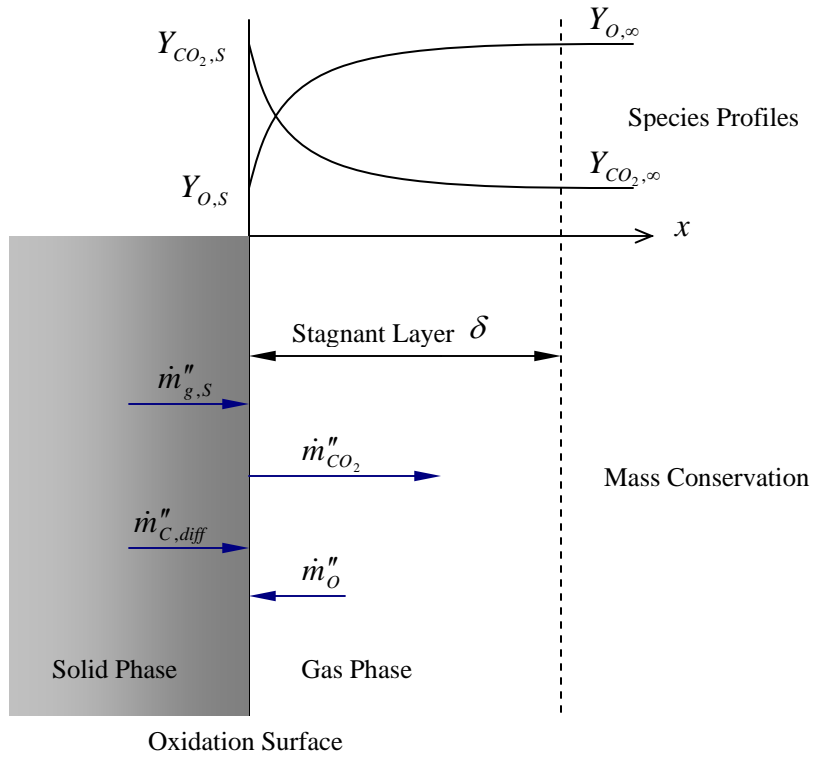


Figure 4.1: Systematic diagram for one-film model diffusion-controlled char surface oxidation

A one-dimensional quasi-steady mass conservation in the gas phase (i.e. $x > 0$) can be written as

$$\frac{d(\rho u)}{dx} = 0. \quad (4.26)$$

Hence integrating Eq. (4.26) yields

$$\rho u = \text{constant} = \dot{m}''_{net} = \dot{m}''_{C,diff} + \dot{m}''_{g,s}, \quad (4.27)$$

where ρu is the convective mass flux in the gas phase.

Without reactions in the gas phase, the gas phase species balance can be expressed as

$$\frac{d(\rho u Y_i)}{dx} = \frac{d}{dx} \left(\rho D \frac{dY_i}{dx} \right), \quad (4.28)$$

where Y_i is the mass fraction of species i , and D is the species diffusivity coefficient.

Considering oxygen species only (Y_o), the species conservation for oxygen becomes

$$\frac{d(\rho u Y_o)}{dx} = \frac{d}{dx} \left(\rho D \frac{dY_o}{dx} \right). \quad (4.29)$$

Integrate Eq. (4.29) from the oxidation surface ($x = 0$) outward, we obtain

$$\rho u Y_o - \rho u Y_{o,s} = \rho D \left(\frac{dY_o}{dx} \right) - \rho D \left(\frac{dY_o}{dx} \right)_s, \quad (4.30)$$

where subscript “S” indicates the values at the oxidation surface ($x = 0$).

At the oxidation surface, the oxygen consumed due to char surface oxidation is balance by the oxygen convection and diffusion in the gas phase. Hence, the oxygen species balance at the surface is

$$-\dot{m}_O'' = \rho u Y_{O,S} - \left(\rho D \frac{dY_O}{dx} \right)_s, \quad (4.31)$$

where the negative sign in front of the oxygen mass flux indicates that the oxygen is consumed at the surface.

From the stoichiometric reaction between oxygen and char (carbon), we have

$$\dot{m}_O'' = \nu_{CO_2} \dot{m}_{C,diff}'' . \quad (4.32)$$

Substituting Eq. (4.31), (4.32) into Eq. (4.30) gives

$$\rho u Y_O = \rho D \left(\frac{dY_O}{dx} \right) - \nu_{CO_2} \dot{m}_{C,diff}'' . \quad (4.33)$$

From Eq. (4.27), we can recast Eq. (4.33) in terms of $\dot{m}_{C,diff}''$ and $\dot{m}_{g,S}''$ as

$$\nu_{CO_2} \dot{m}_{C,diff}'' + (\dot{m}_{C,diff}'' + \dot{m}_{g,S}'') Y_O = \rho D \left(\frac{dY_O}{dx} \right),$$

or

$$\dot{m}_{C,diff}'' = \frac{\rho D}{(\nu_{CO_2} + (1 + \gamma) Y_O)} \left(\frac{dY_O}{dx} \right), \quad (4.34)$$

where $\gamma \equiv \dot{m}_{g,s}'' / \dot{m}_{C,diff}''$ represents the blowing effect due to unburnt pyrolysis mass flux.

The boundary conditions for Eq. (4.34) are

$$\text{At } x = 0: \quad Y_O = Y_{O,S}, \quad (4.35a)$$

$$\text{At } x = \delta: \quad Y_O = Y_{O,\infty}. \quad (4.35b)$$

Integrating Eq. (4.34) from $x = 0$ to $x = \delta$ gives

$$\dot{m}_{C,diff}'' = \frac{\rho D}{\delta} \left(\frac{1}{1+\gamma} \right) \ln \left(\frac{\nu_{CO_2} + (1+\gamma)Y_{O,\infty}}{\nu_{CO_2} + (1+\gamma)Y_{O,S}} \right). \quad (4.36)$$

With unity Lewis number ($\rho D = k_g / c_{P,g}$), Eq. (4.36) becomes

$$\dot{m}_{C,diff}'' = \frac{1}{c_{P,g}} \frac{k_g}{\delta} \left(\frac{1}{1+\gamma} \right) \ln \left(\frac{\nu_{CO_2} + (1+\gamma)Y_{O,\infty}}{\nu_{CO_2} + (1+\gamma)Y_{O,S}} \right), \quad (4.37)$$

where $c_{P,g}$ and k_g are the specific heat and heat conductivity of gas respectively.

We can estimate the ratio of k_g / δ as the convective heat transfer coefficient (h) over the solid surface, then the diffusion-controlled char surface oxidation becomes

$$\dot{m}_{C,diff}'' = \frac{h}{c_{P,g}} \left(\frac{1}{1+\gamma} \right) \ln \left(\frac{v_{CO_2} + (1+\gamma)Y_{O,\infty}}{v_{CO_2} + (1+\gamma)Y_{O,S}} \right). \quad (4.38)$$

To emphasize the blowing effect due to unburnt pyrolysis mass flux, Eq. (4.38) can be recast as

$$\dot{m}_{C,diff}'' = \frac{h}{c_{P,g}} \ln \left(\frac{v_{CO_2} + Y_{O,\infty}}{v_{CO_2} + Y_{O,S}} \right) + \frac{h}{c_{P,g}} \ln \left[\left(\frac{v_{CO_2} + (1+\gamma)Y_{O,\infty}}{v_{CO_2} + (1+\gamma)Y_{O,S}} \right)^{\left(\frac{1}{1+\gamma} \right)} \middle/ \left(\frac{v_{CO_2} + Y_{O,\infty}}{v_{CO_2} + Y_{O,S}} \right) \right]. \quad (4.39)$$

The first term on the RHS is the char oxidation rate without the blowing effect, while the second term is the diluted effect due to unburnt pyrolysis mass flux. If the unburnt pyrolysis mass flux is small ($\dot{m}_{g,s}'' \sim \text{small}$, $\gamma \rightarrow 0$), the second term vanishes. However, when the pyrolysis mass flux increases, we cannot neglect the blowing effect ($\gamma \neq 0$); thus, the second term acts in such a way that decreasing of the char oxidation mass flux occurs.

In terms of B , the mass transfer number, the diffusion-controlled char surface oxidation can be expressed as

$$\dot{m}_{C,diff}'' = \frac{h}{c_{P,g}} \ln(B+1) + \frac{h}{c_{P,g}} \ln \left(\frac{(B_{\text{mod}} + 1)^{\left(\frac{1}{1+\gamma} \right)}}{(B+1)} \right), \quad (4.40)$$

where

$$B = \frac{Y_{O,\infty} - Y_{O,s}}{\nu_{CO_2} + Y_{O,s}}, \quad (4.41a)$$

and

$$B_{\text{mod}} = \frac{(1 + \gamma)(Y_{O,\infty} - Y_{O,s})}{\nu_{CO_2} + (1 + \gamma)Y_{O,s}}. \quad (4.41b)$$

The B and B_{mod} are considered as the potential of oxygen mass fraction driving the char surface oxidation process in the diffusion-controlled regime.

There are two unknowns in the diffusion-controlled char surface oxidation equation (Eq. (4.38)): the char surface oxidation mass flux ($\dot{m}''_{C,diff}$), and the surface oxygen mass fraction ($Y_{O,s}$). In order to complete this problem, the surface oxygen mass fraction must be found from a relationship with chemical kinetics.

4.3.3 Kinetic-Controlled Char Surface Oxidation

For general chemical kinetics, the heterogeneous char surface oxidation depends on the oxygen and char mass fraction at the surface, and the surface temperature. Assuming the reaction rate follows the Arrhenius rate, the char surface oxidation governed by kinetics ($\dot{m}''_{C,kin}$) becomes

$$\dot{m}''_{C,kin} = (Y_{Char,S})^{n_{Char}} (Y_{O,S})^{n_{OX}} A_C \exp(-E_{A,C} / RT_S), \quad (4.42^*)$$

where $Y_{Char,S}$ is the surface char mass fraction, n_{Char} is the char reaction order, $Y_{O,S}$ is the surface oxygen mass fraction, n_{OX} is the oxygen reaction order, T_S is the surface temperature, R is the universal gas constant, and A_C and $E_{A,C}$ are the char surface oxidation pre-exponential factor and the activation energy, respectively.

There are four kinetic parameters ($n_{Char}, n_{OX}, A_C, E_{A,C}$) that need to be evaluated. The kinetic parameters depend on many factors such as char reaction model (surface or volume reaction), sample species and size, as well as an experimental technique in which the kinetic parameters are estimated.

Saastamoinen et al. [83] studied combustion of charcoal. They considered that the kinetic reaction took place only at the surface. The reaction rate was independent of the surface char mass fraction (e.g. $n_{Char} = 0$). They suggested the kinetic parameters as followings: $n_{OX} = 1$, $A_C = 465 \text{ kg/m}^2\cdot\text{s}$, and $E_{A,C} = 68 \text{ kJ/mol}$. Branca and Di Blasi [86] calculated wood char kinetic parameters based on TGA experiments. They assumed that the char reaction rate did not depend on the surface oxygen mass fraction (e.g. $n_{OX} = 0$). With best fit to the experimental data, the kinetic parameters were $n_{Char} = 0.86$, $A_C = 1.10 \times 10^6 \text{ s}^{-1}$, and $E_{A,C} = 114.5 \text{ kJ/mol}$. Kashiwagi and Nambu [79] applied TGA technique to determine the kinetic parameters of paper char. They proposed that the char reaction must depend on both char and oxygen mass fraction as well as temperature. The char reaction took place over the entire volume of a small specimen. Their estimated kinetic parameters were $n_{OX} = 0.78$, $n_{Char} = 1$, $A_C = 5.670 \times 10^9 \text{ s}^{-1}$, and $E_{A,C} = 160 \text{ kJ/mol}$.

Differences in the char oxidation kinetic parameters become apparent as we searched through the literature. The main reason seems to come from whether the char reaction takes place only at the surface or the entire volume of the char layer. As observed from the experiments, the char surface did crack while undergoing the heating process. Therefore, we expected that a major contribution for the char reaction would come from the surface not in-depth since any char oxidation in the cracks would rapidly decrease as the oxygen concentration and temperature decreased from the surface. For these reasons, we confine our analysis to the char reaction only on the surface; thus the appropriate kinetic parameters shall follow Saastamoinen's values. The kinetic-controlled char surface oxidation reduces to

$$\dot{m}_{C,kin}'' = Y_{O,S} A_C \exp(-E_{A,C} / RT_S). \quad (4.42)$$

4.3.4 Overall Char Surface Oxidation

The char surface oxidation process occurs in series as first diffusion of oxygen from the surrounding to the surface, then kinetic consuming that oxygen; hence the diffusion-controlled char surface oxidation must be equal to the kinetic-controlled char surface oxidation i.e.

$$\dot{m}_{C,diff}'' = \dot{m}_{C,kin}'' \equiv \dot{m}_C'', \quad (4.43)$$

where \dot{m}_C'' is the overall char surface oxidation mass flux.

We may imagine the oxidation process as a circuit [85] in which the \dot{m}_C'' flows through the two resistances as shown in Fig. 4.2; thus the overall char surface oxidation rate can be expressed as

$$\dot{m}_C'' = \frac{Y_{O,\infty} - 0}{R_{diff} + R_{kin}} = \frac{Y_{O,\infty}}{R_{total}}, \quad (4.44)$$

where

$$R_{diff} = \left(\frac{c_{P,g} (1 + \gamma)}{h} \right) \left(\frac{Y_{O,\infty} - Y_{O,S}}{\ln(1 + B_{mod})} \right), \quad (4.45a)$$

and

$$R_{kin} = \frac{1}{A_C \exp(-E_{A,C} / RT_S)}. \quad (4.45b)$$

The R_{diff} and R_{kin} are the diffusion and kinetic resistances, respectively.

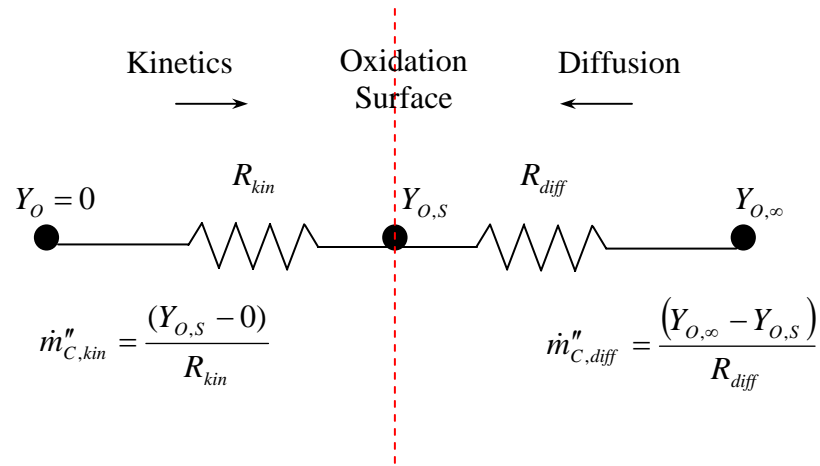


Figure 4.2: Systematic diagram for char surface oxidation electrical circuit series.

The idea of diffusion and kinetic resistances is illustrated in Fig. 4.3. Depicting a case of $\dot{q}'' = 40 \text{ kW/m}^2$ and $Y_{O,\infty} = 0.233$, following by solving Eq. (4.38), (4.42), and (4.45) for a given surface temperature, the two char surface oxidation resistances as a function of surface temperature are obtained. When the wood surface is exposed to a heat flux, initially the surface temperature is low and plenty of oxygen is available at the surface. Here, the char surface oxidation depends on the surface temperature, which is kinetic-controlled (i.e. $R_{kin} > R_{diff}$). As time progresses, the surface temperature increases, and the oxygen concentration at the surface decreases due to the char reaction. The char surface oxidation depends on how much oxygen from the surrounding diffuses to the char surface. Therefore, now the char surface oxidation is controlled by the oxygen diffusion (i.e. $R_{diff} > R_{kin}$). For normal atmospheric oxygen concentration ($Y_{O,\infty} = 0.233$), R_{diff} is greater than R_{kin} at approximately $400 \text{ }^\circ\text{C}$. Thus we can define this temperature as a

transition point for the char surface oxidation to change from kinetic-controlled to diffusion-controlled.

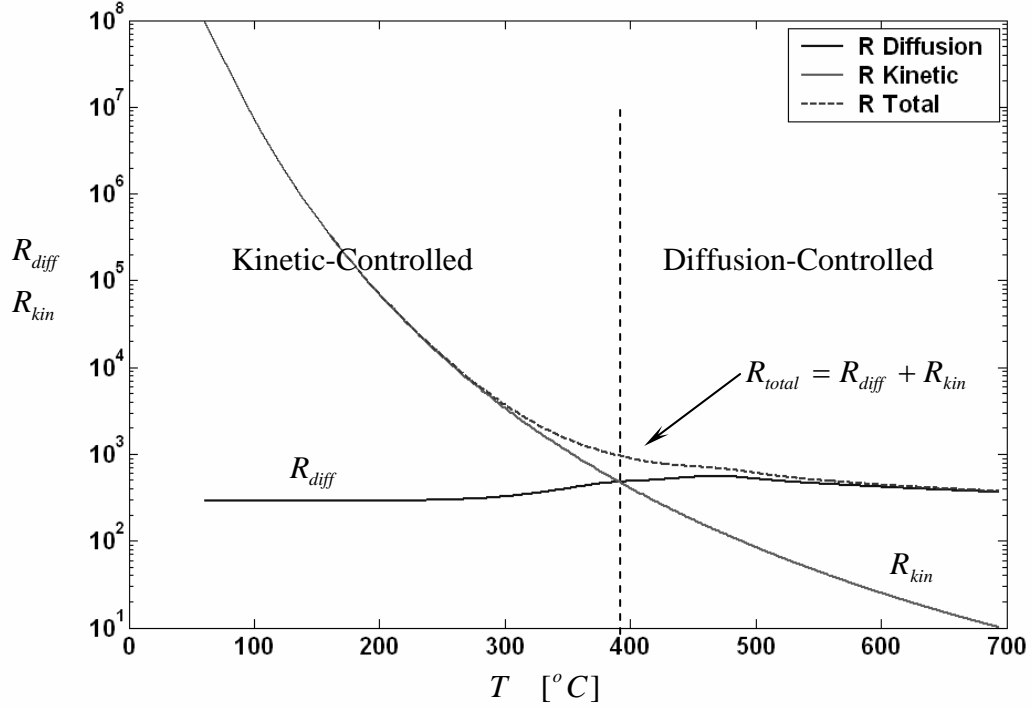


Figure 4.3: Diffusion and kinetic resistances as a function of surface temperature

$$(\dot{q}'' = 40 \text{ kW/m}^2, Y_{O,\infty} = 0.233)$$

As the char layer on the wood surface undergoes surface oxidation, the wood surface regresses. This surface regression rate (regression velocity, v_0) can be calculated as

$$v_0 = \frac{\dot{m}_C''}{\rho_f}, \tag{4.46}$$

and the remaining wood thickness ($L(t)$) decreases with time as

$$L(t) = L_0 - \int_{t=0}^t v_0 dt . \quad (4.47)$$

where ρ_f is the final char density, and L_0 is the initial wood thickness.

The governing equations and boundary conditions together with the char surface oxidation model form a set of nonlinear partial differential equations, which can be solved numerically. The implicit Crank-Nicolson is employed to integrate the energy equation. To account for a surface regression due to char surface oxidation, a moving boundary algorithm is introduced [87]. Discussions of solid phase numerical methods can be found in Appendix A.

4.4 Glowing Ignition Criteria

Oxidation of the surface can play a significant role in flaming ignition because it can act as a “pilot”. However, glowing ignition (the onset of surface combustion) is also a critical transition. It marks the transition from oxidation to combustion. Analogous to Semenov’s ignition theory [88], a criterion for glowing ignition can be defined in terms of the surface energy balance (Eq. (4.19b)). The LHS of Eq. (4.19b) is the energy gain ($G(T_s)$), which is the sum of energy supplied from the external heat flux (\dot{q}_i'') and char surface oxidation ($\dot{q}_{ox}'' = \dot{m}_c'' \Delta H_c$). The energy gain is a function of the surface temperature only which is

$$G(T_s) = \dot{q}_i'' + \dot{q}_{ox}'' . \quad (4.48)$$

The RHS of Eq. (4.19b) is the energy loss ($L(T_s, t)$) due to the convective and radiative losses to the surrounding and the conductive loss into the solid matrix. The conductive loss may be simplified as

$$-k_s \frac{\partial T}{\partial x} = \frac{k_s (T_s - T_{ref})}{\delta(t)}, \quad (4.49)$$

where $\delta(t)$ is the thermal diffusion length. Consequently, the energy loss becomes

$$L(T_s, t) = k_s \frac{(T_s - T_{ref})}{\delta(t)} + h(T_s - T_{ref}) + \varepsilon \sigma (T_s^4 - T_{ref}^4), \quad (4.50)$$

The energy loss is a function of time as $\delta(t)$ changes as well as T_s explicitly. The exact numerical solution is used to compute $\delta(t)$ as the computation progressed in time so that plots of $L(T_s, t = t_{fix})$, fixed time and varied surface temperature, as a function of T_s can be drawn in Fig. 4.4a. In this way, we can show how a “jump” can occur in the surface temperature history (point **C** Fig. 4.4b).

Imagine a small region where the surface reaction is occurring over a small volume of finite depth at the surface. In reality, this finite depth could occur due to absorption of oxygen into the char or from porosity effects. Then the transient energy conservation on this finite region is

$$\frac{dE}{dt} = G(T_s) - L(T_s, t), \quad (4.51)$$

where dE/dt is the rate of change of the energy in the finite depth volume.

When $G(T_s) > L(T_s, t)$, we have a thermal runaway. Depicting a low heat flux condition where $\dot{q}_i'' = 15 \text{ kW/m}^2$ and $Y_{O,\infty} = 0.4$, plots of $G(T_s)$ and $L(T_s, t)$, and its corresponding T_s history are shown in Fig. 4.4a and 4.4b, respectively. For any given time, the solution for T_s is the intersection point between $G(T_s)$ and $L(T_s, t)$. As the time increases, $L(T_s, t)$ moves downward to the right; therefore, T_s increases along the $G(T_s)$ curve. When the heating process begins we have, for example, intersections of points **O**. These are stable and only indicate oxidation. As some critical time, the $L(T_s, t)$ curve is tangent to the $G(T_s)$ curve at the unstable point **C**; this we define as the onset of surface combustion (glowing ignition). Here it occurs at 305 °C and 224 seconds. A small increase in T_s (while holding t fixed), results in an unbalance of energy at the oxidation surface. At the next instant of time, the $L(T_s, t)$ curves intersect the $G(T_s)$ curve at point **G**, which is the “glowing” stage of combustion or might be called sustained smoldering. The surface temperature in the glowing stage is approximately 600°C. In the corresponding T_s , there is a clear inflection point at **C** where the exothermic effects of oxidation are pronounced, i.e. “surface combustion”.

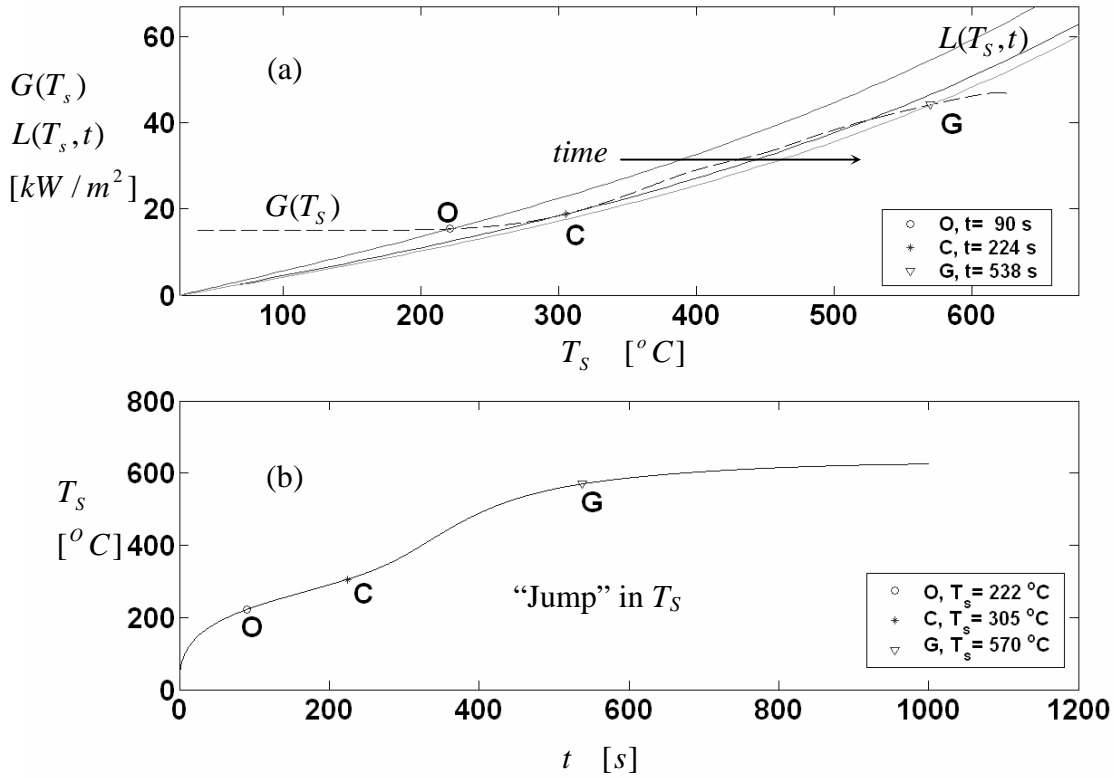


Figure 4.4: Surface energy balance and its corresponding T_s history

$$(\dot{q}_i'' = 15 \text{ kW/m}^2, Y_{O,\infty} = 0.4)$$

At the critical point **C**, the $G(T_s)$ curve is tangent to the $L(T_s, t)$ curve. A mathematical expression for the critical point **C** is $dG(T_s)/dT_s = dL(T_s, t)/dT_s$ (see Fig. 4.4a). However, if the char surface oxidation heat flux ratio ($\equiv \dot{q}_{ox}'' / \dot{q}_i''$) decreases either due to \dot{q}_{ox}'' decreasing (decreasing $Y_{O,\infty}$) or \dot{q}_i'' increasing (char surface oxidation is not important compared to \dot{q}_i''), this critical point **C** approaches a saddle point of the $G(T_s)$ curve. A saddle point is the point at which $dG(T_s)/dT_s$ maximum or $d^2G(T_s)/dT_s^2 = 0$

(see Fig. 4.5a). At some critical value of $\dot{q}_{ox}'' / \dot{q}_i''$, a tangent point between the $G(T_s)$ curve and the $L(T_s, t)$ curve cannot be obtained. Thus, the glowing ignition might be defined as the saddle point of the $G(T_s)$ curve.

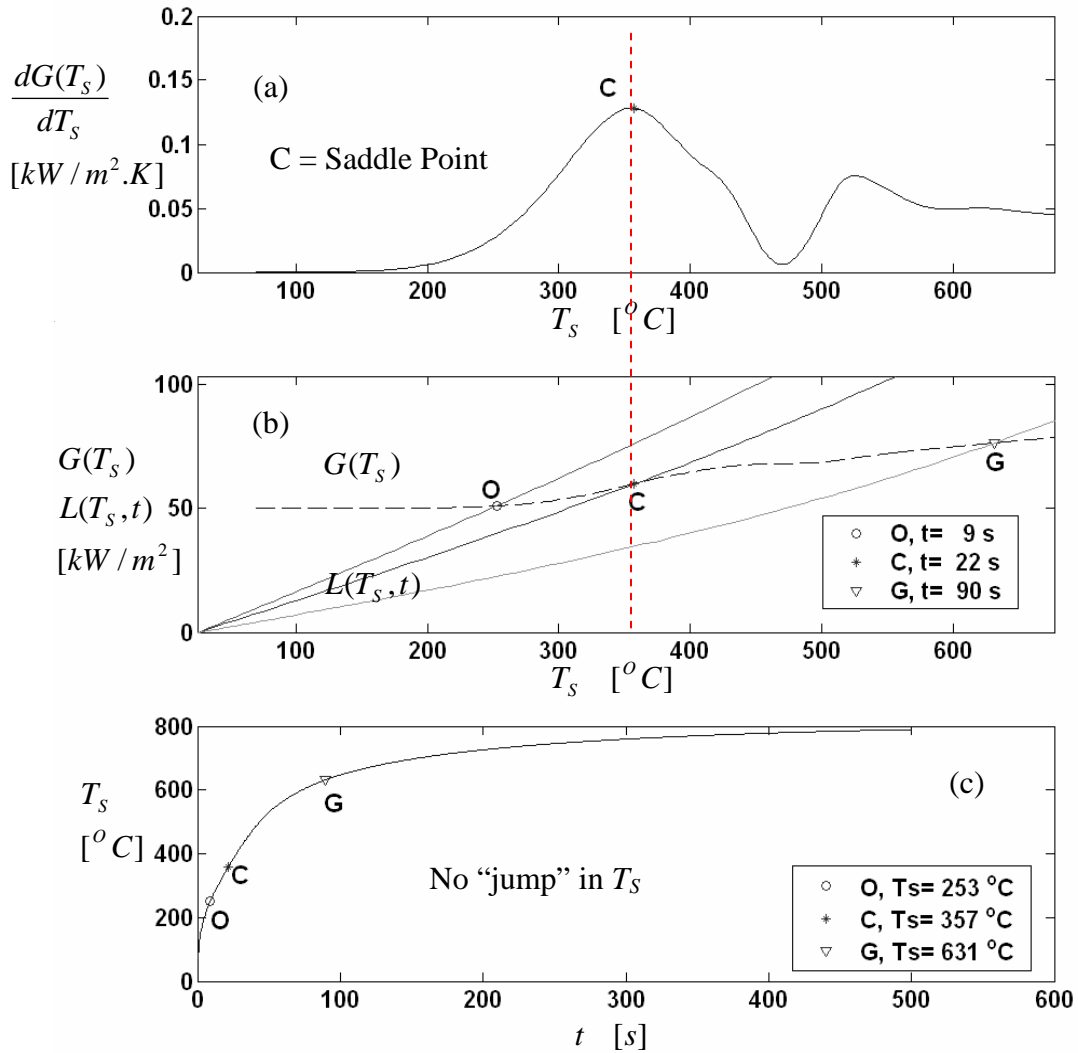


Figure 4.5: $dG(T_s)/dT_s$ vs. T_s and its surface energy balance

$$(\dot{q}_i'' = 50 \text{ kW/m}^2, Y_{O,\infty} = 0.40)$$

For instance, increasing \dot{q}_i'' to 50 kW/m² while keeping $Y_{O,\infty}$ constant, the critical point **C** approaches a saddle point as shown in Fig. 4.5a. Thus the glowing ignition is defined at the saddle point (point **C**). The glowing ignition takes place at 357 °C and 22 seconds. After the surface glowing ignites, $dG(T_s)/dT_s$ decreases even as T_s increases. This is due to depletion of the surface oxygen concentration ($Y_{O,s}$). The saddle point condition coincides with the “steady-stage” solution of $G(T_s)=L(T_s,t)$, which means glowing ignition coincides with sustained smoldering, i.e. no “jump”.

The char surface oxidation heat flux ratio at glowing ignition, $\dot{q}_{OX,glowing}'' / \dot{q}_i''$, for various $Y_{O,\infty}$ as a function of \dot{q}_i'' in which $\gamma \rightarrow 0$ in the char surface oxidation model (Eq. (4.39)) is illustrated in Fig. 4.6. The plot shows approximately two distinctive regimes: (1) the kinetic-controlled regime where the $\dot{q}_{OX,glowing}'' / \dot{q}_i''$ is roughly constant independent of $Y_{O,\infty}$ and \dot{q}_i'' , and (2) diffusion-controlled regime, where the $\dot{q}_{OX,glowing}'' / \dot{q}_i''$ decreases with increasing \dot{q}_i'' . In the kinetic-controlled regime, the available surface oxygen concentration is relatively high; the glowing ignition depends only on T_s . Varying $Y_{O,\infty}$ or \dot{q}_i'' does not change the glowing ignition conditions; thus the $\dot{q}_{OX,glowing}'' / \dot{q}_i''$ remains constant at approximately 0.25~0.35. In the diffusion-controlled regime, as \dot{q}_i'' increases, T_s quickly increases. Therefore, the glowing ignition depends on how much oxygen from the surroundings diffuses to the oxidation surface. Thus $Y_{O,\infty}$ increases, $\dot{q}_{OX,glowing}''$ increases, and ultimately the $\dot{q}_{OX,glowing}'' / \dot{q}_i''$ increases for a certain incident heat flux. In a

case of given $Y_{O,\infty}$, increasing \dot{q}_i'' resulting in decreasing $\dot{q}_{OX,glowing}'' / \dot{q}_i''$ explicitly. The glowing ignition in the kinetic-controlled regime is found to be determined by the tangent point criteria while in the diffusion-controlled regime is determined by the saddle point criteria.

As quoted in Babrauskas' work [80], Lengelle` et al. suggested that for propellants, the critical $\dot{q}_{OX,glowing}'' / \dot{q}_i''$ was found empirically to be 0.15. Assuming a normal atmosphere oxygen concentration ($Y_{O,\infty} = 0.233$) for this study, it is interesting to point out that the present calculation of $\dot{q}_{OX,glowing}'' / \dot{q}_i''$ for glowing ignition of wood approaches Lengelle` criteria asymptotically as the incident heat flux increases.

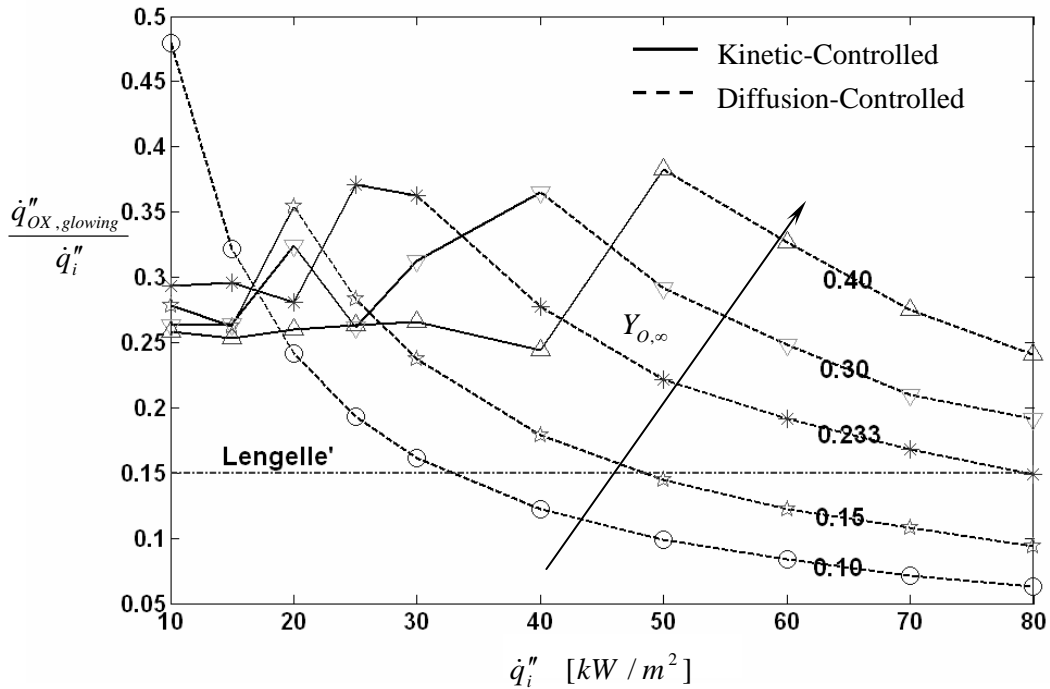


Figure 4.6: A plot of $\dot{q}_{OX,glowing}'' / \dot{q}_i''$ vs. \dot{q}_i'' for various $Y_{O,\infty}$

($\gamma \rightarrow 0$, in the char surface oxidation model)

4.5 Solid Phase Results and Discussions

4.5.1 Numerical Grid Refinement

To ensure a grid size is sufficiently fine to reduce numerical errors, a grid refinement study is performed. Four non-dimensional grid sizes ($\Delta\hat{x}$) are chosen: 0.01, 0.005, 0.0025, and 0.00125 corresponding to 0.04, 0.02, 0.01, and 0.005 cm physical length respectively. For $\dot{q}_i'' = 40 \text{ kW/m}^2$ and $Y_{O,\infty} = 0.233$, plots of surface temperature and pyrolysis mass flux histories for the four grid sizes are shown in Fig. 4.7. The percent differences for surface temperature and pyrolysis mass flux are defined as decreasing the grid size from one to another as

$$\%DiffTemp = \frac{|T_s - T_{s,ref}|}{T_{s,ref}}, \quad (4.52a)$$

and

$$\%DiffMass = \frac{|\dot{m}_{g,S}'' - \dot{m}_{g,S,ref}''|}{\dot{m}_{g,S,ref}''}, \quad (4.52b)$$

where the subscript “*ref*” denotes to a reference value. As $\Delta\hat{x}$ is decreased from 0.01 to 0.005, 0.005 to 0.0025, and 0.0025 to 0.00125, the maximum percent differences for surface temperature are 10 %, 3.72 %, and 1.15 %, and the maximum percent differences for pyrolysis mass flux are 49.46 %, 9.57 %, and 3.39 % respectively. Within 5 % of the maximum percent difference for both surface temperature and pyrolysis mass flux, a non-dimensional grid size of 0.00125 is chosen.

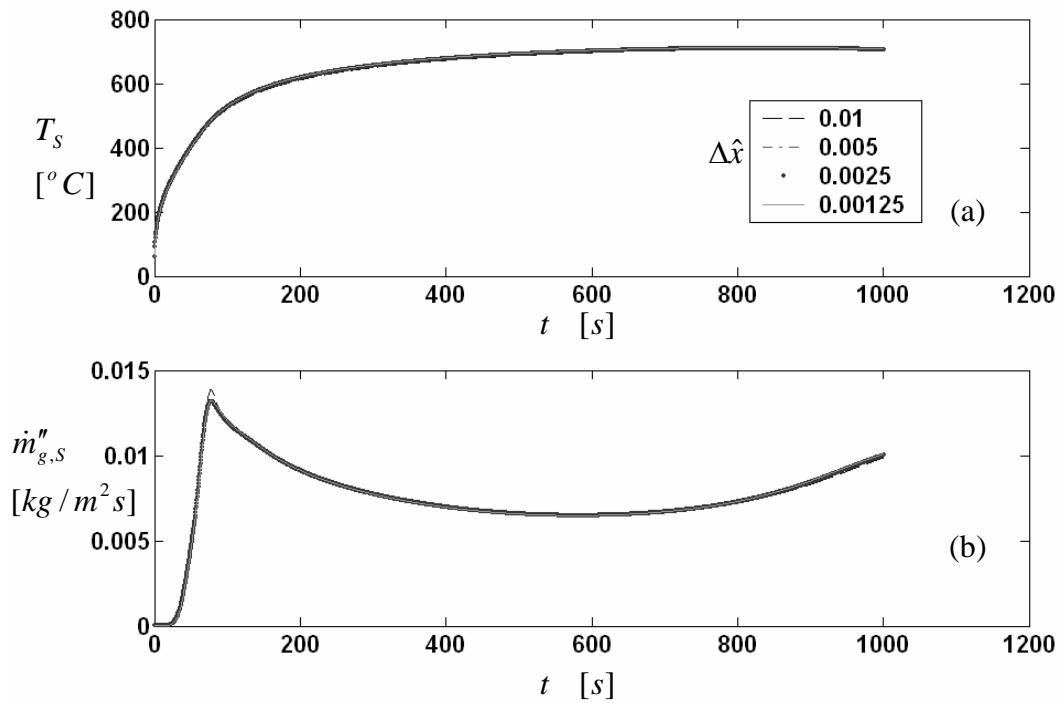


Figure 4.7: Surface temperature and pyrolysis mass flux history for various grid sizes

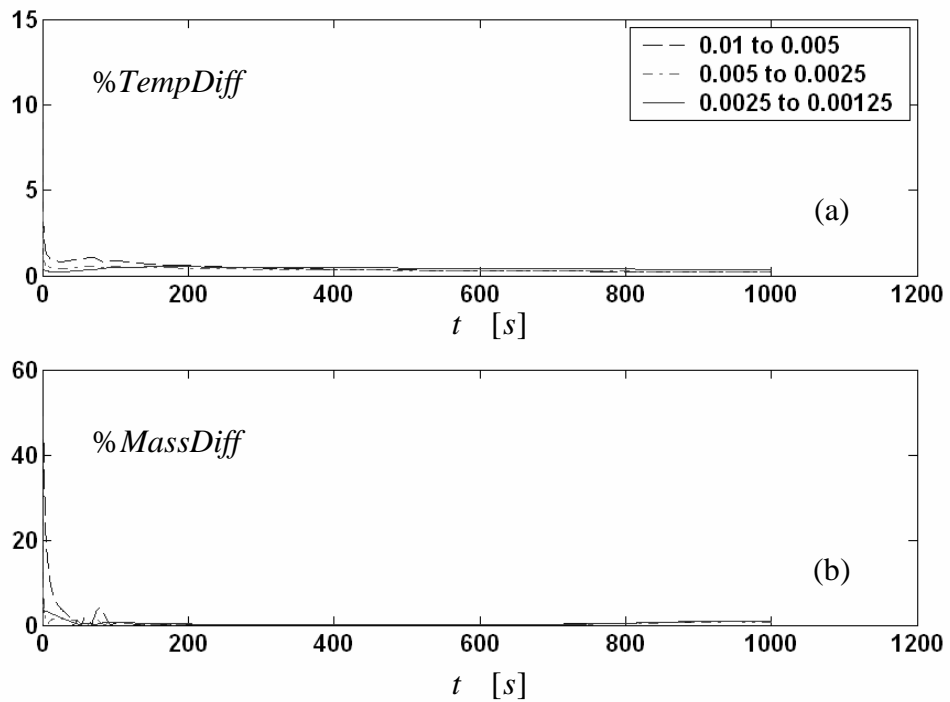


Figure 4.8: Percent difference for (a) surface temperature and (b) pyrolysis mass flux

4.5.2 Gasification Rate in Nitrogen Environment

Experimental gasification rates [33] of Douglas Fir samples subjected to external heat fluxes of 20, 40, and 60 kW/m² in a nitrogen environment (i.e. no combustion) compared with the values calculated from the present solid phase model are graphed in Fig. 4.9. Unfortunately, no data was reported for the surface temperature. The experiment data was taken from Ritchie et al [33] with sample thickness of 1.9 cm. The initial and final char densities were 514 and 118 kg/m³ respectively. The kinetic input parameters for the numerical model were adopted directly from Ritchie's which can be found in Table 3.3, Chapter 3. At the front boundary of the energy equation (Eq. (4.19)), the char surface oxidation term was omitted since there was no combustion.

A large initial spike of the gasification rate occurred at an early stage of the heating process for the external heat fluxes of 40 and 60 kW/m². The magnitude of the spike increased with increasing heat flux. After the spike, the gasification rate decreased due to a char formation on the surface blocking the outflow of volatiles. Later on, the gasification rate increased again due to the "back effect". In the experiment, the backside of the sample was insulated in both mass and heat transfer. This experimental back insulation effect was taken into account in the numerical model via the adiabatic wall boundary for the energy equation and zero mass flux for the mass transfer equation. For the external heat flux of 20 kW/m², no initial spike was observed. The gasification rate gradually increased and reached a constant value until the back effect occurred.

The calculated gasification rate slightly over predicted for the 20 kW/m² case. For the fluxes of 40 and 60 kW/m², the numerical predictions tended to follow the experimental data. Considering the number of inputs required, the variations of the material properties through the wood/char phases, the present model worked reasonably well at predicting the gasification rate at high heat flux.

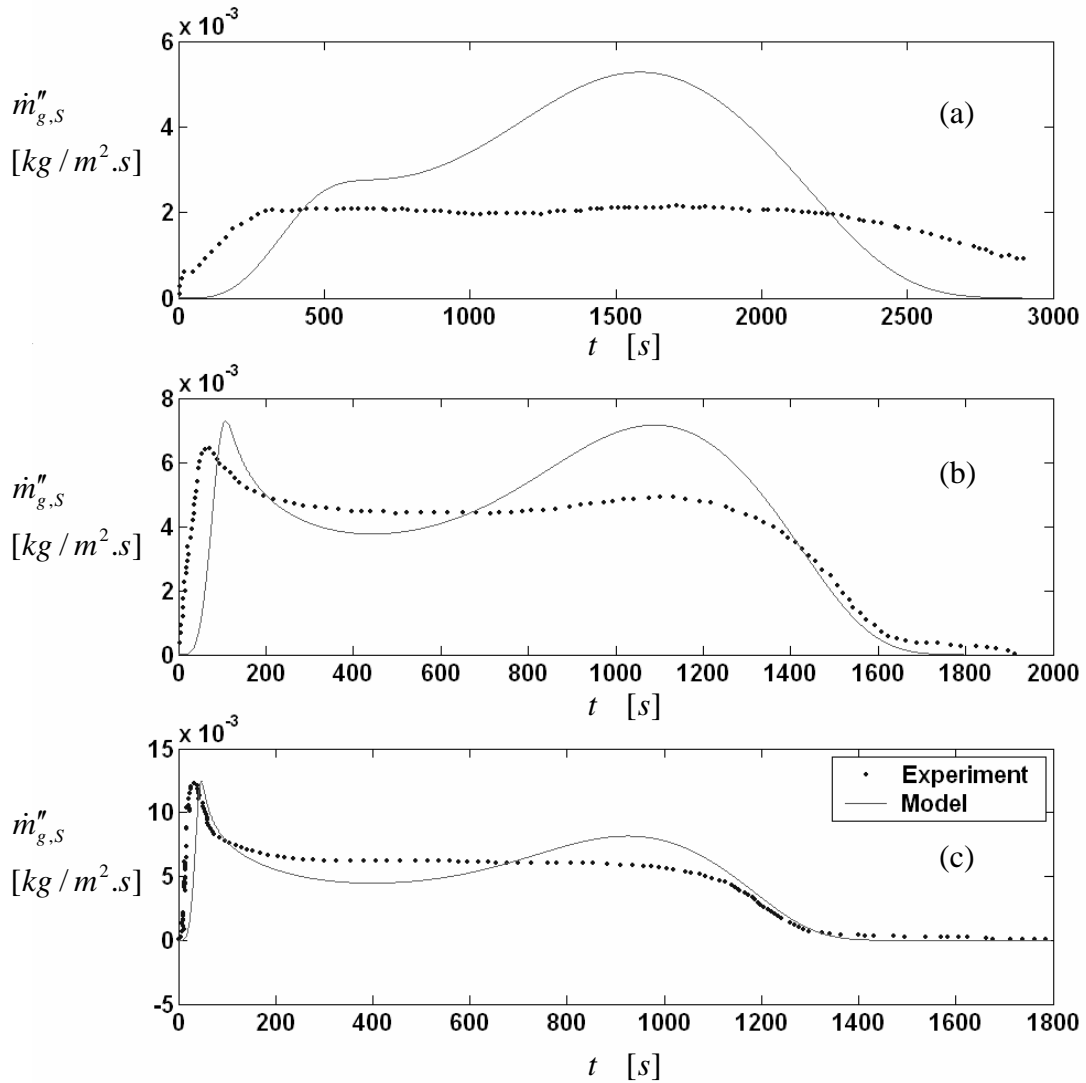


Figure 4.9: Gasification rate in N₂ atmosphere for (a) $\dot{q}''_i = 20 \text{ kW/m}^2$, (b) $\dot{q}''_i = 40 \text{ kW/m}^2$, and (c) $\dot{q}''_i = 60 \text{ kW/m}^2$; experimental gasification rates were taken from Ritchie

et al. [33]

4.5.3 Wood Combustion

For wood combustion in air ($Y_{O,\infty}$), comparisons between the model predictions and the experimental data for surface temperature (T_s) and pyrolysis mass flux ($\dot{m}''_{g,s}$) histories are given in Fig. 4.10. The experimental data depicts the case in which the Redwood sample was heating along the grain with $\dot{q}''_i = 25 \text{ kW/m}^2$. For the numerical results, a summary of the model input parameters is presented in Table 4.1

Table 4.1: Summary of the numerical input parameters

Symbol	Definition	Value	Source
a_p	Wood decomposition pre-exponential factor	$1.41 \times 10^9 \text{ [s}^{-1}\text{]}$	
$E_{a,1}, E_{a,2}, E_{a,3}$	Activation energy of cellulose, hemicellulose, and lignin	141, 125, 165 [kJ/mol]	
X_1, X_2, X_3	Mass fraction of cellulose, hemicellulose, and lignin	0.75, 0.15, 0.10 [-]	
A_c	Char surface oxidation pre-exponential factor	465 [kg/m ² .s]	[83]
$E_{A,c}$	Char surface oxidation activation energy	68 [kJ/mol]	[83]
L_0	Initial sample thickness	0.04 [m]	
ρ_w	Initial wood density	320 [kg/m ³]	
ρ_f	Final char density	64 [kg/m ³]	
ΔH_c	Char heat of combustion	32.76 [kJ/kg-C]	[85]
Q_p	Heat of wood pyrolysis	0 [kJ/kg]	[4]
h	Average convective heat transfer coefficient	10 [W/m ² .K]	
ε	Surface emissivity	0.7 [-]	[19]

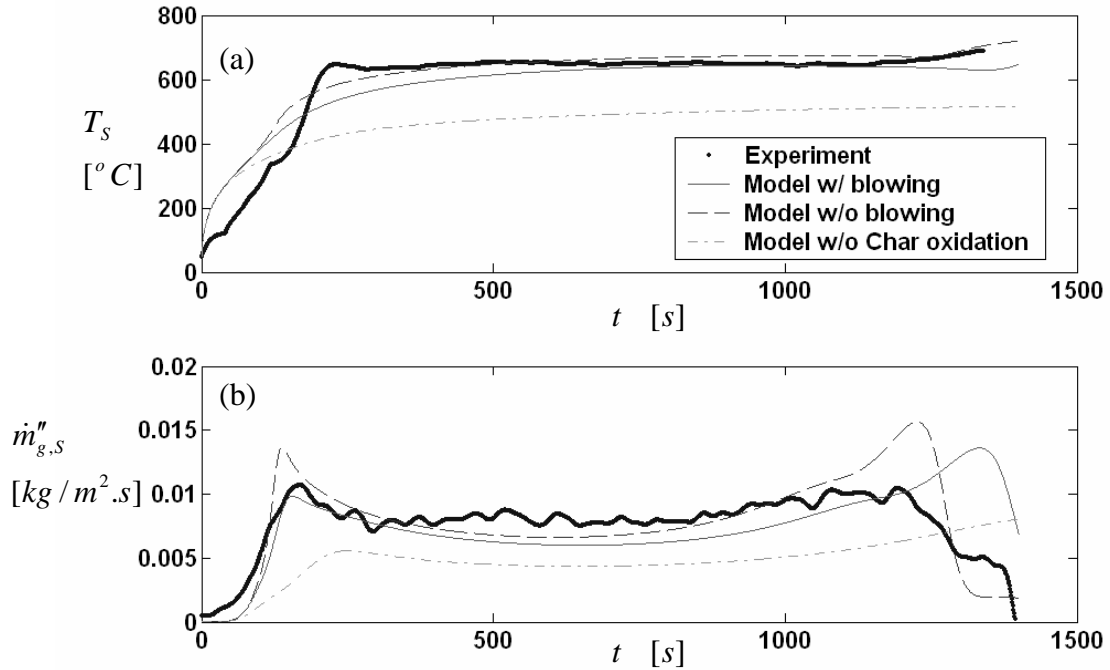


Figure 4.10: (a) surface temperature, and (b) pyrolysis mass flux histories

$$(\dot{q}_i'' = 25 \text{ kW/m}^2, Y_{O,\infty} = 0.233)$$

The predicted $\dot{m}_{g,s}''$ from the model with-char-surface-oxidation generally agrees well with the experimental data except for some discrepancy at the first, and the second peaks. The discrepancy may be due to uncertainties for the wood kinetic parameters, which were derived from a very small sample in the TGA study in contrast to the larger sample in the experiment. For T_s , the model with char surface oxidation slightly over predicts at the early stage of the pyrolysis process. This may result from a surface emissivity variation occurring during the heating process. However, the predicted T_s agrees well with the experiment when the emissivity variation is negligible (i.e. the entire surface becomes

glowing), and the radiant heat loss dominates the energy balance at the surface (i.e. $T_s \sim \text{constant}$).

Fig. 4.10 also illustrates the effect of char surface oxidation on the predicted results. Initially, the predicted $\dot{m}''_{g,s}$ and T_s from the model with and without char surface oxidation are approximately the same. However, once the char surface oxidation is pronounced, the additional energy from the char combustion ramps up T_s and also $\dot{m}''_{g,s}$ to agree with the experimental values. This observation suggests the char surface oxidation is important and needs to be included. The point at which the predicted T_s with char surface oxidation deviates from the predicted T_s without char surface oxidation indicates the onset of surface combustion.

The blowing effect (γ) due to the unburnt pyrolysis mass flux is also demonstrated in Fig. 4.10. At the early stage when the unburnt pyrolysis mass flux ($\dot{m}''_{g,s}$) is low, the blowing effect is insignificant (i.e. $\gamma \rightarrow 0$); thus the model with and without the blowing effect is generally equivalent. However, as the $\dot{m}''_{g,s}$ increases, it dilutes the char surface oxidation mass flux (\dot{m}''_c) as shown in Fig. 4.11a. The difference of \dot{m}''_c between the model with and without blowing effect is essentially the second term of the RHS of Eq. (4.39). Decreasing of \dot{m}''_c results in a decreasing of the additional energy due to the char surface combustion on the oxidation surface, which ultimately decreases $\dot{m}''_{g,s}$.

Fig. 4.11b, however, shows that the blowing of the unburnt mass flux has minor effect on the surface oxygen mass fraction ($Y_{o,s}$). Starting from an initial oxygen concentration ($Y_{o,\infty}$), the oxygen concentration on the surface decreases as it is consumed by the char surface oxidation.

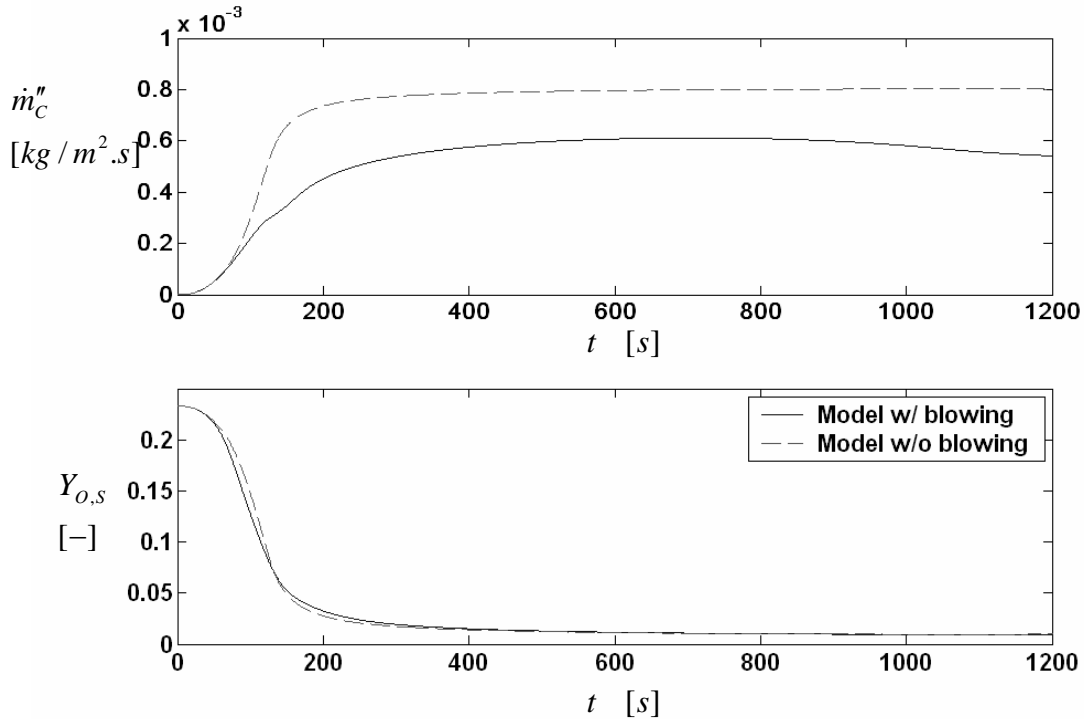


Figure 4.11: (a) char surface oxidation mass flux, and (b) surface oxygen mass fraction histories; ($\dot{q}_i'' = 25 \text{ kW/m}^2$, $Y_{o,\infty} = 0.233$)

4.5.4 In-depth Solid Profiles

Plots of in-depth temperature, density, and reaction rate profiles for $\dot{q}_i'' = 25 \text{ kW/m}^2$ are shown in Fig. 4.12. The plot of density profile shows that as the wood decomposes, the active wood density continuously changes from the virgin wood density to the final char density. The wood surface is completely pyrolyzed at approximately 150 seconds. At this

point, a char layer starts to form on the wood surface. As the time goes by, the pyrolysis front moves toward the back surface. It can be noticed from the temperature profile that the thermal wave reaches the back surface at about 300 seconds. Since an adiabatic boundary was employed on the back surface, the back temperature rises in time with a zero gradient. The surface temperature increases with time, and it approaches a constant value as the char layer becomes thicker. A starting point of the temperature profile shifts from left to right as the front surface regresses due to the char surface oxidation. The rightmost profile is obtained when the exposure time is approximately 1000 seconds. At this time the front surface is regressed by about 20 % of its initial length.

It should be noted that at the time when the reaction rate at the surface ($\partial\rho/\partial t$ at $\hat{x} = 0$) first goes to zero (see Fig. 4.12c, the third profile from the left; $t \approx 150$ seconds), the sample surface completely becomes char. At the same time, the pyrolysis mass flux ($\dot{m}''_{g,s}$) reaches its first peak (see Fig. 4.10b model w/ blowing). This can be explained by the fact that after the surface reaction rate goes to zero; the char layer starts to form at the surface insulating heat and mass transfer between the front surface and the interior virgin wood. As the char layer thickens, the heat transfer to the virgin wood decreases resulting in decreasing of the pyrolysis mass flux. The peak of the reaction rate moves toward the back surface as the wood decomposes. By tracking this peak, an average speed of the pyrolysis wave can be identified. In this case, the estimated average speed is about 2.5×10^{-5} m/s.

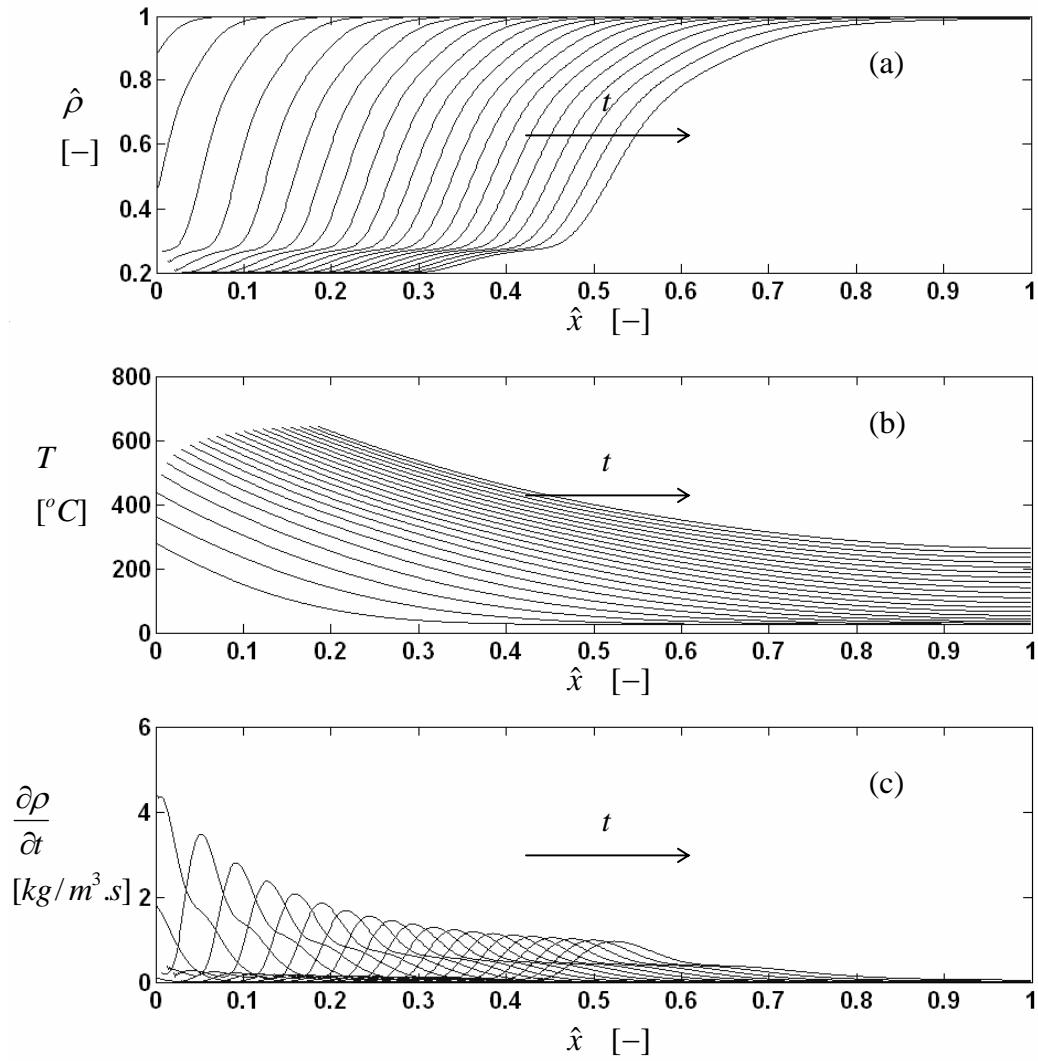


Figure 4.12: (a) in-depth non-dimensional wood density profiles, (b) in-depth temperature profiles, and (c) in-depth solid reaction rate profiles;

profiles starting at 44.80 seconds with 44.80 second time-step increments

$$(\dot{q}_i'' = 25 \text{ kW/m}^2, Y_{O,\infty} = 0.233)$$

4.5.5 Glowing Ignition: Experimental and Theoretical Results

Based on the glowing ignition criteria, quantitative comparisons between experimental and theoretical values at glowing ignition are presented. Two sets of experimental data are considered: (1) from present study and (2) from previous study by Boonmee and Quintiere [2].

In present study, the experiments were conducted in heat fluxes ranging from 9 kW/m² to 30 kW/m². The glowing ignition was identified when a measured surface temperature (signal from an IR thermocouple) rapidly increases “jumps”. Detailed discussions of the experimental glowing ignition can be found in Chapter 2.

The experimental data taken from the previous study [2] were performed with heat fluxes ranging from 20 kW/m² to about 70 kW/m². In this case, the glowing ignition was based on the assumption that T_s of the wood should be lower than T_s of the adjoining insulator if the wood is inert, since the thermal inertia ($k\rho c_p$) of wood is greater than the insulator. However, if wood undergoes surface oxidation, T_s of wood can be higher than the insulator. Thus, the experimental glowing ignition was defined, as when the T_s of wood was greater than the T_s of the insulator.

Fig. 4.13 plots theoretical and experimental glowing ignition times ($t_{glowing}$) as a function of the incident heat flux. Generally, good agreement between the theoretical and experimental values is obtained. It should be noted that in the experiment, for $\dot{q}_i'' > 40$

kW/m^2 , flaming ignition took place soon after the wood was exposed to the incident heat flux, thus it was difficult to distinguish between the glowing and flaming ignition time. However, it was expected that the glowing ignition should take place just an instant before a visible flame was observed. The lowest heat flux that the glowing ignition could achieve in the experiment was 10 kW/m^2 . Thus this heat flux can be considered as a critical heat flux for glowing ignition. In the model, the lowest heat flux that glowing ignition could occur within two hours physical time was 5 kW/m^2 . The model under predicts the critical heat flux for glowing ignition. The reason may be due to an uncertainty of the kinetic parameters in the char surface oxidation model.

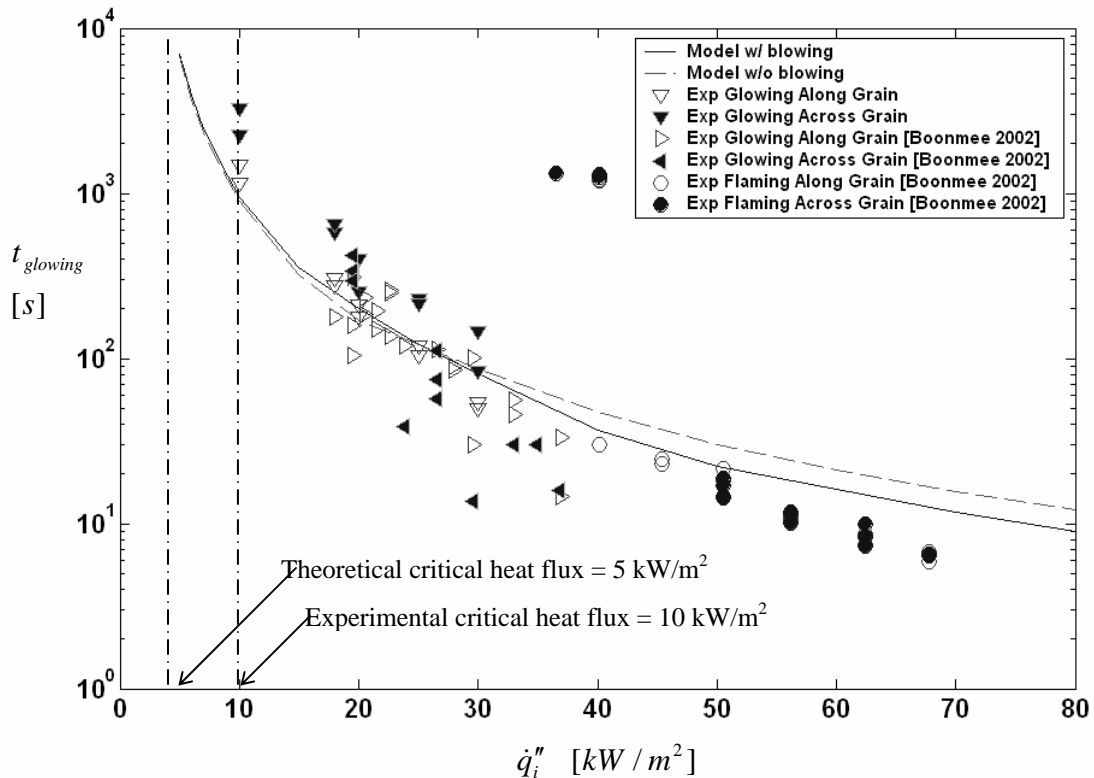


Figure 4.13: Glowing ignition time as a function of incident heat flux

The effect of blowing due to the unburnt pyrolysis mass flux ($\dot{m}''_{g,s}$) is negligible on the glowing ignition time at low heat flux as one could see in Fig. 4.13. This is because at low heat flux, only a small amount of $\dot{m}''_{g,s}$ can be generated before the glowing ignition occurs; thus the blowing effect is insignificant. However, as the heat flux increases, the model with blowing effect achieves glowing ignition at a lower surface temperature than the one without the effect (see Fig. 4.14). Accordingly, the glowing ignition can occur easier resulting in a faster glowing ignition time.

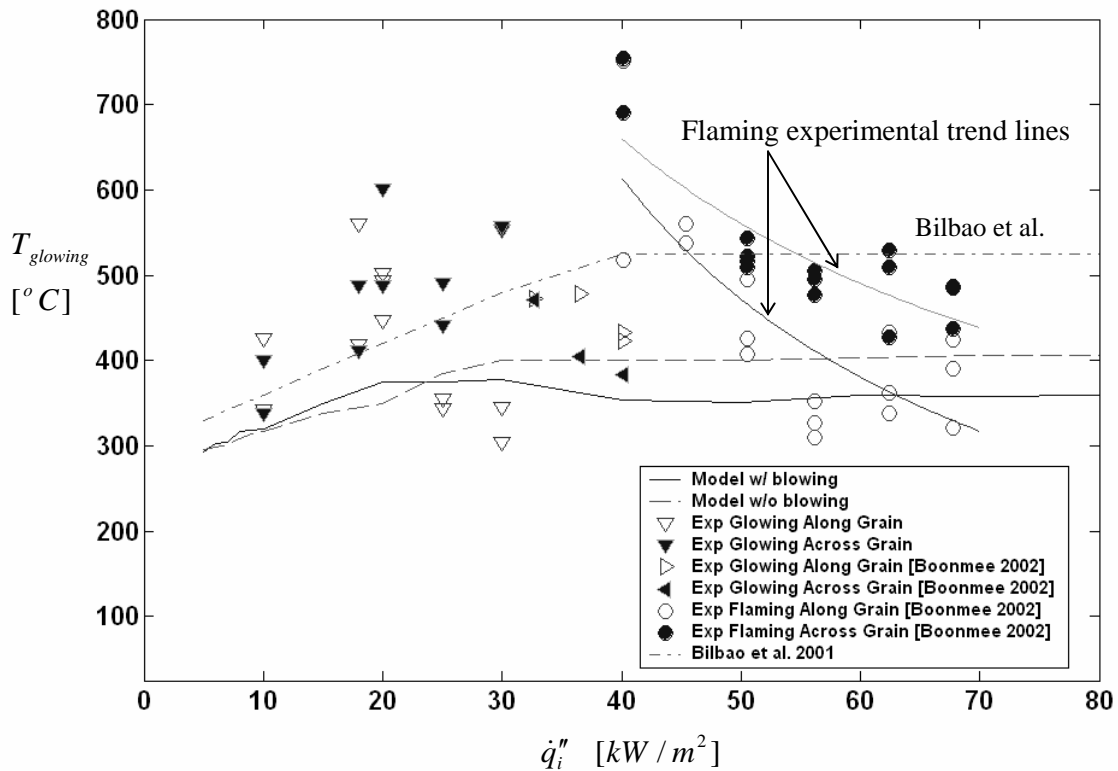


Figure 4.14: Glowing ignition surface temperature as a function of incident heat flux

A plot of surface temperature at glowing ignition ($T_{glowing}$) as a function of incident heat flux is illustrated in Fig. 4.14. Although the experimental data are scattered, the data trends suggest that $T_{glowing}$ increases with increasing \dot{q}_i'' at low heat flux ($\dot{q}_i'' < 30$ kW/m²). In the cases that flaming ignition is occurred, the surface temperature at flaming ignition decreases with increasing \dot{q}_i'' . The theoretical glowing ignition temperature slightly increases from 317 to 400°C as the incident heat flux increases from 10 to 30 kW/m². After 30 kW/m², the predicted glowing ignition temperature is fairly constant. For high heat flux (> 40 kW/m²), it was experimentally observed that the wood flaming ignited soon after it was exposed to the heater. Thus only flaming ignition temperatures were registered. However, as the incident heat flux increases the experimental flaming ignition temperature decreases and approaches the predicted glowing ignition temperature asymptotically. This observation may confirm the hypothesis that glowing ignition occurs just an instant before flaming ignition occurs.

Bilbao et al. [22] experimentally observed a glowing (smoldering) ignition temperature for pine wood (*Pinus Pinaster*). They correlated the experimental data as

$$\begin{aligned} \dot{q}_i'' < 40 \text{ kW/m}^2 : \quad T_{glowing} &= 300 + 6\dot{q}_i'' , \\ \dot{q}_i'' > 40 \text{ kW/m}^2 : \quad T_{glowing} &= 525 , \end{aligned}$$

where $T_{glowing}$ is in °C, and \dot{q}_i'' is in kW/m². The correlation is also plotted in Fig. 4.14. A similar trend is observed as the $T_{glowing}$ increases proportionally with \dot{q}_i'' for low heat

flux, and approaches a constant value for high heat flux. This observational criterion supports our criteria for glowing ignition. Indeed, visible signs of ignition might lag “true” ignition.

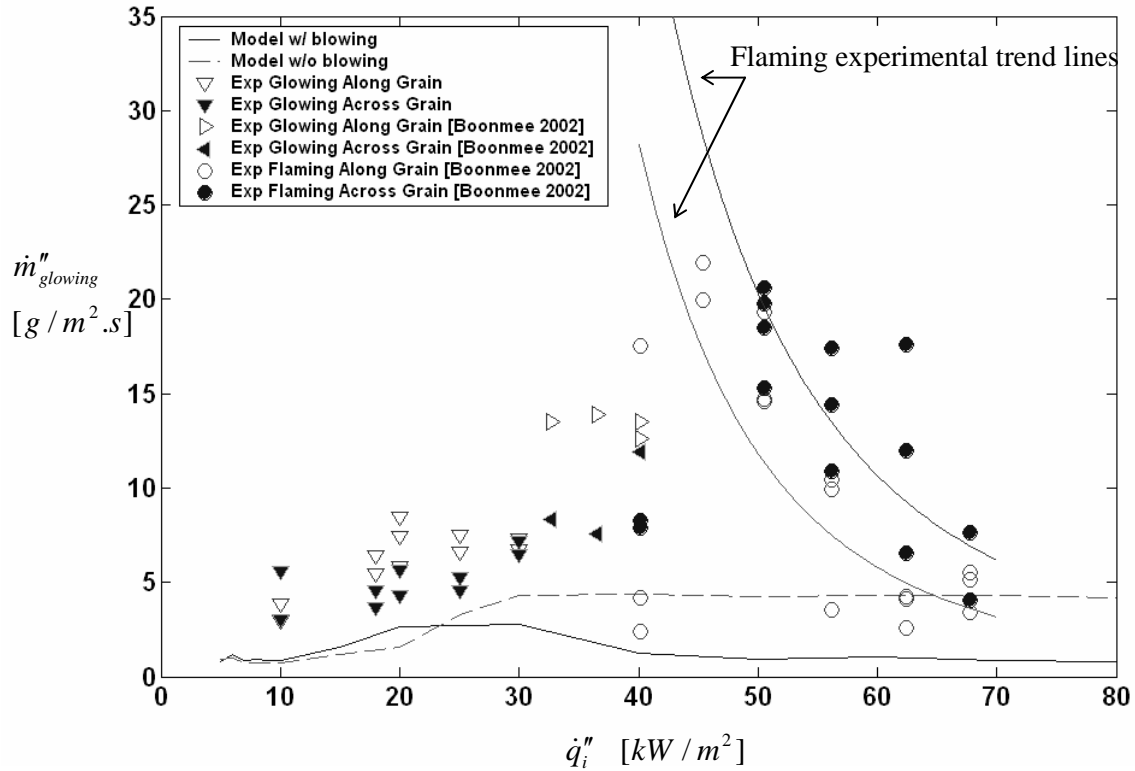


Figure 4.15: Glowing ignition mass flux as a function of incident heat flux

Theoretical and experimental pyrolysis mass flux at glowing ignition ($\dot{m}''_{glowing}$) as a function of incident heat flux is reported in Fig. 4.15. The predicted $\dot{m}''_{glowing}$ gradually increases at low heat flux (< 30 kW/m²) and approaches a constant value of 4 g/m².s (the model without blowing effect) and 1g/m².s (the model with blowing effect). An under-prediction is observed when compared to the experimental data. The flaming ignition mass flux is also illustrated in Fig. 4.15. Again, as the incident heat flux increases, the

flaming ignition mass flux decreases and approaches the theoretical glowing ignition mass flux asymptotically. Interestingly, the asymptotic theoretical glowing ignition mass flux at high heat flux agrees with the minimum ignition mass flux for piloted ignition commented by Kanury [89] ($\dot{m}''_{i,g,\min} \approx 1 - 4 \text{ g/m}^2\cdot\text{s}$). This minimum ignition mass flux is one of the fundamental requirements for flaming ignition to occur. Nonetheless, for flaming ignition to take place, sufficient additional energy either from a pilot source (piloted ignition) or a high gas temperature (autoignition) is required.

Regarding the blowing effect due to the unburnt pyrolysis mass flux, the model with blowing effect predicts the glowing ignition temperature and mass flux slightly lower than the model without blowing effect at high heat flux ($\dot{q}''_i > 40 \text{ kW/m}^2$). This can be explained in that the unburnt pyrolysis mass flux dilutes the char oxidation mass flux at the moment of glowing ignition. Indeed, the glowing ignition temperature and mass flux are lower than those without the blowing effect.

4.5.6 Effect of the Surrounding Oxygen Concentration

The effect of the surrounding oxygen concentration ($Y_{O,\infty}$) on glowing ignition is theoretically examined. Fig. 4.16a shows a variation of the glowing ignition temperature as a function of incident heat flux for various values of $Y_{O,\infty}$. At high incident heat flux ($> 50 \text{ kW/m}^2$), glowing ignition occurs roughly at a constant temperature of $400 \text{ }^\circ\text{C}$. The glowing ignition at a constant temperature can imply that glowing ignition is primarily due to the incident heat flux [4]. This is because at high incident heat flux, the surface temperature rises quickly; therefore, as soon as the surface temperature reaches the

ignition temperature (e.g. 400 °C), glowing ignition occurs independent of $Y_{O,\infty}$. On the other hand, at low heat flux ($< 50 \text{ kW/m}^2$), the surface temperature increases slower; thus the kinetics of char surface oxidation is important. For a given incident heat flux, increasing $Y_{O,\infty}$ enhances the char surface oxidation rate; hence, glowing ignition can occur at a lower surface temperature. As a result, the glowing ignition temperature decreases as $Y_{O,\infty}$ increases.

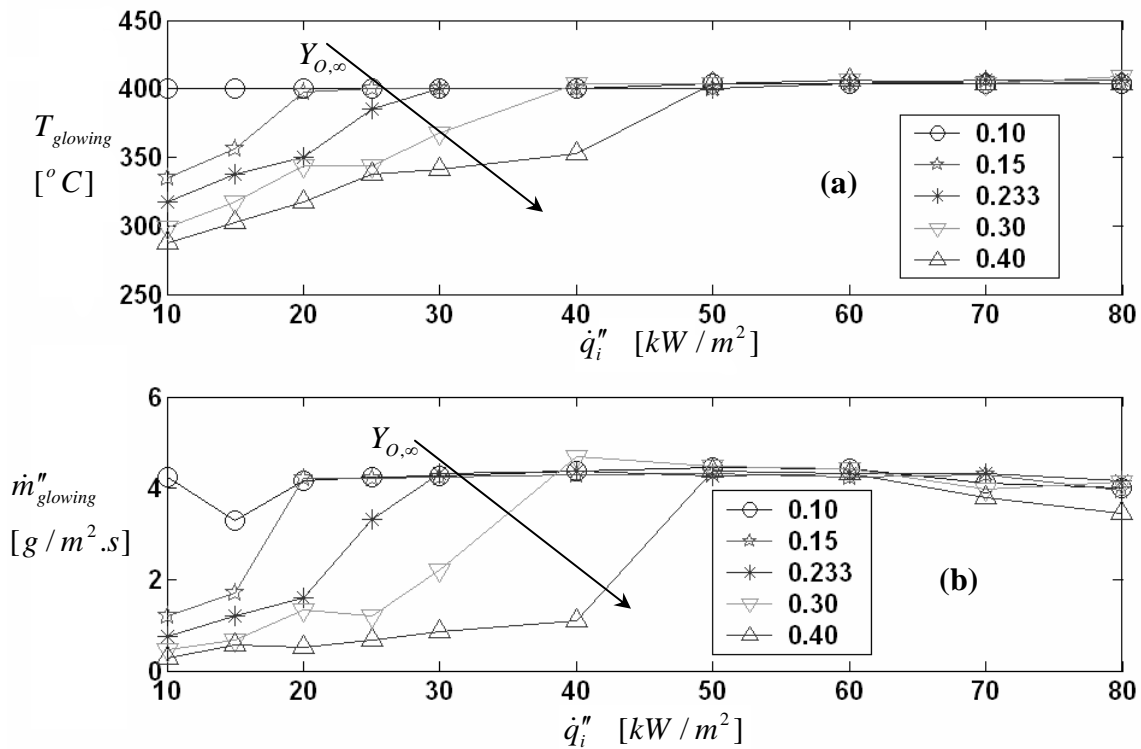


Figure 4.16: Theoretical glowing ignition surface temperature and mass flux as a function of incident heat flux for various oxygen mass fraction.

Recall that the transition for the char surface oxidation from kinetic-controlled to diffusion-controlled occurs approximately at 400 °C. At a temperature lower than the

transition, the char oxidation is kinetic-controlled while at a temperature higher than the transition it is diffusion-controlled. Consequently, the glowing ignition temperature increases as the incident heat flux increases in the kinetic-controlled regime while the glowing ignition temperature is approximately constant in the diffusion-controlled regime. For the mass flux at glowing ignition (see Fig. 4.16b), the same behavior, as seen with the glowing ignition temperature, is observed as the incident heat flux increases. The ignition mass flux increases in the kinetic-controlled regime, while remaining approximately constant independent of $Y_{O,\infty}$ in the diffusion-controlled regime.

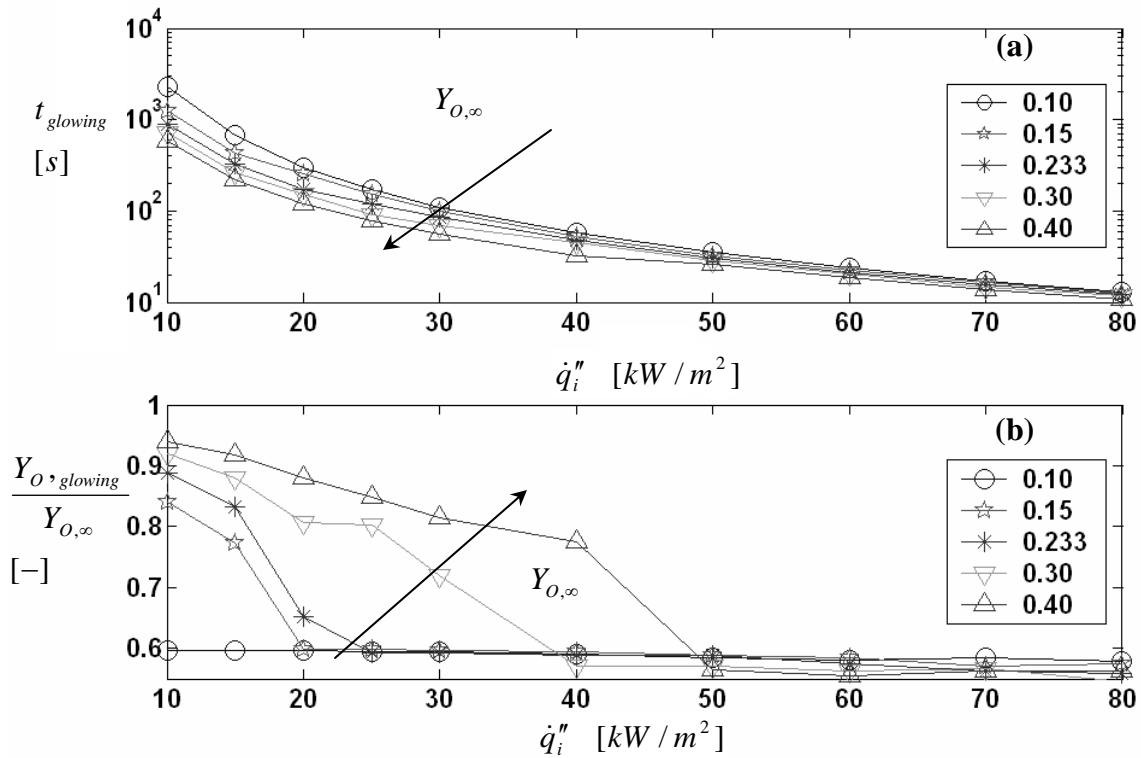


Figure 4.17: Theoretical glowing ignition time and $Y_{O, glowing} / Y_{O, \infty}$ as a function of incident heat flux for various ambient oxygen mass fraction.

As one might expect, the oxidation surface undergoes glowing ignition faster when $Y_{O,\infty}$ increases, as shown in Fig. 4.17a. The effect is more pronounced when the incident heat flux is low. A plot of surface oxygen concentration at glowing ignition normalized by its initial value ($Y_{O,glowing}/Y_{O,\infty}$) is shown in Fig. 4.17b. Two distinctive regions are noticed. At low heat flux ($< 50 \text{ kW/m}^2$), increasing $Y_{O,\infty}$ accelerates the glowing ignition; hence less oxygen is consumed on the surface. As a result, the ratio $Y_{O,glowing}/Y_{O,\infty}$ increases with increasing $Y_{O,\infty}$. At high heat flux ($> 50 \text{ kW/m}^2$), the glowing ignition is solely due to the external heat source. Therefore, the ratios $Y_{O,glowing}/Y_{O,\infty}$ for all different initial ambient oxygen concentration approach a constant value of 0.6.

4.6 Conclusions

A theoretical solid phase model accounting for kinetic decomposition, and heat and mass transfer of wood subjected to a radiant heat source has been developed. The model includes variations of thermal properties of wood and char. Comparisons between the theoretical and experimental surface temperature and pyrolysis mass flux are given. With a number of the model inputs required, the theoretical values agree reasonably well with the experiments.

The char surface oxidation, which can lead to “glowing” ignition, is included at the solid-gas interface surface. The criteria for glowing ignition for wood (or charring material in general) are developed based on an energy balance at the oxidation surface. Two

distinctive regimes for the char surface oxidation are illustrated. The char surface oxidation is kinetic-controlled at the early stage of the heating process while diffusion-controlled takes place at the latter stage. The transition temperature for kinetic-controlled to diffusion-controlled is approximately 400 °C. Good agreement between the theoretical and experimental results at glowing ignition is demonstrated confirming a validation of the proposed glowing ignition criteria. At high heat flux, glowing ignition occurs irrespective of the surrounding oxygen concentration; while at low heat flux, the effect of the surrounding oxygen concentration is prominent.

Chapter 5

The Gas Phase

5.1 Introduction

As the fuel volatiles emanate from the pyrolyzed wood, they mix with air from the surrounding creating a boundary layer of combustible mixtures. At the same time the boundary layer adjacent to the solid surface is heated by heat conduction from the solid. As a result of the heating, the gas temperature in the boundary layer rapidly increases together with the heat release rate. As the combustible mixtures reach a critical condition, a thermal runaway can be accomplished and autoignition occurs without any help of a local heat source.

A theoretical model accounting for physical and chemical processes in the gas phase described above is developed in this chapter. The gas phase transport model is coupled with the wood pyrolysis model described in Chapter 4 via the solid-gas interface surface. The aims of this chapter are to explore the physical and chemical processes underlining the gas phase autoignition of wood. Criteria to determine the gas phase flaming autoignition are discussed and justified. Gas phase flaming autoignition behavior for low and high heat flux is distinguished. Comparisons between the theoretical and experimental results are presented to demonstrate capabilities and limitations of the present model.

5.2 Theoretical Model

5.2.1 Assumptions

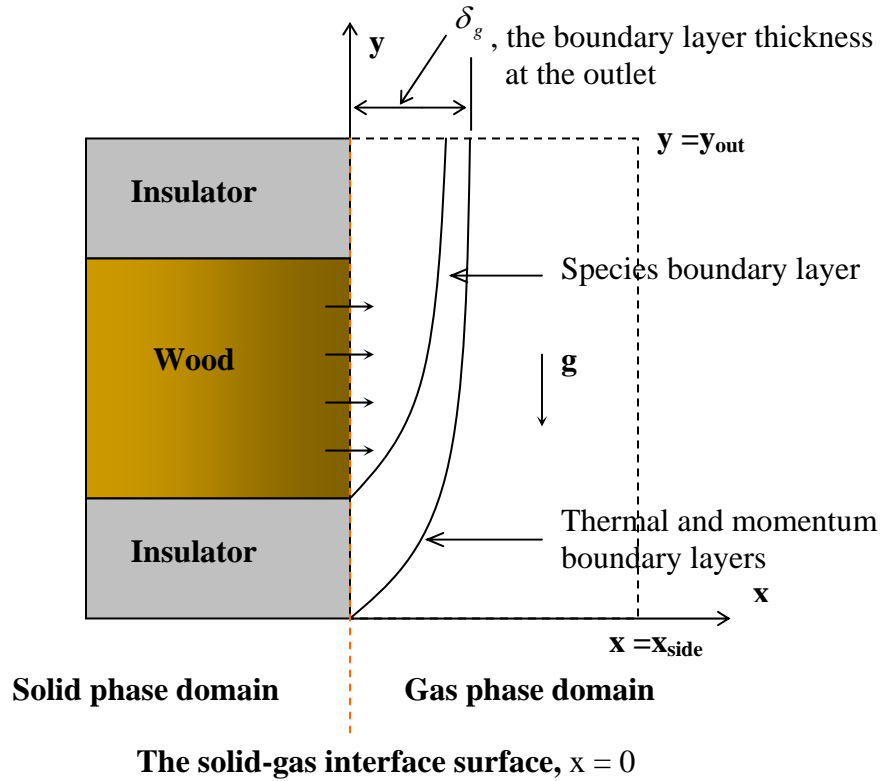


Figure 5.1: Systematic diagram for gas phase boundary layer model

The problem considered here is illustrated in Fig. 5.1. The computational domain is divided into solid phase and gas phase domains. In the solid phase domain, the problem is formulated as a one-dimensional heat conduction in the direction perpendicular to the solid-gas interface surface (i.e. x -direction). The solid phase domain is subdivided into wood and insulator portions. In the wood portion, the wood pyrolysis model including char surface oxidation described in Chapter 4 is used to solve for the wood surface

temperature and pyrolysis mass flux. In the insulator portion, the surface temperature is calculated from a transient heat conduction equation. In the gas phase domain, the gas phase transport equations for momentum, energy, and species, are formulated as a two-dimensional transient boundary layer approximation. The following assumptions are imposed in order to simplify the gas phase model.

1. The flow is two-dimensional, laminar, transient buoyancy driven boundary layer flow.
2. The gas mixture behaves like a perfect gas.
3. The gas density change due to a temperature variation is taken into account and the gas density can be calculated directly from the equation of state.
4. The gas thermal properties depend on temperature and can be expressed by a power law relation [59].
5. The pressure in the computational domain is assumed to be constant at 1 atm.
6. The Lewis number is constant and equal to unity for every gas species.
7. The Prandtl number is constant with the value of 0.7.
8. The gas radiation absorption is small and can be neglected.
9. The gas kinetic reaction follows a one-step, second-order Arrhenius finite-rate reaction. Prior to ignition the gas reaction rate is small and thus can be omitted from the gas phase transport equations.
10. The gas reaction rate is post-calculated from the successive solution of the gas phase transport equations.

11. Flaming autoignition is achieved when the gas reaction rate exceeds a critical value. The criteria for gas phase flaming autoignition will be discussed in Section 5.4.
12. The gas phase transport equations are coupled with the solid phase model via the solid-gas interface boundary conditions.
13. The wood surface regression due to the char surface oxidation is neglected. Thus, the gas phase boundary layer approximation is valid for all the simulation time.

5.2.2 Governing Equations and Boundary Conditions

The governing equations for compressible transient gas phase transport equations without reaction terms in the boundary layer are:

Conservation of mass:

$$\frac{\partial \rho_g}{\partial t} + \frac{\partial \rho_g u}{\partial x} + \frac{\partial \rho_g v}{\partial y} = 0, \quad (5.1)$$

Conservation of momentum for x-direction (cross-stream):

$$\frac{\partial P}{\partial x} = 0, \quad (5.2)$$

Conservation of momentum for y-direction (streamwise):

$$\rho_g \left(\frac{\partial v}{\partial t} + u \frac{\partial v}{\partial x} + v \frac{\partial v}{\partial y} \right) = \frac{\partial}{\partial x} \left(\mu_g \frac{\partial v}{\partial x} \right) - (\rho_g - \rho_{g,\infty}) g, \quad (5.3)$$

Conservation of energy:

$$\rho_g c_{P,g} \left(\frac{\partial T_g}{\partial t} + u \frac{\partial T_g}{\partial x} + v \frac{\partial T_g}{\partial y} \right) = \frac{\partial}{\partial x} \left(k_g \frac{\partial T_g}{\partial x} \right), \quad (5.4)$$

Conservation of species:

$$\rho_g \left(\frac{\partial Y_i}{\partial t} + u \frac{\partial Y_i}{\partial x} + v \frac{\partial Y_i}{\partial y} \right) = \frac{\partial}{\partial x} \left(\rho_g D_g \frac{\partial Y_i}{\partial x} \right) \quad \text{for } i = F, O, \quad (5.5a)$$

$$\text{and } Y_{In} = 1 - \sum Y_i \quad (5.5b)$$

The gas coordinate system is set as shown in Fig. 5.1. The solid-gas interface surface is essentially the y-axis. The streamwise direction is the y-direction and the cross-stream direction is the x-direction. The subscript “g” refers to gas. The streamwise velocity component is v and the cross-stream velocity component is u . P is the pressure, T_g is the gas temperature, and Y_i is the mass fraction of species i (F, fuel; O, oxygen; In, inert gas). μ_g is the gas kinematics viscosity, k_g is the gas thermal conductivity, and D_g is the gas mass diffusivity. \mathbf{g} is the gravity (9.81 m/s²)

The x-momentum equation suggests that the pressure is constant across the boundary; thus the pressure variation is only due to the hydrostatic pressure (e.g. $P = \rho_g g(y_{ref} - y)$, y_{ref} is the reference level). The hydrostatic pressure combined with the body force is written in the last term on the RHS of the y-momentum equation.

The gas density is evaluated from the equation of state:

$$P = \rho_g \left(\frac{R}{M_{air}} \right) T_g, \quad (5.6)$$

where R is the universal gas constant (8.314 kJ/kmol.K), M_{air} is the molecular weight of air (28.97 kg/kmol).

The boundary conditions are

At the inlet ($y = 0$):

$$u = 0, \quad v = V_{in},$$

$$T_g = T_{g,\infty},$$

$$Y_F = 0, \quad Y_O = Y_{O,\infty}, \quad (5.7a)$$

At the outlet ($y = y_{out}$):

$$\frac{\partial u}{\partial y} = \frac{\partial v}{\partial y} = \frac{\partial T_g}{\partial y} = \frac{\partial Y_F}{\partial y} = \frac{\partial Y_O}{\partial y} = 0, \quad (5.7b)$$

At the solid-gas interface, the coupled conditions ($x=0$):

insulator portions,

$$u = v = 0,$$

$$T_g = T_s,$$

$$\frac{\partial Y_F}{\partial x} = \frac{\partial Y_O}{\partial x} = 0,$$

wood portion,

$$u = u_s = \frac{\dot{m}_{net}''}{\rho_{g,s}}, \quad v = 0,$$

$$T_g = T_s,$$

$$(\rho_{g,s} u_s) Y_{i,s} - \rho_{g,s} D_g \left. \frac{\partial Y_i}{\partial x} \right|_s = \dot{m}_{i,s}'' \quad \text{for } i = F, O \quad (5.7c)$$

At the side wall ($x = x_{side}$):

$$\frac{\partial u}{\partial x} = \frac{\partial v}{\partial x} = \frac{\partial T_g}{\partial x} = 0,$$

$$Y_F = 0, \quad Y_O = Y_{O,\infty}, \quad (5.7d)$$

where V_{in} is the vertical inlet velocity, $T_{g,\infty}$ is the ambient temperature (298 K), $Y_{O,\infty}$ is the ambient oxygen mass fraction (0.233), u_s is the blowing velocity, \dot{m}_{net}'' is the net

pyrolysis mass flux ($= \dot{m}_f'' + \dot{m}_c''$), \dot{m}_i'' is the generation rate of fuel ($i=f$), or the destruction rate of oxygen ($i=O$), and T_s is the solid surface temperature.

The coupled conditions in the wood portion are determined from solving the one-dimensional wood pyrolysis model (Chapter 4). The boundary condition for wood pyrolysis model is modified from Eq. (4.19b) to account for the heat conduction from the gas adjacent to the interface surface as

$$\dot{q}_i'' + \dot{m}_c'' \Delta H_c = -k_s \left. \frac{\partial T}{\partial x} \right|_{Solid} - k_g \left. \frac{\partial T}{\partial x} \right|_{gas} + \varepsilon \sigma (T_s^4 - T_{ref}^4), \quad (5.8)$$

where the subscripts, “*solid*” indicate the temperature gradient evaluated on the solid phase side, “*gas*” indicate the temperature gradient evaluated on the gas phase side.

In the insulator portions, the surface temperature is calculated from a one-dimensional transient heat conduction:

$$\frac{\partial T}{\partial t} = \alpha_{in} \frac{\partial^2 T}{\partial x^2}, \quad (5.9)$$

subjected to the boundary conditions:

solid-gas interface:

$$\dot{q}_i'' = -k_{in} \left. \frac{\partial T}{\partial x} \right|_{Solid} - k_g \left. \frac{\partial T_g}{\partial x} \right|_{gas} + \varepsilon \sigma (T_s^4 - T_{ref}^4), \quad (5.10a)$$

back surface:

$$\left. \frac{\partial T}{\partial x} \right|_{Solid} = 0, \quad (5.10b)$$

where k_{in} is the insulator thermal conductivity, and α_{in} is the insulator thermal diffusivity. The thermal properties of the insulator are taken from the insulator manufacture (Kaowool® Board type M).

5.2.3 Non-dimensional Governing Equations and Boundary Conditions

The proper characteristic length is the thermal boundary layer thickness (δ_g) evaluated at the outlet of computational domain ($y = y_{out}$) which $\delta_g \approx 1$ cm. The characteristic velocity is chosen as the thermal diffusion velocity (U_C) such that

$$U_C = \frac{\alpha_{g,\infty}}{\delta_g}, \quad (5.11)$$

where $\alpha_{g,\infty}$ is the gas thermal diffusivity evaluated at the ambient temperature (air at 298 K). The characteristic time scale for gas phase is the thermal diffusion time (t_C), which

$$t_C = \frac{\delta_g}{U_C} = \frac{\delta_g^2}{\alpha_g}. \quad (5.12)$$

The non-dimensional gas temperature is written as

$$\theta = \frac{(T_g - T_{g,\infty})}{(\bar{T}_s - T_{g,\infty})}, \quad (5.13)$$

where \bar{T}_s is the average solid surface temperature over the wood portion.

The characteristic gas density is the ambient gas density ($\rho_{g,\infty}$), and the characteristic

mass flux is $\dot{m}''_{g,C} = \rho_{g,\infty} \alpha_{g,\infty} / \delta_g$.

Normalized the gas phase governing equations with the characteristic variables, the non-dimensional gas phase governing equations are

Conservation of mass:

$$\frac{\partial \hat{\rho}_g}{\partial \hat{t}} + \frac{\partial \hat{\rho}_g \hat{u}}{\partial \hat{x}} + \frac{\partial \hat{\rho}_g \hat{v}}{\partial \hat{y}} = 0, \quad (5.14)$$

Conservation of momentum for y-direction (streamwise):

$$\hat{\rho}_g \left(\frac{\partial \hat{v}}{\partial \hat{t}} + \hat{u} \frac{\partial \hat{v}}{\partial \hat{x}} + \hat{v} \frac{\partial \hat{v}}{\partial \hat{y}} \right) = \text{Pr} \frac{\partial}{\partial \hat{x}} \left(\hat{\mu}_g \frac{\partial \hat{v}}{\partial \hat{x}} \right) + Gr \hat{\rho}_g \theta \quad (5.15)$$

Conservation of energy:

$$\hat{\rho}_g \left(\frac{\partial \theta}{\partial \hat{t}} + \hat{u} \frac{\partial \theta}{\partial \hat{x}} + \hat{v} \frac{\partial \theta}{\partial \hat{y}} \right) = \frac{\partial}{\partial \hat{x}} \left(\frac{\hat{k}_g}{\hat{c}_{p,g}} \frac{\partial \theta}{\partial \hat{x}} \right), \quad (5.16)$$

Conservation of species:

$$\hat{\rho}_g \left(\frac{\partial Y_i}{\partial \hat{t}} + \hat{u} \frac{\partial Y_i}{\partial \hat{x}} + \hat{v} \frac{\partial Y_i}{\partial \hat{y}} \right) = Le \frac{\partial}{\partial \hat{x}} \left(\hat{\rho}_g \hat{D}_g \frac{\partial Y_i}{\partial \hat{x}} \right), \quad \text{for } i = F, O. \quad (5.17)$$

where the ^ sign indicates a non-dimensional variable. All the gas thermal properties are normalized by their ambient value evaluated at 298 K.

The dimensionless numbers appearing in the non-dimensional governing equations are defined as follows:

$$Pr = \frac{\mu_{g,\infty}}{\rho_{g,\infty} \alpha_{g,\infty}}, \quad \text{the Prandtl number;} \quad (5.18a)$$

$$Gr = \frac{g \beta (T_s - T_{g,\infty}) \delta_g^3}{\alpha_{g,\infty}^2}, \quad \text{the Grashof number;} \quad (5.18b)$$

$$Le = \frac{D_{g,\infty}}{\alpha_{g,\infty}}, \quad \text{the Lewis number.} \quad (5.18c)$$

In deriving the non-dimensional y-momentum equation, the density difference term is simplified with the equation of state [90] as

$$\rho_{g,\infty} - \rho_g = \beta \rho_g (T_g - T_{g,\infty}),$$

where β is thermal expansion coefficient ($= 1/T_g$ for perfect gas).

The non-dimensional thermal properties have a power law dependence on the temperature [59] as

$$\hat{\mu}_g = \left(\frac{T_g}{T_{g,\infty}} \right)^{0.7}, \quad (5.19a)$$

and the non-dimensional dynamics viscosity is $\hat{\nu}_g = \hat{\mu}_g / \hat{\rho}_g$. The Prandtl number is constant, thus $\hat{\alpha}_g = \hat{\nu}_g$ providing that

$$\frac{\hat{k}_g}{\hat{c}_{P,g}} = \hat{\mu}_g. \quad (5.19b)$$

With the unity Lewis number $\hat{D}_g = \hat{\alpha}_g$, and therefore

$$\hat{\rho}_g \hat{D}_g = \hat{\mu}_g. \quad (5.19c)$$

The non-dimensional boundary conditions are

At the inlet ($y = 0$):

$$\begin{aligned}\hat{u} &= 0, \quad \hat{v} = \frac{V_{in}}{U_C}, \\ \theta &= 0, \\ Y_F &= 0, \quad Y_O = Y_{O,\infty},\end{aligned}\tag{5.20a}$$

At the outlet ($y = y_{out}$):

$$\frac{\partial \hat{u}}{\partial \hat{y}} = \frac{\partial \hat{v}}{\partial \hat{y}} = \frac{\partial \theta}{\partial \hat{y}} = \frac{\partial Y_F}{\partial \hat{y}} = \frac{\partial Y_O}{\partial \hat{y}} = 0,\tag{5.20b}$$

At the solid-gas interface, the coupled conditions ($x=0$):

insulator portions,

$$\begin{aligned}\hat{u} &= \hat{v} = 0, \\ \theta &= \theta_s = \frac{T_s - T_{g,\infty}}{T_s - T_{g,\infty}}, \\ \frac{\partial Y_F}{\partial \hat{x}} &= \frac{\partial Y_O}{\partial \hat{x}} = 0,\end{aligned}$$

wood portion,

$$\hat{u} = \hat{u}_s = \frac{u_s}{U_C}, \quad \hat{v} = 0,$$

$$\theta = \theta_s = \frac{T_s - T_{g,\infty}}{\bar{T}_s - T_{g,\infty}},$$

$$(\hat{\rho}_{g,s} \hat{u}_s) Y_{i,s} - \hat{\rho}_{g,s} Le \frac{\partial Y_i}{\partial \hat{x}} \Big|_s = \hat{m}_{i,s}'' , \quad \text{for } i = F, O \quad (5.20c)$$

At the side wall ($x = x_{\text{side}}$):

$$\frac{\partial \hat{u}}{\partial \hat{x}} = \frac{\partial \hat{v}}{\partial \hat{x}} = \frac{\partial \theta}{\partial \hat{x}} = 0 ,$$

$$Y_F = 0 , Y_O = Y_{O,\infty} . \quad (5.20d)$$

An explicit second-order Runge-Kutta finite difference scheme [91] was used to integrate the non-dimensional gas phase governing equations together with the boundary conditions. Detail of the gas phase numerical method is discussed in Appendix B.

5.2.4 Coupled Procedure for Solid and Gas Phase Calculations

To couple between the gas phase and solid phase models, the numerical procedure is performed as follows:

- 1) Solve the solid phase governing equations for a given heat flux. In addition to the solid phase variables, this step also computes the pyrolysis mass flux, and the surface temperature to be used in the solid-gas interface boundary conditions for the gas phase equations.
- 2) Solve the gas phase governing equations (momentum, energy, and species) with the boundary conditions that use the previous values of the pyrolysis mass flux

and the solid surface temperature. This step allows a new distribution of the heat flux feedback to the solid surface to be computed and then used as a boundary condition in the solution of solid phase equations at the next time-step.

Steps 1 and 2 are repeated until the autoignition occurs. In the solid phase, the implicit time advance scheme is used; thus, it is unconditionally stable. However, the gas phase calculation is conditional stable because the explicit time advance scheme is employed. The overall computational time-step is constrained by the gas phase time-step. The gas phase time-step is controlled either by convection time-step (CFL) or diffusion time-step (Fo). The minimum value between convection and diffusion time-steps is used to advance the overall calculation. Typically, the overall time-step was in the order of 10^{-3} seconds.

In the present gas phase model, the gas phase kinetics is omitted from the gas phase transport equations. This simplification greatly reduces computational difficulty since the computational time is not limited by the chemical time-step, which is very small (order of 10^{-5} seconds). The simplification is reasonable for our purpose of determining the flaming autoignition for the following reason. Prior flaming ignition, the gas reaction rate is relatively small due to a low gas temperature. Thus it does not significantly affect the solution of the gas phase model and hence the ignition time. However, after the ignition the gas phase calculation results can only be viewed as qualitative trends due to the drastic variations of the gas temperature and density near the flame.

5.3 Numerical Validation

5.3.1 A Natural Convection Flow over A Vertical Isothermal Hot Wall

A numerical simulation of a natural convection of a flow over a vertical isothermal wall is performed to validate the computer code developed to simulate the gas phase problem. The problem considered here is illustrated in Fig. 5.2. An isothermal wall of 400 K is assigned to the left wall. A rectangular computational domain is 3.5 cm wide and 8 cm high. A 40x64 with uniform mesh in y-direction and non-uniform mesh in x-direction (the mesh is clustered near the wall) is used to discretize the computational domain. The boundary conditions are as shown Fig. 5.2.

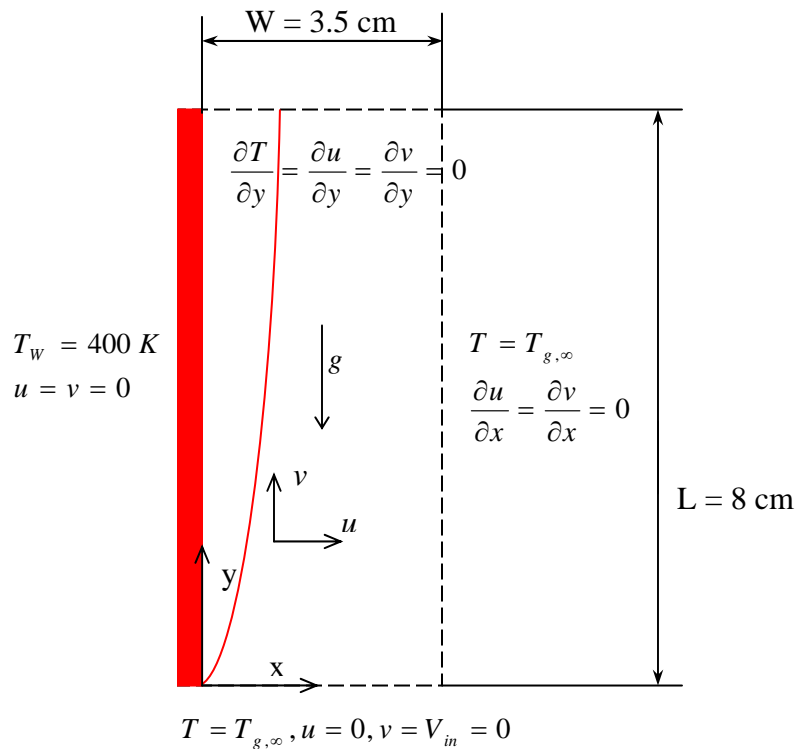


Figure 5.2: Problem configuration of a natural convection over a vertical wall

The gas density is assumed to be constant except the buoyancy term in the y-momentum (Boussinesq approximation). The gas thermal properties are constant and the Prandtl of 0.72 (air) is employed. The numerical integration starts from the initial condition where the fluid is at rest until the steady state solution is achieved ($\min(\partial\phi/\partial t) < 10^{-4}$, where ϕ are velocity and temperature).

The exact solution of this problem can be found in Ref. [63]. The solutions for the v -velocity component and temperature are presented in the forms of similarity variables defined as

$$f' = \frac{vy}{2\nu_g} Gr_y^{-1/2}, \quad \text{the similarity velocity variable;} \quad (5.21)$$

$$\theta = \frac{T_g - T_{g,\infty}}{T_w - T_{g,\infty}}, \quad \text{the similarity temperature variable,} \quad (5.22)$$

where Gr_y is the Grashof number at position y , a vertical distance from the leading edge ($y = 0$). The Gr_y is defined as

$$Gr_y = \frac{g\beta(T_w - T_{g,\infty})y^3}{\nu_g^2}, \quad (5.23)$$

where $T_{g,\infty}$ is the ambient temperature (298 K), ν_g is the gas dynamics viscosity, and T_w is the wall temperature.

The f' and θ are functions of the similarity variable η only where

$$\eta = \frac{x}{y} \left(\frac{Gr_y}{4} \right)^{1/4} \quad (5.24)$$

Comparisons of the steady state v -velocity and temperature (presented in similarity variable forms) for four locations downstream obtained from the numerical calculation with the exact solution [63] are shown in Fig. 5.3. Good agreement is observed providing us with confidence to proceed with the subsequent gas phase autoignition problem.

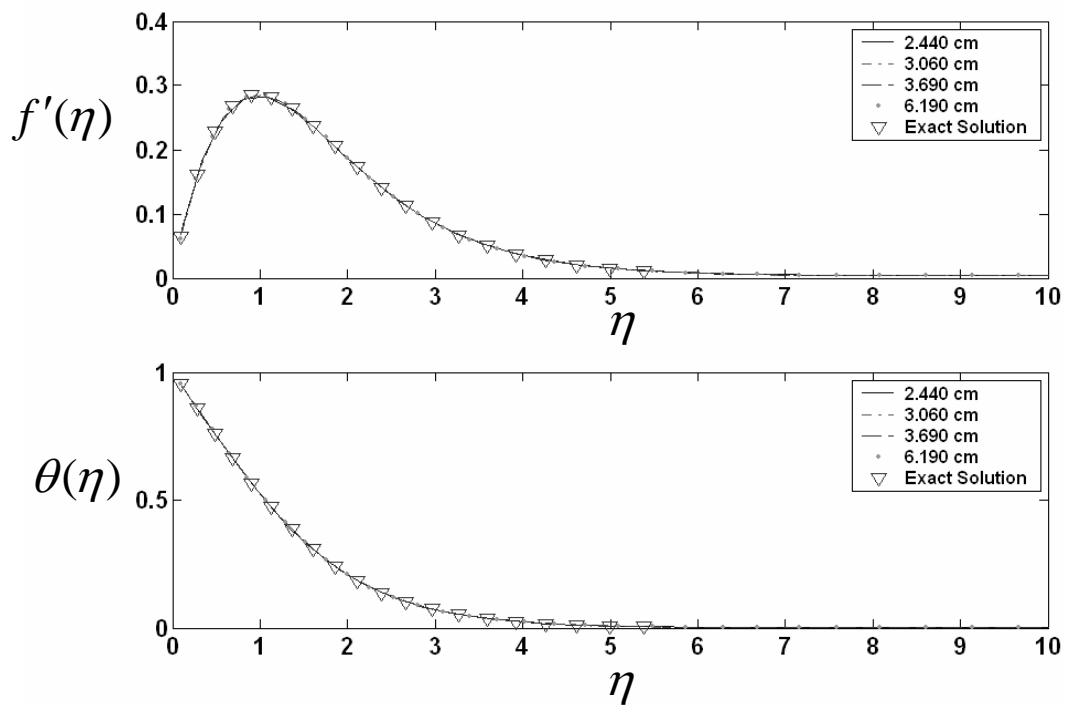


Figure 5.3: Comparisons of steady state v -velocity and temperature for a natural convection flow over a vertical isothermal wall of 400 K; the exact solution is taken from

Ref. [63].

5.3.2 Grid Refinement Study

A grid refinement study was conducted to find an optimal computational mesh size. The computational domain is a rectangle with the x-axis along the width and the y-axis along the height (see Fig. 5.1). The domain width of 3.5 cm is chosen such that the width is about 3.5 times of the thermal boundary layer thickness ($\delta_g \approx 1$ cm) evaluated at the domain outlet. The domain height is 8 cm (2 cm insulator portion, 4 cm wood portion, and 2 cm insulator portion), which is the same as in the experimental setup. The mesh size is varied as shown in Table.5.1. The mesh is non-uniform in the x-direction with grid concentrated near the solid-gas interface and uniform in the y-direction.

Table 5.1: A summary of mesh size in grid refinement study

Number of points ($N_x \times N_y$)	Δx_{\min} [cm]	Δx_{\max} [cm]	Δy [cm]
20x32	0.120	0.243	0.250
40x40	0.038	0.167	0.200
40x64	0.038	0.167	0.125
64x64	0.028	0.095	0.125
80x64	0.018	0.085	0.125

Note: The mesh size of 40x64 is chosen for all the calculations of gas phase flaming autoignition.

Fig. 5.4 and 5.5 show the maximum gas temperature and the maximum gas reaction rate time histories for various mesh sizes. These depict calculations of the solid and gas phase models with incident heat flux of 60 kW/m^2 . The gas reaction rate is calculated with the

gas kinetic parameters of $E_{a,g} = 67$ kJ/mol and $A_g = 8 \times 10^5$ m³/kg.s. The maximum gas temperature increases with increasing a number of points. This is because the maximum gas temperature is usually located at the first point in the gas phase domain near the heated wall. Increasing the number of grid points moves the first point close to the wall; hence, the maximum gas temperature increases. The gas reaction rate is directly related to the gas temperature. Therefore, as the gas temperature increases, the gas reaction rate also increases. Increasing the number of points improves the calculation accuracy while the tradeoff is a more expensive computational cost. However, as the number of points is increased more than 40x64 points, the maximum gas temperature and reaction rate do not significantly change which can imply as grid-independence of the calculation results. Therefore, within a reasonable computational cost and numerical accuracy, the mesh size of 40x64 is selected for all the gas phase calculations.

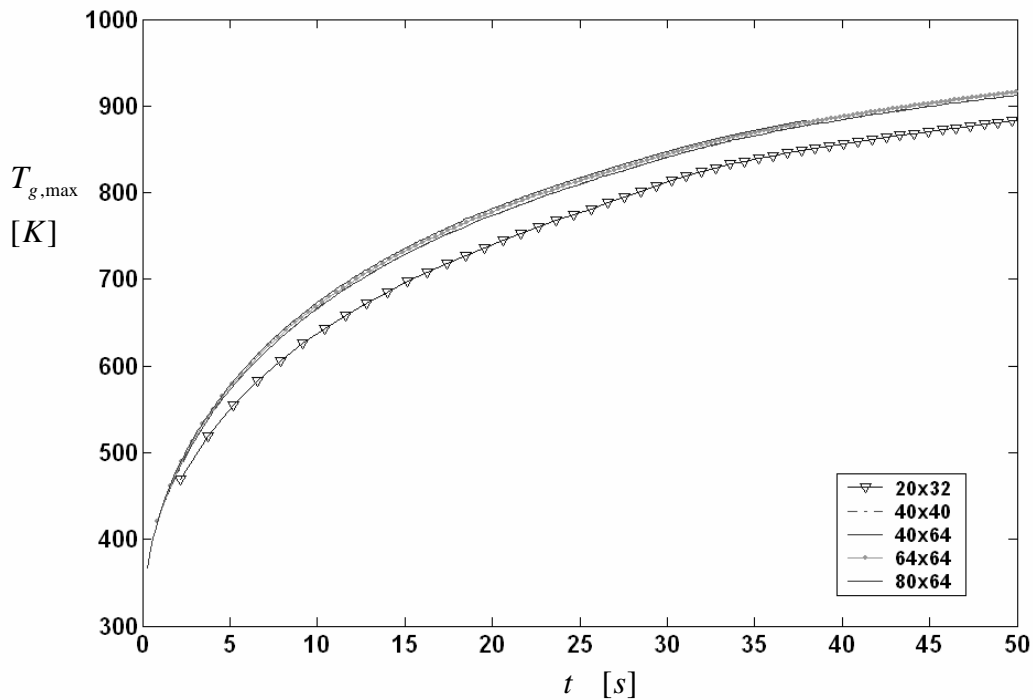


Figure 5.4: Plots of maximum gas temperature history for various mesh sizes

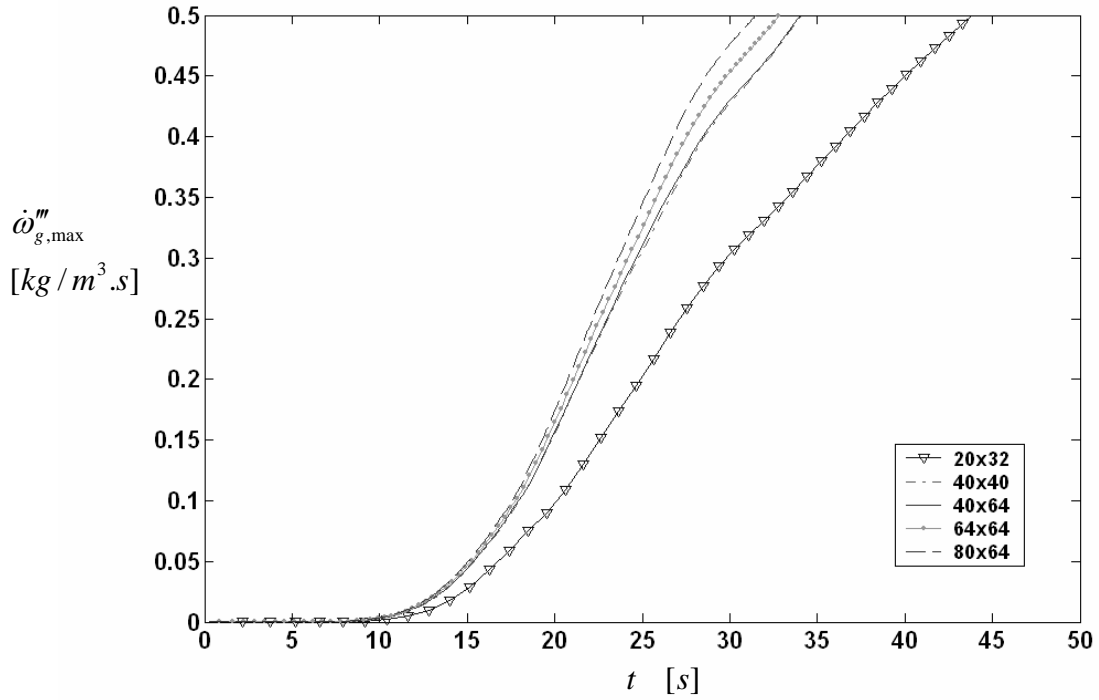


Figure 5.5: Plots of maximum gas reaction rate history for various mesh sizes

5.4 Flaming Autoignition Criteria

In this section, flaming autoignition criteria are discussed. In an experiment, ignition may define as the first light emission for the combustible gas [45, 58]. This criterion is reasonable and consistent with our natural sense. In a theoretical viewpoint, the ignition may be defined as a thermal runaway in the gas phase reaction (Semenov's theory [88]). The thermal runaway is usually defined as a dramatic increase of a physical variable (e.g. solid surface temperature, gas temperature, gas reaction rate), exceeding a predefined critical value. However, a specific physical variable as well as its critical value is

somewhat arbitrary. Therefore, it is necessary to find an appropriate criterion for our calculation of gas phase flaming autoignition of wood.

Many flaming ignition criteria have been proposed based on various physical variables. Generally, the flaming ignition criteria may be categorized into two main groups based on (1) solid phase variables (e.g. solid surface temperature, solid pyrolysis mass flux, etc.) and (2) gas phase variables (e.g. gas temperature, gas reaction rate, etc.).

In the first group where ignition criteria based on the solid phase variables, quoted in Gandhi's work [43], Bamford experimentally studied flaming ignition of wood in 1946, and suggested that flaming ignition is expected when the pyrolysis mass flux reaches a certain value of $2.5 \text{ g/m}^2\cdot\text{s}$. Kanury [89] further commented on Bamford's criterion that before the flaming ignition could achieve, the minimum pyrolysis mass flux of at least 1 to $4 \text{ g/m}^2\cdot\text{s}$ is required. Simms [9] argued that the pyrolysis mass flux at flaming ignition is not constant. It increases with increasing heat flux. He proposed that the appropriate criterion would be determined from a thermal balance of the specimen, which yielded an ignition criterion based on a critical average solid temperature. Ignition occurred when the average solid temperature was approximately $525 \text{ }^\circ\text{C}$. Martin [20], and Alvares and Martin [92] suggested that autoignition occurs when the surface temperature reaches a constant value of $600 - 650 \text{ }^\circ\text{C}$ regardless of radiant heat flux intensity. Other ignition criteria based on solid phase variables, for instant, critical char depth, critical solid surface temperature increasing rate could be found in the reviews by Gandhi [43] and Atreya [4].

Flaming ignition is a gas phase phenomenon involving a thermal runaway condition. Thus, it might not be appropriated to determine the flaming ignition criteria solely from the solid phase variables. Kashiwagi [45] considered a one-dimensional transient gas phase ignition model of a solid fuel and recommended that the ignition criterion should include the effect of the chemical reaction process. He proposed that flaming ignition is accomplished when the total reaction rate in the boundary layer of the combustible gases adjacent to the solid surface exceeds a critical value. Gandhi [43] commented that the gas phase ignition occurs when the gas phase reaction becomes significant and the gas starts to heat the solid surface. Thus the reversal of sign for the gas temperature gradient at the solid-gas interface could be used as the ignition criterion. In a numerical investigation of forced flow piloted ignition of PMMA, Zhou et al.[53] considered that piloted ignition occurred when the maximum gas temperature reached a predefined value. Tsai et al. [55] experimentally and numerically studied autoignition and piloted ignition of PMMA in a cone calorimeter. Their criterion for ignition was considered as a maximum increasing rate of the maximum gas temperature (e.g. $\partial T_{g,\max} / \partial t = 0$). In an extensive review of autoignition (spontaneous ignition) criteria of solid fuel, Nakamura and Takeno [58] commented that the ignition criteria should not depend on ambient oxygen concentration and gravity. They pointed out that one-dimensional ignition criteria [43, 45] are inadequate for a prediction of ignition in multidimensional gas phase calculations. They suggested that the appropriate ignition criterion, which can be used for wide range of ambient oxygen concentrations and gravities is that the maximum gas reaction rate exceeds a critical value of $0.1 \sim 0.3 \text{ kg/m}^3 \cdot \text{s}$.

A summary of the gas phase flaming ignition criteria utilized by various investigators is presented in Table 5.2.

Table 5.2: Summary of the flaming ignition criteria

References	Ignition Criteria	Mathematical Expression	Ignition Mode
Bamford (quoted in Ref. [43])	Critical pyrolysis mass flux	$\dot{m}_{g,s}'' \geq 2.5 \text{ g/m}^2 \cdot \text{s}$	Piloted ignition of wood
Kanury [89]	Critical pyrolysis mass flux	$\dot{m}_{g,s}'' \geq 1 \sim 4 \text{ g/m}^2 \cdot \text{s}$	Autoignition and piloted ignition
Simms [9]	Critical average solid temperature	$\bar{T}_{Solid} = 525 \text{ }^\circ\text{C}$	Autoignition of cellulose fuel
Martin [20], and Alvares et al. [92]	Critical solid surface temperature	$T_s = 600 \sim 650 \text{ }^\circ\text{C}$	Autoignition of cellulose fuel
Sauer (quoted in Ref. [43])	Critical char depth	$\delta_c \geq \delta_c^*$	-
Price (quoted in Ref. [43])	Critical solid surface temperature increasing rate	$\partial T_s / \partial t > (\partial T_s / \partial t)^*$	-
Kashiwagi [45]	Critical total gas reaction rate	$\int \dot{\omega}_g''' dx \geq \left(\int \dot{\omega}_g''' dx \right)^*$	Autoignition of solid fuel
Gandhi [43]	Critical gas temperature gradient reversal at the solid-gas interface	$\left(\partial T_g / \partial x \right)_{Surface} = 0$	Autoignition of cellulose fuel
Zhou et al. [53]	Critical maximum gas temperature	$T_{g,max} \geq T_{g,max}^*$	Piloted ignition of PMMA
Tsai et al. [55]	Critical maximum gas temperature increase rate	$\partial T_{g,max} / \partial t = 0$	Autoignition and piloted ignition of PMMA
Nakamura and Takeno [58]	Critical gas reaction rate	$\dot{\omega}_g''' \geq 0.1 \sim 0.3 \text{ kg/m}^3 \cdot \text{s}$	Autoignition of cellulose fuel

Note: the asterisks indicate the critical value of those critical criteria.

For solid flaming ignition to occur, three steps proceed in sequence [93]. First the solid must be heated. The heat conduction from the solid surface into the solid interior raises its temperature. As the solid temperature increases, the solid starts to decompose generating fuel gases that flow out to the surrounding. The time taken for the solid to start decomposing can be considered as the pyrolysis time (t_{py}). Second, the fuel gases are transported to mix with the air from the surroundings creating a boundary layer of combustible mixtures. If a piloted source is placed in the boundary layer of the combustible gases and the gas concentration is in the flammable limit, flaming piloted ignition occurs. For autoignition, not only must the gas concentration have to be in the flammable region, but the gas temperature must also be sufficiently high to accelerate the gas phase reactions to cause a thermal runaway. The time needed for the fuel gases to transport and mix with the air until the gas mixtures reach a suitable condition for ignition (both concentration and temperature) is considered as the gas mixing time (t_{mix}). Finally, once the ingredients for ignition are complete, the energy release from the gas chemical reactions can cause a gas phase thermal runaway to establish a diffusion flame. The time needed for this final process is the chemical time (t_{chem}).

The flaming ignition time (t_{ig}) is the sum of all the there steps [94]; thus

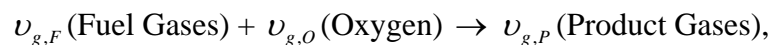
$$t_{ig} = t_{py} + t_{mix} + t_{chem} . \quad (5.25)$$

Typically the chemical time is vary fast and can be neglected [93]. The ignition time reduce to

$$t_{ig} = t_{py} + t_{mix}. \quad (5.26)$$

The pyrolysis time is already considered in the solid phase model (Chapter 4). For piloted ignition, the mixing time is relatively small comparing to the pyrolysis time [93], and thus it can also be neglected. For this reason, it is possible to determine the flaming piloted ignition based on the solid variable criteria. However, for autoignition, not only is the proper gas mixture concentration required but also the gas temperature must be sufficiently high. Therefore, the mixing time for autoignition is longer and cannot be neglected. Flaming autoignition criteria must include the gas phase transport effects hence the ignition criteria should be based on the gas phase variables. The mixing time can be evaluated as the time taken for the fuel gas concentration and temperature reach a certain value that sufficiently provides the gas reaction rate to cause the thermal runaway. Accordingly, it seems reasonable to adopt the flaming ignition criterion based on the maximum gas reaction rate [58] for our gas phase analysis of flaming autoignition.

A detailed kinetic modeling of gas phase reaction might be impossible due to the lack of knowledge for the compositions of the combustible mixtures as well as uncertainties of their kinetics mechanisms. Fortunately, the problem can be alleviated as we consider a simplified global kinetic reaction yet still reproduce experimental data over wide ranges of operating conditions [95]. A global kinetic reaction can be expressed as



where $\nu_{g,F}$, $\nu_{g,O}$, and $\nu_{g,P}$ are the stoichiometric coefficient for fuel, oxygen and product gases.

The gas reaction rate ($\dot{\omega}_g'''$) follows a second-order Arrhenius rate:

$$\dot{\omega}_g''' = A_g \rho_g^2 Y_F Y_O \exp\left(\frac{-E_{a,g}}{RT_g}\right), \quad (5.23)$$

where A_g is the gas pre-exponential factor, $E_{a,g}$ is the gas activation energy, ρ_g is the gas density, Y_F is the fuel mass fraction, Y_O is the oxygen mass fraction, and T_g is the gas temperature.

In present calculation, the gas density, temperature, and fuel and oxygen mass fractions are obtained from the solution of the gas phase transport equations. The gas kinetic constants (A_g , $E_{a,g}$) are the kinetic input parameters. With these ingredients, a scalar field of the gas reaction rate at every time-step can be calculated.

The gas reaction rate strongly depends on the gas kinetic parameters (A_g , $E_{a,g}$) and hence the autoignition time. The kinetic parameters vary in previous studies. These variations are mainly due to investigators seeking to match experimental data or to simply keep the computational cost within reasonable limits. The larger the gas activation energy, the

thinner the flame thickness, and thus the more expensive the computational cost [96]. A summary of the gas phase kinetic parameters utilized by various investigators is presented in Table. 5.3

Table 5.3: Summary of the gas kinetic parameters

References	A_g [m ³ /kg.s]	$E_{a,g}$ [kJ/mol]	Legend in Fig. 5.6	Note
Tsai et al. [55]	1.53x10 ¹³	176	K1	Predict an autoignition and piloted ignition of PMMA in a cone calorimeter
Zhou et al. [53]	1.60x10 ¹⁶	3x10 ⁵	K2	Predict a piloted ignition of PMMA in a boundary layer flow over horizontal flat plate
Dun et al. [97]	3.12x10 ⁷	74	K3	Predict a flame spread over a paper
Frey and T'ien [96]	3.12x10 ⁷ ~ 7.18x10 ⁵	63	K4	Predict a flame spread over a solid cellulose
Di Blasi et al. [98]	3.13x10 ⁷	63	K5	Predict a flame spread over a thick cellulose
Nakamura et al. [58] Nakabe et al. [56]	8.00x10 ⁵	67	K6	Predict an autoignition of a cellulose paper

Note: The gas kinetic parameter K6 is chosen for all the calculations of gas phase flaming autoignition.

To illustrate dependency of the autoignition time on the gas kinetic parameters, the maximum gas reaction rate time history calculated from the six sets of the gas kinetic parameters reported in Table 5.3 is plotted in Fig. 5.6. This depicts the case of the gas

phase simulation of $\dot{q}_i'' = 60 \text{ kW/m}^2$ and $Y_{O,\infty} = 0.233$. Autoignition occurs when the maximum gas reaction rate reaches some critical value. The plot shows that for a certain critical gas maximum reaction rate (e.g. $0.2 \text{ kg/m}^3\cdot\text{s}$), increasing $E_{a,g}$ or decreasing A_g shift $\dot{\omega}_{g,\max}'''$ to the right, and thus increases the autoignition time. As we adopted the critical maximum gas reaction rate of Nakamura [58] for the present flaming autoignition criterion thus $E_{a,g}$ of 67 kJ/mol and A_g of $8.00 \times 10^5 \text{ m}^3/\text{kg}\cdot\text{s}$ are employed in all calculations of the gas reaction rate. The flaming autoignition is achieved when the maximum gas reaction rate reaches a critical value of $0.2 \text{ kg/m}^3\cdot\text{s}$ [58].

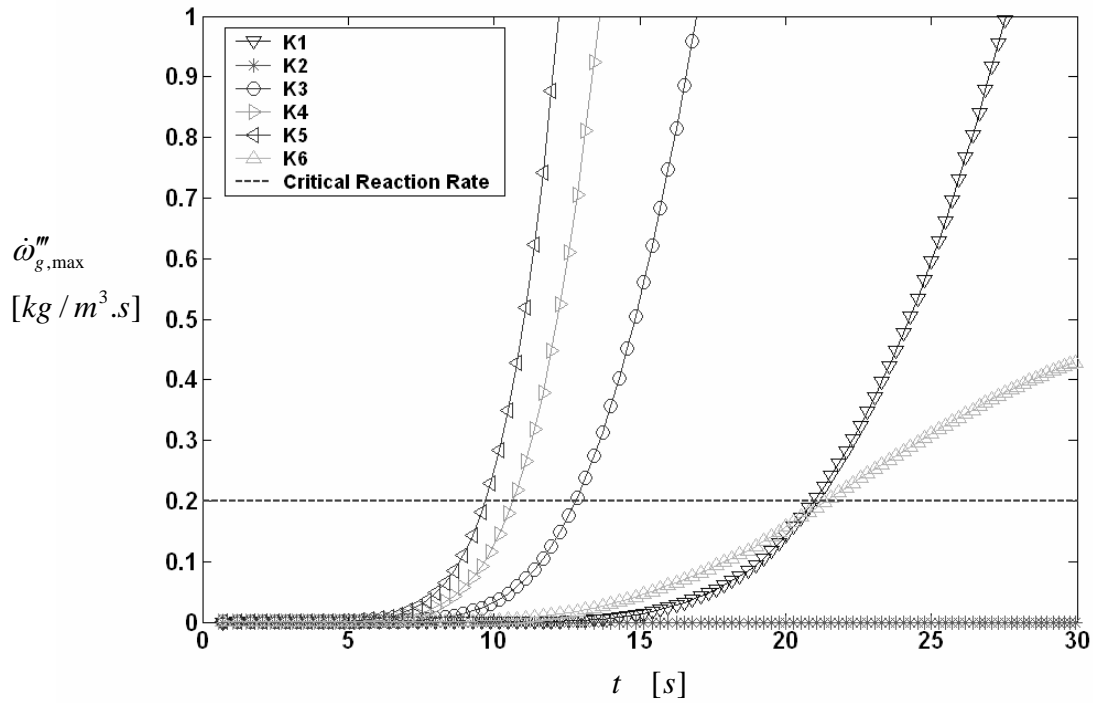


Figure 5.6: Plot of the maximum gas reaction rate ($\dot{\omega}_{g,\max}'''$) history for various sets of the gas kinetic parameters listed Table 5.3 ($\dot{q}_i'' = 60 \text{ kW/m}^2$)

It is interesting to note that the heat release rate is directly related to the gas reaction rate. If the critical maximum gas reaction rate represents the local heat loss rate, the maximum gas reaction rate is greater than the critical value implying the local heat release is greater than the local heat loss [58]. This is essentially the same as the Semenov's ignition theory; the ignition is achieved when the local heat release is greater than the local heat loss. This illustrates that the concept of the Semenov's ignition theory still holds.

5.5 Gas Phase Results and Discussions

Numerical studies of gas phase flaming autoignition were performed. The incident heat flux was varied from 20 kW/m² to 70 kW/m² as a parametric input. In all numerical calculations, the computational domain was the same as that described in Section 5.3.2. An initial ambient oxygen mass fraction ($Y_{O,\infty}$) was 0.233. Comparisons between the numerical results and the experimental data are discussed in this section.

5.5.1 Flaming Autoignition Behavior

Two types of flaming autoignition were observed from the numerical calculations depending on an incident heat flux: (I) at high heat flux ($\dot{q}_i'' > 40$ kW/m²), gas flaming autoignition occurs just an instant after solid glowing ignition, and (II) at low heat flux ($\dot{q}_i'' < 40$ kW/m²), solid glowing ignition leads to gas flaming autoignition after considerably delay.

For type I autoignition, when gas flaming autoignition occurs just an instant after the solid glowing ignition, plots of various quantities are shown in Fig. 5.7 for wood pyrolysis mass flux and surface temperature, insulator surface temperature and gas maximum temperature time histories, Fig. 5.8 for fuel and oxygen mass fraction contours, Fig. 5.9 for gas temperature and gas reaction rate contours, and Fig 5.10 for the gas velocity vector and streamlines at the instant of autoignition. The incident heat flux imposed on this calculation is 50 kW/m^2 .

The average surface quantities (surface temperature, pyrolysis mass flux) over the wood portion is used to evaluate the wood glowing ignition. The glowing ignition criteria are based on a surface energy balance of the wood surface as discussed in Section 4.4. Fig. 5.7 shows that the wood undergoes glowing ignition at about 30 seconds. Then just 2 seconds later, the gas mixture achieves flaming autoignition ($t_{flaming} = 32$ seconds). Due to a very short time interval between wood glowing ignition and gas flaming ignition, the wood glowing ignition does not significantly increase the wood surface temperature; thus the wood surface temperature is still lower than the insulator at the moment of ignition. Consequently, the gas temperature near the insulator surface is hotter than that near the wood surface (see Fig. 5.9a). The fuel gases injected from the wood surface mix the oxygen flow from the surroundings creating a boundary layer of the gas mixture. Then the gas mixture is convected upward (see Fig.5.8). Although the gases near the insulator at the lower portion have a high temperature, insignificant gas reaction rate is observed. This is because the fuel gases cannot propagate upstream due to the buoyancy; the fuel gas concentration upstream remains zero and hence there is no gas reaction rate

(Fig 5.9b). By tracking the maximum gas reaction rate downstream, the onset of flaming autoignition can be determined when the local gas reaction rate exceeded the critical value ($0.2 \text{ kg/m}^3 \cdot \text{s}$). As indicated above, the gas near the insulator surface at the top portion is hotter than that near the wood surface. Therefore, most of the gas reactions are confined near the top insulator flux portion. The local maximum gas reaction rate exceeds the critical value at approximately 32 seconds and thus this time is defined as the flaming autoignition time. At this moment the wood pyrolysis mass flux does significantly affect the u -velocity component as one can see from the streamlines in Fig. 5.10. The autoignition is located approximately at $y = 7.6 \text{ cm}$.

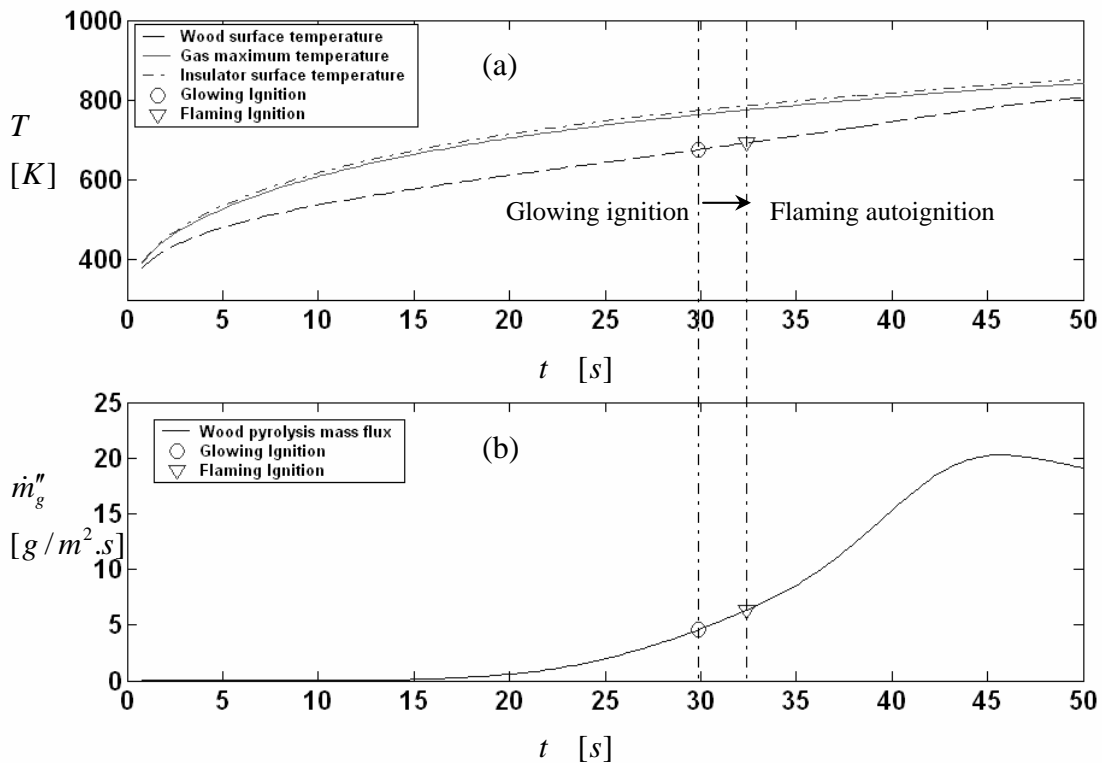


Figure 5.7: (a) Gas maximum temperature, and wood and insulator surface temperature time histories and (b) pyrolysis mass flux time history

(Autoignition type I, $\dot{q}_i'' = 50 \text{ kW/m}^2$, $t_{flaming} = 32 \text{ s}$, $t_{glowing} = 30 \text{ s}$)

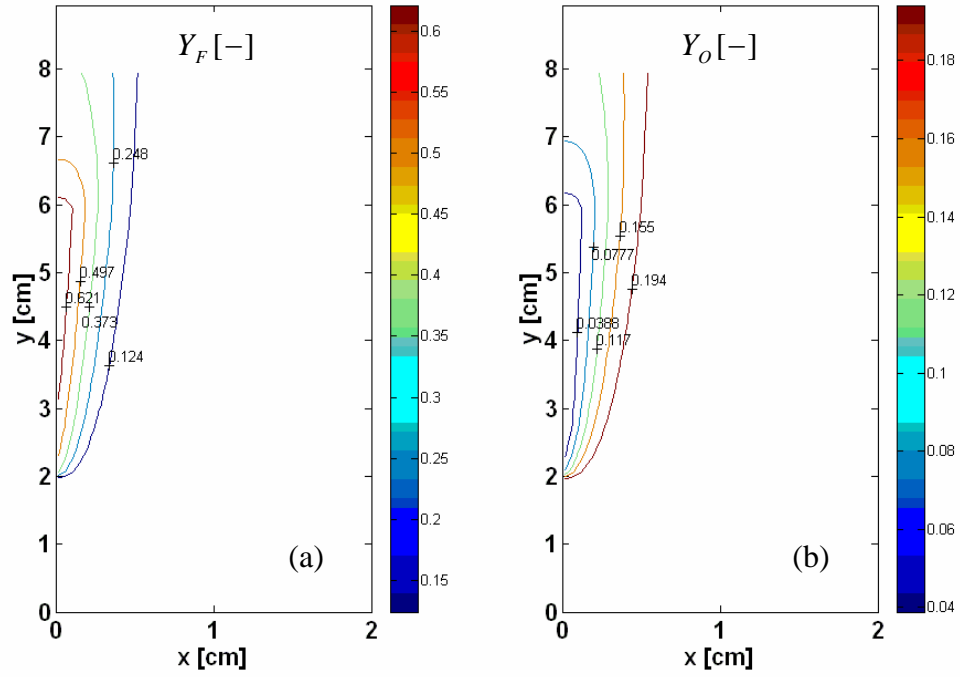


Figure 5.8: Contour plots of (a) fuel and (b) oxygen mass fraction at the instant of

flaming autoignition (Autoignition type I, $\dot{q}_i'' = 50 \text{ kW/m}^2$, $t_{flaming} = 32 \text{ s}$)

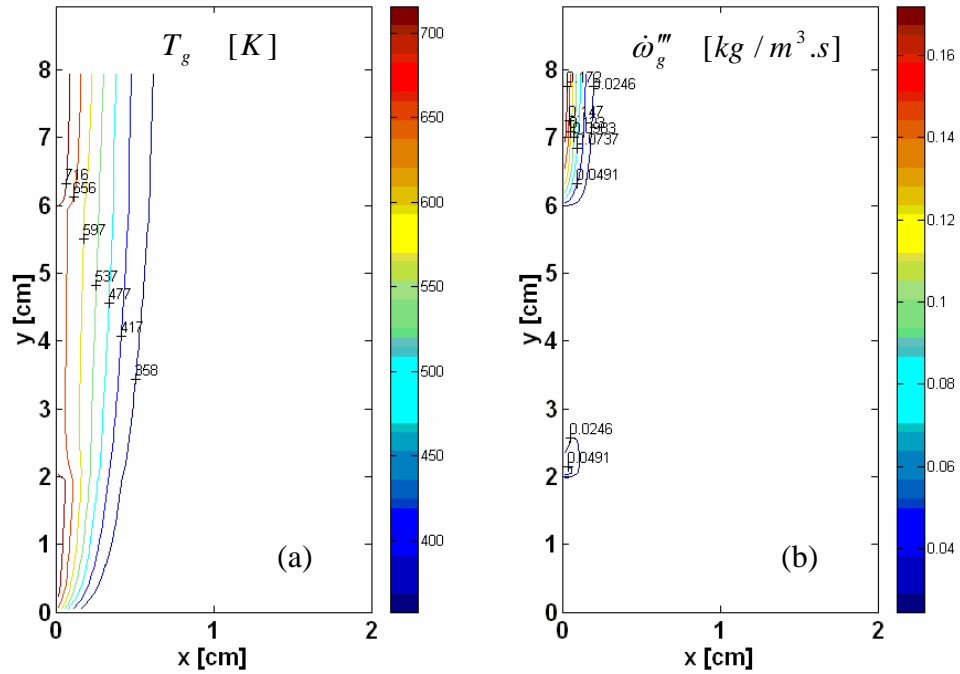


Figure 5.9: Contour plots of (a) gas temperature and (b) gas reaction rate at the instant of

flaming autoignition (Autoignition type I, $\dot{q}_i'' = 50 \text{ kW/m}^2$, $t_{flaming} = 32 \text{ s}$)

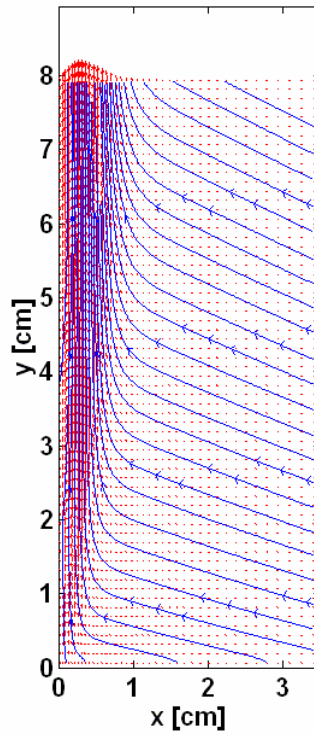


Figure 5.10: Velocity vector field and streamlines at the instant of flaming autoignition

(Autoignition type I, $\dot{q}_i'' = 50 \text{ kW/m}^2$, $t_{flaming} = 32 \text{ s}$)

As the incident heat flux decreases below 40 kW/m^2 , the second type of flaming autoignition is achieved. Depicting the case when the wood surface is heated with $\dot{q}_i'' = 30 \text{ kW/m}^2$, the solid glowing ignition leading to the gas flaming autoignition is demonstrated. Fig. 5.11 shows that, the wood surface achieves glowing ignition at about 86 seconds. The additional energy from the char surface oxidation increases the wood surface temperature to be greater than the insulator surface temperature. At the instant of flaming autoignition, the fuel mass fraction near the wood surface is high, however, the oxygen mass fraction is nearly consumed due to the char surface oxidation (see Fig.

5.12); the mixture concentration here is extremely rich. As a result, the gas reaction rate near the wood surface is relatively low even though the gas temperature is high. As we move away from the wood surface (both horizontally and vertically), the oxygen become more available, and thus the gas reaction rate increases. The high wood surface temperature widens the gas reaction boundary near the wood surface (see Fig 5.13b); therefore the gas reaction boundary at low heat flux is thicker than at high heat flux. The blowing due to the fuel pyrolysis mass flux is considerable. It tends to push the streamlines away from the wood surface (see Fig. 5.14). Flaming autoignition is detected above the wood surface ($y = 7.6$ cm) at approximately 126 seconds.

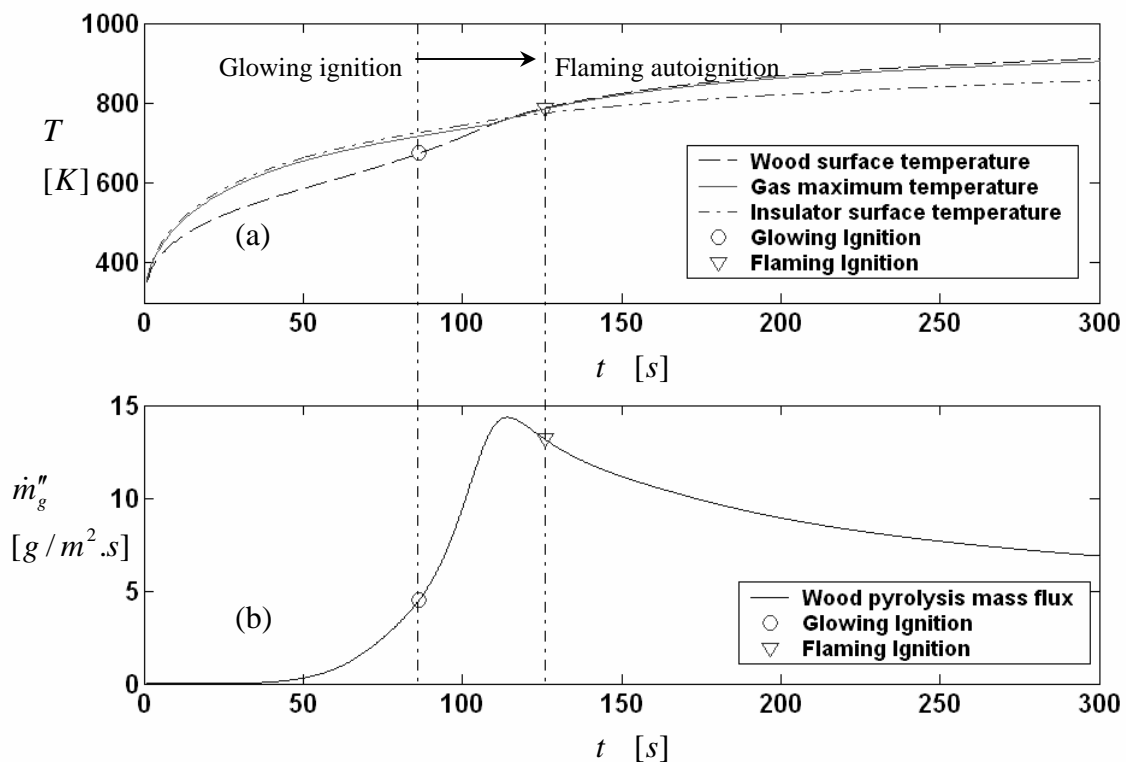


Figure 5.11: (a) Gas maximum temperature, and wood and insulator surface temperature time histories and (b) pyrolysis mass flux time history

(Autoignition type II, $\dot{q}_i'' = 30 \text{ kW/m}^2$, $t_{flaming} = 126 \text{ s}$, $t_{glowing} = 86 \text{ s}$)

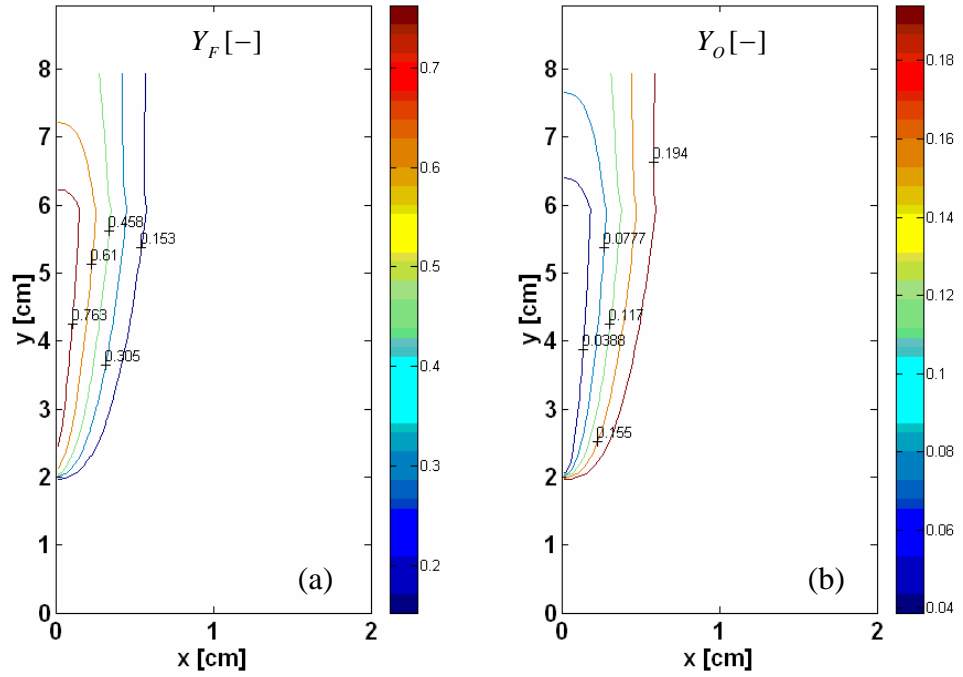


Figure 5.12: Contour plots of (a) fuel and (b) oxygen mass fraction at the instant of flaming autoignition (Autoignition type II, $\dot{q}_i'' = 30 \text{ kW/m}^2$, $t_{flaming} = 126 \text{ s}$)

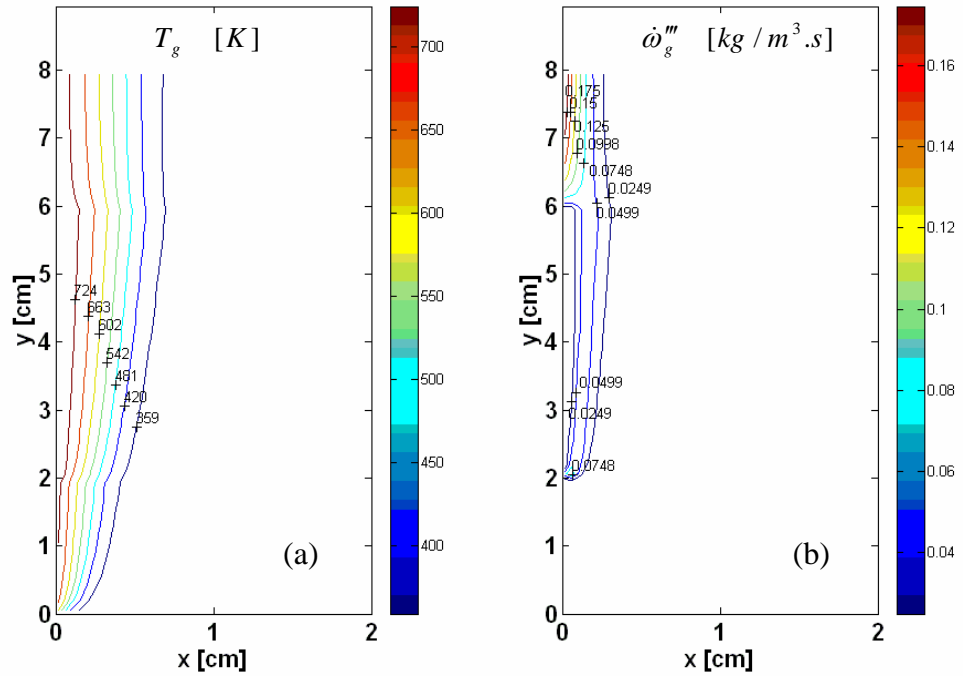


Figure 5.13: Contour plots of (a) gas temperature and (b) gas reaction rate at the instant of flaming autoignition (Autoignition type II, $\dot{q}_i'' = 30 \text{ kW/m}^2$, $t_{flaming} = 126 \text{ s}$)

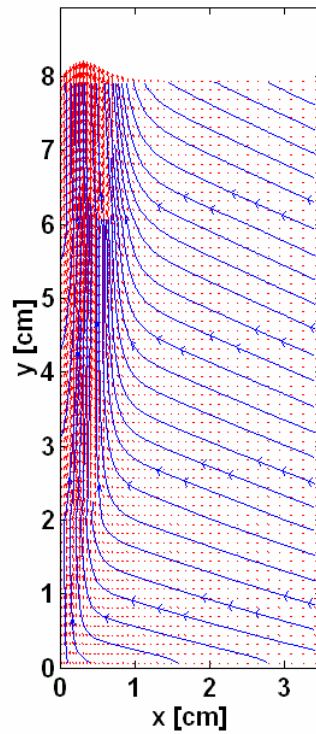


Figure 5.14: Velocity vector field and streamlines at the instant of flaming autoignition

(Autoignition type II, $\dot{q}_i'' = 30 \text{ kW/m}^2$, $t_{flaming} = 126 \text{ s}$)

The numerical model prediction of the autoignition location for type II differs from the experimental observation where the autoignition occurs close to the wood surface. The discrepancy may be due to the following reason. In the experiment, wood surface regression due to char surface oxidation was observed before the flaming autoignition occurred. The surface regression created a cavity between the wood surface and the insulator. Autoignition was typically detected inside or close to this cavity. However, the wood surface regression was neglected in the numerical model since it was too expensive in terms of computational cost. This might be the reason why the autoignition location

predicted from the model is different from the experimental observation. Regardless this discrepancy, the model is able to explain the physical behavior of gas phase autoignition processes, at least qualitatively.

It should be noted that the use of boundary approximation in the gas phase transport equations implies that heat and mass transfer cannot propagate upstream. Thus only downstream variables after the wood portion can be used to calculate the onset of autoignition. This constraint limits the present model to not be able to calculate a more complex flow such as a flow with recirculation region.

5.5.2 Flaming Autoignition: Theoretical and Experimental Results

Fig. 5.15 plots theoretical and experimental times for flaming autoignition and solid glowing ignition as a function of incident heat flux. The theoretical flaming autoignition time was determined based on the critical gas reaction rate as discussed in Section 5.4. At high incident heat flux ($> 40 \text{ kW/m}^2$), autoignition occurs just an instant after solid glowing ignition (autoignition type I). As the incident heat flux decreases ($< 40 \text{ kW/m}^2$), a time interval between solid glowing ignition and flaming autoignition considerably increases (autoignition type II). This is because the external heat flux supplied to the combustible mixtures is inadequate to accelerate the gas reaction; thus the flaming autoignition cannot occur. However, as the solid surface undergoes glowing ignition, it supplies an extra energy to the gas mixture, which can bring the gas temperature to its ignition temperature. This process requires some time interval. This time interval increases as the incident heat flux decreases. It was found experimentally that within 2

hours exposed time flaming autoignition was not observed for heat fluxes lower than 20 kW/m². Thus the critical heat flux for flaming autoignition is considered to be 20 kW/m². No numerical calculation for heat fluxes lower than the flaming autoignition critical heat flux was performed.

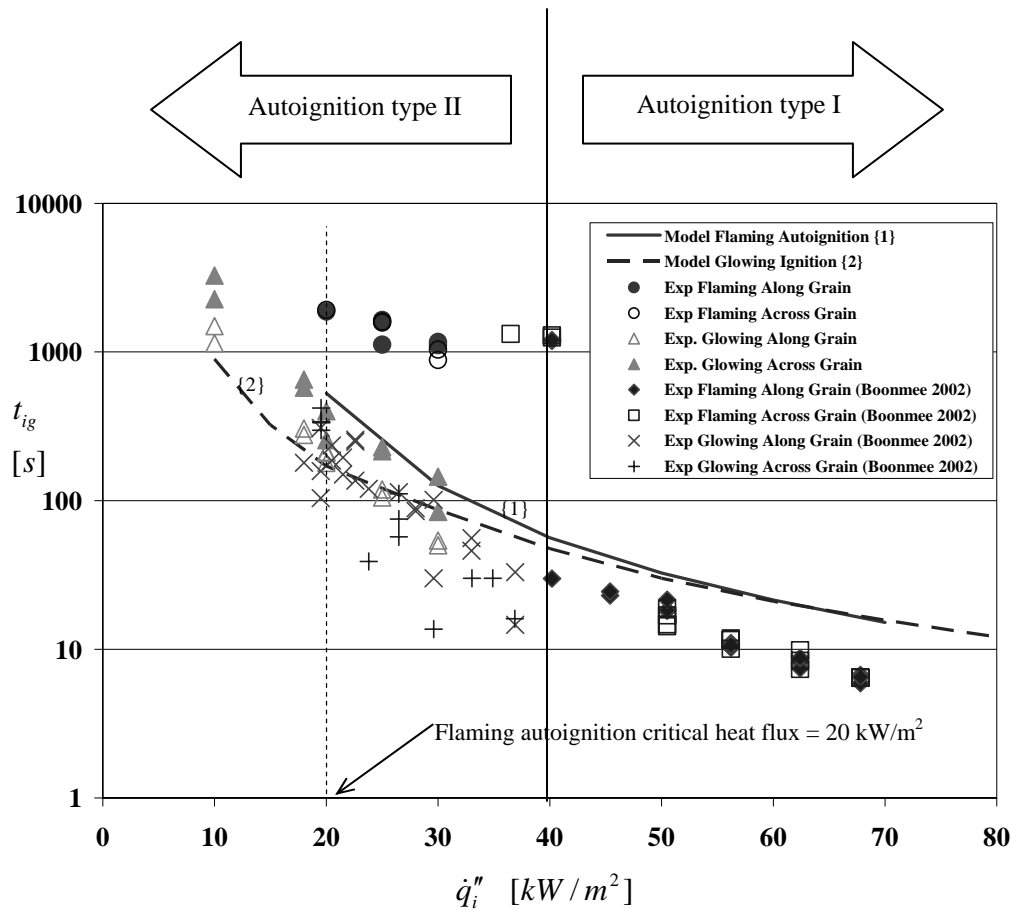


Figure 5.15 Flaming autoignition and glowing ignition times as a function of incident heat flux

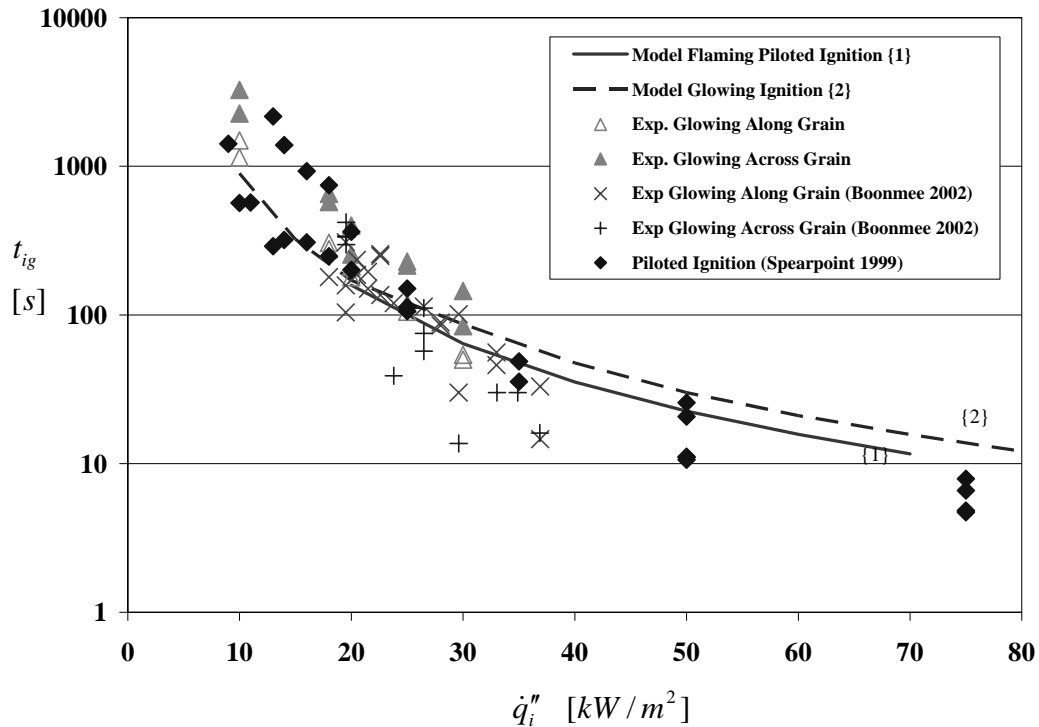


Figure 5.16 Flaming piloted ignition and glowing ignition times as a function of incident heat flux

Fig. 5.16 plots theoretical and experimental piloted ignition time. The experimental data was taken from Spearpoint [23]. For the theoretical values, piloted ignition was considered to occur when the fuel gas concentration (Y_F) at a prescribed igniter located in the gas phase computational domain ($x_{igniter} = 0.25$ cm, $y_{igniter} = 6.36$ cm) reaches a lower flammable limit of the gas mixtures ($Y_{F,LFL}$). The lower flammable limit (LFL) can be estimated from a relation between the adiabatic flame temperature and fuel gas concentration [93] as

$$Y_{F,LFL} = \frac{c_{P,g}(T_{f,ad} - T_g)}{\Delta H_C}, \quad (5.24)$$

where $Y_{F,LFL}$ is the lower flammable limit fuel mass fraction, $T_{f,ad}$ is the adiabatic flame temperature, T_g is the gas temperature, ΔH_C is the heat of combustion, and $c_{P,g}$ is the specific heat capacity .

For most hydrocarbon-based fuel, a typical adiabatic flame temperature is 1300 °C [99]. The specific heat capacity is taken from air as 1.2 kJ/kg.K. The heat of combustion is essentially the heat of combustion of wood, which is 12.4 kJ/g.K for the actual value [100]. At a gas temperature T_g , we can estimate a corresponding $Y_{F,LFL}$ from Eq. (5.24). Thus, the theoretical piloted ignition occurs when Y_F at the igniter is greater than $Y_{F,LFL}$.

It should be noted that to accomplish ignition, two necessary conditions must be simultaneously satisfied [14]: (1) sufficient amount of fuel gas concentration (i.e. within LFL), and (2) the gas temperature must be sufficiently high enough to accelerate the gas reaction. For autoignition, both two conditions are required; however, for piloted ignition, only the first condition must be satisfied since the high gas temperature can be achieved with help of the piloted source. Assuming the numerical piloted source provides sufficient energy to the gas mixture to cause flaming ignition, thus we can consider that the numerical piloted ignition occurs when the fuel gas concentration reaches a critical value ($Y_{F,LFL}$).

At high heat flux, a difference between flaming autoignition and piloted ignition time is relatively small. Moreover a time for solid glowing ignition is close to a time for gas flaming ignition. This observation suggests that the gas flaming ignition process at high heat flux is basically governed by the solid heating process. On the other hand, at low heat flux, the autoignition time deviates from the piloted ignition time implying that the gas reaction plays a role in the flaming ignition process. Gas flaming ignition at low heat flux is strongly reaction-dependent [55]. The gas kinetics plays a significant role; thus the simple global gas reaction model used in present study is not adequate to capture complex gas kinetics phenomena. This may explain why the predicted autoignition time at low heat flux greatly diverges from the experimental values. Nonetheless, the flaming piloted ignition and solid glowing ignition times at low heat flux still follow the same trend as they do at high heat flux (see Fig. 5.16) meaning that flaming piloted ignition is essentially controlled by the solid heating processes irrespective of incident heat flux.

A plot of autoignition temperatures as a function of incident heat flux is illustrated in Fig. 5.17. The experimental and theoretical solid glowing ignition temperatures are also plot to portrait the overall ignition process. It is an obvious trend that the solid surface temperatures at flaming autoignition from both the predictions and experimental data increase with decreasing incident heat flux. This trend is confirmed by the experimental observations of Kashiwagi [14, 15] where the surface ignition temperature for autoignition of red oak increases with decreasing incident heat flux. The reason is that as the incident heat flux decreases, significant char forms before flaming autoignition occurs. The char layer causes a high ignition surface temperature. The calculated flaming

autoignition temperatures of the gas however are fairly constant at about 500 °C. The flaming autoignition temperature for the solid surface is higher than for the gas at low heat flux (autoignition type II) confirming the idea that glowing ignition leads flaming autoignition at low heat flux.

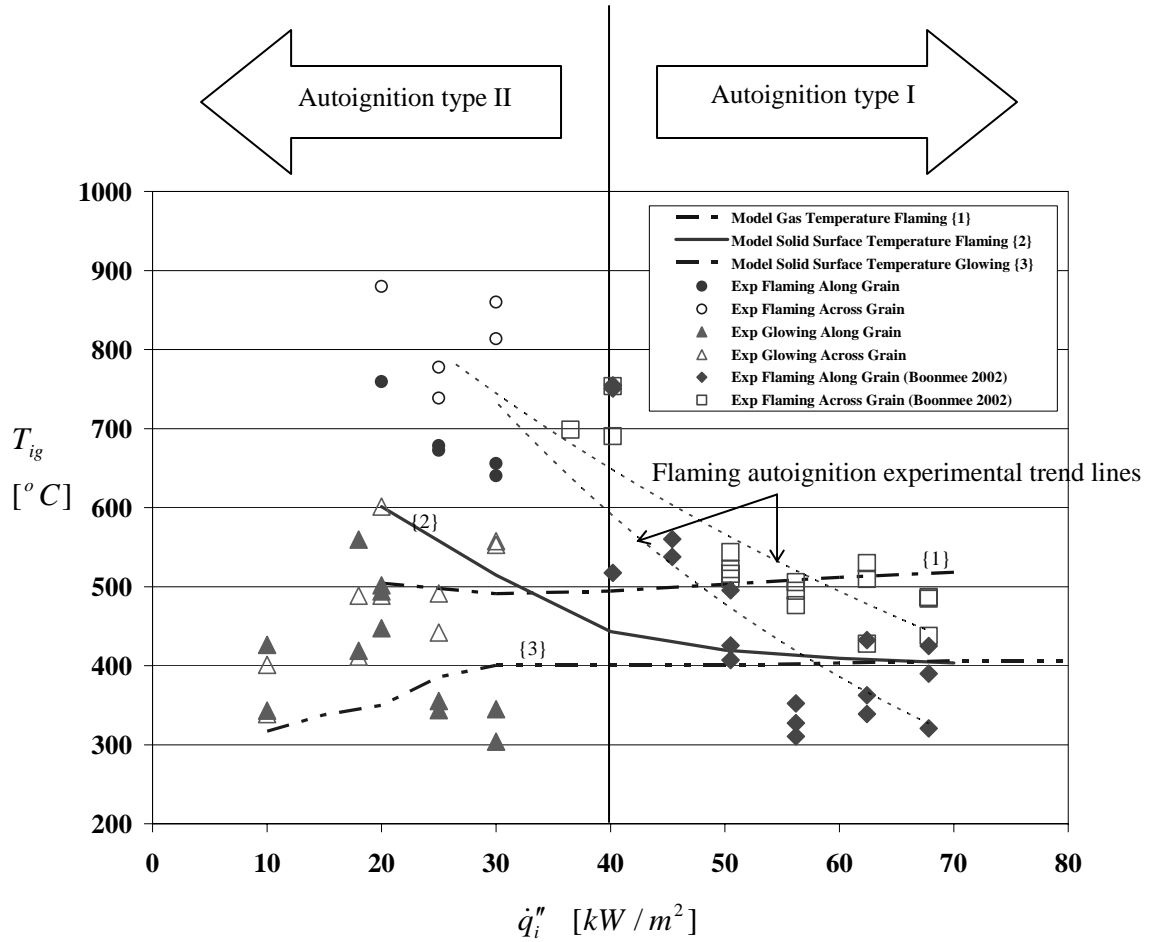


Figure 5.17 Flaming autoignition and glowing ignition temperatures as a function of incident heat flux

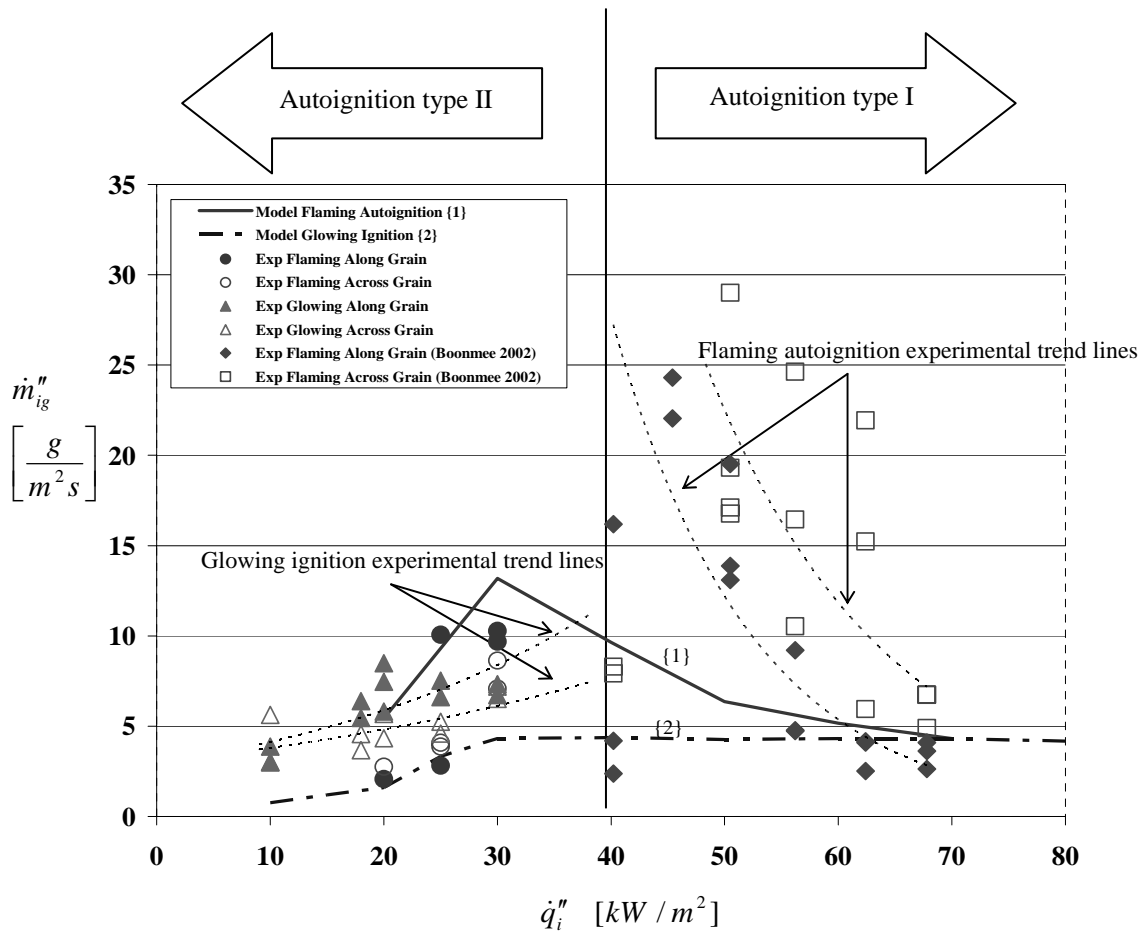


Figure 5.18: Flaming autoignition and glowing ignition mass flux as a function of incident heat flux

Fig. 5.18 illustrates ignition mass flux at glowing and flaming autoignition varying with incident heat flux. In the autoignition type I region, the flaming autoignition mass flux increases with decreasing incident heat flux. This is because before flaming autoignition occurs, insignificant char layer have been formed; therefore, the pyrolysis mass flux increases monotonically with time (i.e. similar to a non-charring material). As the incident flux increases, the flaming autoignition time decreases and hence the flaming ignition mass flux decreases. On the other hand, in the autoignition type II region, the

char surface combustion creates a considerable char layer over the heated surface. The char layer blocks the flow of the volatiles resulting in a decreasing of the pyrolysis mass flux. The amount of char layer increases with decreasing incident heat flux. As a consequence, the flaming ignition mass flux decreases with decreasing incident heat flux. Due to uncertainty in the kinetic models, complete quantitative agreement between the prediction and experiment could not be obtained; however, qualitative agreement is demonstrated. It should be note that at high heat flux, the autoignition is solely controlled by the solid phase; therefore, the predicted mass flux for flaming autoignition approaches the glowing autoignition value.

5.5.3 Flammability Diagram

A flammability diagram illustrating the ignitibility of wood is shown in Fig. 5.19. The diagram plots fuel mass fraction (Y_F) on the ordinate and gas temperature (T_g) on the abscissa. Theoretical results for the fuel mass fraction ($Y_{F,ig}$) and gas temperature ($T_{g,ig}$) at flaming autoignition are plotted on the flammability diagram. $Y_{F,ig}$ ranges from 0.3 to 0.55 which may be considered as the lower and upper limits for flaming autoignition. On the other hand $T_{g,ig}$ is fairly constant. The lowest $T_{g,ig}$ can be considered as the autoignition temperature (AIT); thus here the AIT of wood is about 490 °C. The AIT is fundamentally the temperature at which the combustible mixtures entering the explosion regime [101]. Below the AIT, ignition is not possible unless sufficient external energy is added (e.g. piloted ignition).

Zabetakis [99] reported AIT for various fuel-air systems. For instance, the AIT of paraffin hydrocarbons in air ranges from 537 °C for methane (CH₄) to 205 °C for n-hexadecane (n-C₁₆H₃₄). The AIT decreases as the average carbon chain length increases. In fact, the more highly branched a combustible is, the higher its AIT [99]. Quintiere and McCaffrey [102] reported a chemical composition of wood (sugar pine with 6.5% moisture) as (CH_{1.74})*0.0966H₂O which is relatively closed to a low carbon-atom paraffin hydrocarbon. Thus, it is interesting to point out that the AIT of wood of 490 °C obtained from the numerical prediction is comparable to those of paraffin hydrocarbons.

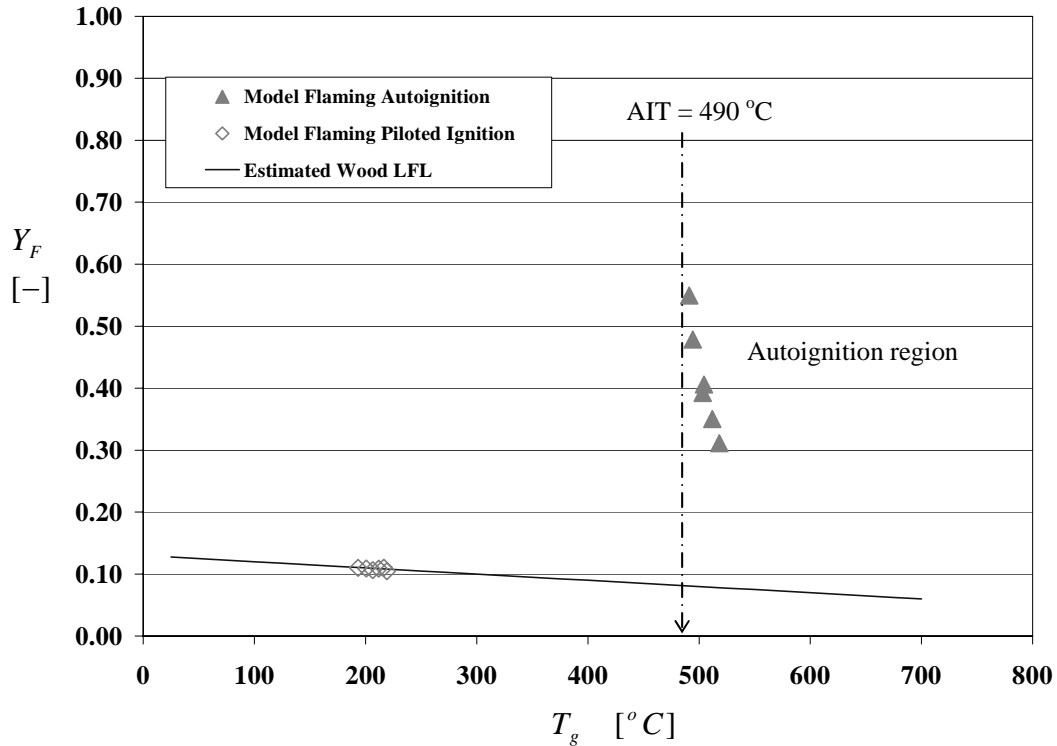


Figure 5.19: Flammability diagram of wood

The lower flammable limit of wood is also drawn on the wood flammability diagram. The fuel mass fraction at LFL ($Y_{F,LFL}$) is calculated from Eq.(5.24). $Y_{F,LFL}$ decreases with

increasing gas temperature. For a certain gas temperature, ignition is not possible if Y_F is less than $Y_{F,LFL}$ corresponding to that gas temperature. The predicted Y_F and ignition gas temperature at piloted ignition are coincided with the estimated wood LFL. This suggests that if a piloted source is placed at the igniter location, ignition can occur.

5.6 Conclusions

A theoretical model for gas phase flaming autoignition has been developed. The gas phase transport equations are considered as a transient two-dimensional laminar boundary layer approximation. The changes of gas density and thermal properties due to a temperature variation are included. The coupled conditions between the gas and solid phase models are made through the solid-gas interface surface. Gas phase flaming autoignition is considered to occur when the local maximum gas reaction rate exceeds a critical value. Depending on incident heat flux, two types of autoignition are distinguished. Autoignition type I occurs when the incident heat flux is high ($> 40 \text{ kW/m}^2$). The gas flaming autoignition occurs just an instant after the solid glowing ignition. On the other hand, when the incident heat flux is low ($< 40 \text{ kW/m}^2$), Autoignition type II where the solid undergoes glowing ignition long before the gas flaming ignition is observed. At high heat flux, the solid heating process controls the overall flaming autoignition process while at low heat flux, the solid glowing ignition as well as the gas kinetic reaction play an important role. Qualitative agreement between the experimental and theoretical values for ignition time, ignition temperature, and ignition mass flux is demonstrated. Based on the calculation values at the gas flaming

autoignition, a flammability diagram of wood can be drawn. The diagram suggests that the autoignition temperature (AIT) of wood is about 490 °C, which is comparable to a typical AIT of paraffin hydrocarbons.

Chapter 6

Conclusions and Future Work

6.1 Conclusions

Experimental and theoretical study of autoignition of wood has been conducted. Conclusions can be drawn as the followings.

The experimental study of autoignition of wood performed in Chapter 2 suggests that as the wood subjected a low incident heat flux, the wood surface experiences significant char surface combustion before the char surface combustion eventually causes the combustible gases adjacent to undergo flaming autoignition. By analyzing the infrared thermocouple data, four regimes of the process of surface glowing ignition leading to gas flaming autoignition are distinguished as (1) transient inert heating stage, (2) steady inert heating stage, (3) transient glowing ignition stage and (4) steady char combustion stage. Within two hours exposed time we obtain that the critical heat flux for flaming autoignition is 20 kW/m^2 and for glowing ignition is 10 kW/m^2 .

A three independent single-step first order parallel reaction model for the wood kinetic decomposition has been introduced in Chapter 3. Each reaction represents a kinetic decomposition of the main three components of wood: hemicellulose, cellulose, and lignin. Extracting from the TGA experimental data, a set of the wood kinetic parameters

of $1.41 \times 10^9 \text{ s}^{-1}$ for the pre-exponential factor and 125, 141, and 165 kJ/mol for the activation energy of hemicellulose, cellulose, and lignin respectively is obtained. With the derived wood kinetic parameters, the calculated kinetic decomposition rate is in good agreement with the experimental data.

In Chapter 4, the physical and chemical processes of wood pyrolysis in the solid phase have been investigated. The char surface oxidation, which is an important mechanism leading glowing to ignition, is included. The criteria for glowing ignition of wood have been developed based on an energy balance at the oxidation surface. The theoretical results show that the char surface oxidation process can be distinguished into two regimes namely (1) kinetic-controlled at the early stage of the pyrolysis process and (2) diffusion-controlled regime at the latter stage. The transition temperature for the char surface oxidation from kinetic-controlled to diffusion-controlled is approximately 400 °C. Good agreement between the theoretical and experimental results at glowing ignition is demonstrated confirming a validation of the proposed glowing ignition criteria. At high heat flux, glowing ignition occurs irrespective of the surrounding oxygen concentration; while at low heat flux, the effect of the surrounding oxygen concentration is prominent. The glowing ignition time decreases with increasing the ambient oxygen concentration.

The gas phase model coupled with the solid phase has been constructed in Chapter 5. The theoretical result shows that autoignition of wood behaves in two fashions depending on the incident heat flux. Autoignition type I occurs when the incident heat flux is high ($> 40 \text{ kW/m}^2$). The gas flaming autoignition occurs just an instant after the solid glowing

ignition. In contrast, when the incident heat flux is low ($< 40 \text{ kW/m}^2$), autoignition type II where the solid undergoes glowing ignition long before the gas flaming ignition is observed. At high heat flux, the solid heating process controls the overall flaming autoignition process while at low heat flux, the solid glowing ignition as well as the gas kinetic reaction play an important role. Qualitative agreement between the experimental and theoretical values for ignition time, ignition temperature, and ignition mass flux has been demonstrated. The flammability diagram for autoignition of wood is drawn based on the numerical calculation. The diagram suggests that the autoignition temperature (AIT) of wood is about $490 \text{ }^\circ\text{C}$, which is comparable to a typical AIT of paraffin hydrocarbons.

6.2 Future Work

This dissertation has improved our understanding of the physical and chemical processes governing the glowing ignition and flaming autoignition of wood. The conclusions are not a stopping point for this research topic but rather serve as a beginning of the questions that have been raised. The theoretical model developed is not perfect. Some considerations for future work are suggested as follows.

As pointed out in Section 5.5, the theoretical model does not predict the flaming autoignition location correctly. This may be due to the fact that the wood surface regression effect is not taken into account in the coupled calculation of the solid and gas phase models. It might be interesting to include this effect. However, the full Navier-

Stokes equations have to be solved rather than the boundary layer approximation model presented in this work.

Another concern should be paid to the gas radiation absorption. As commented by Di Blasi et al. [46], the gas radiation absorption plays a role in radiative ignition of solid fuels. In the present theoretical model, the gas radiation absorption is neglected; thus the mechanism that can lead to gas flaming autoignition is only the heat conduction. If the gas radiation absorption is included, it will provide more complete mechanisms that can lead the gas to flaming autoignition.

Although the one-dimensional solid phase model seems to be sufficient to explain the glowing ignition process of wood, it might be interesting to extend the present solid phase model to account for multidimensional effects because in a real fire a heat flux to the wood surface may not be uniform, as imposed in the experiment.

Porous effects within the decomposed wood may be one of interest for future considerations. Effects of heat and mass transfer of the volatiles within the solid matrix can be included by considering the Darcy's law for the flow of volatiles. However, permeability parameters for the Darcy flow are required.

It has been commented by many investigators that a single-step global gas kinetic reaction is inadequate to capture flaming ignition at low heat flux and thus a more detailed gas kinetic reaction should be used. In addition, the flaming ignition criteria that

have been utilized are strongly dependant on the gas kinetics. However, it is still impossible to couple a detailed gas kinetic reaction with a multidimensional gas transport model because first it is too expensive to compute numerically and second even though we can afford the computational cost, the compositions of the gas mixtures generated from the decomposing wood are still poorly known. Therefore these questions need future examination to answer them.

“Life is complex. It has real and imaginary parts...”

Appendix A

Solid Phase Numerical Methods

A-1: Solid Phase Model

The implicit Crank-Nicolson finite difference scheme is employed to integrate the system of non-dimensional governing equations (Eq. (4.20-4.22)) together with the boundary conditions (Eq. (4.23-4.24)). A uniform one-dimensional collocated finite difference grids including ghost points (shaded points) [91] is depicted to discretize the slab of wood as shown in Fig. A1.

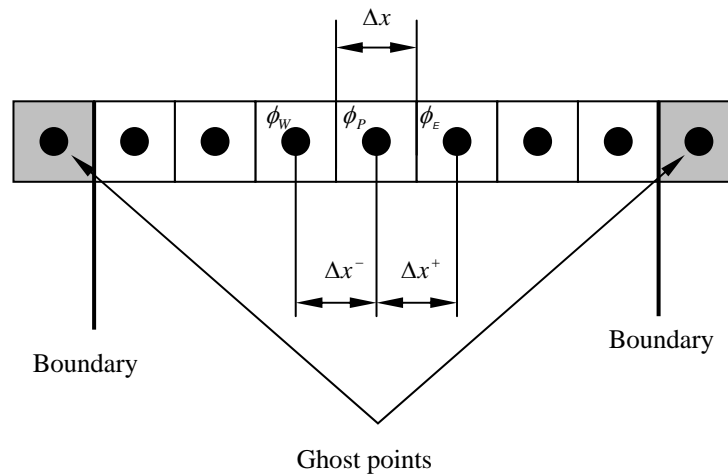


Figure A1: Schematics of the finite grid

First and second spatial derivatives of all variables at point P are approximated by a second order central finite difference. A temporal derivative is approximated by a first

order forward finite difference. The expressions for spatial and temporal finite differences at point P are

$$\left. \frac{\partial \phi}{\partial x} \right|_P \approx \left. \frac{\delta \phi}{\delta x} \right|_P = \frac{\phi_E - \phi_P}{2\Delta x}, \quad (\text{A1})$$

$$\left. \frac{\partial^2 \phi}{\partial x^2} \right|_P \approx \left. \frac{\delta^2 \phi}{\delta x^2} \right|_P = \frac{1}{\Delta x} \left(\frac{\phi_E - \phi_P}{\Delta x^+} - \frac{\phi_P - \phi_W}{\Delta x^-} \right), \quad (\text{A2})$$

$$\left. \frac{\partial \phi}{\partial t} \right|_P \approx \left. \frac{\delta \phi}{\delta t} \right|_P = \frac{\phi_P^{n+1} - \phi_P^n}{\Delta t}, \quad (\text{A3})$$

where the operators $\delta(\)/\delta x$, $\delta^2(\)/\delta x^2$, and $\delta(\)/\delta t$ indicate finite difference operators at point P.

The governing equations can be discretized as

Kinetic Decomposition:

$$\left(\frac{\delta \hat{\rho}_j}{\delta \hat{t}} \right)_i = \left(\frac{\hat{\rho}_j^{n+1} - \hat{\rho}_j^n}{\Delta \hat{t}} \right)_i = -\hat{a}_{P,j} (\hat{\rho}_i^{n+\frac{1}{2}} - \hat{\rho}_f) \exp(-T_{e,j}/\hat{T}_i^{n+\frac{1}{2}}), \quad (\text{A4})$$

and the total decomposition rate is

$$\left(\frac{\delta \hat{\rho}}{\delta \hat{t}} \right)_i = \sum_{j=1}^3 X_j \left(\frac{\delta \hat{\rho}_j}{\delta \hat{t}} \right)_i, \quad (\text{A5})$$

where the subscript j refers to the j^{th} component of wood ($j = 1, \text{cellulose}; j = 2, \text{hemicellulose}; j = 3, \text{lignin}$).

Mass Conservation:

$$\left(\hat{m}_g^n\right)_i^{n+1} = -\sum_i^{np \times} \left(\frac{\delta \hat{\rho}}{\delta \hat{t}}\right)_i \Delta x_i, \quad (\text{A6})$$

Energy Conservation:

$$\begin{aligned} \frac{\hat{T}_i^{n+1} - \hat{T}_i^n}{\Delta \hat{t}} = & \frac{1}{2} \left[\left(\left(\frac{1}{\hat{\rho} \hat{c}_{ps}} \right) \left(\frac{\delta}{\delta \hat{x}} \left(\hat{k} \frac{\delta \hat{T}}{\delta \hat{x}} \right) \right) \right)_i^{n+1} + \left(\left(\frac{1}{\hat{\rho} \hat{c}_{ps}} \right) \left(\frac{\delta}{\delta \hat{x}} \left(\hat{k} \frac{\delta \hat{T}}{\delta \hat{x}} \right) \right) \right)_i^n \right] + \\ & + \left(\hat{m}^n\right)_i^{n+1} \left(\frac{\delta \hat{h}_g}{\delta \hat{x}}\right)_i^{n+\frac{1}{2}} + \left(\hat{Q}_p - \frac{1}{1-X_c} \hat{h}_a + \frac{X_c}{1-X_c} \hat{h}_c + \hat{h}_g\right)_i^{n+\frac{1}{2}} \left(\frac{\delta \hat{\rho}}{\delta \hat{t}}\right)_i \end{aligned} \quad (\text{A7})$$

The subscript i indicates position i . The superscripts $n+1$ indicate a value evaluated at $n+1$ time-step, n indicate a value evaluated at n time-step, and $n+1/2$ indicate an average value between $n+1$ and n time-step.

At the boundary, an average value between a first point in the domain and a ghost is assigned to the Derichlet condition e.g.

$$\frac{\phi_1 + \phi_{ghost}}{2} = \phi_{boundary}, \quad (\text{A8})$$

where ϕ_1 is the value of the first point in the domain, ϕ_{ghost} is the value of the ghost point, and $\phi_{boundary}$ is the value at the boundary.

For the Normann condition, a difference between a first point in the domain and a ghost point is employed such that

$$\frac{\phi_{ghost} - \phi_1}{\Delta x} = \left. \frac{\partial \phi}{\partial x} \right|_{boundary}, \quad (\text{A9})$$

where $(\partial \phi / \partial x)_{boundary}$ is the assigned gradient at the boundary.

The nonlinear radiative term on the energy boundary condition is linearized by lagging coefficient by on time-step [103] as the following manner:

$$\left(\hat{T}_S^{n+1}\right)^4 = \left(\hat{T}_S^n + \delta \hat{T}_S^{n-1}\right)^4, \quad (\text{A10})$$

where $\delta \hat{T}_S^{n-1} = \hat{T}_S^n - \hat{T}_S^{n-1}$.

The initial conditions are

$$\text{at } \hat{t} = 0, \quad \hat{T} = 1, \hat{m}'' = 0, \hat{\rho} = 1. \quad (\text{A11})$$

Since the system is nonlinear, an iterative method is used to calculate the unknown variables $(\hat{m}'', \hat{\rho}, \hat{T})$ as the following procedure: First, from the initial conditions, assuming $\hat{T}_i^{n+1} = \hat{T}_i^n$ and estimating ρ_i^{n+1} from Eq. (A4) and (A5), and $(\hat{m}_g'')_i^{n+1}$ from Eq. (A6). Substitute the new values of ρ_i^{n+1} and $(\hat{m}_g'')_i^{n+1}$ into Eq. (A7) to obtain \hat{T}_i^{n+1} . The iteration is repeated until a relative change of \hat{T}^{n+1} is less than a tolerance (typically 10^{-4} or 10^{-6}).

A-2: Moving Boundary Algorithm

Due to char surface oxidation, the wood sample surface regresses. A moving grid system is introduced after Crank and Gupta [87] to account for the surface regression. A systematic diagram for the moving grid is illustrated in Fig. A2.

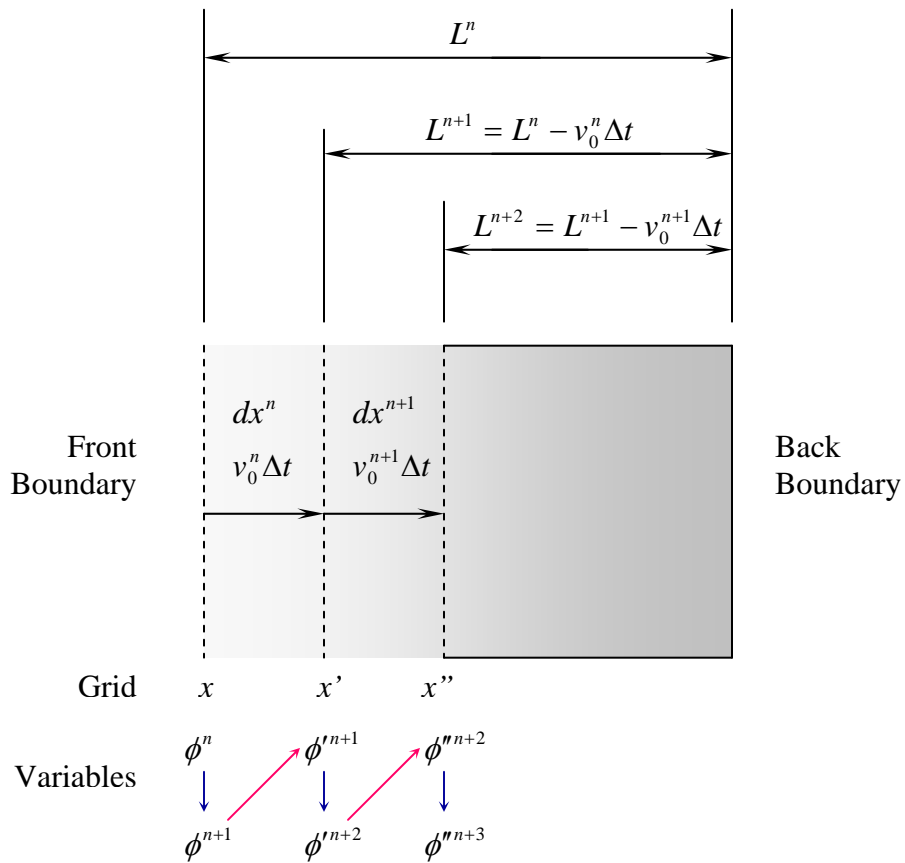


Figure A2: Systematic diagram for moving boundary algorithm

To advance the solid solution from time-step n to $n+1$, the following procedure is performed. Starting at time-step n , all the solid variables ϕ^n (mass flux, \dot{m}_g^n ; solid

density, ρ ; solid temperature, T) storing in grid system x are calculated according to the solid phase governing equations to obtain the solid variables at time-step $n+1, \phi^{n+1}$. Then the surface regression velocity at time-step n (v_0^n) is calculated as

$$v_0^n = \frac{\dot{m}_C^{n,n}}{\rho_s^n}, \quad (\text{A10})$$

where $\dot{m}_C^{n,n}$ is the overall char oxidation mass flux at time-step n , and ρ_s^n is the surface solid density at time-step n . A regression length at time-step n (Δx^n) is estimated as following

$$\Delta x^n = v_0^n \Delta t, \quad (\text{A11})$$

where Δt is denoted for the time-step size. The wood thickness for the time-step $n+1$ is updated as

$$L^{n+1} = L^n - v_0^n \Delta t. \quad (\text{A12})$$

The grid system x' is now regenerated. The grid system x' is calculated based on the updated wood thickness L^{n+1} .

The solid variables at time-step $n+1$ storing in the grid system x (ϕ^{n+1}) are transferred to the grid system x' (ϕ'^{n+1}) by a second order Taylor expansion as

$$\phi'^{n+1} = \phi^{n+1} + \left(\frac{\delta \phi^{n+1}}{\delta x} \right) \Delta x^n + \left(\frac{\delta^2 \phi^{n+1}}{\delta x^2} \right) \frac{(\Delta x^n)^2}{2!}. \quad (\text{A13})$$

The operators $\delta() / \delta x$, $\delta^2() / \delta x^2$ are based on the grid system x .

Now the solid variables at time-step $n+1$ are stored in the grid system x' . The procedure is repeated to advance from time-step $n+1$ to time-step $n+2$ and so on.

Appendix B

Gas Phase Numerical Method

The non-dimensional gas phase transport equations can be arranged in the forms:

Continuity:

$$\frac{\partial \hat{\rho}_g}{\partial \hat{t}} + \frac{\partial \hat{\rho}_g \hat{u}}{\partial \hat{x}} + \frac{\partial \hat{\rho}_g \hat{v}}{\partial \hat{y}} = 0 \quad (\text{B1})$$

Conservation of y-momentum, energy, and species:

$$\frac{\partial \phi}{\partial \hat{t}} = - \left(\hat{u} \frac{\partial \phi}{\partial \hat{x}} + \hat{v} \frac{\partial \phi}{\partial \hat{y}} \right) + \frac{\Gamma}{\hat{\rho}_g} \frac{\partial}{\partial \hat{x}} \left(\Pi \frac{\partial \phi}{\partial \hat{x}} \right) + S, \quad (\text{B2})$$

where the ϕ variables in Eq. (B2) are defined in Table B1.

Table B1: Definition of variables in Eq. (B2)

Equation	ϕ	Γ	Π	S
y-momentum	\hat{v}_g	Pr	$\hat{\mu}_g$	$Gr\theta$
Energy	θ	1	$\frac{\hat{k}_g}{\hat{c}_{p,g}}$	0
Species	Y_i	Le	$\hat{\rho}_g \hat{D}_g$	0

A collocated finite difference grid system including ghost points is used to discretize the gas phase computational domain. A grid arrangement is the same as shown in Fig. A1. All variables are evaluated at the cell center. A uniform grid is used in the y-direction (streamwise) while a non-uniform grid with grid confinement near the wall is used in the x-direction (cross-stream).

The continuity equation is discretized followed Tannehill et al. [104].

$$\begin{aligned} & \frac{(\hat{\rho}_g)_{i,j+1}^{n+1} - (\hat{\rho}_g)_{i,j+1}^n}{\Delta t} + \frac{(\hat{\rho}_g \hat{u})_{i,j+1}^{n+1} - (\hat{\rho}_g \hat{u})_{i-1,j+1}^{n+1}}{\Delta x^-} + \\ & \frac{(\hat{\rho}_g \hat{v})_{i,j+1}^{n+1} - (\hat{\rho}_g \hat{v})_{i,j}^{n+1} + (\hat{\rho}_g \hat{v})_{i-1,j+1}^{n+1} - (\hat{\rho}_g \hat{v})_{i-1,j}^{n+1}}{2\Delta y^+} = 0 \end{aligned} \quad (\text{B3})$$

An upwind finite difference is employed to discretize the convective term of Eq. (B1) as

$$\hat{u} \frac{\partial \phi}{\partial \hat{x}} + \hat{v} \frac{\partial \phi}{\partial \hat{y}} = \hat{u}_{i,j} \frac{\phi_{i,j} - \phi_{i-1,j}}{\Delta x^-} + \hat{v}_{i,j} \frac{\phi_{i,j} - \phi_{i,j-1}}{\Delta y^-}, \quad (\text{B4})$$

where here the coefficients $\hat{u}_{i,j}$ and $\hat{v}_{i,j}$ are regarded as positive. A forward finite difference shall be used when the coefficients are negative.

A second-order central difference is used to discretize the diffusion term of Eq. (B1) as

$$\frac{\Gamma}{\hat{\rho}_g} \frac{\partial}{\partial \hat{x}} \left(\Pi \frac{\partial \phi}{\partial \hat{x}} \right) = \frac{\Gamma}{(\hat{\rho}_g)_{i,j}} \frac{1}{\Delta x} \left[\left(\frac{\Pi_{i+1,j} + \Pi_{i,j}}{2} \right) \left(\frac{\phi_{i+1,j} - \phi_{i,j}}{\Delta x^+} \right) - \left(\frac{\Pi_{i,j} + \Pi_{i-1,j}}{2} \right) \left(\frac{\phi_{i,j} - \phi_{i-1,j}}{\Delta x^-} \right) \right]. \quad (\text{B5})$$

An average value between a first point in the domain and a ghost point is assigned for the Dirichlet boundary condition. For the Normann boundary condition, a difference between a first point in the domain and a ghost point is employed. Discretized forms of the boundary condition equations are the same as those shown in Eqs. (A8-A9).

The discretized gas phase transport equations are advanced in time via a second-order Runge-Kutta. The second-order Runge-Kutta [91] is expressed as

$$\phi_{i,j}^* = \phi_{i,j}^n + \frac{\Delta t}{2} f(\Delta t, \phi_{i,j}^n) \quad (\text{B6a})$$

$$\phi_{i,j}^{n+1} = \phi_{i,j}^n + \frac{\Delta t}{2} f(\Delta t, \phi_{i,j}^*) \quad (\text{B6b})$$

where the f function is the RHS of Eq. (B1).

The numerical calculation is conditional stable due to the explicit time-advance scheme. The time-step is constrained by the CFL (Courant-Friedrichs-Lewy) and Fo (Fourier) conditions. To control the numerical stability, the minimum time-step between the time-steps determined from these two conditions is used for the calculation.

The time-step constrained by the CFL condition is written as

$$\Delta t_{CFL} = \frac{CFL}{\max\left(\frac{\hat{u}}{\Delta \hat{x}}, \frac{\hat{v}}{\Delta \hat{y}}\right)}, \quad (B7)$$

where CFL is the CFL number (typically 0.2-0.3).

The time-step determined by the Fo condition is expressed as

$$\Delta t_{Fo} = \frac{Fo}{Pr} \min(\Delta \hat{x}^2, \Delta \hat{y}^2), \quad (B8)$$

where Fo is the Fourier number (typically 0.2-0.3), and Pr is the Prandtl number.

Then the time-step is the minimum value between the CFL and Fo time-steps:

$$\Delta t = \min(\Delta t_{CFL}, \Delta t_{Fo}). \quad (B9)$$

The gas phase computational procedure can be summarized as follows:

1. From the initial and boundary conditions, the temperature field is calculated.
2. Based on the new temperature field, the gas density is calculated from the equation of state and the gas thermal properties are updated.

3. With the new temperature and gas density, the y-momentum is solved for the v velocity component.
4. The u velocity component is then computed from the continuity equation.
5. With the new temperature and velocity field, the species concentrations are updated.
6. The time-step is calculated to satisfy the stability condition (Eq. (B9)).
7. The calculations are proceeded to the next time step. Continuing in this manner, the velocities, temperature, and species with in the boundary layer are obtained as a function of time until a desired physical time is reached.

Appendix C

Summary of Experimental Data

Table C1: Summary of Experimental Data; Heating Along the Grain

\dot{q}_i''	Test ID (Figure)	$t_{glowing}$	$T_{glowing}$	\dot{m}_g'' (glowing)	$t_{flaming}$	$T_{flaming}$	\dot{m}_g'' (flaming)
[kW/m ²]		[s]	[°C]	[g/m ² .s]	[s]	[°C]	[g/m ² .s]
30	30-4-AL (Fig. C1)	50	304	7.32	1165	640	9.68
30	30-5-AL (Fig. C2)	54	345	6.72	1110	656	10.28
25	25-10-AL (Fig. C3)	119	355	7.53	1120	673	10.06
25	25-10-AL (Fig. C4)	105	344	6.61	1639	678	2.82
20	20-14-AL (Fig. C5)	210	494	5.82	NI	-	-
20	20-15-AL (Fig. C6)	213	448	7.46	1869	759	2.07
20	20-16-AL (Fig. C7)	179	502	8.49	NI	-	-
18	18-18-AL (Fig. C8)	306	560	6.39	NI	-	-
18	18-20-AL (Fig. C9)	277	419	5.46	NI	-	-
10	10-22-AL (Fig. C10)	1145	343	3.00	NI	-	-
10	10-31-AL (Fig. C11)	1493	426	3.87	NI	-	-
9	9-25-AL (Fig. C12)	NG	-	-	-	-	-

Note: NG = Not glowing within 2 hours, NI = Not flaming autoignition within 2 hours

Table C2: Summary of Experimental Data; Heating Across the Grain

\dot{q}_i''	Test ID (Figure)	$t_{glowing}$	$T_{glowing}$	\dot{m}_g'' (glowing)	$t_{flaming}$	$T_{flaming}$	\dot{m}_g'' (flaming)
[kW/m ²]		[s]	[°C]	[g/m ² .s]	[s]	[°C]	[g/m ² .s]
30	30-7-AC (Fig. C13)	84	553	7.19	882	860	8.63
30	30-9-AC (Fig. C14)	145	558	6.51	1035	814	7.08
25	25-12-AC (Fig. C15)	229	442	5.25	1600	739	3.58
25	25-13-AC (Fig. C16)	215	491	4.58	1605	778	3.87
20	20-17-AC (Fig. C17)	255	489	4.33	NI	-	-
20	20-23-AC (Fig. C18)	399	601	5.68	1919	880	2.75
18	18-19-AC (Fig. C19)	576	489	4.56	NI	-	-
18	18-24-AC (Fig. C20)	653	412	3.67	NI	-	-
10	10-26-AC (Fig. C21)	3267	401	5.62	NI	-	-
10	10-29-AC (Fig. C22)	2264	339	3.02	NI	-	-
9	9-34-AC (Fig. C23)	NG	-	-	-	-	-

Note: NG = Not glowing within 2 hours, NI = Not flaming autoignition within 2 hours

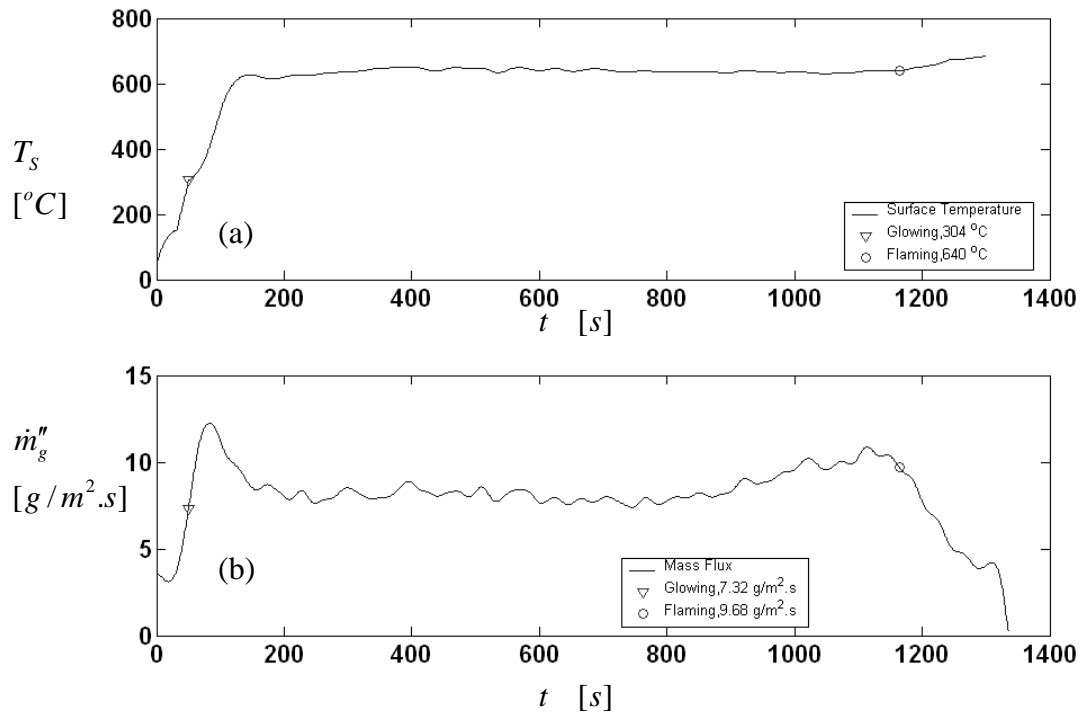


Figure C1: (a) surface temperature and (b) mass flux time histories (Test ID: 30-4-AL)

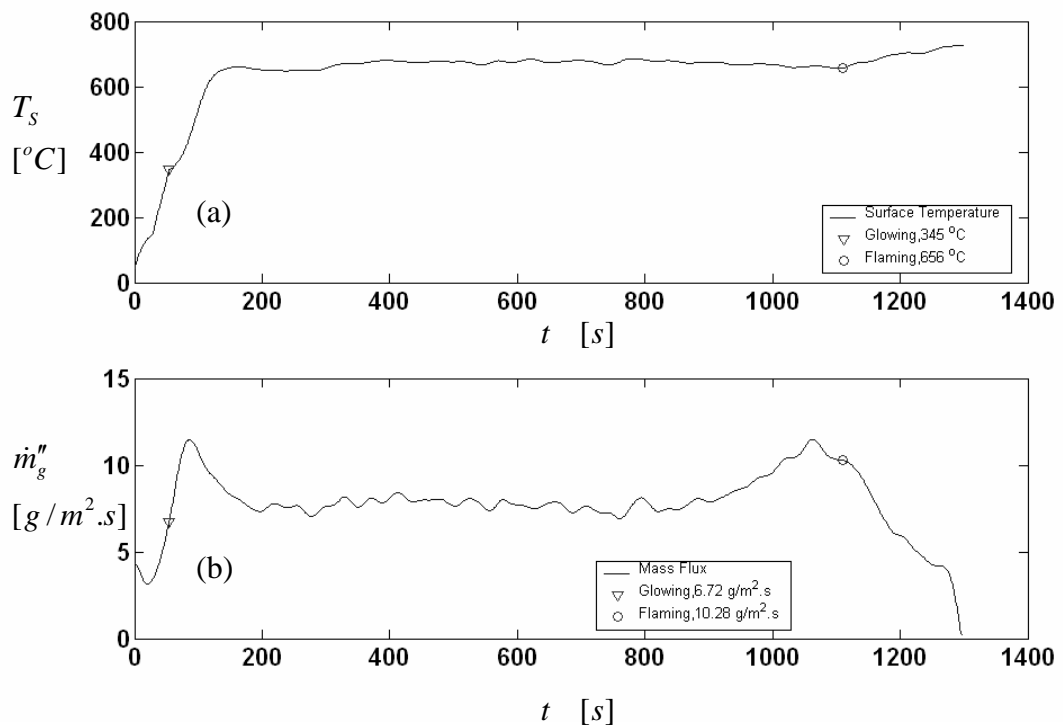


Figure C2: (a) surface temperature and (b) mass flux time histories (Test ID: 30-5-AL)

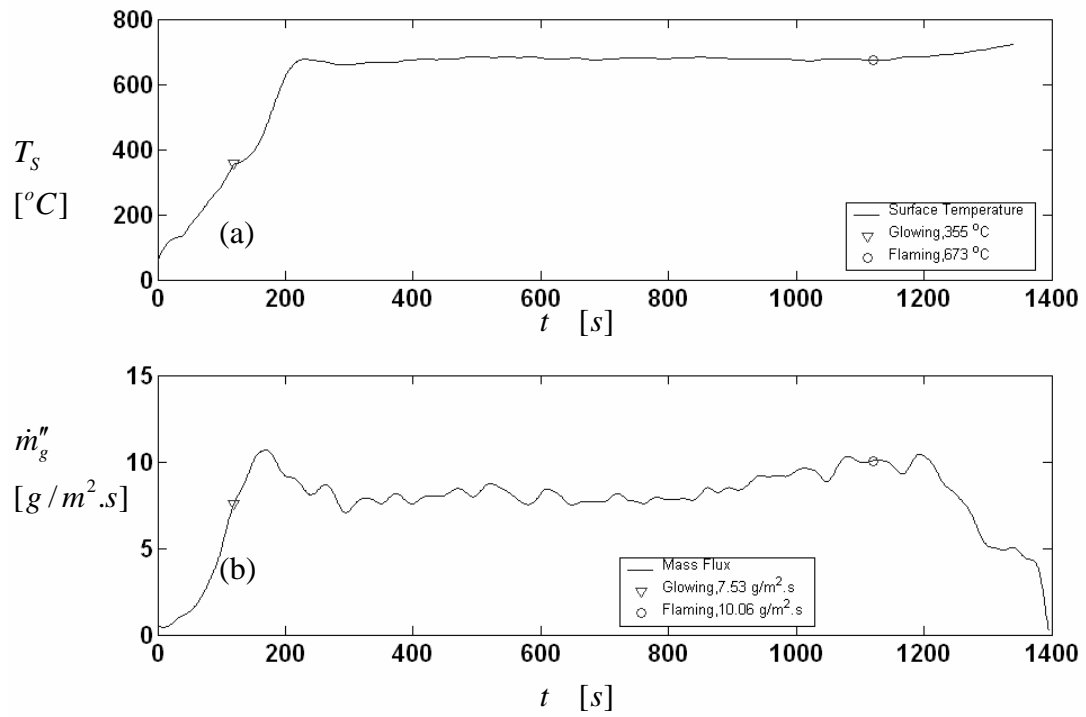


Figure C3: (a) surface temperature and (b) mass flux time histories (Test ID: 25-10-AL)

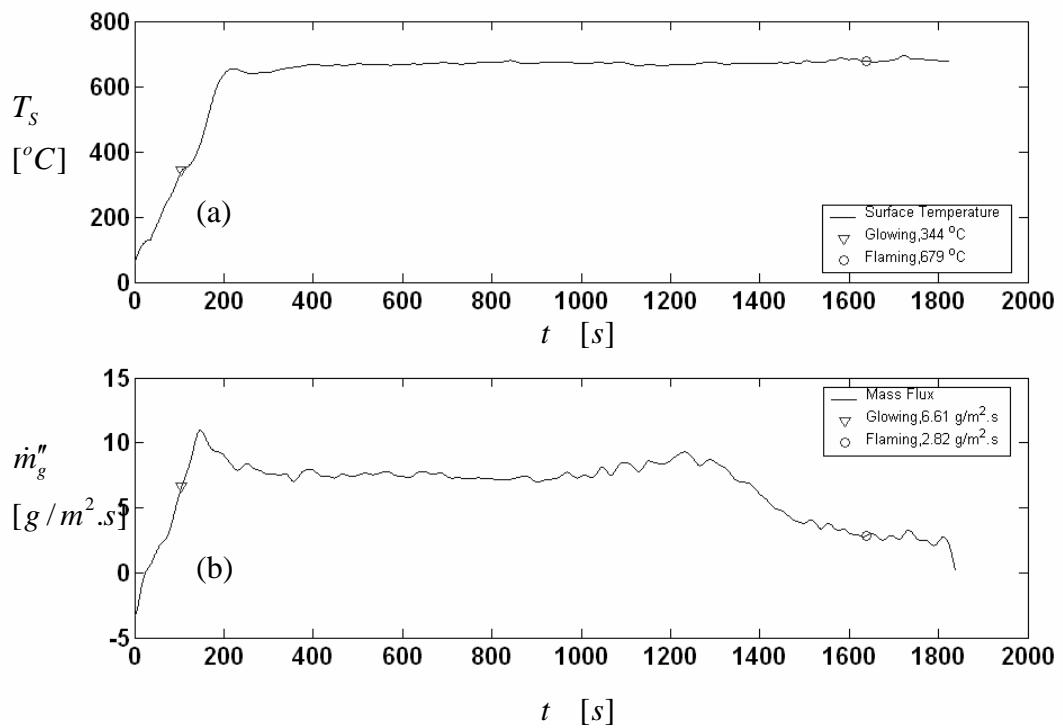


Figure C4: (a) surface temperature and (b) mass flux time histories (Test ID: 25-11-AL)

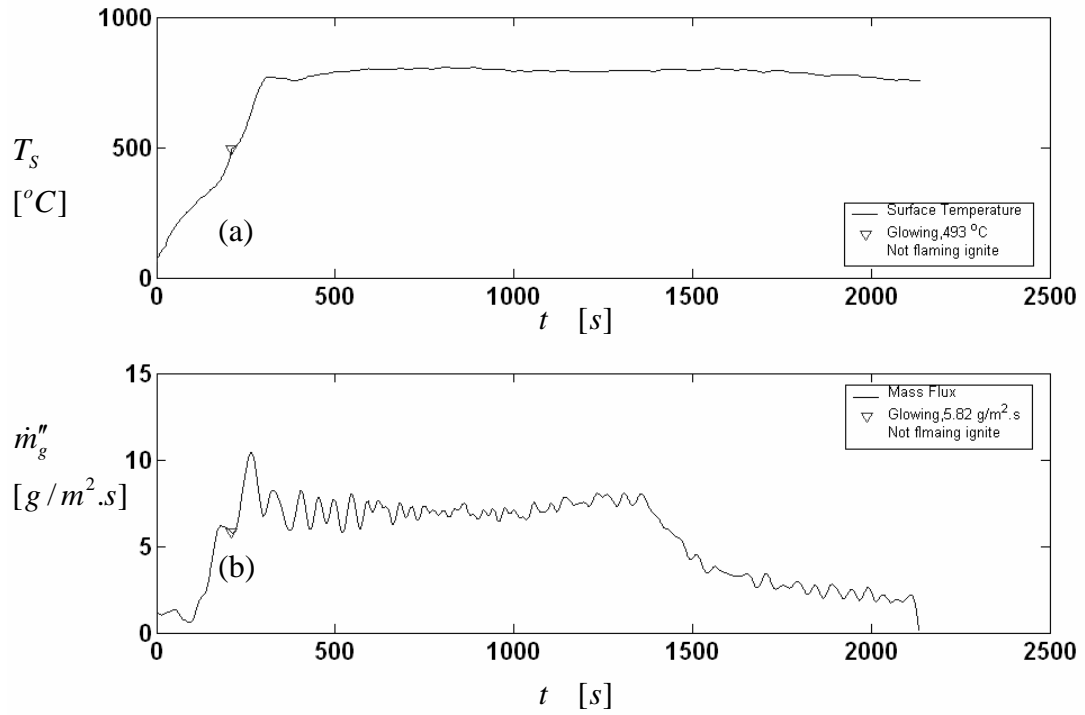


Figure C5: (a) surface temperature and (b) mass flux time histories (Test ID: 20-14-AL)

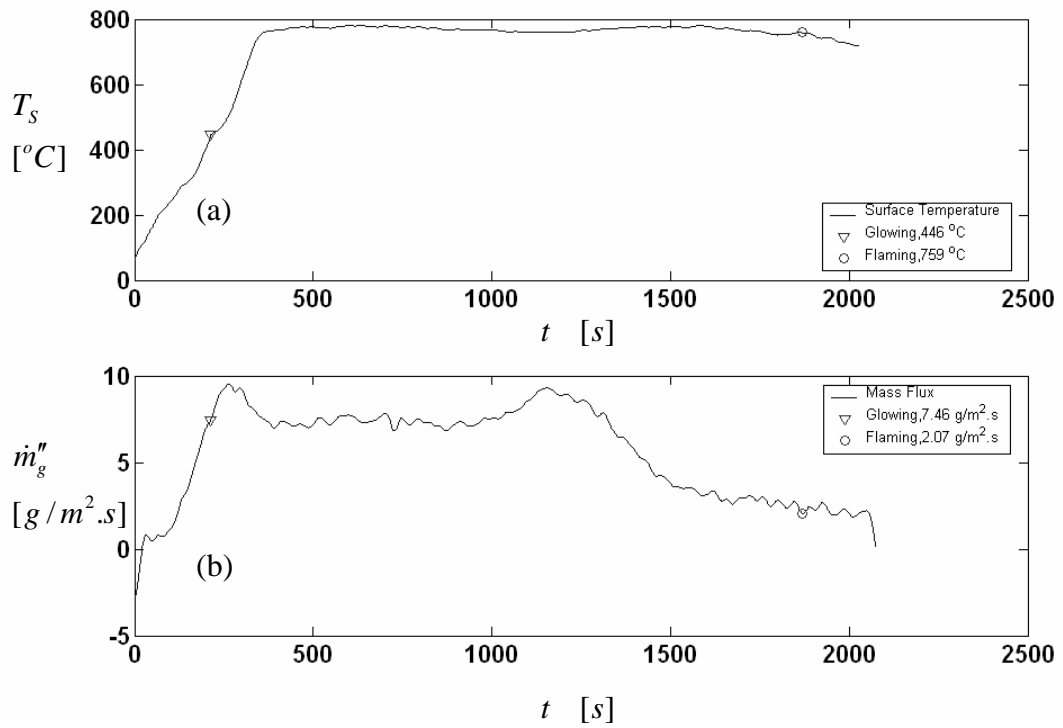


Figure C6: (a) surface temperature and (b) mass flux time histories (Test ID: 20-15-AL)

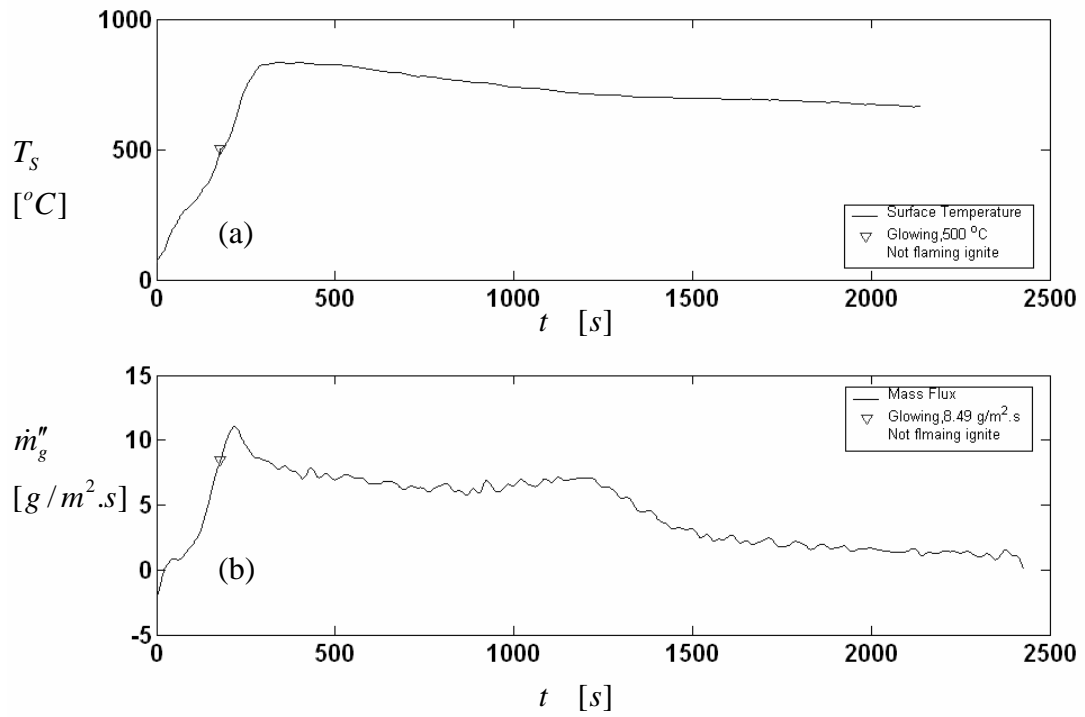


Figure C7: (a) surface temperature and (b) mass flux time histories (Test ID: 20-16-AL)

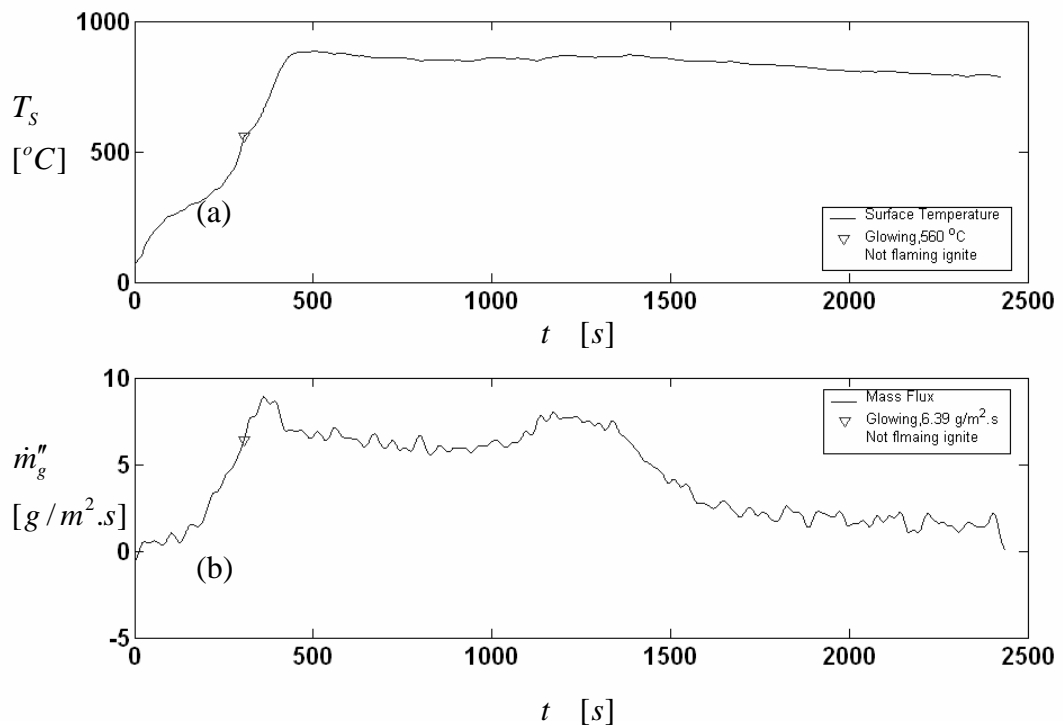


Figure C8: (a) surface temperature and (b) mass flux time histories (Test ID: 18-18-AL)

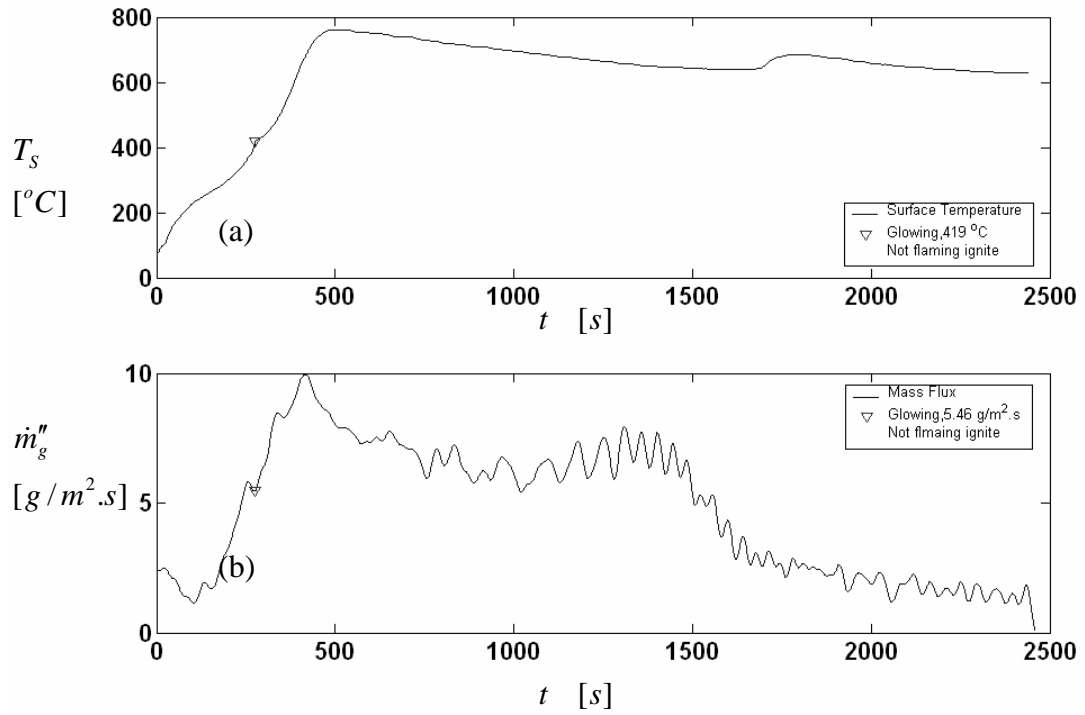


Figure C9: (a) surface temperature and (b) mass flux time histories (Test ID: 18-20-AL)

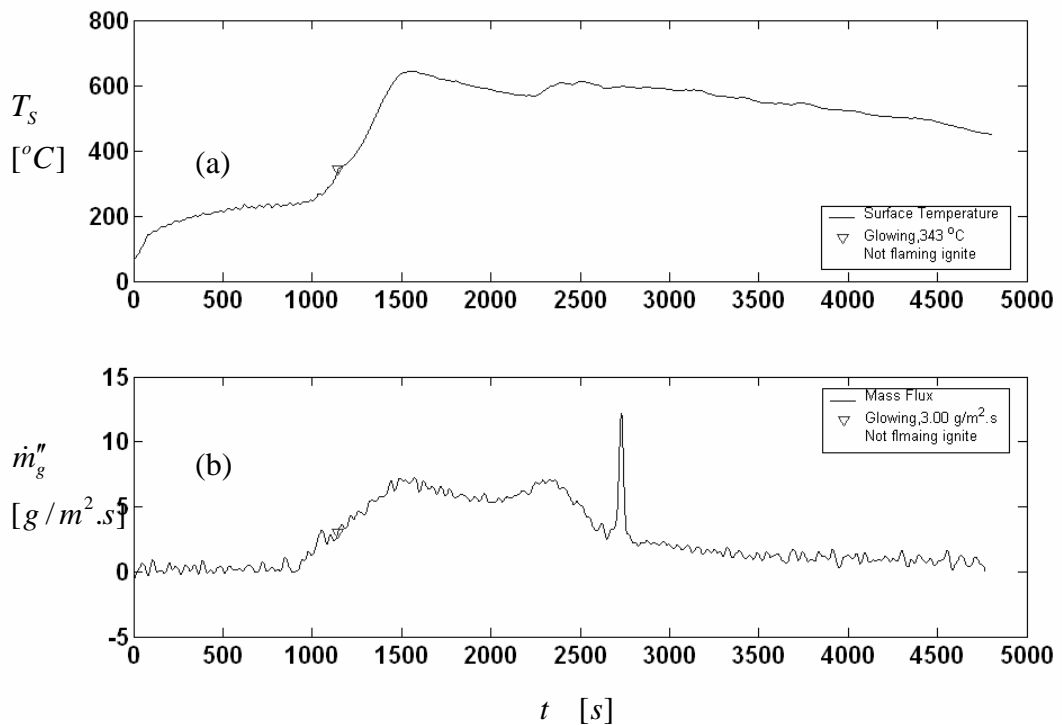


Figure C10: (a) surface temperature and (b) mass flux time histories (Test ID: 10-22-AL),

Note: a spike peak on the mass flux plot was a noise from the load cell signal.

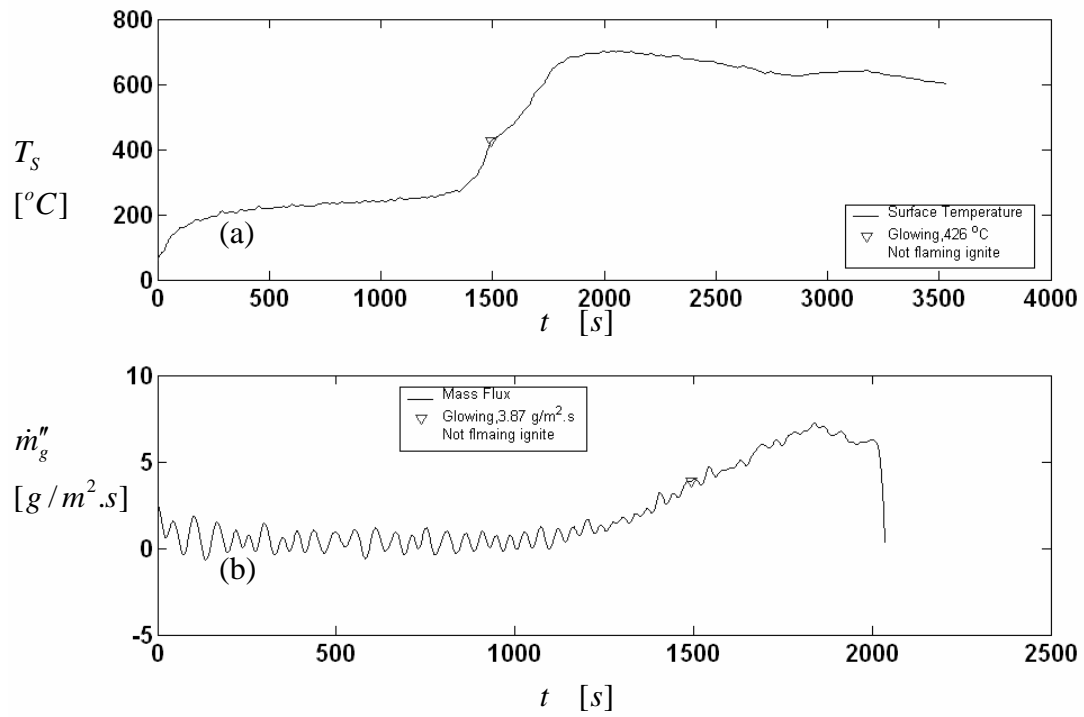


Figure C11: (a) surface temperature and (b) mass flux time histories (Test ID: 10-31-AL)

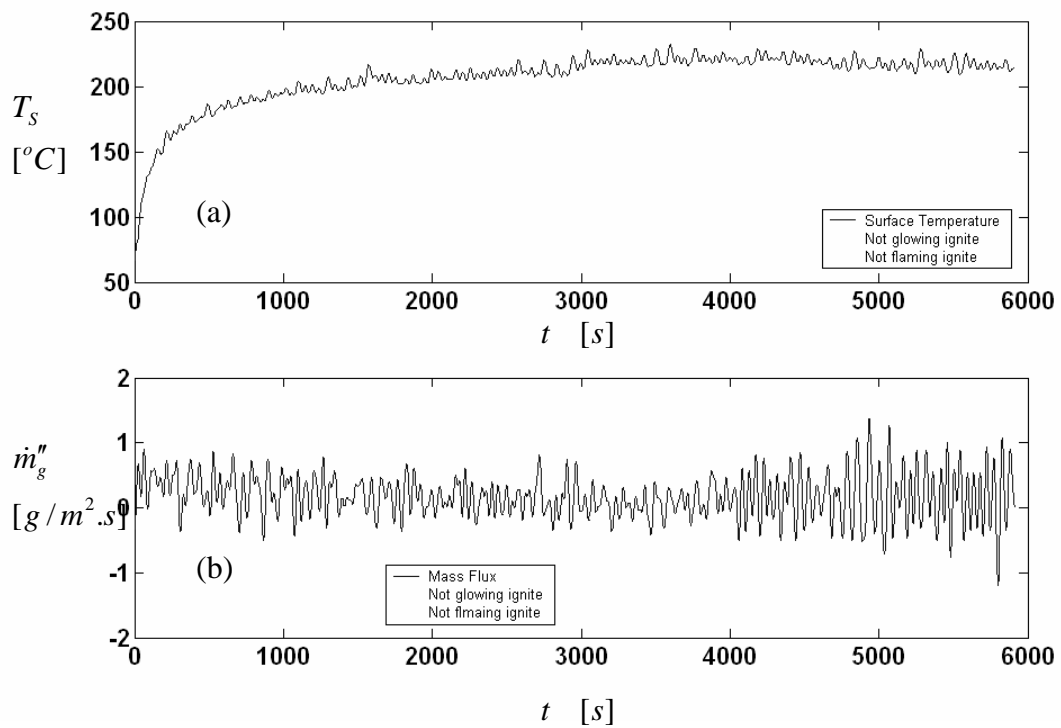


Figure C12: (a) surface temperature and (b) mass flux time histories (Test ID: 9-25-AL)

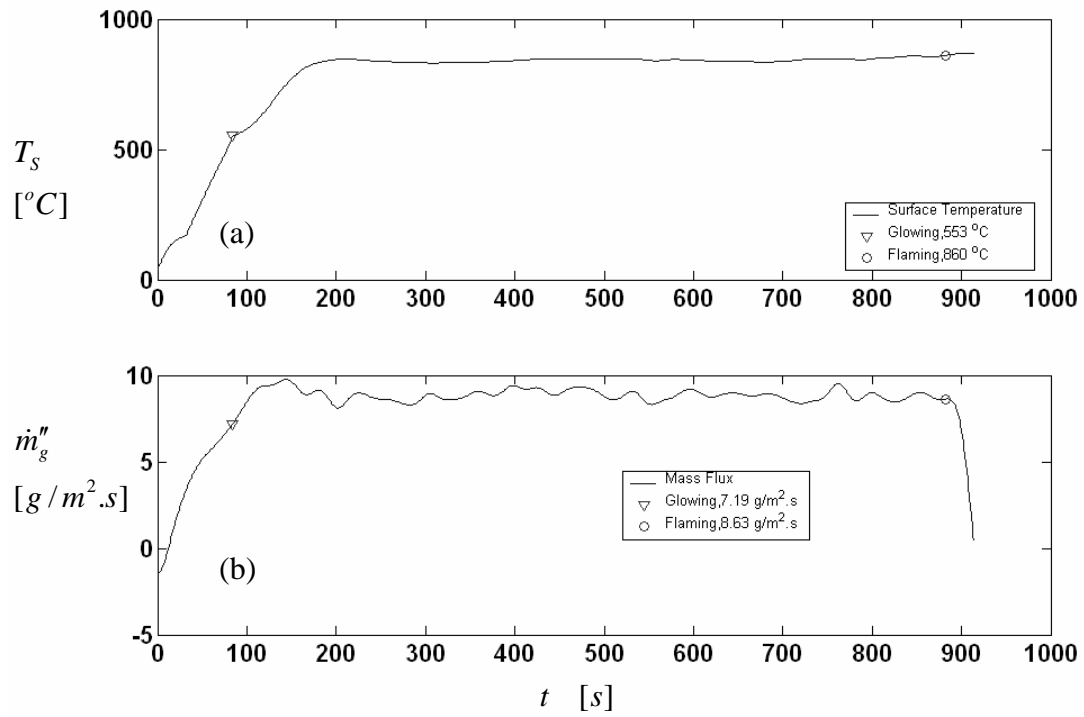


Figure C13: (a) surface temperature and (b) mass flux time histories (Test ID: 30-7-AC)

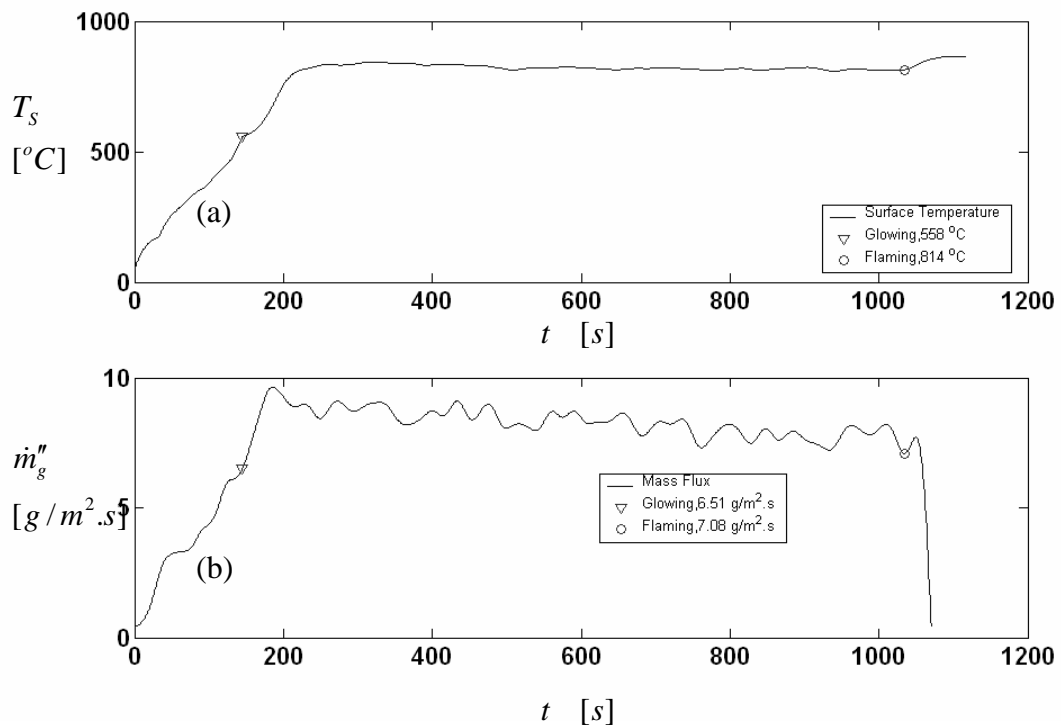


Figure C14: (a) surface temperature and (b) mass flux time histories (Test ID: 30-9-AC)

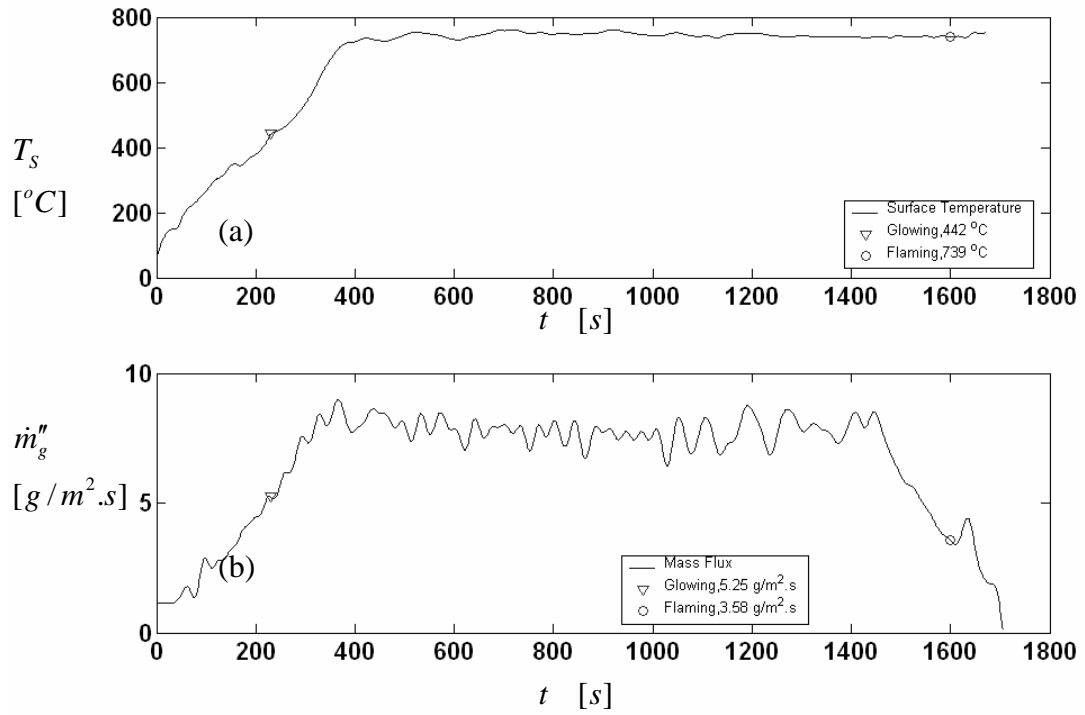


Figure C15: (a) surface temperature and (b) mass flux time histories (Test ID: 25-12-AC)

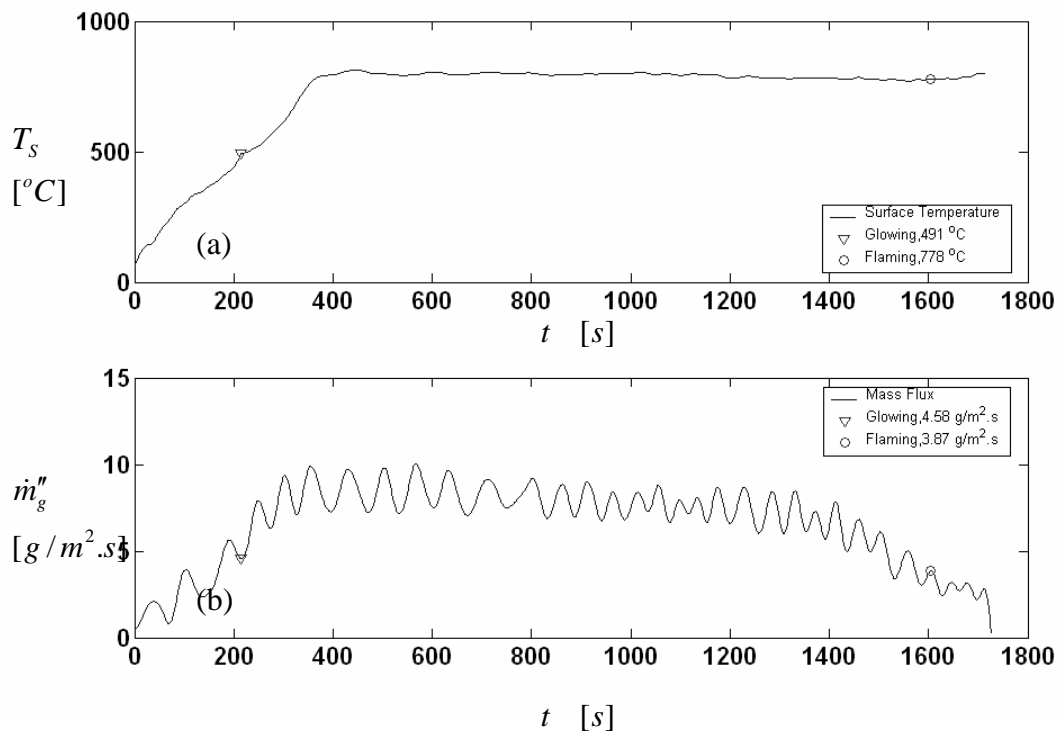


Figure C16: (a) surface temperature and (b) mass flux time histories (Test ID: 25-13-AC)

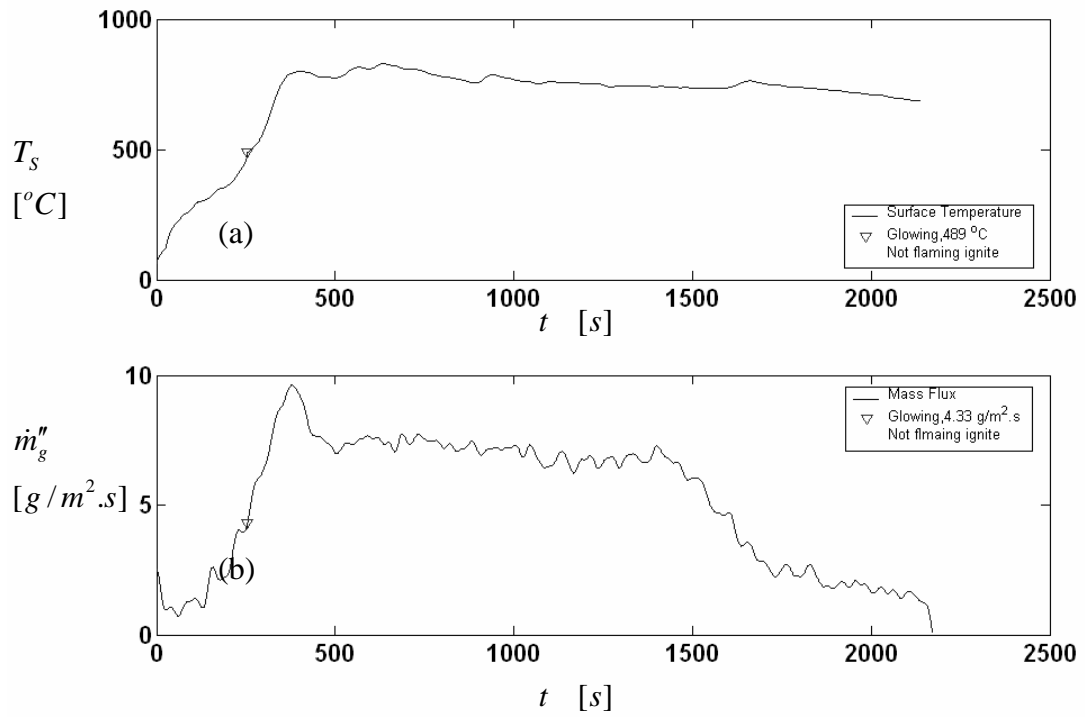


Figure C17: (a) surface temperature and (b) mass flux time histories (Test ID: 20-17-AC)

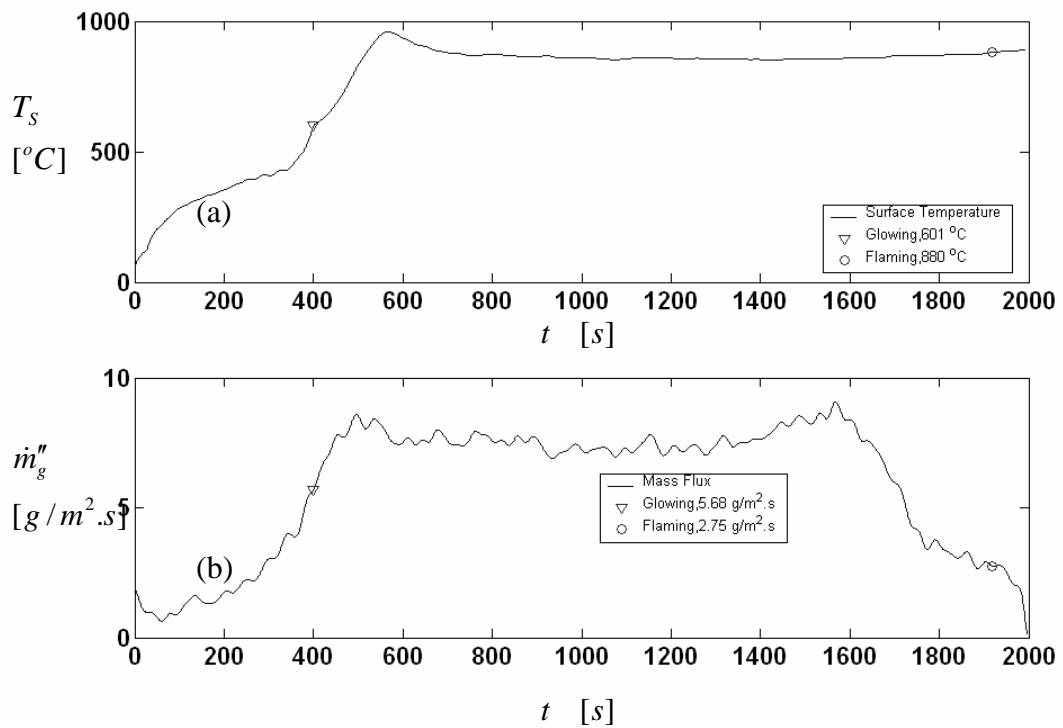


Figure C18: (a) surface temperature and (b) mass flux time histories (Test ID: 20-23-AC)

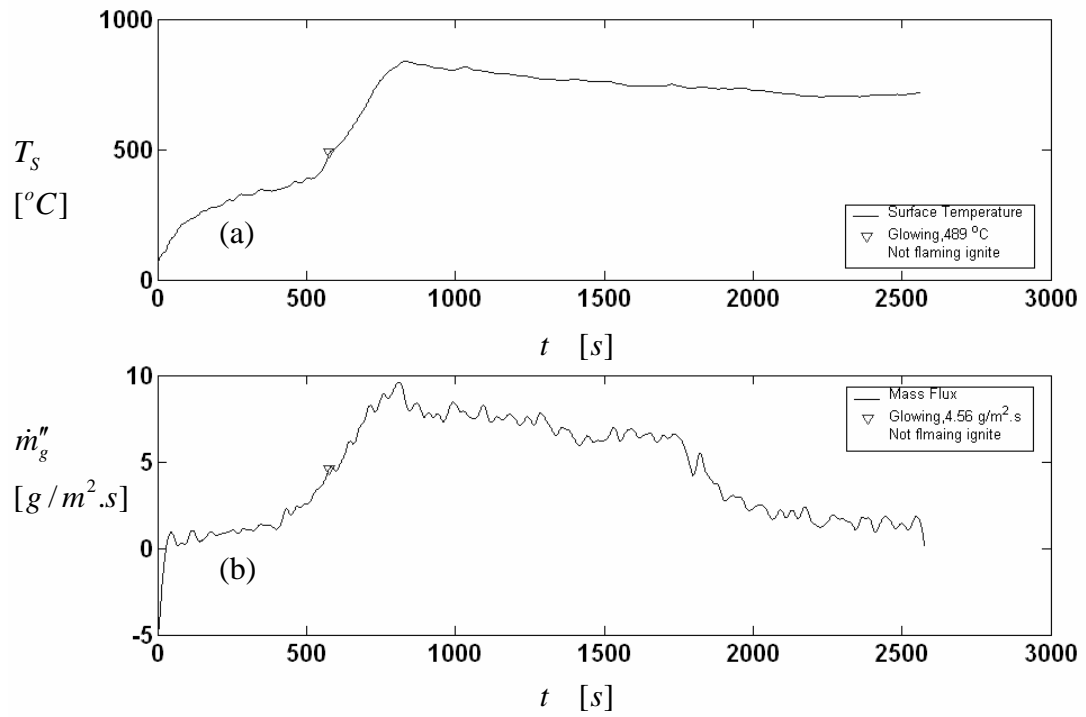


Figure C19: (a) surface temperature and (b) mass flux time histories (Test ID: 18-19-AC)

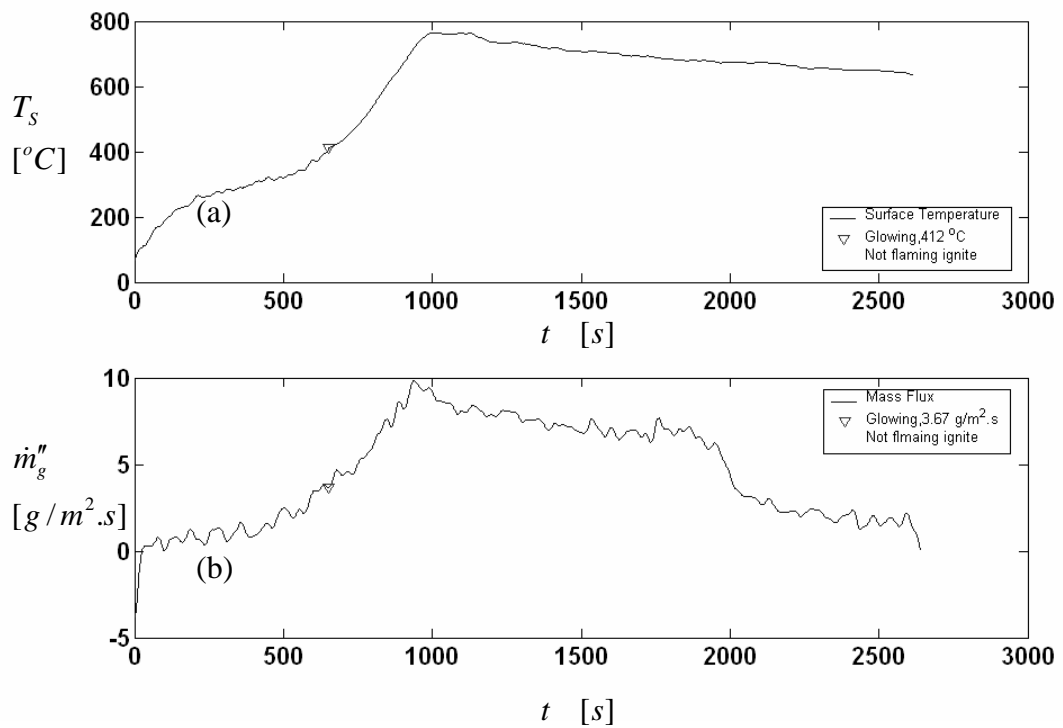


Figure C20: (a) surface temperature and (b) mass flux time histories (Test ID: 18-25-AC)

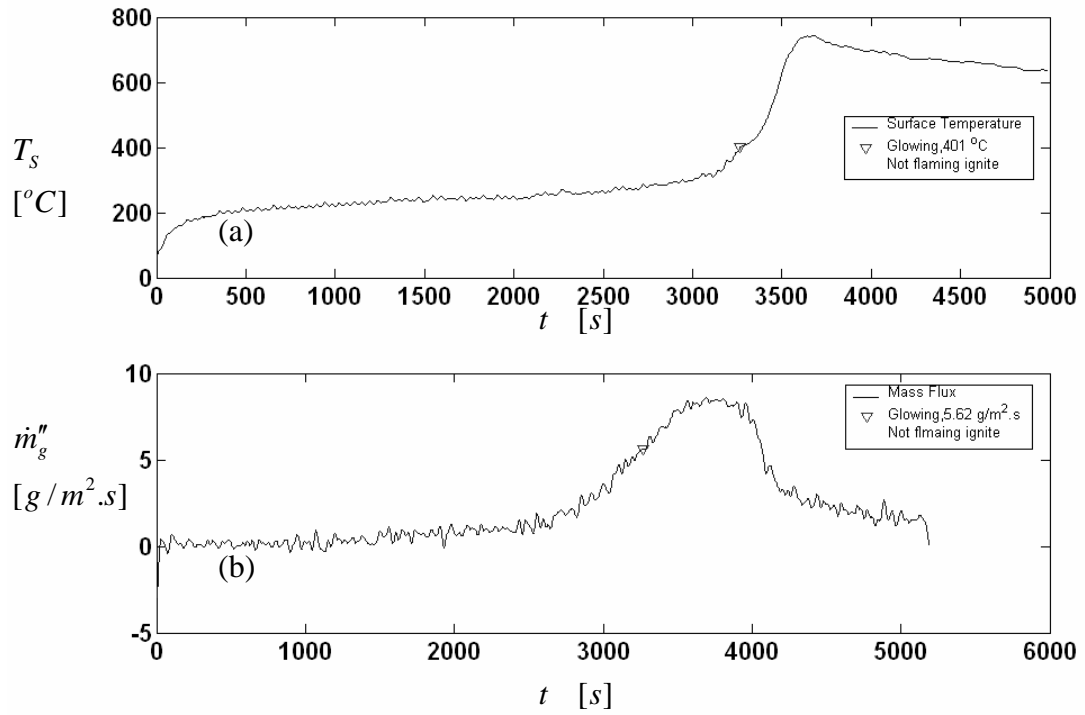


Figure C21: (a) surface temperature and (b) mass flux time histories (Test ID: 10-26-AC)

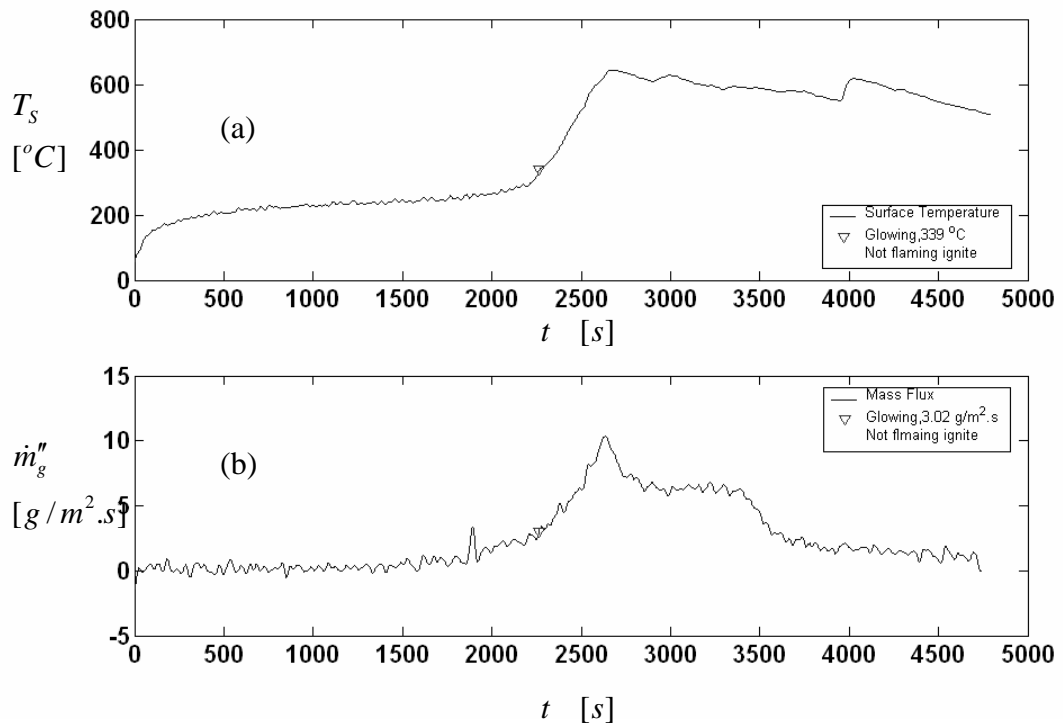


Figure C22: (a) surface temperature and (b) mass flux time histories (Test ID: 10-29-AC)

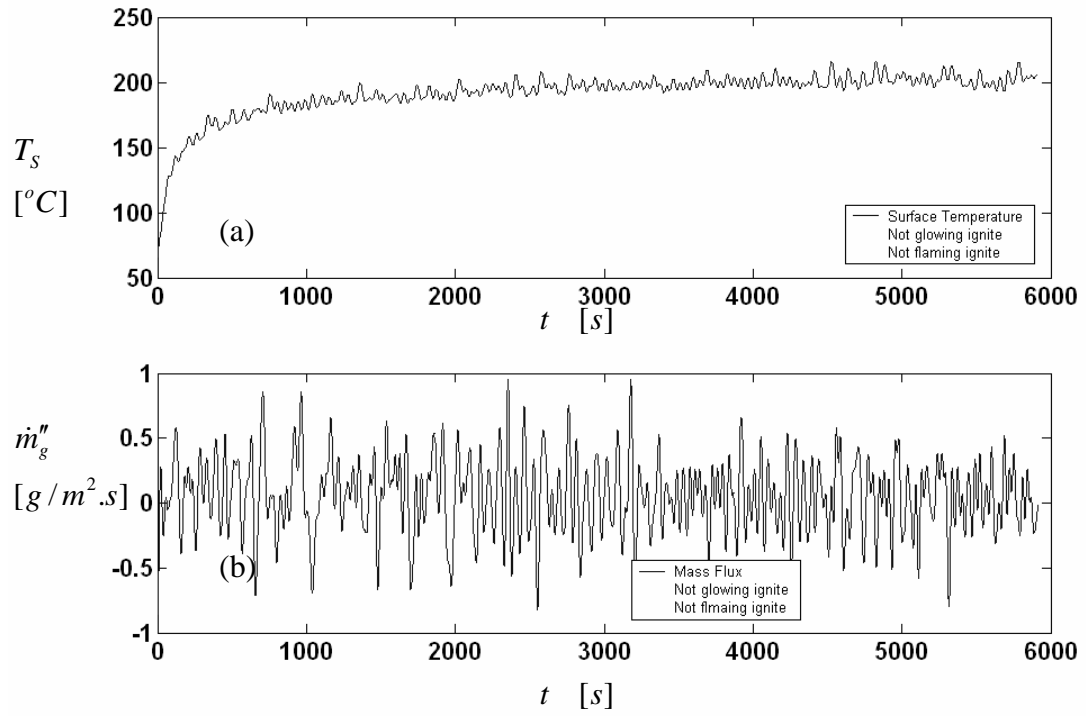


Figure C23: (a) surface temperature and (b) mass flux time histories (Test ID: 9-34-AC)

References

1. Boonmee, N., Quintiere, J.G., *Radiant Auto-Ignition of Wood*, Master Thesis, in *Fire Protection Engineering*. 2001, University of Maryland: College Park.
2. Boonmee, N., Quintiere, J.G., *Glowing and Flaming Auto-Ignition of Wood*. Twenty-Ninth Symposium (International) on Combustion, 2002. **29**: p. 289-296.
3. Janssens, M., *Piloted Ignition of Wood: A Review*. *Fire and Materials*, 1991. **15**: p. 151-167.
4. Atreya, A., *Ignition of Fire*. *Philosophical Transaction of the Royal Society of London*, 1998. **356**: p. 2787-2813.
5. Babrauskas, V., *Ignition of wood: A Review of the State of the Art*. *Journal of Fire Protection Engineering*, 2002. **12**: p. 163-189.
6. Di Blasi, C., *Ignition and Flame Spread Across Solid Fuels*, in *Numerical Approaches to Combustion Model*, E.S. Oran ,J.P. Boris, Editors. 1991, Progress in Astronautics and Aeronautics. p. 643-671.
7. Di Blasi, C., *Modeling and Simulation of Combustion Processes of Charring and Non-Charring Solid Fuels*. *Progress in Energy and Combustion Science*, 1993. **19**: p. 71-104.
8. Simms, D.L., *On the Pilot Ignition of Wood by Radiation*. *Combustion and Flame*, 1963. **7**: p. 253-261.
9. Simms, D.L., *Ignition of Cellulosic Materials by Radiation*. *Combustion and Flame*, 1960. **4**: p. 293-300.

10. Simms, D.L., Law, M., *The Ignition of Wet and Dry Wood by Radiation*. Combustion and Flame, 1967. **11**: p. 377-388.
11. Lee, C.K., Diehl, J.R., *Combustion of Irradiated Dry and Wet Oak*. Combustion and Flame, 1981. **42**: p. 123-138.
12. Vyas, R.J., Welker, J.R., *End-Grain Ignition of Wood*. J. Fire & Flammability, 1975. **6**: p. 355-361.
13. Kashiwagi, T., *Effects of Sample Orientation on Radiative Ignition*. Combustion and Flame, 1982. **44**: p. 223-245.
14. Kashiwagi, T., *Experimental Observation of Radiative Ignition Mechanisms*. Combustion and Flame, 1979. **34**: p. 231-244.
15. Kashiwagi, T., *Effects of Attenuation of Radiation on Surface Temperature for Radiative Ignition*. Combustion Science and Technology, 1979. **20**: p. 225-234.
16. Kashiwagi, T., Ohlemiller, T.J., *A Study of Oxygen Effects on Nonflaming Transient Gasification of PMMA and PE during Thermal Irradiation*. Nineteenth Symposium (International) on Combustion, 1982. **19**: p. 815-823.
17. Yoshizawa, Y., Kubota, H., *Experimental Study on Gas-Phase Ignition of Cellulose under Thermal Radiation*. Nineteenth Symposium (International) on Combustion, 1982. **19**: p. 787-795.
18. Atreya, A., Capentier, C., Harkleroad, M., *Effect of Sample Orientation on Piloted Ignition and Flame Spread*. Fire Safety Science Proceedings of the First International Symposium, 1985: p. 97-109.

19. Suuberg, E.M., Milosavljevic, I., Lilly, W.D., *Behavior of Charring Materials in Simulated Fire Environments*, NIST-GCR-94-645. 1994, National Institute of Standards and Technology: Gaithersburg, Maryland.
20. Martin, S.B., *Diffusion-Controlled Ignition of Cellulosic Materials by Intense Radiant Energy*. Tenth Symposium (International) on Combustion, 1964. **10**: p. 877-896.
21. Anthenien, R.A., Fernandez-Pello, A.C., *A Study of Forward Smoldering Ignition of Polyurethane Foam*. Twenty-Seventh Symposium (International) on Combustion, 1998. **27**: p. 2683-2690.
22. Bilbao, R., et al., *Experimental and Theoretical Study of the Ignition and Smoldering of Wood Including Convective Effects*. Combustion and Flame, 2001. **126**: p. 1363-1372.
23. Spearpoint, M.J., *Predicting the Ignition and Burning Rate of Wood in the Cone Calorimeter Using an Integral Model*, NIST GCR 99-775. 1999, National Institute of Standards and Technology.
24. Spearpoint, M.J., Quintiere, J.G., *Predicting the Burning of Wood Using an Integral Model*. Combustion and Flame, 2000. **123**: p. 308-324.
25. Spearpoint, M.J., Quintiere, J.G., *Predicting the Piloted Ignition of Wood in the Cone Calorimeter Using an Integral Model-Effect of Species, Grain Orientation and Heat Flux*. Fire Safety Journal, 2001. **36**(4): p. 391-415.
26. Kung, H.C., *A Mathematical Model of Wood Pyrolysis*. Combustion and Flame, 1972. **18**: p. 185-195.

27. Kung, H.C., Kalelkar, A.S., *On the Heat of Reaction in Wood Pyrolysis*. Combustion and Flame, 1973. **20**: p. 91-103.
28. Sibulkin, M., *Heat of Gasification for Pyrolysis of Charring Materials*. Fire Safety Science Proceedings of the First International Symposium, 1985: p. 391-400.
29. Parker, W.J., *Prediction of the Heat Release Rate of Wood*. Fire Safety Science Proceedings the First International Symposium, 1985: p. 207-216.
30. Tinney, R.E., *The Combustion of Wooden Dowels in Heated Air*. Tenth Symposium (International) on Combustion, 1964: p. 925-930.
31. Weatherford, W.D., Jr., Sheppard, D.M., *Basic Studies of the Mechanism of Ignition of Cellulosic Materials*. Tenth Symposium (International) on Combustion, 1964: p. 897-910.
32. Roberts, A.F., *Problems Associated with the Theoretical Analysis of the Burning of Wood*. Thirteenth Symposium (International) on Combustion, 1970: p. 893-903.
33. Ritchie, S.J., et al., *The Effect of Sample Size on the Heat Release Rate of Charring Materials*. Fire Safety Science Proceedings of the Fifth International Symposium, 1997: p. 177-188.
34. Panton, R.L., Rittmann, J.G., *Pyrolysis of A Slab of Porous Material*. Thirteenth Symposium (International) on Combustion, 1970: p. 881-889.
35. Di Blasi, C., *Influence of Physical Properties on Biomass Devolatilization*. Fuel, 1997. **76**: p. 957-964.

36. Wichman, I.S., Atreya, A., *A Simplified Model for the Pyrolysis of Charring Materials*. Combustion and Flame, 1987. **68**: p. 231-247.
37. Rhodes, B.T., Quintiere, J.G., *Burning Rate and Flame Heat Flux for PMMA in a Cone Calorimeter*. Fire Safety Journal, 1996. **26**: p. 221-240.
38. Delichatsios, M.A., Panagiotou, T.H., Kiley, F., *The Use of Time to Ignition Data for Characterizing the Thermal Inertia and the Minimum (Critical) Heat Flux for Ignition or Pyrolysis*. Combustion and Flame, 1991. **84**: p. 323-332.
39. Kansa, J.E., Perlee, H.E., Chaiken, R.F., *Mathematical Model of Wood Pyrolysis Including Internal Forced Convection*. Combustion and Flame, 1977. **29**: p. 311-324.
40. Di Blasi, C., *On the Influence of Physical Process on the Transient Pyrolysis of Cellulosic Samples*. Fire Safety Science Proceedings of the Fourth International Symposium, 1994: p. 229-240.
41. Fredlund, B., *A Model for Heat and Mass Transfer in Timber Structures during Fire: A Theoretical, Numerical and Experimental Study*, LUTVDG/(TBB-1003). 1988, Institute of Science and Technology, Department of Fire Safety Engineering, Lund University, Sweden.
42. Yuen, R., et al., *A Three-Dimensional Mathematical Model for the Pyrolysis of Wet Wood*. Fire Safety Science Proceedings of the Fifth International Symposium, 1997: p. 189-200.
43. Gandhi, P.D., Kanury, A.M., *Criterion for Spontaneous Ignition of Radiantly Heated Organic Solids*. Combustion Science and Technology, 1986. **50**: p. 233-254.

44. Gandhi, P.D., Kanury, A.M., *Thresholds for Spontaneous Ignition of Organic Solids Exposed to Radiant Heating*. Combustion Science and Technology, 1988. **57**: p. 113-128.
45. Kashiwagi, T., *A Radiative Ignition Model of a Solid Fuel*. Combustion Science and Technology, 1974. **8**: p. 225-236.
46. Di Blasi, C., et al., *Numerical Model of Ignition Processes of Polymeric Materials Including Gas-Phase Absorption of Radiation*. Combustion and Flame, 1991. **83**: p. 333-344.
47. Atreya, A., Wichman, I.S., *Heat and Mass Transfer During Piloted Ignition of Cellulosic Solids*. Transaction of the ASME Journal of Heat Transfer, 1989. **111**: p. 719-725.
48. Tzeng, L.S., Atreya, A., Wichman, I.S., *A One-Dimensional Model of Piloted Ignition*. Combustion and Flame, 1990. **80**: p. 94-106.
49. Kung, H.C., *The Burning of Vertical Wooden Slabs*. Fifteenth Symposium (International) on Combustion, 1974. **15**: p. 243-253.
50. Kim, J.S., De Ris, J., Kroesser, F.W., *Laminar Free-Convective Burning of Fuel Surfaces*. Thirteen Symposium (International) on Combustion, 1971. **13**: p. 949-961.
51. Ahmad, T., *Investigation of the Combustion Region of Fire-Induced Plume along Upright Surface, Ph.D. Dissertation*, in *Mechanical Engineering*. 1978, The Pennsylvania State University.

52. Zhou, Y.Y., *Computational Analysis of Pyrolysis and Ignition of Polymeric Materials PhD Thesis*, in *Department of Mechanical Engineering*. 2001, University of California Berkeley, California: Berkeley.
53. Zhou, Y.Y., Walther, D.C., Fernandez-Pello, A.C., *Numerical Analysis of Piloted Ignition of Polymeric Materials*. *Combustion and Flame*, 2002. **131**: p. 147-158.
54. McGrattan, K.B., et al., *Fire Dynamics Simulator (Version 2) - Technical Reference Guide*, NISTIR 6783. 2001, National Institute of Standards and Technology: Gaithersburg, Maryland.
55. Tsai, T.H., et al., *Experimental and Numerical Study of Autoignition and Piloted Ignition of PMMA Plates in a Cone Calorimeter*. *Combustion and Flame*, 2001. **124**: p. 466-480.
56. Nakabe, K., et al., *Ignition and Transition to Flame Spread over a Thermally Thin Cellulosic Sheet in a Microgravity Environment*. *Combustion and Flame*, 1994. **98**: p. 361-374.
57. Nakamura, Y., Yamashita, H., Takeno, T., *Effects of Gravity and Ambient Oxygen on a Gas-Phase Ignition over a Heated Solid Fuel*. *Combustion and Flame*, 2000. **120**: p. 34-48.
58. Nakamura, Y., Takeno, T., *Appropriate Criterion of Spontaneous Ignition of an Externally Heated Solid Fuel in Numerical Study*. *JSME International Journal*, 2001. **44**(2): p. 288-298.
59. Shih, I.Y., Tien, J.S., *A Three-Dimensional Model of Steady Flame Spread over a Thin Solid in Low-Speed Concurrent Flows*. *Combustion Theory Modeling*, 2003. **7**: p. 677-704.

60. Nakamura, Y., et al., *Enclose Effects on Flame Spread Over Solid Fuels in Microgravity*. Combustion and Flame, 2002. **130**: p. 307-321.
61. Mell, W.E., Kashiwagi, T., *Dimensional Effects on the Transition from Ignition to Flame Spread in Microgravity*. Twenty-Seventh Symposium (International) on Combustion, 1998: p. 2635-2641.
62. Urbas, J., Parker, W.J., *Surface Temperature Measurement on Burning Wood Specimens in the Cone Calorimeter and the Effect of Grain Orientation*. Fire and Materials, 1993. **17**: p. 205-208.
63. Incropera, F.P., DeWitt, D.P., *Fundamentals of Heat and Mass Transfer*. 4th ed. 1996, New York: John Wiley & Sons.
64. Roberts, A.F., *A Review of Kinetics Data for the Pyrolysis of Wood and Related Substances*. Combustion and Flame, 1970. **14**: p. 264-272.
65. Antal, M.J., Varhegyi, G., *Cellulose Pyrolysis Kinetics: The Current State of Knowledge*. Industrial Engineering Chemical Research, 1995. **34**: p. 703-717.
66. Kanury, A.M., *Thermal Decomposition Kinetics of Wood Pyrolysis*. Combustion and Flame, 1972. **18**: p. 75-83.
67. Lewellen, P.C., Peters, W.A., Howard, J.B., *Cellulose Pyrolysis Kinetics and Char Formation Mechanism*. Sixteenth Symposium (International) on Combustion, 1976: p. 1471-1480.
68. Milosavljevic, I., Suuberg, E.M., *Cellulose Thermal Decomposition Kinetics: Global Mass Loss Kinetics*. Industrial Engineering Chemical Research, 1995. **34**: p. 1081-1091.

69. Suuberg, E.M., Milosavljevic, I., Oja, V., *Two-Regime Global Kinetics of Cellulose Pyrolysis: The Role of Tar Evaporation*. Twenty-Sixth Symposium (International) on Combustion, 1996: p. 1515-1521.
70. Orfao, J.J.M., Antunes, F.J.A., Figueiredo, J.L., *Pyrolysis Kinetics of Lignocellulosic Materials-Three Independent Reactions Model*. Fuel, 1999. **78**: p. 349-358.
71. Orfao, J.J.M., Figueiredo, J.L., *A Simplified Method for Determination of Lignocellulosic Materials Pyrolysis Kinetics from Isothermal Thermogravimetric Experiments*. Thermochemica Acta, 2001. **380**: p. 67-78.
72. Wu, Y., Dollimore, D., *Kinetics Studies of Thermal Degradation of Natural Cellulosic Materials*. Thermochemica Acta, 1998. **324**: p. 49-57.
73. Gronli, M.G., Varhegyi, G., Di Blasi, C., *Thermogravimetric Analysis and Devolatilization Kinetics of Wood*. Industrial Engineering Chemical Research, 2002. **41**: p. 4201-4208.
74. Broido, A., Nelson, M.A., *Char Yield on Pyrolysis of Cellulose*. Combustion and Flame, 1975. **24**: p. 263-268.
75. Flynn, J.H., *A General Differential Technique for the Determination of Parameters for $d\alpha/dt = f(\alpha)A\exp(-E/RT)$: energy of activation, pre-exponential factor and order of reaction (when applicable)*. Journal of Thermal Analysis, 1991. **37**: p. 293-305.
76. Lyon, R.E., *An Integral Method of Nonisothermal Kinetic Analysis*. Thermochemica Acta, 1997. **297**: p. 117-124.

77. Hatakeyama, T., Quinn, F.X., *Thermal Analysis Fundamentals and Application to Polymer Science*. 1999, Chichester: John Wiley & Sons.
78. Rath, J., et al., *Heat of Wood Pyrolysis*. Fuel, 2003. **82**: p. 81-91.
79. Kashiwagi, T., Nambu, H., *Global Kinetic Constants for Thermal Oxidation Degradation of a Cellulosic Paper*. Combustion and Flame, 1992. **88**: p. 345-368.
80. Babrauskas, V., *Ignition Handbook*. 2003, Issaquah: Fire Science Publishers.
81. Baer, A.D., Ryan, N.W., *Ignition of Composite Propellants by Low Radiant Fluxes*. AIAA Journal, 1965. **3**: p. 884-889.
82. Moussa, N.A., Toong, T.Y., Garris, C.A., *Mechanism of Smoldering of Cellulosic Materials*. Sixteenth Symposium (International) on Combustion, 1976: p. 1447-1457.
83. Saastamoinen, J.J., Aho, M.J., Linna, V.L., *Simultaneous Pyrolysis and Char Combustion*. Fuel, 1993. **72**: p. 599-609.
84. Kanury, A.M., *Introduction to Combustion Phenomena*. 2nd ed. 1977, New York: Gordon and Breach Science Publishers.
85. Turns, S.R., *An Introduction to Combustion: Concepts and Applications*. 2nd ed. 2000, New York: McGraw Hill.
86. Branca, C., Di Blasi, C., *Global Kinetics of Wood Char Devolatilization and Combustion*. Energy & Fuels, 2003. **17**: p. 1609-1615.
87. Crank, J., Gupta, R.S., *A Method for Solving Moving Boundary Problems in Heat Flow Using Cubic Splines or Polynomials*. J. Inst. Maths. Applics, 1972. **10**: p. 296-304.

88. Semenov, N.N., *Chemical Kinetics and Chain Reactions*. 1935, London: Oxford Univ. Press.
89. Kanury, A.M., *Ignition of Cellulosic Solid: Minimum Pyrolysate Mass Flux Criterion*. *Combustion Science and Technology*, 1977. **16**: p. 89.
90. Kays, W.M., Crawford, M.E., *Convective Heat and Mass Transfer*. 3rd ed. 1993: McGraw-Hill, Inc, New York, NY, USA.
91. Ferziger, J.H., Peric, M., *Computational Methods for Fluid Dynamics*. 3rd ed. 2002, New York: Springer.
92. Alvares, N.J., Martin, S.B., *Mechanisms of Ignition of Thermally Irradiated Cellulose*. Thirteenth Symposium (International) on Combustion, 1970: p. 905-914.
93. Quintiere, J.G., *Fundamentals of Fire Phenomena: Chapter 7, Ignition of Solids (Draft)*.
94. Fernandez-Pello, A.C., *The Solid Phase*, in *Combustion Fundamentals of Fire*, G. Cox, Editor. 1995, Academic Press, London, UK.
95. Westbrook, C.K., Dryer, F.L., *Chemical Kinetic Modeling of Hydrocarbon Combustion*. *Progress in Energy and Combustion Science*, 1984. **10**: p. 1-57.
96. Frey, A.E., Jr., Tien, J.S., *A Theory of Flame Spread over a Solid Fuel Including Finite-Rate Chemical Kinetics*. *Combustion and Flame*, 1979. **36**: p. 263-289.
97. Duh, F.C., Chen, C.H., *A Theory of Downward Flame Spread over a Thermally Thin Flue*. *Combustion Science and Technology*, 1991. **77**: p. 291-305.

98. Di Blasi, C., et al., *Numerical Simulation of Opposed Flow Flame Spread over a Thermally Thick Solid Fuel*. Combustion Science and Technology, 1987. **54**: p. 25-36.
99. Zabetakis, M.G., *Flammability Characteristics of Combustion Gases and Vapors*, Bulletin 627. 1965, Bureau of Mines.
100. Tewarson, A., *Generation of Heat and Chemical Compounds in Fire*, in *SFPE Handbook of Fire Protection Engineering*, P.J. DiNenno, Editor. 1995, NFPA, Quincy, MA. p. 3-35 - 3-124.
101. Glassman, I., *Combustion*. 3rd ed. 1996, New York: Academic Press.
102. Quintiere, J.G., McCaffrey, B.J., *The Burning of Wood and Plastic Cribs in an Enclosure: Volume I*, NBSIR 80-2054. 1980, National Bureau of Standards.
103. Ozisik, M.N., *Finite Difference Methods in Heat Transfer*. 1st ed. 1994, Boca Raton, FL, USA: CRC Press, Inc.
104. Tannehill, J.C., Anderson, D.A., Pletcher, R.H., *Computational Fluid Mechanics and Heat Transfer*. 2nd ed. 1997: Taylor&Francis Publisher, Washington, DC, USA.